Characterisation and Optimisation of the Herschel-SPIRE Imaging Photometer Through Simulations

by

Bruce Sibthorpe

A thesis submitted to

Cardiff University

for the degree of

Doctor of Philosophy

2007

ProQuest LLC
789 East Eisenhower Parkway
P.O. Box 1346
Ann Arbor, MI 48106-1346

Acknowledgments

Foremost I would like to thank my supervisor Matt Griffin for his support throughout this project, and particularly for his help in drafting this thesis. I also thank Phil Mauskopf, Tim Waskett, and Pete Hargrave for their significant contributions to this work, and for their advice.

Furthermore I would like to thank Emma for the love and encouragement she has given me over the course of this work.

I must also acknowledge the entire BLAST consortium for their help and friendship. I would specifically like to recognise Edward Chapin and Guillaume Patanchon for their contributions to the BLAST work presented in this thesis.

In addition to those directly involved with my work I would also like to thank Derek Ward-Thompson, Dave Nutter, Jason Kirk, Haley Gomez and Lloyd Watkin, all of whom have provided useful guidance throughout this project.

I'd like to thank my housemates Robbie Auld, Gustav Teleberg and Mike Zemcov, as well as all of my friends for their help, support, and friendship. They have made my time on this project a fun and happy one.

Finally I thank my parents for their continued support and encouragement in this and future work.

Abstract

The Spectral and Photometric Imaging Receiver (SPIRE) is one of the three instruments on-board the European Space Agency's Herschel Space Observatory, due for launch in 2008. SPIRE is a dual instrument comprising a photometer, and imaging Fourier transform spectrometer.

This thesis deals with the design and operation of a software simulator for the SPIRE photometer. The simulator architecture and modelling methods are described, and the fidelity of its output verified.

This simulation software is then used to optimise and characterise data from the SPIRE photometer. The optimum observing parameters are derived, in order to maximise observing efficiency, and data quality. The impact of uncorrelated $1/f$ noise on the extraction of sources of arbitrary scale is assessed, and quantified. This work is also extended to include the impact of uncorrelated $1/f$ noise on observations of sources in a confused environment. These results provide important information regarding the quality of SPIRE photometer data for the planning of large survey observations. The simulator is also an active tool within the SPIRE Instrument Control Centre team, and its use in the selection of the SPIRE map making algorithm is described.

This thesis also contains an analysis of observations of the Cassiopeia A supernova remnant made with the Balloon-borne Large Aperture submillimetre Telescope (BLAST), an instrument based on the SPIRE photometer design. This analysis assesses the hypothesis that supernovae might be a significant dust formation mechanism in the universe, as proposed in recent literature. Results from this study suggest that this hypothesis may be correct, but that evidence from previous observations might in fact be upper limits to the total mass of dust, rather than an absolute measurement.

Contents

List of Figures

List of Tables

Chapter 1

Introduction

1.1 FIR and Submillimetre Astronomy

The far infrared (FIR) and submillimetre (submm) portions of the electromagnetic spectrum span a wavelength range of approximately 30 μm – 1 mm. It was not until the 1980's that it became possible to perform scientifically useful observations within this region, due to both low instrument sensitivity, and high atmospheric attenuation. Excluding radiation from the cosmic microwave background (CMB), approximately half of the total energy emitted by the universe falls within this band, as shown in Figure 1.1. It is therefore a wavelength band of significant importance to astronomy.

Ultra-violet (UV) radiation will be either scattered or absorbed upon interaction with interstellar dust grains. Assuming for the moment that these grains emit as blackbodies, then absorbed energy will be re-emitted according to the Planck function,

$$B(\lambda, T) = \frac{2hc^2}{\lambda^5} \frac{1}{\exp\left(\frac{hc}{\lambda k_b T}\right) - 1}, \tag{1.1}$$

where $B(\lambda, T)$ is the intensity radiated by a blackbody as a function of wavelength, λ, and temperature T. The Planck constant is h, c is the speed of

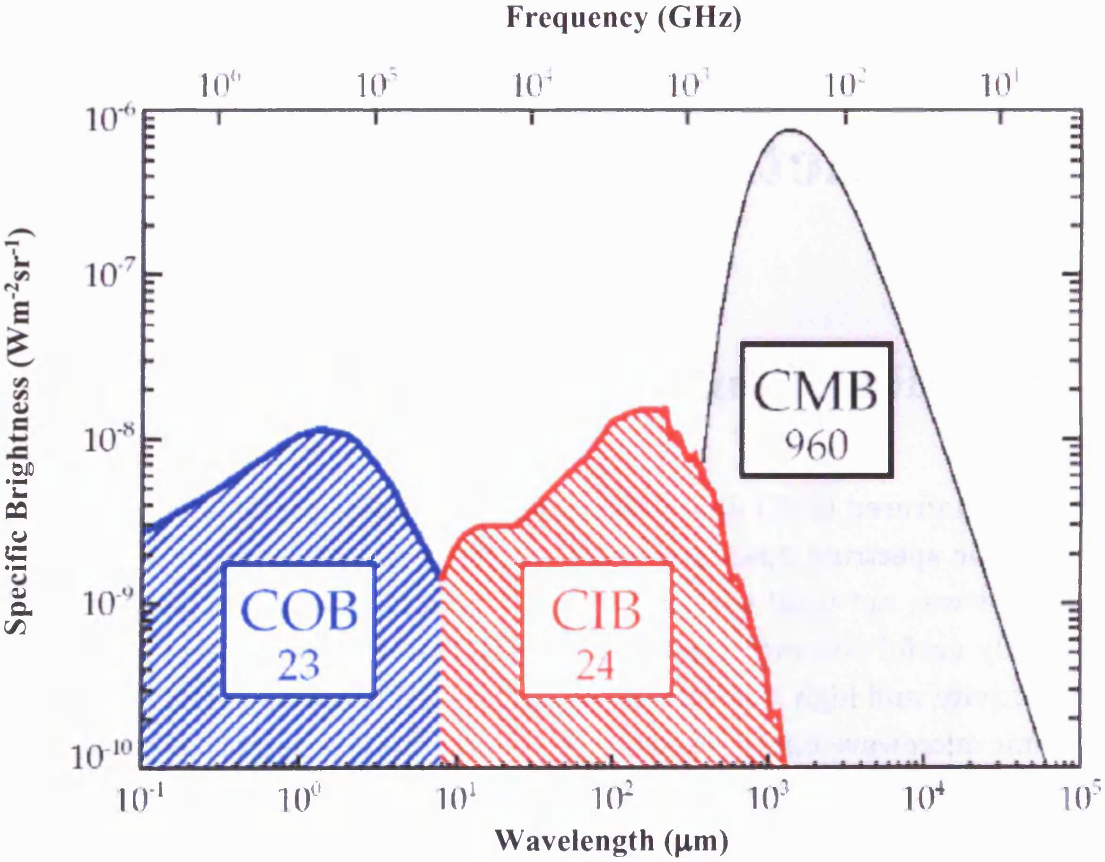

Figure 1.1: Specific brightness of the extragalactic background, showing the major contributions to the: cosmic optical background (COB), cosmic infrared background (CIB) and cosmic microwave background (CMB). The approximate specific brightness contributions are given in the boxes in units of nWm^{-2}sr^{-1} (Dole et al., 2006).

light, and k_b is Boltzmann's constant.

The Planck function peaks in the FIR/submm for sources with a temperature of ~10–50 K. Cold cosmic dust is within this temperature range, making this waveband ideal for dust observations.

For optically thin dust sources, the observed flux density depends on both dust temperature and density. This makes the determination of the source physical parameters difficult, as the same observed brightness could be due to a number of different combinations of parameters. In order to break this temperature/density degeneracy, a range of multi-wavelength measurements, which span the peak of the spectral energy distribution (SED), is required. If a good estimate of the peak cannot be made, then it is not possible to determine with any accuracy the temperature of the source, and hence physical conditions of the cloud.

The FIR/submm emission from a galaxy can account for approximately ~30-100% of its total flux (de Jong, 1984). As a result a great deal of research can be carried out in a wide range of galactic and extra-galactic studies, such as the formation and life cycles of stars, the origin and composition of the interstellar medium (ISM), and studies of both nearby and distant galaxies. The peak emission of many distant galaxies for example, is redshifted into this wavelength range. In some cases (redshift ~ 5) galaxies can appear brighter with increasing redshift (see Figure 1.2). It is therefore possible to observe the very earliest galaxies and study their distribution and population statistics.

FIR/submm observations play a key role in the field of star formation. The condensing cloud cores, from which stars form, are located within dense clumps of interstellar material, which shield the cores from the interstellar radiation field. Therefore these cores are cool, and thus their emission peaks in the FIR/submm. Current surveys of these cores are limited by an incomplete census of young prestellar and protostellar cores.

The ability to see through the surrounding molecular cloud, which is optically thin at these wavelengths, and observe directly the embedded object, enables the study of a vital point in the star formation process, which oth-

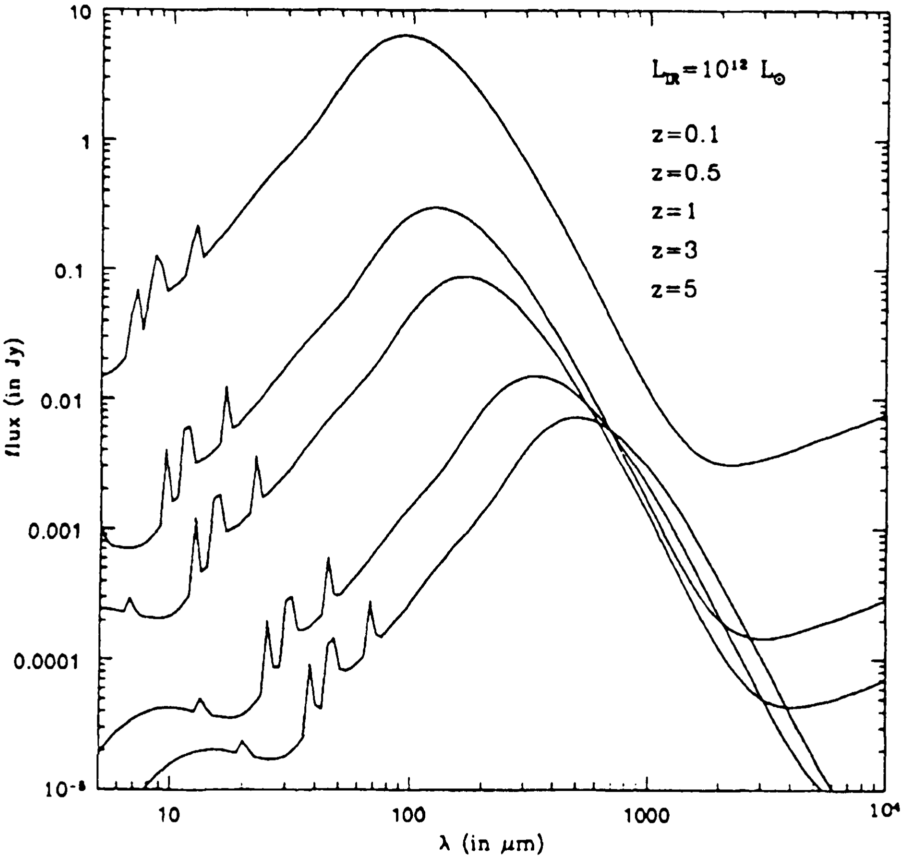

Figure 1.2: Galaxy spectrum in the submm/FIR region for a galaxy with luminosity of $10^{12}L_\odot$ at redshifts of z = 0.1, 0.5, 1, 3, 5 from top to bottom respectively (Guiderdoni et al., 1998).

erwise could only be studied theoretically. Multi-wavelength observations provide the data required to determine the temperature and density of these newly forming stars, and thus derive their mass (see Section 2.4.2), as well as information relating to the initial conditions of star formation.

The FIR/submm waveband also contains a wide range of atomic, molecular, and fine structure line features. A sample spectrum from a ground based survey is given in Figure 1.3. The emission and absorption features due to the atmosphere are shown by the top line in the figure, and the astronomical features are shown below. A high density of features can be clearly seen. This spectrum was obtained at the ground based Caltech Submillimetre Observatory (CSO) in Hawaii.

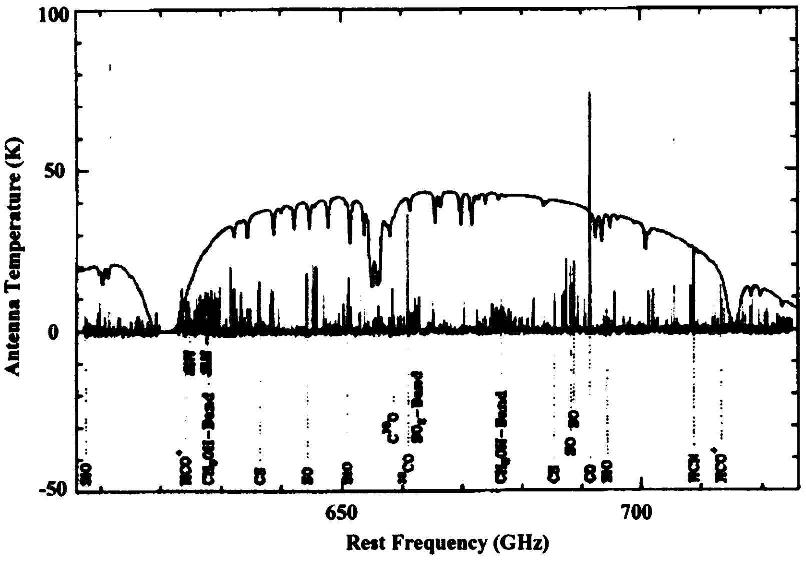

Figure 1.3: Sample spectrum in the FIR/submm band taken at the CSO. The top line is atmospheric emission/absorption, and the bottom line is the astronomical spectrum (de Graauw et al., 2005).

Measurement of the gas emission provides physical information about the region, such as gas abundances, density, temperature and kinematics. Detection of various types of gas also help to characterise regions. The bright CO emission line for example, seen in Figure 1.3, is typically a tracer of molecular hydrogen, and thus molecular clouds.

1.1.1 Observing in the FIR and Submillimetre

There are two principal obstacles to observing at FIR/submm wavelengths. The first is the high atmospheric attenuation of FIR/submm radiation due to absorption by water vapour. The level of atmospheric attenuation is a function of the line-of-sight water vapour concentration. Therefore in an attempt to reduce this, observatories are often sited at high altitude sites, such as Mauna Kea in Hawaii at 4092 m (site of the James Clarke Maxwell Telescope, JCMT). In an effort to reduce yet further the effects of atmospheric attenuation, some telescopes have been flown from aircraft, such as the Kuiper Airborne Observatory, KAO (Cameron, 1976), or higher yet from high altitude balloons such as the Balloon-borne Large Aperture Submillimetre Telescope, BLAST (Devlin et al., 2004). The only way to eliminate entirely this effect is to site the telescope in space, e.g. Infrared Space Observatory, ISO (Kessler et al., 1996), Infrared Astronomical Satellite, IRAS (Neugebauer et al., 1984), Midcourse Space Experiment, MSX (Mill, 1994), or the Spitzer Space Telescope (Werner, 2006). These air/space borne telescopes suffer however from a lack of resolution, due to size and cost limitations imposed by their transport vehicles. Although much of the atmosphere is opaque within this spectral range, there are a small number of atmospheric transmission windows, in which ground based observations can be made from a good high site, such as Mauna Kea. These windows are at approximately 350, 450, 750, and 850 μm, and have transmissions typically greater than 60% (Figure 1.4). Several of these windows (principally the 450 μm and 850 μm windows) were used by the Submillimetre Common User Bolometer Array (SCUBA) which was mounted on the JCMT (Holland et al., 1999).

The second principal limitation is the high background power recieved by the telescope relative to the astronomical source power. Both the telescope and atmosphere are at approximately 300 K, when observing from the ground, and will thus emit strongly in the FIR, often with intensities many orders of magnitude greater than that of the target source. The situation is analogous to observing at optical wavelengths in daylight using a luminous telescope. Such high background loading results in high photon noise: the noise associated with the random arrival rate of photons at the detector. The re-

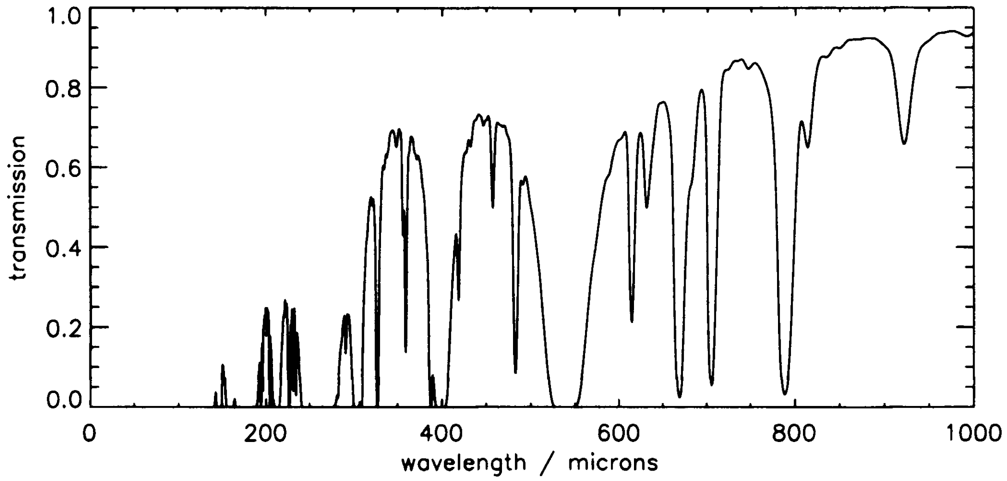

Figure 1.4: Modelled atmospheric transmission at FIR wavelengths for a precipitable water vapour level of 225 μm (Hayton, 2004).

sult is a degraded instrument sensitivity. The primary contribution to this high background comes from atmospheric emission, and is thus impossible to overcome. Whilst clever data reduction methods do allow for the subtraction of some sky effects, the only way to avoid the problem is again to site the telescope in space. Even so the sensitivity of a space telescope may still be limited by the background loading from emission by the telescope or optics. This can be minimised by cooling the optics to cryogenic temperatures, as was done for ISO and Spitzer, though this may not be practical or cost effective when dealing with telescopes with large apertures.

Observations in the submm/FIR are often made by 'chopping' (Figure 1.5). Here the telescope beam is moved alternatively between two positions on the sky, commonly by the use of a moving secondary mirror. The telescope observes first an image of the sky plus source, and then just the sky. The sky background image can then be subtracted from the source plus sky image leaving solely source information. In addition to chopping an observation, a telescope is often "nodded". When nodding, a telescope switches the on and off source chop positions. Therefore, if there is any systematic difference between the two chop positions, such as a variation in the background from the telescope, then this contaminating signal can be removed.

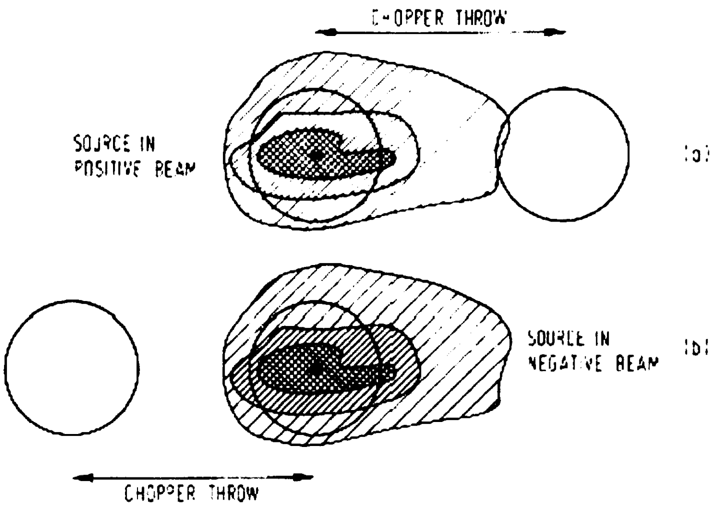

Figure 1.5: Schematic showing beam positions within a chopped observation in both nod positions (Harwit, 2001).

Confusion noise may also affect the sensitivity of an observation. This noise is due to contaminating sources within the telescope beam, due to emission from either galactic cirrus, or background galaxies. This can be reduced by increasing the angular resolution of the telescope, thus reducing the beam size. The origin of confusion noise means than it cannot be integrated down through longer observing times. It therefore determines the ultimate limit to the sensitivity of a telescope of given size.

Recently a number of instruments designed to carry out large area imaging surveys at submm/FIR wavelengths without chopping have been developed. These include BOLOCAM (Mauskopf et al., 2000), BLAST (Devlin et al., 2004), SCUBA-2 (Audley et al., 2003), LABOCA (Kreysa et al., 2003), Planck-HFI (Lamarre et al., 2003), and the PACS (Poglitsch et al., 2005) and SPIRE (Griffin et al., 2006) instruments on board the ESA Herschel space observatory (Pilbratt, 2005). Such 'scanning' instruments are no longer limited in observable source size scale by their chop throw. These systems also observe the source for the entire observation time, thus increasing the observing efficiency by a factor of 2, and the sensitivity by a factor of $\sqrt{2}$. Such instruments are however more sensitive to $1/f$ noise fluctuations, arising from atmospheric variations, or from within the detection system.

The definition of $1/f$ noise is a noise whose power spectrum decreases as one over the frequency until it meets the white noise floor, e_n (Figure 1.6). It therefore contains greater power at low frequencies, resulting in long time scale noise drifts. Longer integration time (t) of $1/f$ noise will not provide the expected $\sqrt{t}$ improvement in signal to noise ratio, and will result in a higher than expected timeline variance, as compared to white noise. $1/f$ noise can be characterised by a knee frequency, f_k. This is defined as the frequency at which the noise voltage spectral density is a factor of $\sqrt{2}$ times greater than that of the white noise voltage spectral density.

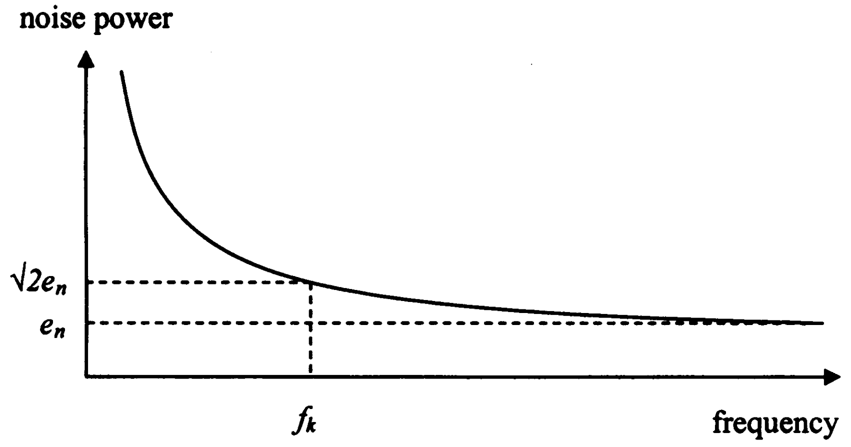

Figure 1.6: Schematic 1/f noise power spectrum illustrating the definition of f_k.

1.2 Herschel

The Herschel Space Observatory, shown in Figure 1.7 (Pilbratt, 2005), is the fourth cornerstone mission in the European Space Agency's (ESA) science programme. It will observe in the FIR and submm spanning a wavelength range of 60–670 μm, performing both photometric and spectroscopic observations. The observatory is due for launch in 2008 onboard an Ariane 5 rocket. The launch will be shared with another ESA satellite, Planck Surveyor (Tauber, 2005), a cosmic background mapping mission.

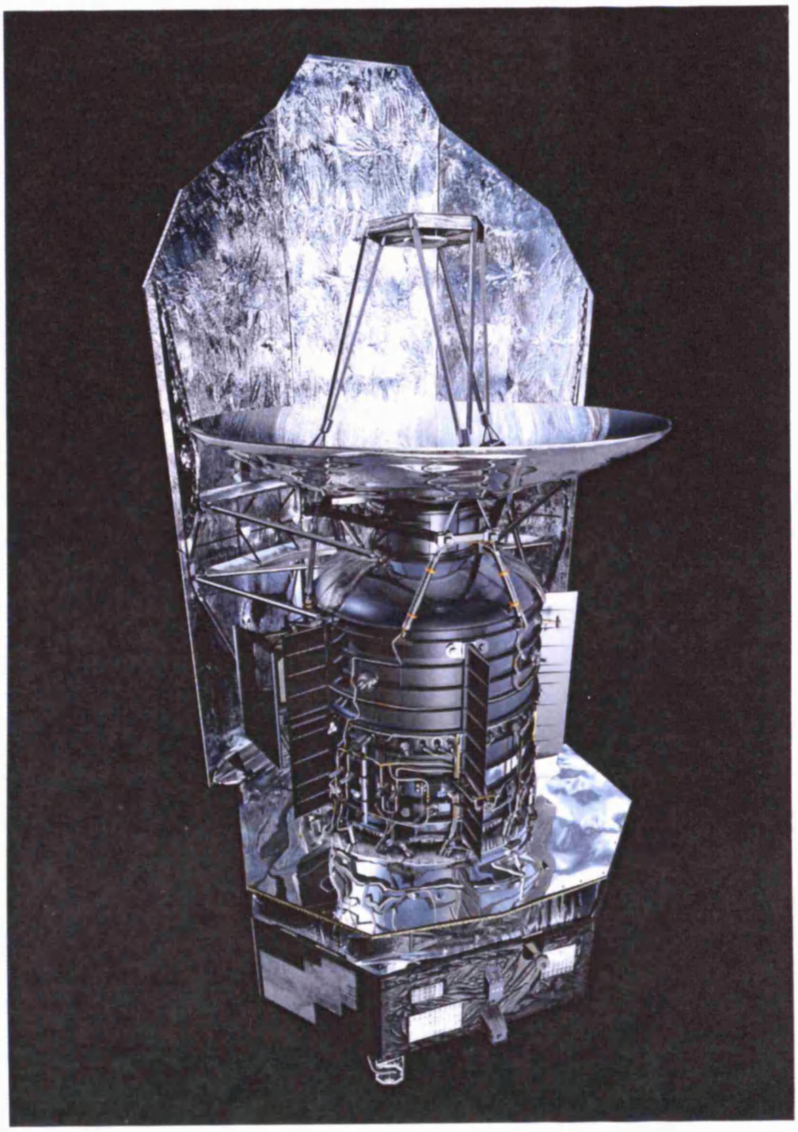

Figure 1.7: Computer generated image of the Herschel Observatory (Pilbratt, 2005).

1.2.1 Herschel Science

Herschel will be the first facility to observe in the FIR and submm wavebands from space, providing high sensitivity observations at relatively high spatial resolution, compared to previous space-borne observatories in this wavelength region. Herschel effectively targets the cold universe, with a wavelength range encompassing both the brightest atomic and molecular emission lines for sources at temperatures from 10 to a few hundred K, and the peak emission from black-body sources at temperatures of 10–50 K. High redshift galaxies will also have their peak emission redshifted into the 'prime' Herschel band, providing the ability to study some of the earliest proto-galaxies. Some prime science goals for Herschel include (Pilbratt, 2005):

- detailed investigations of the formation and evolution of galaxy bulges and elliptical galaxies in the first third of the present age of the Universe;
- detailed studies of the physics and chemistry of the interstellar medium in galaxies, both locally in our own Galaxy as well as in external galaxies;
- the physical and chemical processes involved in star formation and early stellar evolution in our own Galaxy;
- high resolution spectroscopy of a number of comets and the atmospheres of the cool outer planets and their satellites.

Observations made by Herschel will complement those of other forthcoming facilities, such as SCUBA-2 and ALMA, by providing high sensitivity low noise measurements in a similar wavelength range. They will also complement current Spitzer studies.

1.2.2 The Herschel Spacecraft

The Herschel telescope is of a Cassegrain design with a 3.5 m diameter primary mirror which is passively cooled to $\sim$80 K. The satellite will operate at the second Lagrange point of the Sun-Earth system (L2), located approximately 1.5 million km beyond the orbit of the Earth (see Figure 1.8). At this location, the background radiation from the Earth and Moon is reduced, and the satellite maintains an orbital period equal to that of the Earth. Thus, the satellite is always in the same position with respect to the Earth and Sun. This location also provides higher instantaneous sky coverage as compared to satellites in near-Earth orbits.

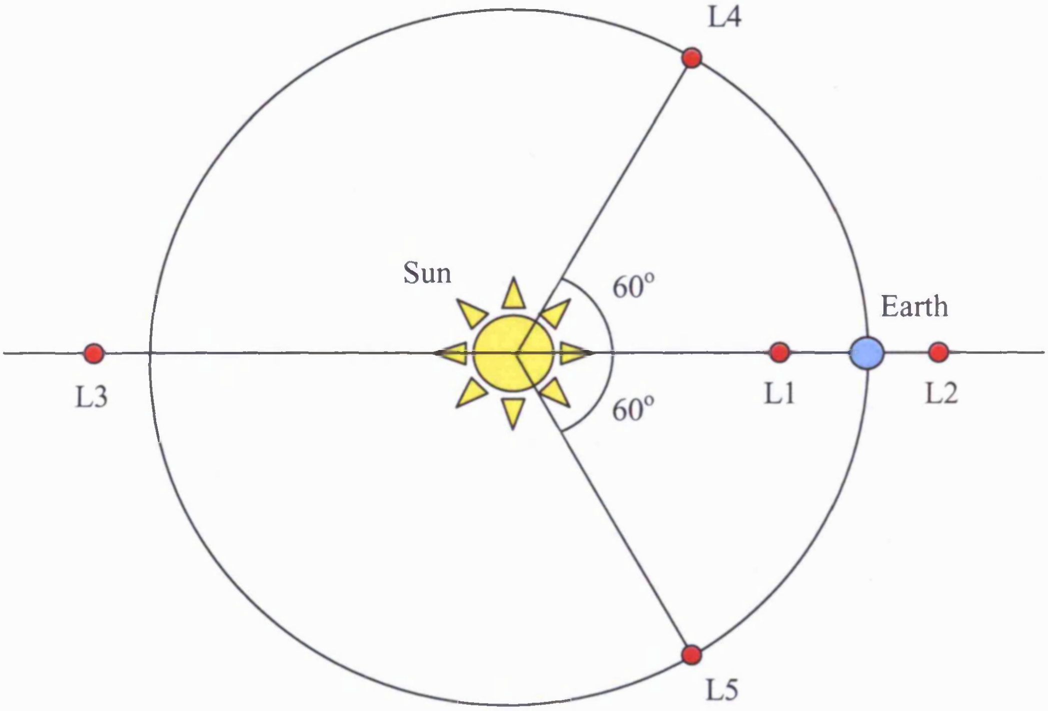

Figure 1.8: Diagram showing the 5 Lagrangian points, including L2, Herschel's operating position, with respect to the Earth and Sun.

Herschel has a payload of three instruments, two photometer/medium resolution spectrometers, PACS and SPIRE, and a high resolution heterodyne spectrometer, HIFI (see Section 1.2.3 for details of the individual instruments). All of the instruments operate at cryogenic temperatures, and are cooled by a 1.7 K superfluid helium cryostat.

The spacecraft is protected from the heat of the Sun by a Sun shield. This shield must be kept facing the Sun at all times to avoid excess boil-off of the on-board cryogens, prevent stray light from entering the system, and maintain thermal stability. This limits the range of satellite movement, and consequently the observable area of sky at a given point in time. With reference to the telescope coordinates shown in Figure 1.9, the satellite is free to rotate about the Z axis, and has $\pm 30^\circ$ movement about the Y axis, dictated by the constraint that the Sun must not shine on the telescope or spacecraft bus. The telescope also has a roll angle constraint of $\pm 1^\circ$. This movement is generally considered to be negligible and does not appear in optimisation studies of the observing modes.

These operational restrictions mean that at any one time the telescope can point to a position within a 60° wide strip of the sky. The observable strip varies throughout the year as the Earth and telescope orbit the Sun. The observing strip will pass over all parts of the sky once during a 6 month half-orbit.

The mission is scheduled to last a minimum of 3 years, and have a total cost of ~€1 billion, resulting in an observing time cost of ~€1 million per day. This cost includes both the spacecraft and instruments. Approximately 2/3 of the observing time will be available to the general community, with the other third being allocated as guaranteed time to the instrument builders and the Herschel Science Centre (HSC) team.

1.2.3 Instruments

PACS

PACS, the Photodetector Array Camera and Spectrometer (Poglitsch et al., 2005), contains both a three colour photometer and a low–medium resolution imaging spectrometer, observing over a wavelength range of ~60–210 μm. The photometer uses two filled silicon bolometer arrays containing 16×32 and 32×64 pixels. Simultaneous operation of both arrays is possible, observing in the 60–90 or 90–130, and 130–210 μm bands. The change in short

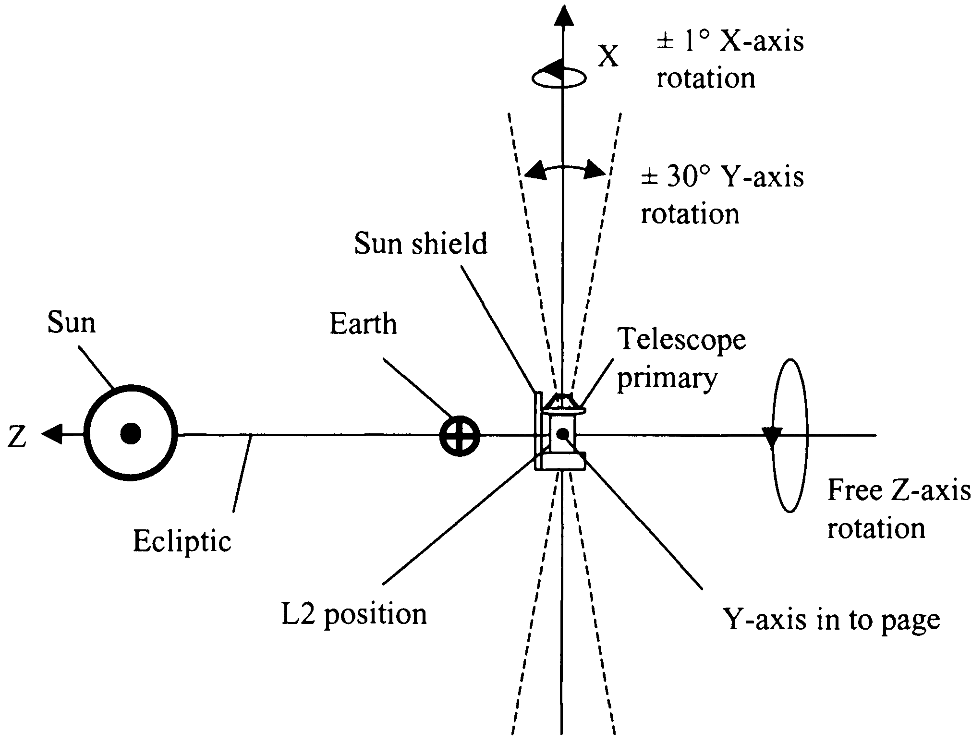

Figure 1.9: Schematic view of Herschel's observing location, L2, and definition of telescope coordinates. Also shown are the restrictions to the telescopes movement for a given observing time

wavelength band is made via a filter wheel. The spectrometer detectors are arrays of stressed and unstressed gallium doped germanium photoconductors. The detector arrays can be seen in Figure 1.10, with the bolometer arrays visible towards the extreme left, represented by the small red and blue cubes, and the photoconductor arrays towards the centre, represented by the large red and blue cubes.

PACS uses a grating spectrometer with an image slicer unit, thus enabling two dimensional spectral imaging to be performed. Spectroscopy can be performed across the full PACS wavelength range with a resolution of 175 km/s, and an instantaneous coverage of $\sim$1500 km/s. The fields of view of PACS are $1.75' \times 3.5'$, and $50'' \times 50''$ for the photometer and spectrometer, respectively. Both sides of the instrument can perform chopped observations via the use of an internal chopper mirror.

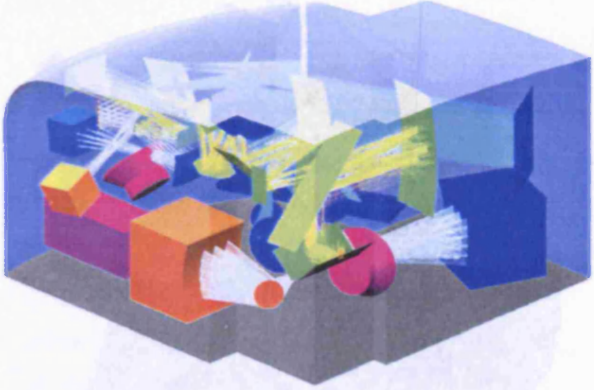

Figure 1.10: Computer generated image of the PACS focal plane unit optics.

HIFI

HIFI, the Heterodyne Instrument for the Far-Infrared (de Graauw et al., 2005), is a very high resolution heterodyne spectrometer. It uses superconductor-insulator-superconductor (SIS) and hot electron bolometer (HEB) mixers to achieve low noise detection. It provides a velocity resolution of 0.3–300 km/s for a single position on the sky. There are seven mixer assemblies (Figure 1.11), each equipped with two orthogonally polarised mixers. The first five bands use SIS mixers and cover a frequency range of 500–1250 GHz. The remaining two bands (6Low and 6High) use HEB mixers and operate in the 1410–1910 GHz band.

The focal plane unit (FPU) feeds the telescope signal to the mixers, along with an appropriate local oscillator source. There are also additional optics which allow the signal to be chopped, or to view a calibration source within the instrument.

SPIRE

Like PACS, the Spectral and Photometric Imaging Reciever, SPIRE, is a three band photometer and a low-medium resolution spectrometer. The photometer includes three broadband detector arrays, operating at 250, 360, and

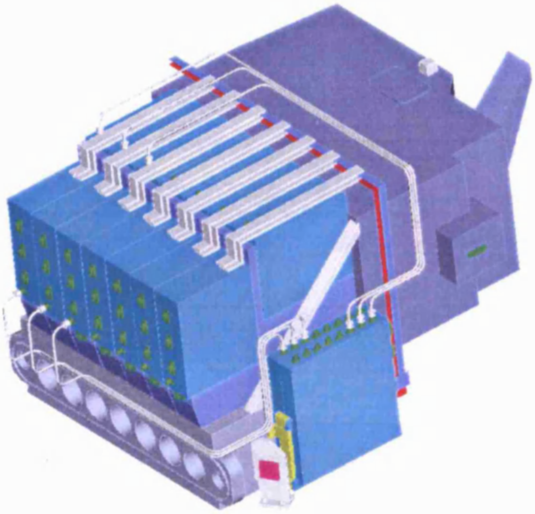

Figure 1.11: Computer generated image of the HIFI focal plane unit optics.

520 μm. The arrays have 139, 88, and 43 bolometers detectors in the 250, 360, and 520 μm bands respectively. Observations are made in all three bands simultaneously. An imaging Fourier transform spectrometer provides spectroscopic capabilities in two bands. A detailed description of the SPIRE instrument is given in Chapter 3.

1.3 BLAST

BLAST, the Balloon-borne Large Aperture Submillimetre Telescope (Devlin et al., 2004), is a balloon-borne telescope, containing an instrument derived from the SPIRE photometer (Figure 1.12). It contains the same bolometer detector technology, and build assembly as the SPIRE photometer, with identical optical filters and detector layout in all three bands. The observing modes used by BLAST, and its data products, are also extremely similar to those of SPIRE. The BLAST detectors are however optimised for the higher atmospheric background. The telescope incorporates a two metre spherical primary mirror, which is surrounded by solar shields, to minimise the stray light from the Earth entering the instrument optics.

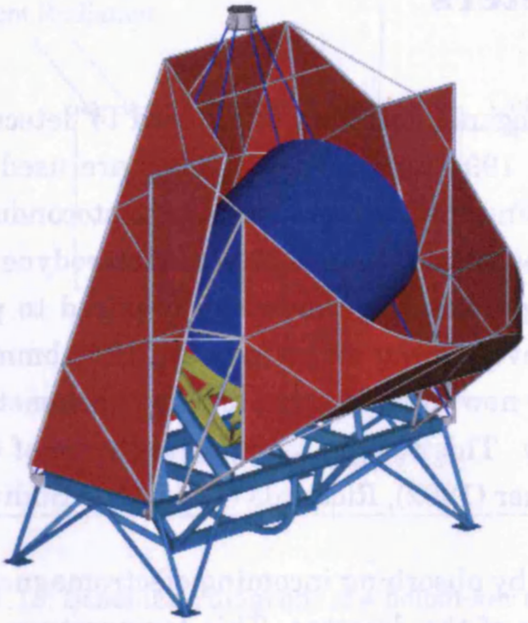

Figure 1.12: Computer generated image of the BLAST gondola (Devlin et al., 2004).

The Long Duration Balloon (LDB) platform allows BLAST to operate at an altitude of ~35 km. At this height, the atmospheric transmission at the SPIRE/BLAST wavelengths, is sufficiently improved, in comparison with that on the ground, to provide useful astronomical data. At the time of writing, two BLAST LDB flights have been completed, one from the Kiruna in Swden in 2005, and the other from McMurdo base in Antarctica in December 2006.

The science goals of BLAST were similar to those of SPIRE (see Section 3.3). Several deep extra-galactic surveys were carried out, in order to identify the amplitude of clustering of submm galaxies, and to perform source counts to place the strongest constraints to date on evolutionary models, and the global star formation history of starburst galaxies at high redshift. Galactic science goals included galactic surveys of the diffuse interstellar emission, molecular clouds, and to identify dense, cold protostellar (Class 0) cores associated with the earliest stages of star formation. These and other science data from the two flights are currently at various stages of data reduction and analysis.

1.4 Bolometers

Bolometers are cryogenic detectors often used to detect submm/FIR radiation (see Richards, 1994 for a review). They are used in this wavelength range as other continuum detectors, such as photoconductors, are unable to work at wavelengths greater than $\sim 200\mu$m. Heterodyne mixers are not used as they unable to provide the bandwidth required to perform broad-band photometry, and have a lower sensitivity at FIR/submm wavelengths. It is also relatively easy now to build large arrays of bolometers, thus improving observing efficiency. This section summarises some of the key points from the papers by Mather (1982), Richards (1994), and Sudiwala et al. (1992).

A bolometer works by absorbing incoming electromagnetic power, causing a rise in temperature of the detector. This temperature change results in a change of resistance of the detector material, which is then read out as a variation in detector voltage. The amplitude of this voltage change is proportional to the power absorbed by the detector.

The device comprises an absorber, a thermistor, and a heat sink at constant temperature, as shown in Figure 1.13. The absorber material, with heat capacity C, absorbs the incoming radiant power Q. The absorber is coupled to a thermistor, often made from NTD germanium, a material which has a temperature-dependent resistance which varies as

$$R = R^{\star} \exp \left(\frac{T_g}{T} \right)^m \tag{1.2}$$

where R is the resistance of the thermistor, $R^{\star}$ is a constant for a given bolometer, T_g is the band gap temperature, a constant for a given material, T is the temperature, and m is a material parameter, often assumed to be equal to $1/2$.

A bias current I flows through the thermistor generating a voltage $V = IR$ across it. The bias current is usually generated by load resistance R_L in series with a voltage source V_{bias} (Figure 1.14). Changes in the absorbed radiation power, Q, give rise to changes in the absorber temperature and

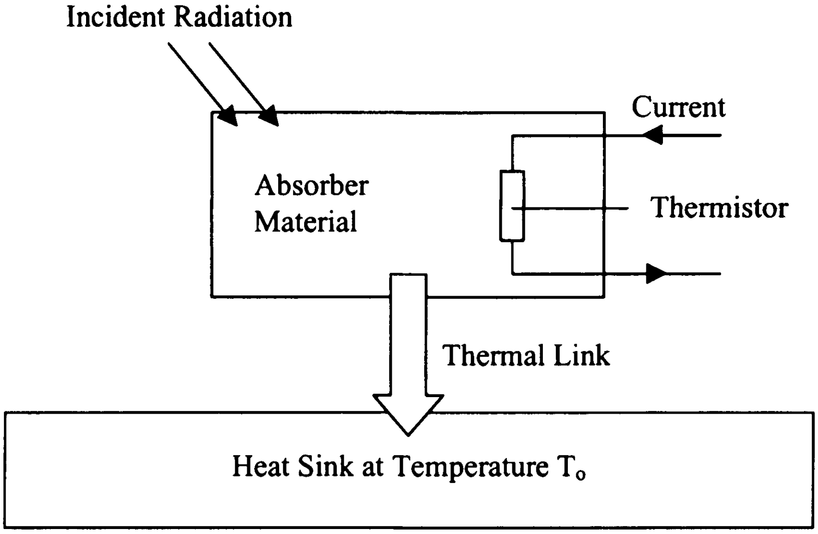

Figure 1.13: Schematic diagram of a bolometer detector

hence thermistor resistance and output voltage V.

In addition to the radiant power absorbed by the absorber, the current which flows through the resistor also causes a dissipation of electrical power, P. The total power dissipated in the bolometer is therefore given by,

$$W = P + Q. \tag{1.3}$$

Any power dissipated in the absorber is removed to the heat sink via a thermal link with thermal conductance G.

Figure 1.15 shows a series of bolometer load curves along with a load line for a range of incident powers, for a bolometer with $R^* = 100\ \Omega$, $T_g = 41.8$ K, $R_L = 20\ \mathrm{M}\Omega$, and $V_{bias} = 20$ mV calculated using the model of Sudiwala et al. (1992). At low current the resistance of the bolometer can be seen to be extremely high. This decreases with increasing current as the absorber absorbs more power. Likewise the presence of an optical loading reduces the resistance, thus suppressing the load curve.

The bolometer operating point is the point where the bolometer load curve

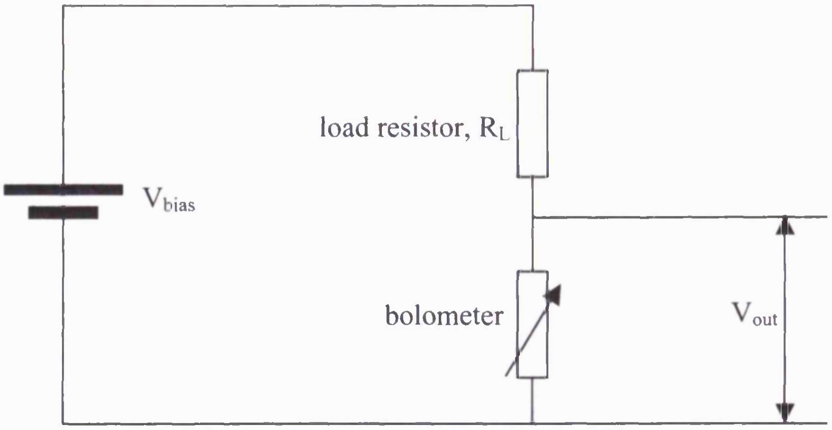

Figure 1.14: Schematic diagram of a bolometer readout circuit

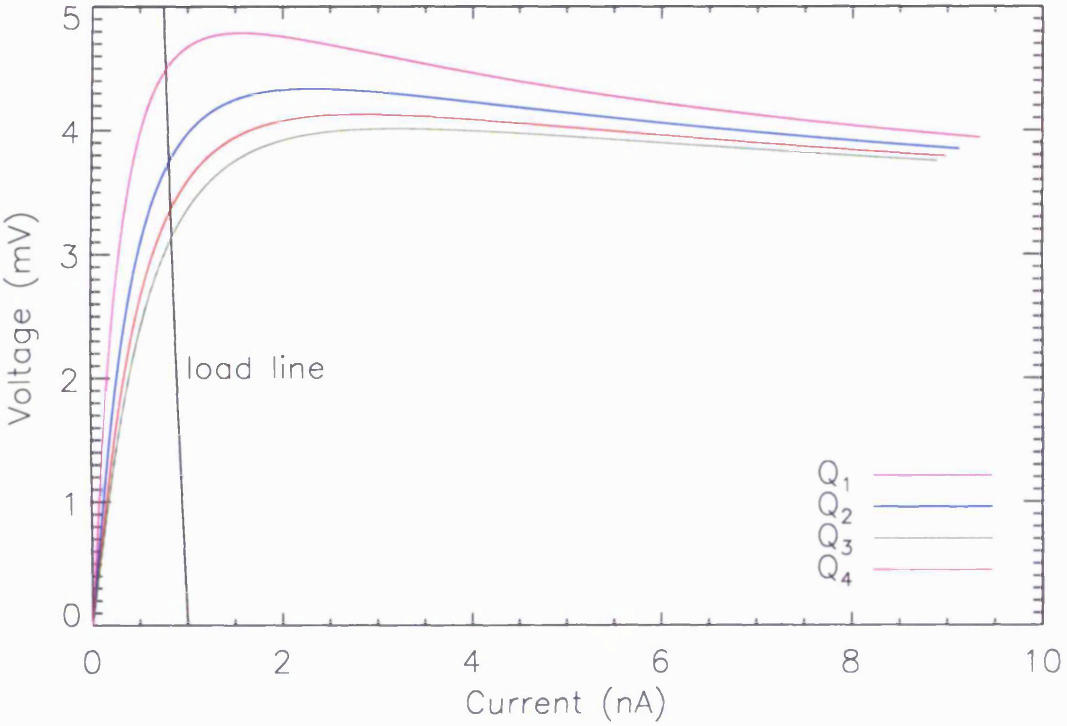

Figure 1.15: A series of simulated bolometer load curves for varying incident power Q, where $Q_1 < Q_2 < Q_3 < Q_4$.

(VI curve) crosses the load line, given by Equation 1.4.

$$V = V_{bias} - IR_L \tag{1.4}$$

In most cases the optical loading on a bolometer is dominated by the background radiation. Therefore when a signal power $\ll$ background power is present, the departure of the load curve from its normal shape can be regarded as negligible. In this instance the bolometer responds in a linear fashion, as defined by its responsivity S,

$$S = \frac{\Delta V}{\Delta Q}. \tag{1.5}$$

However, in the presence of a large signal, the departure of the load curve from its normal shape can no longer be considered to be negligible. Since the bolometer responsivity is a function of operating point, this parameter can not be used for high signal measurements. Instead, the difference between operating point voltages, ΔV is used as a measure of signal power (Figure 1.16). Consequently the bolometer response becomes nonlinear.

A bolometer, as with all systems, does not respond immediately to a change of input power. It can be useful to think of a bolometer as analogous to an *RC* electronic circuit, with *R* and *C* components being analogous to the thermal link resistance, and the absorber head capacity respectively. This gives a thermal time constant as shown in Equation 1.6.

$$\tau = C/G, \tag{1.6}$$

where G is the effective thermal conductance of the thermal link and C is the heat capacity of the absorber material. Both of these parameters vary with temperature and thus are functions of operating point (Sudiwala et al., 1992). Therefore the time constant can be considered to be constant when in the small signal case, but may vary in the high signal case. The response of a bolometer to a step change of input power can be modelled by studying the response of an equivalent circuit, to the same kind of step function. Both will give an exponential response, with time constant τ.

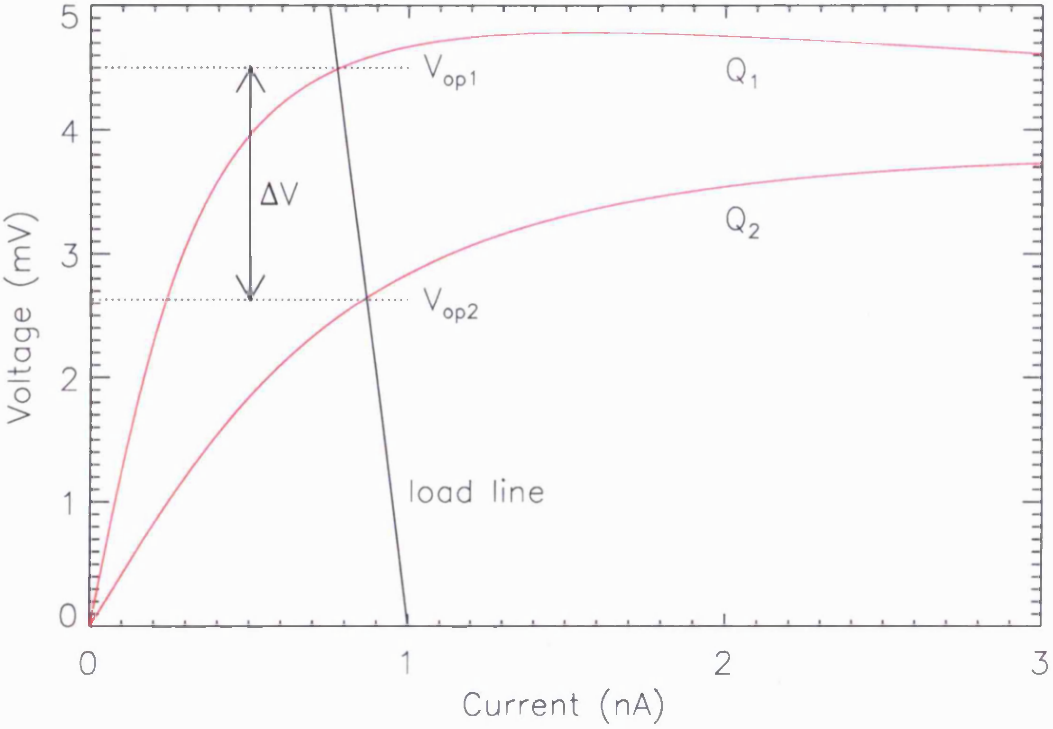

Figure 1.16: Sample bolometer load curves in the high, Q_2, and low, Q_1 signal regime.

The ultimate sensitivity of a detector is defined by its noise equivalent power, NEP. This is defined as the power that will provide a signal to noise ratio (SNR) in a post-detection bandwidth of 1 Hz. Since $\Delta t = 1/2\Delta f$ this equates to an integration time of 0.5 s. The derivation of the factor of 2 in the previous equation is extremely complex and too detailed to be presented here. For a full explanation see page 246 of Kraus (1966).

A low value of NEP represents a detector with high sensitivity. The intrinsic NEP of an ideal bolometer has two contributions: Johnson noise of the bolometer and load resistor, and phonon noise due to the quantised flow of heat from the bolometer to the heat sink, and is given by,

$$NEP_P^2 = 4k_bT^2G, \tag{1.7}$$

Therefore, the NEP is given by,

$$NEP^2 = NEP_J^2 + NEP_P^2, \tag{1.8}$$

where NEP_J is the Johnson noise component and NEP_P is the phonon noise component. Since the two sources of noise are uncorrelated they are summed in quadrature. The specific form of NEP_J is derived in Mather (1982).

In addition to the phonon and Johnson noise, a bolometer is also affected by other forms of noise. The most significant is photon noise, which arises from the quantum nature of the incident radiation. Readout electronics are also a source of noise in any working system.

Another significant source of noise when operating a bolometer device can be thermal fluctuations. The temperature dependent nature of a bolometer means that a stable heat sink is essential. The parameters derived in the thermal modelling of a bolometer (Sudiwala et al., 1992) are almost all temperature dependant, and are often specific to a single detector. As a result the scale of error arising from a temperature fluctuation may be different across a bolometer array. The NEP contribution due to thermal variations is given by,

$$NEP_T^2 = \frac{G^2 S_T}{\eta^2}, \tag{1.9}$$

where S_T is the spectral intensity of fluctuation in the temperature of the heat sink, and η is the bolometer absorptivity (Richards, 1994).

Both thermal variations in the heat sink and electronic noise are expected to have a $1/f$ noise power spectrum.

1.5 Chapter Summary

This chapter has introduced and summarised FIR/submm astronomy, and the techniques by which it is performed. An overview of the Herschel and BLAST projects has also been given, including details of the PACS and HIFI instruments on board Herschel. Finally, a brief review of bolometer operation has been presented.

1.6 Outline of this Thesis

In this thesis I describe the results of an investigation of various systematic aspects of the Herschel/SPIRE photometer system, and their impact on data quality and observing efficiency. These include the observing modes used to collect the data, as well as sources of noise. This has been achieved by developing and using a new, highly detailed and realistic, software simulator of the SPIRE photometer.

The investigations of the instrument systematics have been used to optimise the nominal instrument observing parameters. This work was then extended to investigate the effect on planned observations of targets within our galaxy, including the extraction of large diffuse structure in the presence of $1/f$ noise, and the study of radial profiles of prestellar cores.

In addition I present the analysis of some data from the BLAST experiment. Specifically, I report the first observations of the Cassiopeia A supernova remnant made at 250, 360, and 520 μm. I discuss their relevance and contribution to the on-going debate about the dominant source of dust production in the galaxy.

The specific goals of this work were to:

- develop and test a highly realistic software instrument simulator for the Herschel/SPIRE photometer;
- investigate and optimise the SPIRE photometer observing modes;
- study the systematics which will affect Herschel observations of astronomical sources within our galaxy.
- determine, using BLAST data, the quantity of dust contained in the Cassiopeia A supernova remnant;

Chapter 2 contains an introduction to the physical properties of dust, with a specific focus on their relevance, and consequences, in terms of FIR and submm astronomy. The next chapter covers the SPIRE instrument in more detail. The system hardware and observing modes are described. Chapter 4 describes the architecture and operation of the SPIRE photometer simulator, including information on the modelling of hardware, and sources of error. Following this, Chapter 5 deals with the verification of the simulator output, and considers the data reduction processes required to turn the simulator output timelines into a useful format for data analysis. Chapter 6 outlines the optimisation of the SPIRE observing modes through use of the simulator, and defines the recommended nominal observing parameters. The next chapter contains the data analysis, and conclusions, of the Cassiopeia A BLAST observations. Chapter 8 describes an investigation of the impact of SPIRE instrument systematics on observations of galactic sources. This deals with the recovery of sources of arbitrary scale, and structure, both in a confused and unconfused environment. Finally, Chapter 9 summarises the conclusions of the work in this thesis, and discusses future work and extensions to the current simulator.

Chapter 2

Dust in the Interstellar Medium

Dust may constitute only ~1% of the interstellar medium (ISM), but it plays an extremely important role in its astrophysics. It is crucial in the chemistry, opacity, and thermal balance of the ISM, and governs the processes by which stars form.

In this chapter, I introduce the ISM, and the cycle by which dust is injected and removed from it. I look at some of the main processes involved, including dust grain creation, and star formation. The observational properties of dust are also reviewed, with particular attention paid to the FIR and submm, and to topics that are relevant to the work contained in subsequent chapters of this thesis.

2.1 The Interstellar Medium

The ISM is made up of many components, at different temperatures and in different phases (atomic, molecular, and ionized). Components include dust, high energy particles, and magnetic fields. The most abundant component however is gas, mostly neutral atomic hydrogen (HI), with an average number density of $n_H \sim 10^5$ H atoms m^{-3}, and temperature of ~100 K (Evans, 1994). The density and temperature are by no means uniform however.

Regions of higher density exist, made up largely of molecular hydrogen (H_2). These are known as molecular clouds, and can have number densities of H_2 of up to 10^{10} molecules m^{-3} (Evans, 1994).

The number density of interstellar dust grains is also higher in molecular clouds than in the surrounding ISM. Interstellar dust grains are tiny particles composed of heavy elements, mainly carbon and oxygen, which are injected into the ISM by stars in the late stages of their evolution. It is this dust that enables a great deal of the interstellar chemistry to occur: it absorbs the high energy UV radiation which might otherwise cause molecular dissociation, and it also acts as a substrate for the formation of H_2 molecules. In dense clouds, grains can also acquire a mantle, formed from material condensed out of the gas phase. Hence, a lower hydrogen molecular number density is observed for a given cloud mass (Whittet, 2003).

Dust absorption also shields the inner parts of the molecular clouds, allowing them to cool and fragment, finally forming stars. The absorption efficiency of the dust allows gas clouds to cool and fragment into stars. The dust opacity is also thought to be responsible for stopping the collapse of the core during star formation. A supercritical core will collapse isothermally until such time that the density is sufficiently high that it becomes optically thick. At this point the core will collapse adiabatically, until the internal pressure of the core becomes sufficient to support it against further collapse (Ferrara, 2003). The point at which the material becomes optically thick is a function of the dust opacity.

Cosmic dust plays a vital role in the thermodynamics, chemistry, and physical processes which occur in the ISM. It is observed around active galactic nuclei, the early and late stages of stellar evolution, as well as being fundamental for planet formation (Whittet, 2003).

2.1.1 The Dust Cycle

The elemental composition of the primordial universe ($\sim$13.7 Gyr ago) was dominated by hydrogen. In addition, significant amounts of helium, and trace amounts of lithium were also formed. The fractional compositions by mass of hydrogen, helium, and the sum of all other heavier elements, are commonly denoted as X, Y, and Z respectively. The fractions in the primordial universe are estimated to be $X_p \simeq 0.76$, $Y_p \simeq 0.24$, $Z_p \simeq 0.00$ (Whittet, 2003). Z_p is not identically zero, but is too small to be accounted for in these figures.

This material eventually formed galaxies and the first generation of stars, within which nuclear processing lead to the synthesis of heavier elements. These stars subsequently injected these newly formed elements into the ISM, via stellar winds or through supernovae (SNe). Successive generations of stars continued this enrichment of the ISM, leading to the current fraction of heavy elements seen today, $Z \simeq 0.02$ (Whittet, 2003).

Figure 2.1 is a schematic representation of the cycle through which this material is processed. Material is thought to be lost from the ISM if it becomes contained within white dwarfs, neutron stars, or black holes, all of which have life times greater than the current age of the universe.

The dust cycle is relatively inefficient, with a great deal of material being trapped in collapsed stellar remnants. In addition, a great deal of the material ejected from stars remains hydrogen rich.

2.2 The Origin of Dust in the ISM

Most of the dust in the ISM is thought to be formed in the atmospheres of stars in the latter stages of their evolution. However, recently it has been proposed that SNe may also be a significant source of dust creation. In this section we briefly review these two formation mechanisms, and outline the reason why a significant new dust source, in addition to that from stars, is needed.

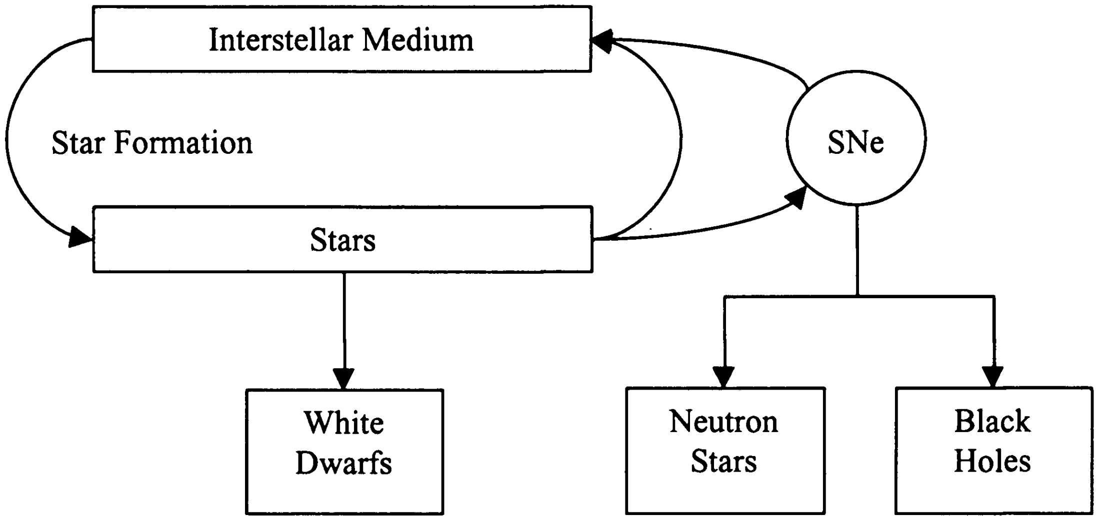

Figure 2.1: A schematic representation of the cosmic dust cycle, adapted from Whittet (2003).

2.2.1 The Classical Theory of Dust Formation

Stars are thought to be the major source of dust formation (Hoyle and Wickramasinghe, 1962; Kamijo, 1963; Gilman, 1969), contributing 86-97% of the total dust mass in the galaxy today (Whittet, 2003). All stars experience mass loss to some degree through stellar winds, however the mass loss rate ($\dot{M}$) is negligible for young stars (e.g. $\sim 10^{-14} M_{\odot} yr^{-1}$ for the Sun (Whittet, 2003)). The loss rate for luminous post-main-sequence stars has been observed to be significantly higher, with particularly massive stars losing up to 90% of the mass of the progenitor (Maeder, 1992). These stars are relatively cool (2500-3500 K), thus placing them in the upper right region on the Hertzsprung-Russell (HR) diagram. This group includes red giants, red supergiants, and asymptotic giant branch (AGB) stars.

Low temperature and pressure are required for grain nucleation to occur. The formation of solids from stellar gas is usually described using classical nucleation theory (Salpeter, 1974; Dominik et al., 1993; Gail and Sedlmayr, 1999). This states that condensation of species X occurs when the partial pressure in the gas exceeds its vapour pressure in the condensed phase (Salpeter, 1974; Whittet, 2003). As a result, dust is formed in a shell surrounding a star, rather than in the chromosphere. The inner radius, r_1, of this shell is defined by the point at which the temperature falls below the condensation temperature, T_c, for a particular grain. For a star of radius $R_\star$, forming grains with $T_c = 1000$ K, Bode (1988) estimates $r_1 \approx 10R_\star$. The physical conditions (temperature and number density of gas particles, $n \sim 10^{19}$ m^{-3}) are optimal at r_1, meaning that grain formation occurs quickest at this radius. The density of material decreases with increased radius, until the edge of the shell is reached, r_2, defined as the point at which the temperature and density of the circumstellar material become comparable to that of the general ISM (Whittet, 2003).

Data for the mean integrated mass loss rates ($\dot{M}_{tot}$, both gas and dust) in the galaxy, for various types of star, are contained in Table 2.1. These estimates were compiled from the literature by Whittet (2003), and derived using,

$$\dot{M}_{tot} = A\dot{M}_\star N_\star, \tag{2.1}$$

where $\dot{M}_\star$ is the mean mass loss rate in M$_\odot$yr^{-1} for stars of surface number density $N_\star$, and $A \approx 1000$ kpc^2 is the cross-sectional area of the galaxy, in the plane of the disc (Whittet, 2003).

In the case of a low to intermediate mass star (1–8 M$_\odot$), mass loss occurs mainly on the asymptotic giant branch, and culminates in the formation of a planetary nebula (Whittet, 2003). The rates quoted in Table 2.1 for AGB stars are dominated by a small number of stars with particularly high loss rates (Thronson et al., 1987). These stars are inherently more difficult to observe, as they are embedded in thick circumstellar dust shells, resulting in possible completeness errors. As a result, the estimates quoted here can be considered lower limits. Taking the figures quoted here, the mass injected into the ISM due to all AGB stars is of 1 M$_\odot$yr^{-1}, with an additional 0.3 M$_\odot$yr^{-1} arising from the formation of planetary nebulae (Maciel, 1981). This gives a final value of 1.3 M$_\odot$yr^{-1}.

While high mass stars have individually greater mass loss rates, and can be expected to lose mass throughout their entire lives, their integrated mass contribution to the ISM is small in comparison to that of low to intermediate mass stars (Jura and Kleinmann, 1990). This is because high mass stars

Stellar Type	$\dot{M}_{tot}$	$10^3\dot{M}_d$
O-rich AGB	0.5	3
C-rich AGB	0.5	3
Supernovae	0.2	1(?)
M giants	0.04	0.2
M supergiants	0.02	0.1
WC stars	0.01	0.06
Novae	0.003	0.02

Table 2.1: Integrated mass-loss rates in $M_\odot yr^{-1}$, for sources of cosmic dust. Column 1 contains the source type, including Oxygen and Carbon rich AGB stars, and WC stars, a subdivision of Wolf Rayet stars which contain carbon and oxygen lines along with the Helium (Abbott and Conti, 1987). Column 2 shows the total mass loss rate, $\dot{M}_{tot}$ (gas and dust), and column 3 contains the mass loss rate for dust, calculated using an assumed dust to gas ratio of $Z_d = 0.006$ (Whittet, 2003).

have a very low number density (Whittet, 2003).

Using the values for integrated mass loss quoted in Table 2.1, and assuming a certain gas to dust ratio of $Z_d \approx 0.006$ (Knapp, 1985; Olofsson et al., 1993), the rate of dust injection to the ISM, $\dot{M}_d$ is given by,

$$\dot{M}_d = Z_d \dot{M}_{tot}. \tag{2.2}$$

Consequently, as with the total mass loss rate, the dust mass formed by stellar sources is dominated by that formed in low to intermediate mass stars.

2.2.2 The Dust Debt

Using the dust injection rate values in Table 2.1, and taking the dust to be 1% of the mass of the galaxy, it is possible to calculate the dust replenishment timescale (Jones et al., 1994, 1997):

$$t_{rep} = \frac{\text{dust mass}}{\text{injection rate}} = \frac{5 \times 10^9 M_\odot \times 0.01}{6 \times 10^{-3} M_\odot yr^{-1}} \sim 10^{10} \text{ yrs}. \tag{2.3}$$

The equivalent timescale for dust destruction has been found by Jones et al. (1997), to be $t_{des} \sim 4 - 6 \times 10^8$ yrs.

These values imply that the dust injection rate is lower than the dust destruction rate. This would suggest that we should see no significant levels of dust in the galaxy, which is clearly not the case. Therefore, one of these values must be incorrect. It is unlikely that the dust injection rates for AGB stars has been underestimated by the required factor to account for this deficit. It is possible that there is an error in the dust destruction rate, but again, it is unlikely to be of the magnitude required to explain this difference.

Observations also provide another obstacle to our current theories of dust formation. Recent observations of galaxies (Dunne et al., 2003b; Hughes et al., 1998; Smail et al., 1997) and quasars (Bertoldi et al., 2003; Archibald et al., 2001) at high redshift have found large amounts of dust ($> 10^8$ $M_\odot$), at a point when the universe was only one tenth of its present age (~1.3 Gyrs old).

It is difficult for this dust to have originated in the stellar winds of evolved stars, such as those on the AGB. The cycle to produce dust first requires enrichment of the ISM by rapidly evolving SNe, followed by star formation and evolution. There is insufficient time for such stellar evolution to occur and produce the quantities of dust seen. Therefore, irrespective of any errors in our estimates of dust formation rate in AGB stars, another significant source of cosmic dust is needed to explain the observations of dust in the early universe (Morgan, 2004).

2.2.3 An Alternative Source of Dust

One proposed solution to the dust debt is that the injection rate from primordial SNe is in fact far higher than that stated in Table 2.1. Models that predict significant dust formation (0.2–4 $M_\odot$) in SNe explosions have been around for some time (Todini and Ferrara, 2001; Clayton et al., 1999; Woosley and Weaver, 1995; Kozasa et al., 1991); however, it is only recently that supporting observational evidence has been available (Dunne et al., 2003a; Morgan et al., 2003).

Infrared data from IRAS and ISO find only very low dust masses, of the order 10^{-4} $M_\odot$, associated with SNe ejecta (Douvion et al., 2001a,b). However, the elemental depletion suggests that the dust mass could be a lot higher (Dwek et al., 1992). These values were used to derive the dust injection rates for SNe in Table 2.1. The discrepancy between the predicted dust masses, and those observed, could be explained if there were a colder (~15 K) population of dust particles (Lucy et al., 1991).

Infrared data are biased towards detection of warm dust (~30 K); far infrared and submm observations are needed to measure cold dust. Weak observational evidence for the existence of cold dust in the Cassiopeia A and Kepler's supernova remnants (SN remnants), has been found by Dunne et al. (2003a) and Morgan et al. (2003), respectively. These observations were obtained using the SCUBA instrument on the JCMT. Dunne et al. (2003a) found a dust mass for Cas A of 2–4 $M_\odot$. These results have been contested however by Krause et al. (2004) (see Chapter 7 for further discussion). If these results can be confirmed, then it would mean that SNe would be the dominant known source of dust in the galaxy. The rapid timescales on which high mass stars form, evolve, and ultimately die, means that these sources are also capable of explaining the high levels of dust seen in the early universe.

2.3 Star Formation

The mechanisms by which stars form are inextricably linked to the physics of dust. The properties of dust are fundamental to the collapse processes which convert dense cores in molecular clouds to stars, and the stars themselves go on to produce more dust. The whole field of star formation research is extremely complex, and will not be dealt with in detail here. Instead I will give a brief overview of the conditions which might lead to core collapse within a molecular cloud, and look at the theoretical collapse solutions, specifically the Bonnor-Ebert sphere model.

2.3.1 Core Structure and Support

Stars typically form in dense molecular clouds. These clouds can be best thought of as having a nested hierarchical structure. Within the cloud medium exists a series of clumps of higher density. These in turn contain a further, more dense, and distinct set of cores (Kirk, 2002). These cores are shielded by the surrounding medium, allowing them to cool to temperatures of ~10 K (Goldsmith and Langer, 1978).

2.3.2 Core Collapse

The star formation rate in the galaxy is approximately 1 $M_{\odot}yr^{-1}$ (Knapp, 1985). If stars formed via free-fall collapse, then this rate would be an order of magnitude larger. Instead, cores are supported against collapse by thermal, turbulent and magnetic pressures (Mouschovias, 1976; Mestel and Spitzer, 1956; Curry and Stahler, 2000; Vazquez-Semadeni et al., 2000). These define a critical mass, M_c, that can be supported against gravitational collapse.

The maximum critical mass of a magnetised non-rotating pressure-confined isothermal molecular core, that can be supported against gravitational collapse, is approximately the sum of the masses that can be separately supported by the kinetic and magnetic energy of the gas (McKee, 1989; Mouschovias, 1976):

$$M_c = M_J + M_{\Phi}. \tag{2.4}$$

Here, M_J is the Jeans mass, the maximum mass of gas that can be supported against collapse by the kinetic energy of the gas (Jeans, 1920), and M_{Φ}, is its magnetic analogue (Mestel and Spitzer, 1956).

A core with $M > M_c$ is termed, *supercritical*, and is unstable against collapse. Conversely a core with $M < M_c$ is termed *subcritical*, and is stable against gravitational collapse.

It is still possible for a subcritical core to collapse however. M_c is related to the external pressure on the core. Therefore, an increase in the external core pressure, due to core collision, or a pressure wave, may reduce the critical mass, making it supercritical (Bhattal et al., 1998; Reynoso and Mangum, 2001). This is an example of triggered star formation, where an otherwise subcritical core becomes supercritical due to an outside influence. It is also possible for the turbulence within a core to decay, to the point the core becomes supercritical (Myers, 1983; Scalo and Pumphrey, 1982).

Another method by which a subcritical core may become critical is ambipolar diffusion. If an initially uniform magnetic field threads a core, then the ions will feel a force perpendicular to the field lines. As a result, the in-fall speed of the ions will be retarded relative to the neutral material. A magnetically subcritical core will undergo collapse when the drift of neutrals into the central region pushes its mass above the local critical mass (Mouschovias, 1976; Basu and Mouschovias, 1994). Low mass stars are believed to require ambipolar diffusion in order to collapse (Mouschovias, 1976).

When the centre of the core is sufficiently dense, a hydrostatic protostellar object is formed. The surrounding material then forms an accretion disc, collapsing along the axis of rotation of the protostar. The protostar subsequently accretes this material, until it has obtained the majority of its final mass. The protostar has now become a pre-main sequence star, and contracts under gravity. The pre-main sequence phase ends when the object's internal temperature becomes high enough for hydrogen fusion to begin, completing its formation process as it becomes a main sequence star.

The stages of protostellar evolution for low mass stars have been observationally determined, and are shown in Figure 2.2. However, the initial conditions for star formation, and the origin of the stellar initial mass function are still not well understood.

This collapse and accretion model of star formation is only applicable to low mass stars. Theoretically, radiation pressure from a protostar of mass >8 $M_\odot$, is sufficient to halt all further accretion of material onto the protostar

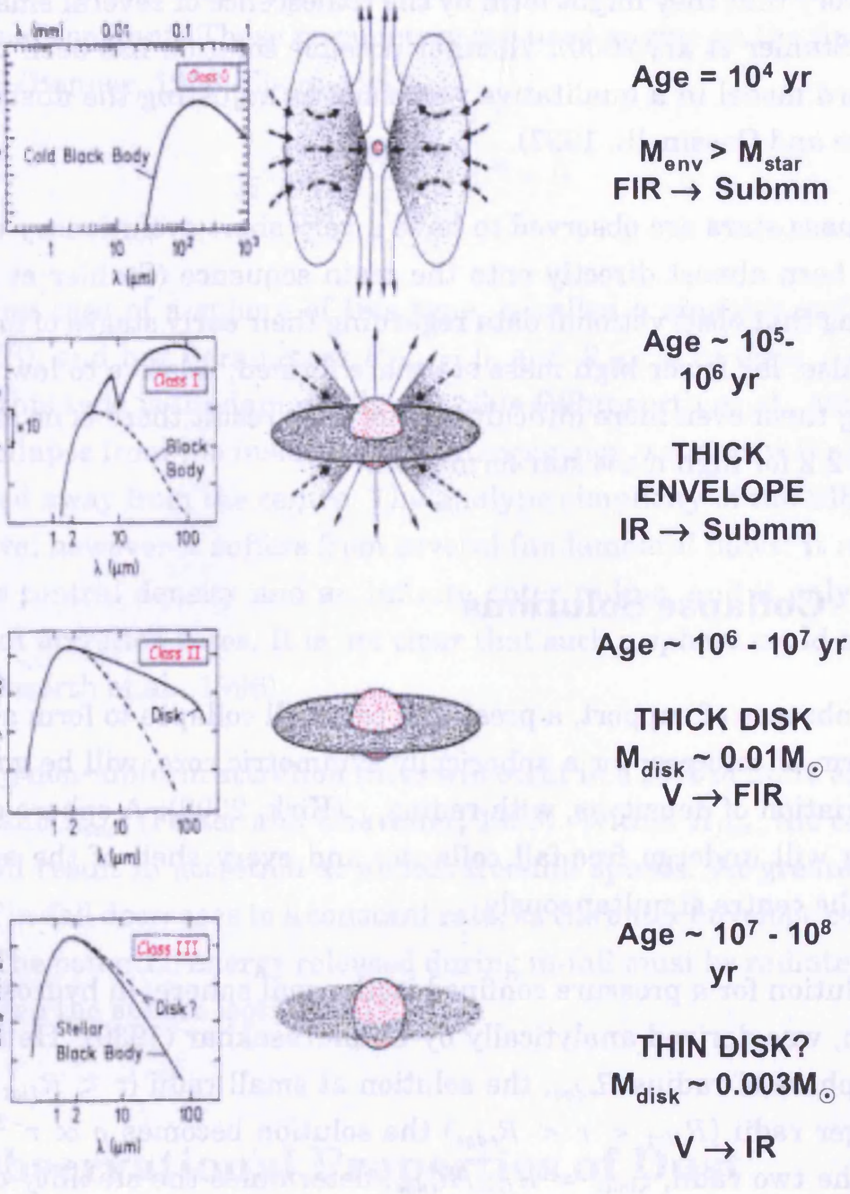

Figure 2.2: Schematic showing the evolution of low mass protostars (André, 1993).

(Stahler et al., 2000). This prevents the formation of stars of mass greater than this from being formed in this way.

High mass stars appear to form in the centers of dense clusters, leading to the theory that they might form by the coalescence of several smaller protostars (Stahler et al., 2000). Another possible solution has been to vary the standard model in a qualitative way, such as adjusting the dust properties (Wolfire and Cassinelli, 1987).

High-mass stars are observed to have a very short evolutionary time-scale, or are born almost directly onto the main sequence (Stahler et al., 2000), meaning that observational data regarding their early stages of formation is rare. Also, far fewer high mass stars are formed, relative to low mass star, making them even more difficult to find. As a result there is no analogue to Figure 2.2 for high mass star formation.

2.3.3 Collapse Solutions

In the absence of support, a prestellar core will collapse to form a protostar. The form of collapse, for a spherically symmetric core, will be governed by the variation of density, ρ, with radius, r (Kirk, 2002). A sphere of uniform density will undergo free-fall collapse, and every shell of the sphere will reach the centre simultaneously.

The solution for a pressure confined isothermal sphere, in hydrostatic equilibrium, was derived analytically by Chandrasekhar (1939). He found that for a sphere of radius R_{edge}, the solution at small radii ($r < R_{flat}$) was flat. At larger radii ($R_{flat} < r < R_{edge}$) the solution becomes $\rho \propto r^{-2}$. The ratio of the two radii, $\xi_{max} = R_{flat}/R_{edge}$, determines the stability of the core and the critical value for ξ_{max}, ξ_{crit}, above which a sphere is unstable against collapse, is 6.5 (Bonnor, 1956; Ebert, 1955). Spheres parameterised in this way are termed Bonnor-Ebert spheres (BES). The equation for a BES uses dimentionless forms for density and radius, ξ and ψ, given by

$$\psi = -\ln\left(\frac{\rho}{\rho_c}\right), \tag{2.5}$$

$$\xi = \frac{r}{a_s}\sqrt{4\pi G\rho_c}, \tag{2.6}$$

where ρ is the local volume density of the gas, ρ_c is the central density, r is the radius of a point within the sphere, a_s is the sound speed, and G is the gravitational constant. These parameters are used to give us the final form of the BES (Bonnor, 1956; Ebert, 1955),

$$\frac{1}{\xi^2}\frac{d}{d\xi}\left(\xi^2\frac{d\psi}{s\xi}\right) - e^{-\psi} = 0. \tag{2.7}$$

The limiting case of a sphere of this type, is called a singular isothermal sphere (SIS), and has parameters $R_{flat} = 0$, and $R_{edge} = \infty$ (Shu, 1977). A sphere of this type is fundamentally unstable (Whitworth et al., 1996) and will will collapse from the inside out, by an expansion wave travelling at the sound speed away from the centre. The analytic simplicity of the SIS model is attractive; however it suffers from several fundamental flaws: it requires an infinite central density and an infinite outer radius, and it only allows for constant accretion rates. It is not clear that such a sphere could actually form (Whitworth et al., 1996).

Conversely, non-uniform accretion rates will occur in a BES of finite and non-zero R_{flat} and R_{edge} (Foster and Chevalier, 1993). Within R_{flat}, the constant density will result in accretion at almost free-fall speeds. At greater radii, the rate of in-fall decreases to a constant rate, as the outer envelope collapses inwards. The potential energy released during in-fall must be radiated away, in order keep the sphere isothermal.

2.4 Observational Properties of Dust

2.4.1 The Interaction of Dust with Radiation

A dust grain may interact with radiation by absorption or scattering. Absorption results in the removal of the radiation, and its energy being transferred to the absorbing grain, resulting in an increase in dust temperature. The absorbed energy is then re-radiated at a longer wavelength, corresponding to the dust grain's cool temperature. Scattering changes the direction of propagation of the radiation, without altering the wavelength. To a distant observer, it would not be possible to determine which process had occurred. Instead, they would simply see a reduction in the intensity of the source. This removal of radiation from the observers line of sight, due to the sum the absorption and scattering processes, is known as extinction.

Interstellar and circumstellar dust grains are typically characterised as spherical in geometry, with a diameter of ~ 1 μm. The way in which they couple to radiation is not however a function of the grain geometry alone. Rather than the cross-section for interaction being πa^2, as you might expect, where a is the radius of the grain, theory predicts and experiments have shown, that for small particles it is given by $Q\pi a^2$. Here, Q is a value which depends on grain properties, such as refractive index and size, and the wavelength of the radiation involved (Evans, 1994). In simple terms it can be regarded as an efficiency factor, and is referred to as the Q-factor.

The absorption and scattering efficiencies for a grain with the same incident radiation can be different, resulting in independent Q-factors for both processes (Q_{abs}, and Q_{sca} respectively). The Q-factor for extinction is then given by $Q_{ext} = Q_{abs} + Q_{sca}$.

If a grain is in thermal equilibrium, then the efficiency of emission, Q_{em} (equivalent to the grain emissivity), is equal to its Q_{abs}. It therefore also varies as a function of grain size, and thus wavelength, following the approximate form $Q_{em} \propto \lambda^{-\beta}$ ($\propto \nu^{\beta}$) (Hildebrand, 1983). The β term can vary for different grain types, for example, $\beta \approx 2$ for crystalline grains, whereas $\beta < 2$ for more amorphous grains (Draine and Lee, 1984; Whittet, 2003).

2.4.2 Estimating Dust Masses

It is possible to quantify the mass of dust from FIR and submm observations (Hildebrand, 1983). Assuming that the dust grains are spherical, with radius a, volume $4/3\pi a^3$, and density ρ, the mass of a cloud of N dust grains, is given by

$$M_d = \frac{4}{3}\pi a^3 N\rho. \quad (2.8)$$

The flux density from a cloud of dust grains in thermal equilibrium is given by $S_\nu = I_\nu \Omega$, where I_ν is the emitted intensity, and Ω is the solid angle. If the background radiation is negligible, then $I_\nu = B(\nu, T)(1 - e^{-\tau_\nu})$, where τ is the optical depth. In the optically thin limit ($\tau \ll 1$), this reduces to $I_\nu = B(\nu, T)\tau_\nu$, where $\tau_\nu = \pi a^2 N Q_{em}$. Therefore, the total flux from the cloud at distance D, and temperature T, is

$$S_\nu = N\frac{\pi a^2}{D^2} Q_\nu B(\nu, T). \quad (2.9)$$

Rearranging Equations 2.8 and 2.9, in terms of N, the mass of dust becomes

$$M_d = \frac{4a\rho D^2 S_\nu}{3Q_{em}B(\nu, T)}. \quad (2.10)$$

The grain dependant parameters are often grouped into a new parameter, known as the dust mass absorption coefficient, κ_ν,

$$\kappa_\nu = \frac{3Q_{em}}{4a\rho}, \quad (2.11)$$

giving the final dust mass as,

$$M_d = \frac{S_\nu D^2}{\kappa_\nu B(\nu, T)}. \quad (2.12)$$

Using this it should be possible to make a good estimate of the dust mass for an observation. However, this relies on an accurate value of κ for the dust being known. A wide range of values of κ have been measured and predicted, from 0.04–0.8 $\mathrm{m}^2\ \mathrm{kg}^{-1}$ at 850 μm (Rowan-Robinson et al., 1986; Sopka et al., 1985; Boulanger et al., 1996; Sodroski et al., 1997; Bianchi et al., 1998; Amure, 2002), depending on the level of processing the dust has undergone, its environment, and structural type (crystalline or amorphous). Pristine dust can have values of κ an order of magnitude greater than for normal interstellar dust.

The dust mass absorption coefficient is also proportional to the dust emissivity index, β, and is a function of Q_{em}. For normal interstellar dust, James et al. (2002) derived a value of κ at $\lambda_0 = 850\ \mu$m of 0.07 $m^2\ kg^{-1}$. Using this as a reference, the value of κ at a given wavelength is given by,

$$\kappa = 0.07 \left(\frac{\lambda_0}{\lambda} \right)^{\beta} . \tag{2.13}$$

The uncertainty in κ is the major source of error in our ability to estimate dust masses from observations.

2.4.3 Cirrus Confusion Noise

The spatial variation in sky background can act as a source of noise, preventing an accurate source flux from being determined. This noise is referred to as confusion noise, and cannot be reduced by performing longer observations. As a result, it represents the fundamental noise limit for an observation. An observation is said to be 'confusion limited' if the instrumental noise level is less than, or equal to, the confusion noise level.

There are two main contributions to confusion noise at FIR wavelengths. The main component is due to dust emission from irregularly shaped interstellar clouds in our own galaxy, the 'galactic cirrus' (Low et al., 1984). The second component is from the Extragalactic Background, built up from the accumulated light of faint unresolved galaxies along the line of sight (Guiderdoni et al., 1997).

The confusion noise due to cirrus was first characterised by Helou and Beichman (1990) and Gautier et al. (1992) using IRAS 100 μm data. The second order structure function, $S(\theta)$, was used,

$$S(\theta) = \left\langle |B(x - \theta) - B(x)|^2 \right\rangle_x , \tag{2.14}$$

where B is the sky brightness, x is the location of the source, and θ is the separation between the source, and the reference sky position. The standard reference configuration used by Gautier et al. (1992) bracketed the source measurement, by two reference measurements, with a Nyquist separation, i.e. $\theta = 2D$, where D is the size of the telescope beam (Figure 2.3).

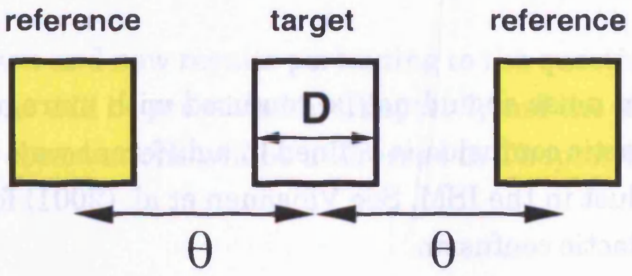

Figure 2.3: Cirrus structure measurement configuration as used by Gautier et al. (1992).

The Fourier power spectrum of cirrus confusion noise at 100 μm, was found to be well represented by a power law with an index of ~1.9 (Gautier et al., 1992). The empirical results of Gautier et al. (1992) were tested for longer wavelengths by Kiss et al. (2001), and found to be valid to within a factor of 2.

Helou and Beichman (1990) derived a practical formula to predict the confusion noise N as follows:

$$\frac{N}{1\ \mathrm{mJy}} = 0.3 \times \left(\frac{\lambda}{100\ \mu\mathrm{m}}\right)^{2.5} \left(\frac{D}{1\ \mathrm{m}}\right)^{-2.5} \left(\frac{B_\lambda}{1\ \mathrm{MJy\ sr}^{-1}}\right)^{1.5}, \tag{2.15}$$

where B_λ is the surface brightness at the wavelength of the observation. The resolution limit of the telescope is represented by the Fraunhofer diffraction value, λ/D. The confusion noise estimate using this equation is consistent to within a factor of 2 of the measurement made by Kiss et al. (2001), using 90-200 μm data from ISO. It also shows that the confusion noise at a given wavelength is dependant on the angular resolution of the telescope performing the observation. The noise level can be reduced very quickly by increasing the size of the telescope primary mirror. As an example, the cirrus confusion limit for Herschel is expected to be 35-55 times lower than that of Spitzer and Akari (SAG 3 GT proposal, 2006a).

Equation 2.15 has been used to estimate the typical confusion noise levels for the regions of interest in the SPIRE SAG 3 Gould Belt survey. The average 1σ noise level is expected to be ~20 mJy/beam in the in the SPIRE

PSW band. This is representative of a region such as Orion (SAG 3 GT proposal, 2006a). The confusion noise will be the limiting source of noise for this survey.

Cirrus confusion noise should not be confused with extragalactic confusion noise. Extragalactic confusion is defined in a different way, and is not due to emission from dust in the ISM. See Väisänen et al. (2001) for more information on extragalactic confusion.

For more information and a good review of cirrus confusion noise at FIR wavelengths, see Kiss et al. (2001, 2005). These articles are particularly applicable to space based observatories, such as Spitzer and Herschel.

2.5 Chapter Summary

This chapter has introduced, and reviewed, a range of processes in which dust plays a major role in the ISM. It has highlighted the important role played by cosmic dust, from chemical processing, to the formation of stars, as well as the cycle through which dust passes, from birth to destruction.

I have reviewed the classical formation mechanism of dust in the atmospheres of evolved (AGB) stars, and compared the overall injection rates with those required to generate the dust fraction seen in the galaxy today. There is a debt in the overall production rate of dust from stars, meaning that another source of dust must be found to explain the observed levels. The need for a new mechanism of dust formation is further supported by the detection of dusty galaxies in the early universe. This dust could not have been formed by AGB stars, as they would not have had time to reach the necessary evolutionary stage. The current evidence for supernovae as the missing source is thus introduced.

The process of star formation, collapse and accretion, was then reviewed. The BES core collapse solution was introduced, and the parameterisation compared to the SIS solution.

Finally, the interaction of dust with radiation, the method by which dust masses are estimated, and the concept of confusion noise are introduced.

Further discussion and new results pertaining to the question of dust formation in supernovae will be presented in Chapter 7, and the effect of confusion noise on SPIRE observations will be addressed in Chapter 8.

Chapter 3

SPIRE

SPIRE (the Spectral and Photometric Imaging Receiver) is a dual instrument comprising a three-band imaging photometer (Figure 3.1(a)) and an imaging Fourier transform spectrometer (FTS, Figure 3.2(a)), spanning a wavelength range of $\sim$200–700 μm. The main scientific objectives for SPIRE are deep extragalactic and galactic imaging surveys, and spectroscopy of star-forming regions in our own, and nearby galaxies.

SPIRE was first proposed in 1998 as an instrument for the Far Infrared and Sub-millimetre Telescope (FIRST), the original name of Herschel. The consortium has members from many institutes in seven countries. At the time of writing, the instrument is undergoing final instrument level tests before being delivered to ESA.

In this chapter the basic features of the SPIRE instrument are described, with emphasis on the photometer. This is to set the scene for the description of the SPIRE photometer simulator in Chapter 4. The photometer observing modes are also reviewed ahead of the optimisation studies in Chapter 6. Finally the SPIRE guaranteed time programmes, currently being planned by the consortium, are presented.

3.1 Instrument Overview

SPIRE comprises a cold focal plane unit (FPU), mounted on the Herschel optical bench (HOB). Modules containing junction field effect transistors (JFETs) and detector pre-amplifier, used for detector read-out, are located next to the FPU. The warm electronics are located on the Herschel service module (SVM), and are connected to the FPU by a cold harness.

To review the SPIRE system it is convenient to regard the instrument as a series of subsystems. In this section an overview of the photometer and FTS will be presented, followed by a more detailed description of the subsystems common to both halves of the instrument.

3.1.1 Photometer

Inside the FPU, the photometer and FTS are arranged back-to-back on either side of a central SPIRE optical bench. The photometer side of the FPU is shown in Figure 3.1. It is a three colour instrument with bands centred at 250, 360, and 520 μm, with band widths of $\lambda/\Delta\lambda \simeq 3$. When the telescope beam enters the instrument it passes through an optical filter (common filter 1, CFIL1, Figure 3.1(b)) into the Level-1 temperature stage (5-K). The beam is then reflected by mirror CM3 before encountering CM4, the beam steering mirror (BSM). The BSM can be used for spatial modulation of the telescope beam, allowing the beam to be chopped and jiggled within SPIRE, without impacting on the operation of the Herschel satellite. This unit also contains a photometer calibration source (PCal), located in a cavity behind the centre of the mirror. This acts as a repeatable calibration signal with which to track drifts in detector responsivity.

Following this the beam continues to CM5, which produces an intermediate focal plane at M6, which has two separate elements, the photometer mirror 6, PM6, and spectrometer mirror 6, M6. Here the spectrometer field of view is separated and sent through a hole in the SPIRE optical bench to the FTS side of the instrument by SM6. The photometer beam continues via the

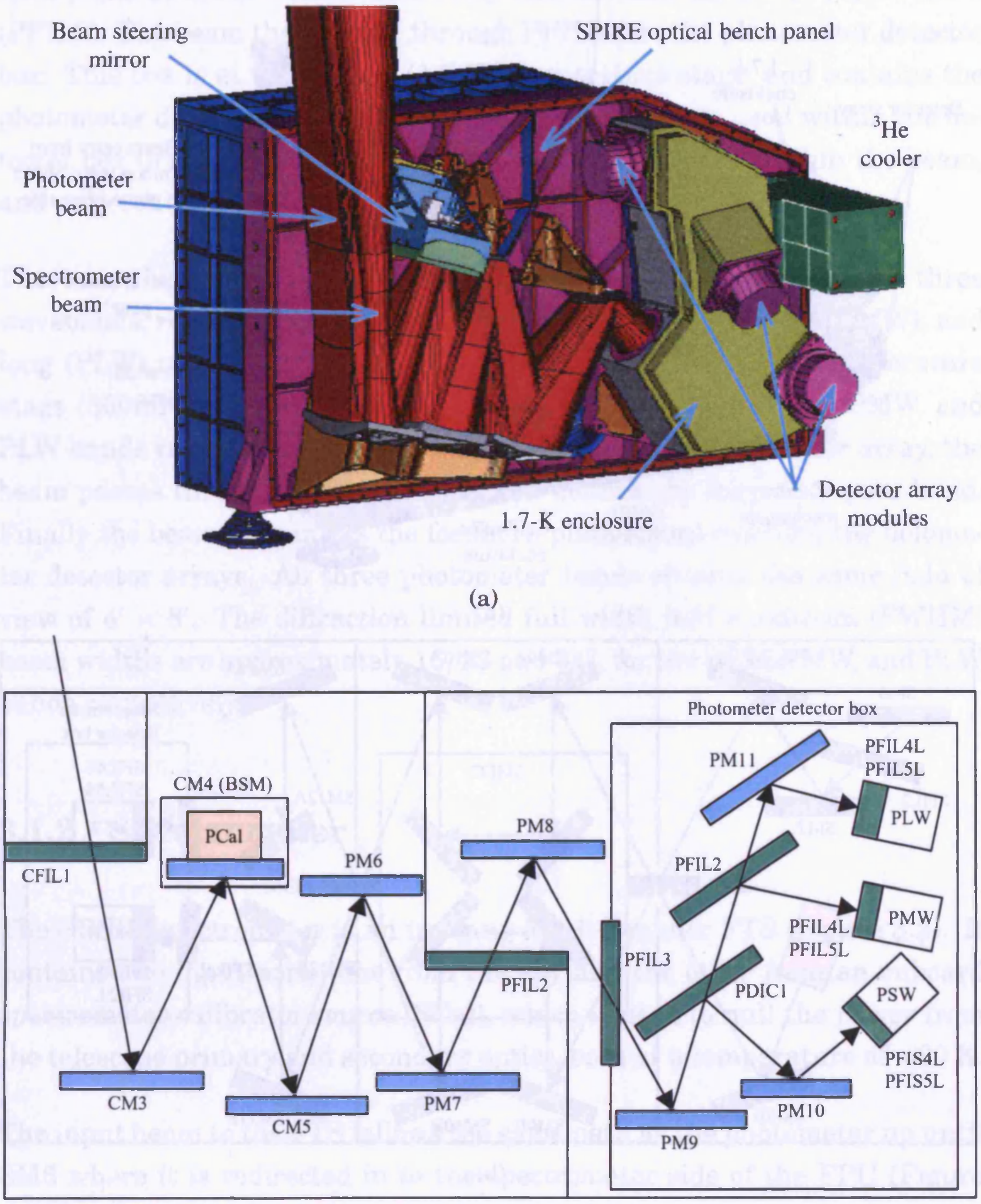

Figure 3.1: (a) Solid model of the SPIRE photometer (4-K cover not shown); (b) schematic of the SPIRE optics box (Griffin et al., 2002b). Optical elements in blue are mirrors, and those in green are optical filters or dichroics.

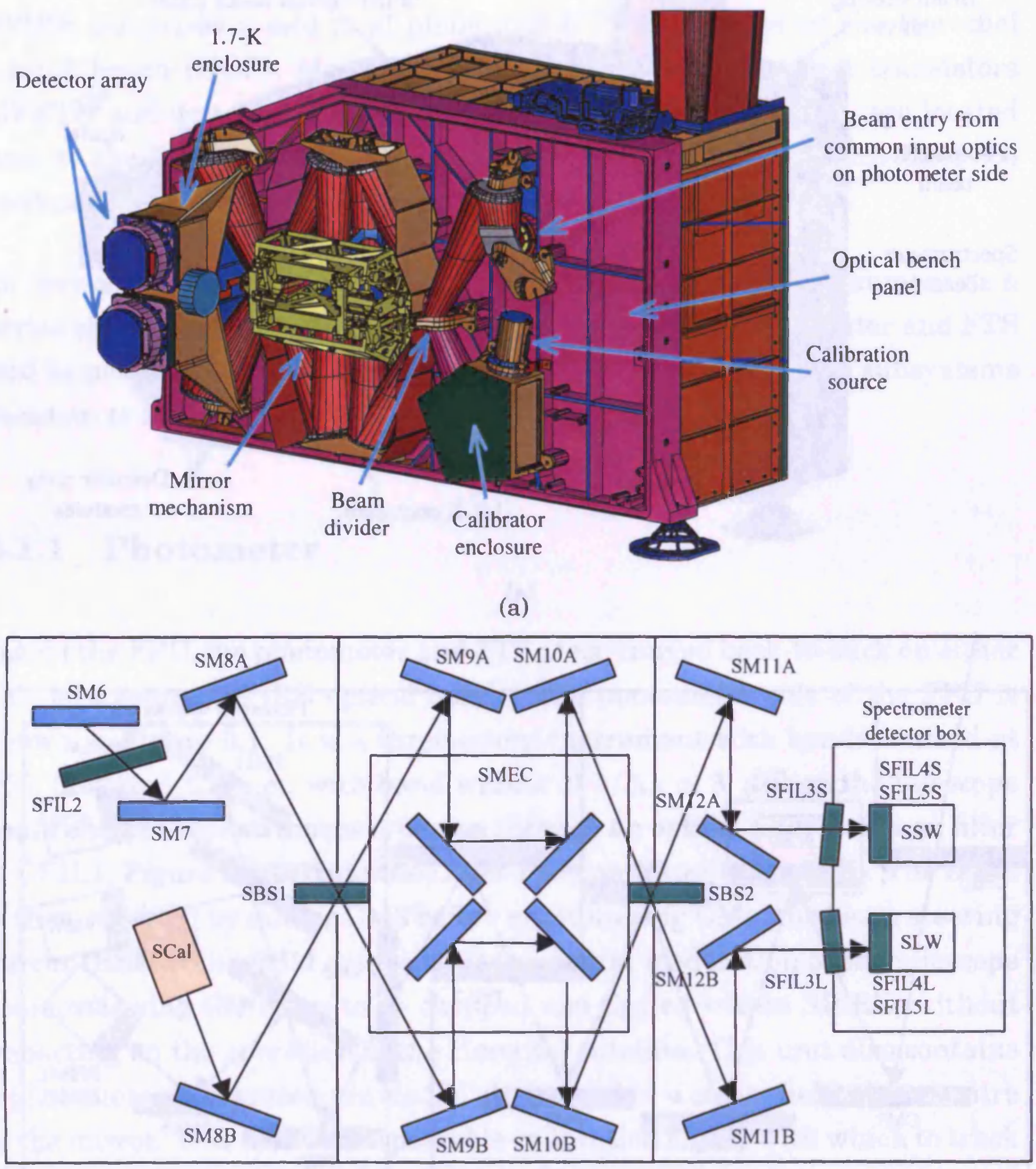

(a)

(b)

Figure 3.2: (a) Solid model of the SPIRE spectrometer; (b) FTS ray diagram (Griffin et al., 2002b). Optical elements in blue are mirrors, and those in green are optical filters or dichroics.

photometer mirrors 7-9 (PM6-PM9), which form an optical relay to create a focal plane at the detectors. This relay also contains the photometer filter 2 (PFIL2). The beam then passes through PFIL3 into the photometer detector box. This box is at the Level-0 (1.7-K) temperature stage, and contains the photometer detector arrays. Dichroic beam-splitters are used within the detector box to separate out the different wavelength bands within the beam, and redirect them to the appropriate detector array.

There are three feedhorn coupled detector arrays corresponding to the three wavebands, referred to as the photometer short (PSW), medium (PMW), and long (PLW) wavelength arrays. The arrays are all at the T_o temperature stage (300mK), and contain 139, 88, and 43 pixels in the PSW, PMW, and PLW bands respectively (Figure 3.3). Upon reaching the detector array, the beam passes through a filter stack which defines the frequency pass-band. Finally the beam encounters the feedhorn plate before reaching the bolometer detector arrays. All three photometer bands observe the same field of view of $4' \times 8'$. The diffraction limited full width half maximum (FWHM) beam widths are approximately 16, 23 and 34$''$, for the PSW, PMW, and PLW bands respectively.

3.1.2 Spectrometer

The SPIRE spectrometer is an imaging Mach-Zehnder FTS (Figure 3.2). It contains two input ports, one from the sky and the other from an onboard spectrometer calibrator source (SCal), which is used to null the power from the telescope primary and secondary optics, both at a temperature of $\sim$80 K.

The input beam to the FTS follows the same path as the photometer up until SM6 where it is redirected in to the spectrometer side of the FPU (Figure 3.2(b)). At this stage all components are at the Level-1 temperature stage. The SCal reference source enters the system SM8 (A – telescope beam, B – SCal). The first beam splitter, SBS1, splits the beam into two, both of which contain power from the telescope and SCal beams.

The next significant component in the FTS optics chain is the spectrometer

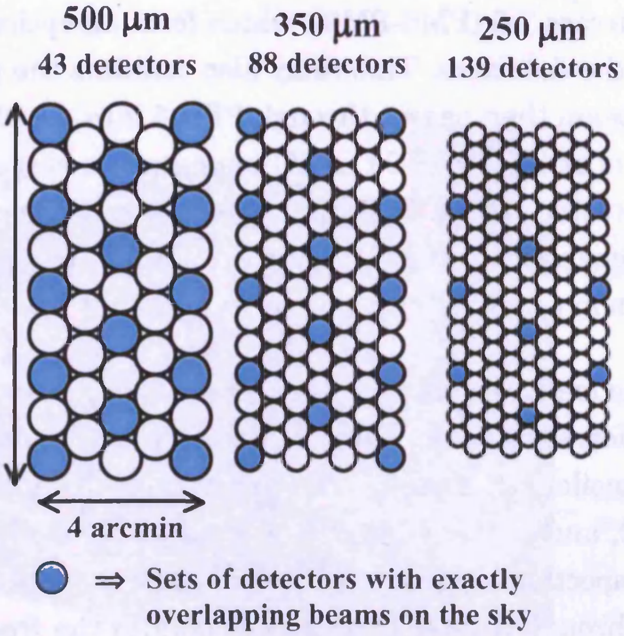

Figure 3.3: Layout of the three photometer arrays, shaded circles are co-aligned on the sky in all bands Griffin et al. (2002b). The circles represent the hexagonally close packed feedhorns ahead of the detector arrays.

scanning mirror mechanism (SMEC), positioned between SM9 and SM10. The mirror drive mechanism can be operated in either continuous scan or step-and-integrate mode, in order to build up an interferogram. This mirror can travel up to 3.5 cm, which, due to the factor of four folding in the optics, gives an adjustable spectral resolution of between 0.04 and 2 cm^{-1}. The continuous scan mode moves the mirror at a nominal pace of 0.5 mm s^{-1}, giving an optical path rate of 2 mm s^{-1}. The mirror position has a relative accuracy of 0.1 μm in order to ensure that mechanism jitter noise is below the photon noise level (Griffin, priv. comm.). For more detail regarding the SPIRE spectrometer observing modes see Griffin et al. (2006).

Once leaving the SMEC, both beams pass through five more mirrors/filters before entering the spectrometer detector box. This box is at the Level-0 temperature stage, and contains the two spectrometer detector arrays, both at a temperature of 300 mK. The arrays cover 200 μm – 325 μm, and 315 μm – 670 μm, for the spectrometer short wavelength (SSW) and the spectrometer long wavelength (SLW) arrays respectively. There are a total of 56 spectrometer detectors with 37 in the SSW array, and 19 in the SLW array

(Figure 3.4). The arrays are operated simultaneously and have a field of view of 2.6′. These arrays are, like those of the photometer, feedhorn coupled, and contain band-pass filters mounted directly ahead of the feedhorn plate.

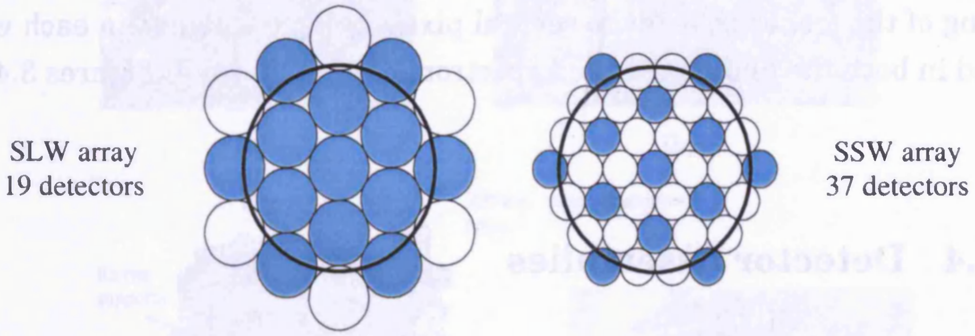

Figure 3.4: Layout of the two spectrometer arrays, shaded circles are co-aligned on the sky in both bands, detectors within the black circles signify unvignetted pixels (Griffin et al., 2002b). The circles represent the hexagonally close packed feedhorns ahead of the detector arrays.

3.1.3 Optics

The SPIRE optical components include mirrors, dichroic beam-splitters, optical filters, and feedhorns, as described above. Due to manufacturing constraints the hole in Herschel's 3.5 m diameter primary mirror is slightly larger than that corresponding to the secondary mirror obscuration. This results in a slightly larger beam sidelobe than would be predicted from the secondary mirror alone.

All SPIRE detectors are coupled to an array of feedhorns with an aperture size of $2F\lambda$, where F is the focal ratio at the detector array, and λ is the central band wavelength. The photometer feedhorns are single moded, while those used in the spectrometer are multi-moded, so that they can accept a wider frequency range. The resulting separation of beams on the sky is $2\lambda/D$, where D is the diameter of the telescope primary mirror. Consequently an observation is not fully sampled within the field of view by a single pointing. Full (Nyquist) sampling can be achieved in any single band by performing a 16-point jiggle map or by scanning the detector array at an appropriate angle (see Chapter 6). In order to sample fully all photometer wavebands simultaneously, when operating in jiggle map mode, a 64-point map must be performed. The beam movement required to perform these maps is performed by the BSM. The hexagonal packing of the arrays and sizing of the feehorns, leads to several pixels being co-aligned in each waveband in both the photometer and spectrometer, as shown in Figures 3.4 and 3.3.

3.1.4 Detector Assemblies

Both the photometer and FTS use feedhorn coupled spider-web neutron transmutation doped (NTD) germanium bolometers (Turner et al., 2001), operating at 300 mK. Each bolometer detector assembly comprises a bolometer array wafer, containing all detectors within a single array, a single feedhorn plate, and the final optical filters. These are all mounted above an Invar block (iron-nickel alloy with low thermal expansion coefficient), and are thermally isolated from the warmer support structure by Kevlar cords (Hargrave et al., 2006). Various stages of BDA construction are shown in Figure 3.5. In addition to the array detectors, each BDA contains two dark pixels, and two thermometers. Each dark pixel is identical in construction to the array detectors, but is positioned outside of the instrument field of view and is blanked. The thermometers are similarly constructed of NTD germanium, however their thermal conductance (G) is significantly greater. Additionally they contain no spider-web absorber. Like the dark pixels, the thermometers are also placed outside of the SPIRE field of view. These additional detectors are used to monitor the thermal stability and environment of the detector arrays during operation.

3.1.5 Thermal System

Each BDA is coupled to a ^{3}He sorption cooler, mounted within SPIRE, and has an effective cooling power on the arrays of $\sim$10 μW (Duband, 1997). The cooler is connected to a 2-K heat sink, and is thermally isolated from its 4-K

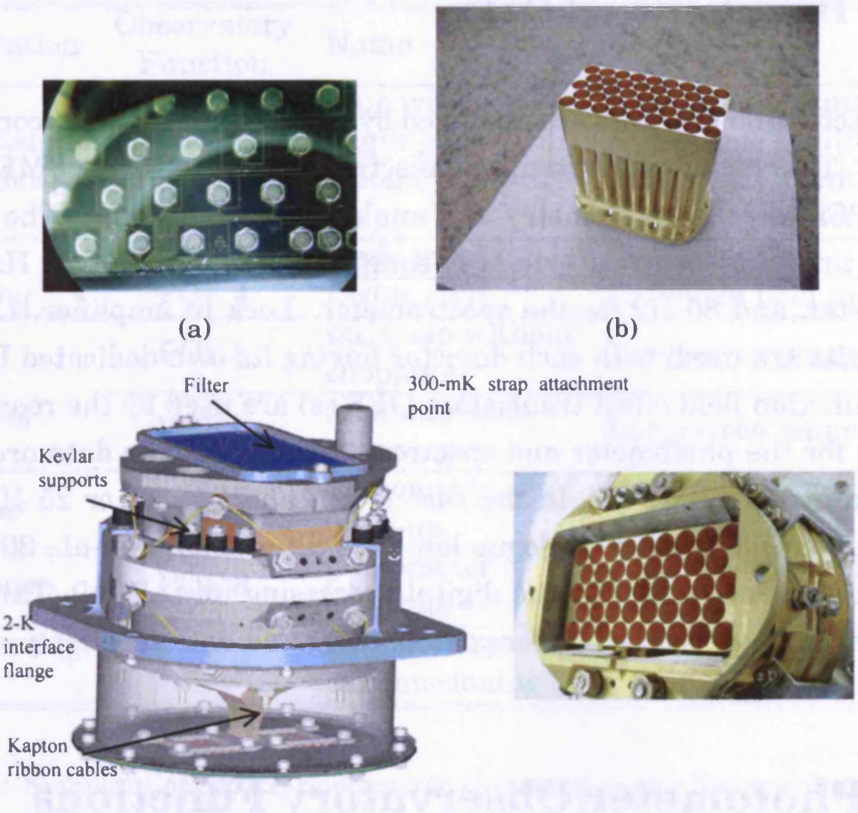

(a) (b) (c)

Figure 3.5: (a) Photograph of one of the SPIRE bolometer array wafers; (b) photograph of the PLW detector feedhorn plate; (c) schematic image, and photograph of the compiled bolometer detector assemblies. Note, the filters have been removed from the photograph of the assembly so that the feedhorn plate can be seen.

support structure. The cooler tip can achieve a temperature of 274 mK. It is connected to the five BDAs via a thermal strap system (Hargrave et al., 2006). The fridge has a hold time of 46 hours and a recycle time of less than 2 hour (Griffin et al., 2003). The straps are thermally isolated from the surrounding 'warm' structure via a Kevlar cords support structure. The large thermal mass of the BDAs, coupled with the thermal straps, results in the suppression of high frequency thermal variations originating in the refrigerator. These components effectively act as a low-pass filter. Low frequency variations may remain however, resulting in drifts in detector temperature.

3.1.6 Detector Read-Out

The detector and readouts are managed by the detector read-out control unit (DRCU). This includes the front-end electronics for the BDAs, SMEC, BSM, cooler, PCal, Scal, thermometry and analogue housekeeping. The detector voltage timelines are read out at a sampling rate of up to 28 Hz for the photometer, and 80 Hz for the spectrometer. Lock in amplifier (LIA) read out circuits are used, with each detector having its own dedicated LIA. Two sets of junction field effect transistors (JFETs) are used by the readout, one set each for the photometer and spectrometer arrays. The data are filtered on board by either a 5 Hz, in the case of the photometer, or 25 Hz, in the case of the spectrometer, analogue low pass filter (Griffin et al., 2003). The on-board software is run by the digital processing unit (DPU). This acts as an interface to the spacecraft for commanding and data telemetry.

3.2 Photometer Observatory Functions

There are nine photometer observing modes (POFs), six relating to scientific observations, and three to instrument calibration and setup, as summarized in Table 3.1. The six scientific observing modes can be split into one of three main classes, point source photometry, field mapping, and scan mapping.

3.2.1 Point Source Photometry

Point source photometry (POF 1) is used for observing isolated compact objects, and is similar to the standard observing mode used on ground-based submillimetre telescopes. Observations can be made by simply chopping the source while pointing the telescope precisely, and nodding if required. If telescope pointing is not sufficiently accurate however, or the source position is not well defined, then a seven-point jiggle map may be used (POF 2). This is constructed from eight individual POF 1 observations, carried out in a symmetrical pattern centred on the source, with the BSM being offset by some

Observation	Observatory Function	Name	Comments
Point source photometry	POF 1	chop without jiggling	Accurate pointing and source position
	POF 2	7 point jiggle map	In accurate pointing or source position
Field mapping	POF 3	jiggle map	Field mapping
	POF 4	raster map	Extended field mapping
Scan mapping	POF 5	scanmap without chopping	Large-area mapping
	POF 6	scanmap with chopping	Large-area mapping
Peak-up	POF 7	photometer peak-up	Determination of pointing offsets
Calibrate	POF 8	photometer calibrate	Detector responsivity tracking
Engineering mode	POF 9	Engineering/ commissioning	

Table 3.1: Summary of SPIRE photometer observing modes Swinyard and Griffin (2002)

angle $\Delta\theta_7$ for each point (see Figure 3.6). The map starts and finishes in the central chop position. Seven-point jiggle mapping has been adopted as the nominal point source observatory function (see Chapter 6).

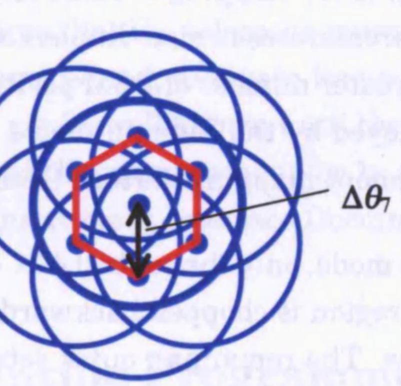

Figure 3.6: Seven-point hexagonal jiggle pattern.

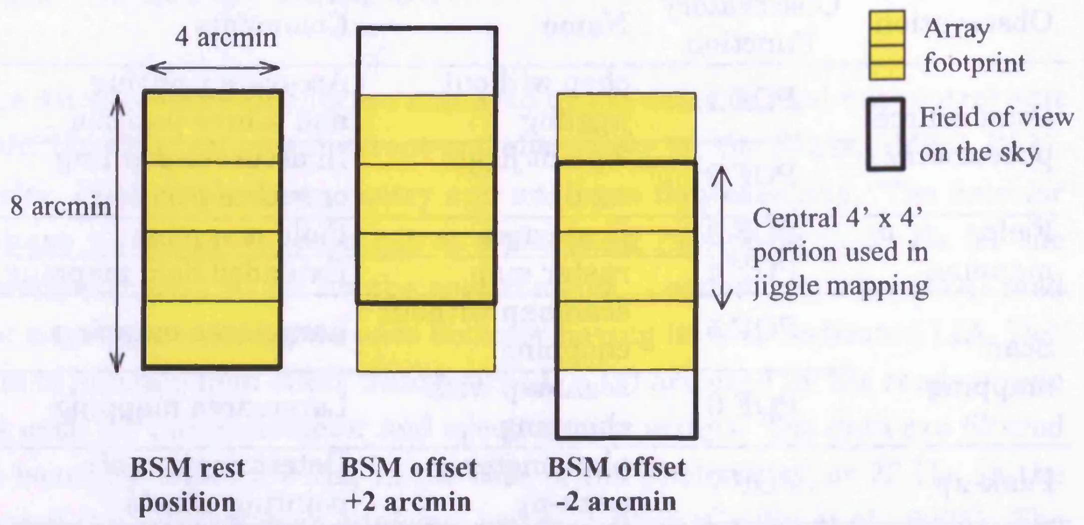

Figure 3.7: Jiggle mapping with the maximum chop throw of 4′. The 4′ × 8′ field of view transmitted by the photometer optics is chopped by +/- 2′ as shown. The detectors in the central square 4′ × 4′ part of the array are alternately chopped from one side of the available field of view to the other. The detectors in the outer 2′ × 4′ portions at each end are chopped between the sky and the instrument cold box, producing no usable data (Swinyard and Griffin, 2002).

3.2.2 Field Jiggle Mapping

POF 3 (jiggle mapping) is for mapping of relatively small objects or regions, no greater than a few arcminutes in size. Implementation is identical to that of POF 1, but with a greater number of BSM positions. This is similar to the jiggle map mode employed by the Submillimetre Common User Bolometer Array (SCUBA) instrument mapping pattern (Holland et al., 1999).

When chopping in this mode, only the central 4′ × 4′ field of view is available (see Figure 3.7). This region is chopped backwards and forwards across the full 4′ × 8′ field of view. The remaining outer sets of detectors are chopped out of the field of view, and so provide no useable data (Swinyard and Griffin, 2002).

POF 4 carries out a series of POF 3 observations at each point in a raster scan, and can therefore be used to scan areas larger than the SPIRE field of view. This is commonly referred to as raster mapping, but is also known as mosaicking.

3.2.3 Scan Mapping

POF 5 (scan mapping) will nominally be used for large area maps – significantly bigger than the SPIRE field of view. However, the exact map size at which a scan map becomes more efficient than a jiggle map will depend on the telescope movement overheads, which are yet to be confirmed. In scan map configuration all three arrays observe simultaneously while the telescope scans across the sky at a rate of up to $1'$ per second. To achieve full spatial sampling with each of the hexagonally packed arrays within a single scan, the telescope scan direction must have a particular angle with respect to one of the array axes (Y or Z). This angle is known as the 'scan angle' (ϕ_{angle}), and is defined in Figure 3.8.

A Boustrophedon (from the Latin, "turns like an ox") scan pattern (Figure 3.8) is performed containing a certain number of scan lines, N_{lines}, at a specified scan rate, $\dot{\theta}$. The observable area, shown as the shaded region in Figure 3.8, is the area within which the telescope is scanning at a continuous rate. Outside this region the telescope performs overhead operations, including acceleration/deceleration, and internal calibration flashes. The pointing stability of the satellite requires that the telescope must return to a calibration 'off' position every fixed time period, to regain its pointing accuracy. The final pointing stability will not be well known until the system is in orbit, but is expected to satisfy the pointing requirement for 1σ absolute pointing error of $3.7''$ (Herschel Planck Instrument Interface Document IID PartA, 2003).

3.3 SPIRE Scientific Programme

The science potential of SPIRE is wide ranging with many different possible fields of investigation. The system provides the unique opportunity to obtain observations of extremely faint sources and structure across a range of scales. There are currently many observing proposals being prepared for

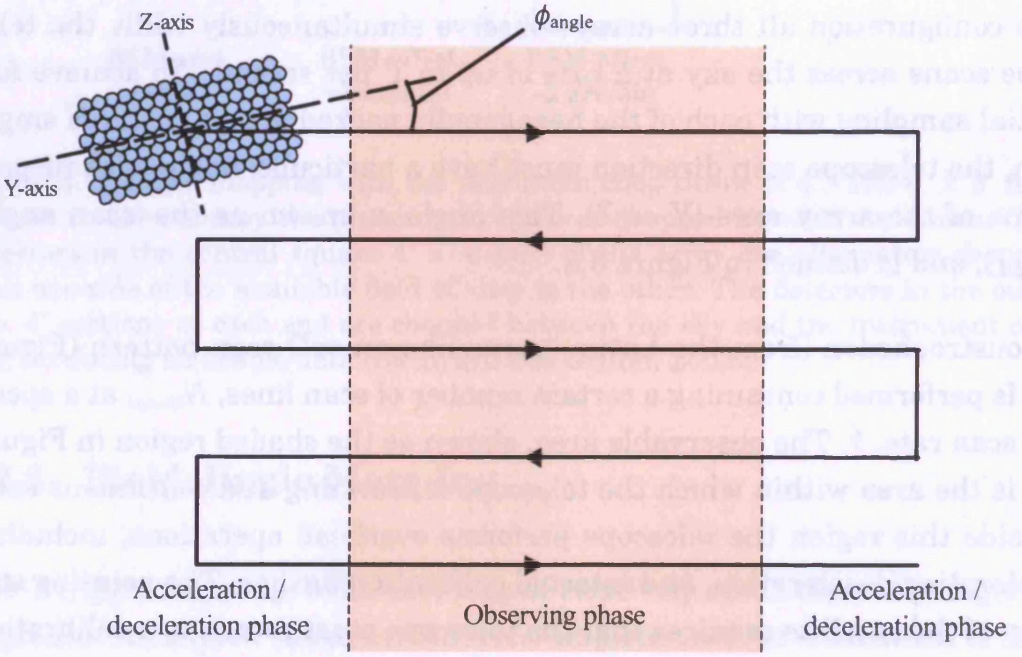

Figure 3.8: POF 5 'Boustrophedon' scan pattern. The shaded region represents the area to be observed, while the residual area is used for telescope acceleration and other overheads. Also shown is the definition of the scan angle parameter.

SPIRE, including those of the SPIRE consortium. The SPIRE consortium is made up of many instrument scientists and astronomers. In return for the time spent in development of the system, the consortium receive a guaranteed 10% of the Herschel mission observing time. This time has been divided between six specialist astronomy groups (SAGs), each focusing on a different area of scientific investigation.

The focus of SAG 1 is the observation of high redshift galaxies. This programme is split into two main sections, the 'Clusters' survey, and the 'Wedding Cake' survey. The first aims to image 15 rich clusters of galaxies, from $z = 0.2$ to > 1, to probe the ultimate depth of SPIRE surveys, exploit gravitational lensing to detect galaxies below the confusion limit, study the evolving member galaxies, and detect the Sunyav ZelDovich (SZ) effect as an increment to the cosmic microwave background signal, and reduce systematic effects from SZ foregrounds (SAG 1 GT proposal, 2004).

The much larger 'Wedding Cake' survey aims to perform a set of blank field extra-galactic surveys with SPIRE and PACS. The goals for this programme include (a) to measure the bolometric luminosity density of the Universe at high redshift ($z \geq 1$) - via number count and luminosity function analysis (b) relate the star formation activity at high redshifts to the masses of halos in which it is occurring - via clustering (c) to provide the best constraints on the statistics of the high redshift galaxies comprising the peak of the FIR/submm background. The survey will also provide a wide variety of other possible science topics which can be addressed since they will provide good samples of rare (luminous or very high redshift) galaxies (SAG 1 GT proposal, 2005).

The second SAG will concentrate on observations of local galaxies. These will be used to bridge the gap between the local universe and primordial galaxies. The proposals put forward by SAG 2 aim to investigate the formation of galaxies, the rapid increase in the dust opacity and luminosity of high redshift luminous galaxies, and their subsequent evolution. Observations of distant galaxies in the FIR/submm will rely on the spectral energy distribution (SED) to draw conclusions on the processes at work in the distant target objects. This SED is almost entirely due to dust emission, and its shape can be altered by a variety of processes. SAG 2 plans to study two of these effects: (1) the star formation activity of the galaxy, which affects the balance between warm and cold dust components, with high star formation activity shifting the SED peak toward shorter wavelengths, and possibly modifying and destroying the dust, and (2) the metallicity, that drives both the total abundance of dust in the interstellar medium, and the dust composition, impacting in turn the heating and cooling properties. Observations of dwarf galaxies will be made as their typical star formation activity ranges over 2 orders of magnitude, with many of them containing super star clusters. Also their metallicity properties span a large range in the local universe, from a nearly solar value to the lowest levels known in galaxies such as IZw18 (1/50 solar metallicity) (SAG 2 GT proposal, 2005b). Both photometric and spectroscopic follow up observations are planned.

Using Herschel's sensitivity to dust in galaxies, SAG 2 also plan to perform a survey of 320 nearby galaxies. Goals for this survey include establishing the importance of dust in galaxies as a source of obscuration in the distant universe, and to study the relationships between star formation and all other components of the interstellar medium, and how they vary with star formation rate. The intergalactic dust cycle will be investigated using observations of dusty halos, dusty superwinds, and tidally stripped dust around galaxies. The local luminosity and dust mass functions will also be measured, along with a further range of objectives (SAG 2 GT proposal, 2005a).

SAGs 3–6 all focus on targets within our own galaxy. The first of the two SAG 3 proposals is a survey of the Gould Belt, a ring of nearby star formation regions tilted with respect to the galactic plane. It is an extensive imaging survey of the densest portion of these star forming complexes with SPIRE at 250-500 μm and PACS 110-170 μm, down to a 5σ column-density sensitivity of $N_{H_2} = 10^{21}$ cm^{-}2 (visual extinction of $A_V \sim 1$). The nominal sensitivity of the survey is well matched to the expected cirrus confusion limit and is such that it should be possible to detect dust emission/structure throughout the maps. The target clouds span a range of physical and environmental conditions from 'active', cluster-forming complexes, to 'quiescent' regions with little or no star formation activity. With $\sim$20 prestellar condensations expected per 0.15 dex mass bin between $0.01\mathrm{M}_\odot$ and $5\mathrm{M}_\odot$, the predicted numbers of objects are both adequate and necessary to derive an accurate prestellar core mass function (CMF) from the substellar to the intermediate-mass regime. The determination of the CMF is one of the main goals of this survey. The large spatial dynamic range of the proposed SPIRE/PACS survey will provide a unique view of the formation of dense cores and protoclusters within molecular cloud complexes, by probing the link between dense cirrus-like structures and compact self-gravitating condensations. The main science goal is to elucidate the initial conditions and physical mechanisms responsible for the formation of prestellar condensations out of the diffuse interstellar medium (SAG 3 GT proposal, 2006a).

SAG 3 also plans to perform a second survey covering a 20 deg^2 area which will encompass all of the high-mass star forming regions at less than 3 kpc from the Sun. This survey will use accurate and high resolution PACS and SPIRE observations to separate individual high-mass protostars from their surroundings and thus determine the fundamental properties of the precursors of OB stars for the first time. The data will also provide an unbiased census of both massive pre-stellar cores and massive Class 0 like protostars, and will trace the large-scale emission of the surrounding clouds. This survey will also yield, for the first time, accurate FIR photometry, and thus good luminosity/mass estimates for a comprehensive and homogeneous sample of OB-type young stellar objects at all evolutionary stages (SAG 3 GT proposal, 2006b).

The scientific motivation of SAG 4 is to trace the evolution of dust grains in relation to changes of the physical, dynamical and chemical properties of the interstellar medium (ISM). This program will provide an unprecedented view of the structure of the ISM at FIR/submm wavelengths and will enable investigation of the impact of dust grains on the ISM physical and chemical state. SPIRE and PACS photometric and spectroscopic observations will provide the low brightness sensitivity, and spectral information, necessary to derive the physical properties of the dust and gas, and so completely characterize dust evolution. The sensitivity of SPIRE to large spatial scales is particularly important for this survey (SAG 4 GT proposal, 2006).

SAG 5 will perform spectroscopic observations of objects in the solar system using all three Herschel spectrometers. HIFI observations of the gas giant planets, Jupiter, Saturn, Uranus, and Neptune, will dominate the programme. Of special interest is the measurement of water in these planets atmospheres, the origin of which is still largely unknown. Measurements of water and other trace elements on Mars may also provide information on photochemistry of the atmosphere. Many elements predicted to exist can only be detected with a very sensitive high resolution instrument such as HIFI. Observations tracing the evolution of water and other molecules from comets as they become active when approaching the Sun are also planned. Low resolution spectral maps of comets will also be performed using the SPIRE FTS (SAG 5 GT proposal, 2004).

Finally, SAG 6 will study circumstellar disc evolution and the contributions of evolved stars and supernovae to the dust content of our Galaxy. Deep imaging of five well known discs (rings) that Herschel can resolve, exploiting the excellent surface brightness sensitivity of the instrument and allowing us to trace spatial variations of the dust properties, will be performed. This programme also builds on a Spitzer legacy survey currently underway which identifies IR-excess stars from a large sample of stars with close to solar masses and spanning the whole range of ages. Spitzer provides for most of the IR-excess stars only one photometric point (at 70 μm) of the dust emission. PACS and SPIRE will together provide six photometric points at wavelengths that cover the peak of the dust emission, and will therefore allow a much better definition physical properties of the discs (SAG 6 GT proposal, 2006a).

The second SAG 6 programme will use Herschel's unique spectral bands and spectroscopic capabilities to identify and characterise the extended diffuse dust emission from sources such as supernova remnants, asymptotic giant branch (AGB) and post-AGB stars. Both photometric and spectroscopic imaging will be employed using SPIRE and PACS. The planned observations will search for shells and multiple shells around AGB stars, post-AGB and planetary nebulae, in order to quantify how much mass is lost at various stages of their evolution, and to attempt to solve the missing mass problem for such objects (see Section 2.2).

SAG 6 also plans to acquire observations of selected evolved stars with specific dust chemistries, in order to characterise fully for the first time dust emission properties in this spectral region. Lastly the group will acquire multi-wavelength imaging photometry of several young supernova remnants, in order to measure the masses of recently formed cold dust present within them and to address the question: are supernovae a major source of dust in galaxies such as our own (SAG 6 GT proposal, 2006b)?

Many of the surveys outlined above will, in addition to achieving the specific goals of the various science teams, provide a wide range of valuable data over a variety of scientific targets. These data will all be public within one year of their observation.

3.4 Chapter Summary

In this chapter I have reviewed the SPIRE instrument hardware, observing modes, illustrated its scientific capabilities by describing some of the SPIRE consortium's proposed science programmes.

Chapter 4

The SPIRE Photometer Simulator

This chapter describes the design and operation of the SPIRE Photometer Simulator (SPS), and outlines the motivation behind its development. A fully detailed description can be found in Appendix A.

4.1 Introduction

Software simulators are becoming a common analysis and diagnostic tool for the development and performance estimation of many complex physical systems, including astronomical instruments. Depending on the sophistication and timing of development, a simulator can be used to assess the impact of various design solutions available during instrument development. This is particularly useful in instances where it is impossible to test the system prior to use in its final operating environment, such as in space.

The consequence of various systematic effects, and noise sources which cannot be easily calculated by theory, can also be studied using a simulator. This can allow investigation of the operational system performance over a wide range of parameter space.

For example, the effect of some change in an instrumental noise parameter, such as the 1/*f* noise knee frequency, can be studied, without the need for further hardware testing. The appropriate changes to observing parameters, such as scanning rate, can then be implemented, thus helping to achieve efficient operation of the facility. This is particularly important in the case of a space mission, as any additional commissioning tests would use valuable in-flight observing time.

Finally, a simulator can provide highly realistic data products, allowing efficient development and evaluation of software tools, capable of storing and processing the data in an optimal manner.

At its most basic a simulator requires three things: an accurate input from which to work, a model of the system, and an output of a form equivalent to that of the real system. In the case of the SPIRE photometer simulator, the input takes the form of a model of the astronomical sky. The complexity of this model can vary and depends on the study being carried out. The system model is a representation of the physical system, and can again vary significantly in complexity, with increased sophistication providing a more faithful output. The simplest form of SPIRE system model would implement an observing pattern for a single detector, and return a sky value for each telescope pointing. Such a model is needed so that the final basic element can be derived; an output with a form equivalent to that of the true system, in this case, astronomical power and telescope pointing time-lines.

In the past some software packages referred to as 'instrument simulators', have in fact been data simulators (e.g. Oliver and Todd, 2000). The output from these systems would often be a beam convolved input sky with some additional noise imposed in the map, thus representing what an astronomer might ultimately want. This does not therefore constitute an instrument simulator as defined above. Results from this type of simulator can, however, be useful to investigate some basic aspects of system performance, such as the effect of the beam size, and white noise level, on the output data quality.

The SPS is a more advanced instrument simulator, composed of a set of detailed subsystem models. It is a modular system coded in Interactive Data Language (IDL), with each module representing a particular subsystem. It allows investigation of a realistic system which incorporates all of the key systematics and noise contributions expected in the final instrument, including the impact of certain observing strategies and methods. It does not however produce data which are identical in all respects to that of the real system. The SPS is highly *representative*, but could never incorporate the inevitable, and as yet unknown, noise and error contributions that might arise in operation. It does however allow us to quantify and characterise the known or anticipated noise and errors which will ideally dominate the system performance.

In summary, the purpose of the SPS is to produce simulated SPIRE photometer data (both science and housekeeping) timelines, derived from a realistic physical model of the instrument which "observes" a simulated astronomical sky using any of the allowed photometer observing functions (POFs). The sensitivity results should be compatible with the photometer sensitivity model, implemented in MATHCAD (Griffin, 2004), but the instrument simulator constitutes a much more sophisticated and versatile tool for evaluating the photometer performance. The system will be upgraded and extended to incorporate improvements made in successive versions of the sensitivity model, and the results from instrument level tests. The simulated data can be analysed using a range of data reduction software and the results compared with the input sky.

The primary use of data derived from the SPS are:

i. to characterise the systematic effects of the SPIRE photometer, and their impact on data quality;

ii. to optimise the observing modes and derive the nominal parameters;

iii. to aid in the development of data pipeline and analysis software;

iv. to help in the planning and optimisation of SPIRE key observations.

4.2 Simulator Development Plan

A final version of the SPS will take a long time to produce, and will not be complete until after launch. I have produced the first version by devising a modular architecture and implementing a form of each module. The modular architecture will allow the simulator to be progressively updated and enhanced in a controlled way. The process of enhancing the simulator will continue as new and more detailed system models are devised, and will incorporate work done by a range of specialists within the consortium. This development is expected to take place throughout instrument building and testing, and also after launch, to ensure that the simulator can represent the real instrument as faithfully as possible.

A similar code has been developed for the FTS Lindner et al. (2004). While this is beyond the scope of this thesis, it should be stated that a similar modular structure has been implemented in this case, meaning that a number of the modules can be shared or straightforwardly adapted as necessary.

4.3 Simulator Architecture

The simulator is made up of modules representing instrument systems or subsystems, called as required to generate time-line data for key instrument and system parameters.

A key feature, necessary to enable organised updates, is that the modules are defined with specific inputs and outputs in such a way that the manner in which the module operates internally (e.g., in physically representing the system or subsystem) can be modified without affecting other modules. In addition to the detector science data timelines, the timelines (actual and sampled) for various other parameters can be accessed (e.g., detector array temperatures, BSM position, etc.)

Time-line generators are based on a single master clock. All samples and the start of all mechanism movements are at clock ticks. This clock always runs at a frequency greater than, or equal to, the SPIRE photometer sampling frequency. This allows processes acting on time scales shorter than the sampling time scale to be included within the system.

4.3.1 Module Summary

A module represents each operational process or system within the Herschel/SPIRE observing system. There are currently 13 modules within the simulator architecture, 10 of which are operational in the current version. The modules are outlined below.

Core: The core module manages and runs all operations specific to operating the simulation software, such as calling other modules in the correct order, performing the required number of simulations, and setting the simulation output file names. It does not represent any physical part of the Herschel-SPIRE system.

Sky: This module produces a simulation of the area of sky to be observed, with a resolution finer than the SPIRE beam. In most cases the sky is loaded from a file; however, for debugging test simulations, a default blank can be created by this module. One sky must be set for each waveband.

Input: The input module specifies the observation in "astronomer's terms", i.e. right ascension and declination. This module is not yet operational in the current version of the simulator.

Optics: This module represents the main optical properties and parameters of the telescope and the SPIRE photometer (including the filters), and the positional mapping of the detectors on the sky. If required, the convolution of the sky with the telescope beam is also performed within this module.

BSM: The BSM module simulates the BSM pointing time-line, i.e. chop and jiggle movements.

Obsfun: The observatory function module specifies the photometer observing mode to be simulated in terms of the appropriate observatory function and its parameters. The input parameters are as defined in the observing modes document (Swinyard and Griffin, 2002). The commanded and actual (i.e. with pointing error) telescope pointing time-lines are also simulated here.

Thermal: This module simulates all information on the temperatures of the instrument and the telescope, and their temporal fluctuations.

Astropower: This module generates a time-line for the power on each detector from the astronomical sky, for each observatory mode pointing (telescope + BSM).

Background: The background power module generates a time-line for the background power incident on each detector, due to all of the contributions from thermal fluctuations.

Detectors: This module produces an output voltage time-line for each detector channel based on inputs from the Astropower and Background modules. A thermal model of the detector is used to generate the correct voltage output, and estimate the detector noise. A voltage time-line with the correct noise properties is also output by this module.

Sampling: The sampling module produces a data time-line filtered by the on-board 5-Hz low pass filter and sampled at the appropriate sampling rate.

HK: The house keeping module outputs time-lines for all instrument temperatures. This module is not yet implemented in the current version of the simulator.

PCal: Finally, the photometer calibrator module produces a timeline of the power incident on each detector from PCal. This module is not yet operational in the current version of the simulator.

4.4 SPS Operation

The SPS runs via a four-phase process. These processes are as follows:

1. Input – parameter input phase, set up of module structures with input parameters;
2. Initialisation – module initialisation and run of non-time step (static) operation modules;
3. Time step – time stepped operation phase, each module is called once each time step;
4. After run – finalisation and post processing of time step time lines, e.g. sampling.

There is the opportunity for each module to run at each stage depending on its functionality and operating processes. In most cases a module will perform its primary task in only one operation phase.

Each phase is initiated via the central SPS core program file, *SPS.pro*.

4.4.1 SPS Control

The *core* control program progresses through each operation phase in turn, as shown in Figure 4.1. Correspondingly there are four calling sequences for each module, one for each phase. These sequences call a routine specific to the current phase of operation for a specific module and pass the required parameters. The parameters within the structures are then converted, as required, into a usable form, before being passed to the central module code. This code contains the modelled subsystem which, once complete, outputs its required data back to the module phase routine. These data are then appended to the module's own parameter structure, and the associated module label parameters updated, before returning to the control program. The module phase routines (file names) contain the suffix *input*, *init*, *step*, or *afterrun*, depending on the specific phase of operation they refer to.

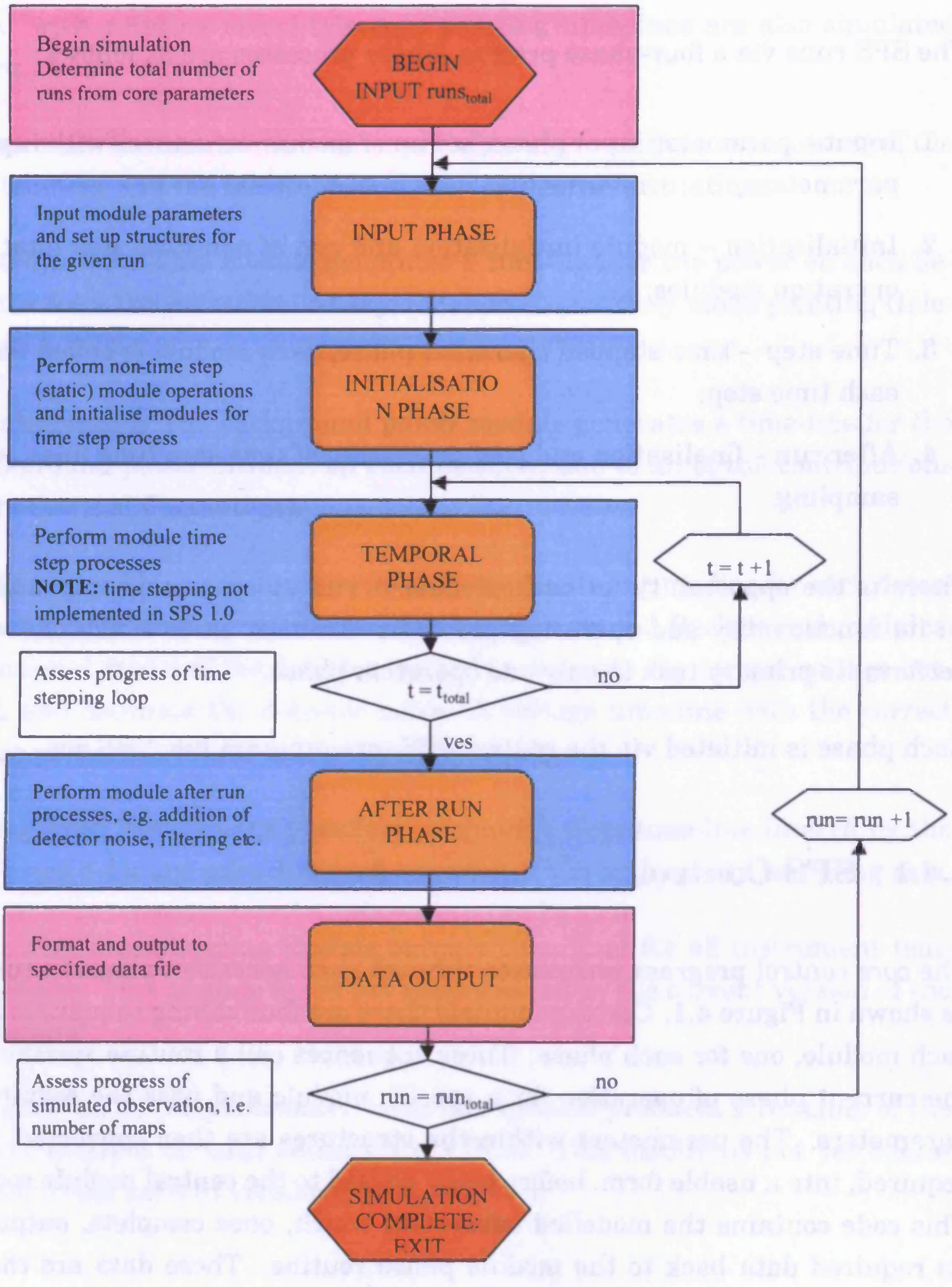

Figure 4.1: SPS operational flow chart

4.4.2 Master Clock

All timeline parameters must be simulated with a time step sufficiently small compared to the data sampling time. The nominal simulator timestep for the photometer detectors is one-third the instrument-sampling rate. Time line output parameters created by modules in the initialisation phase must be created with a sampling time step equivalent to that performed in the time step phase.

The maximum telescope scan rate is 60″/s, so the time to cross $1/10^{th}$ of a beam at 250 μm (approx 2″, the nominal input map resolution) is 1/30 s. To ensure that all quantities are sufficiently finely sampled, a master clock step of no more than $\sim$30 ms is therefore required. A nominal step size of 12 ms is preferred for a system sampling rate of 28 Hz. The total number of master clock ticks in an observation timeline is given by

$$n_{ticks} = \frac{t_{tot}}{\Delta t_{clk}} \tag{4.1}$$

4.4.3 Parameters

There exists an independent 'structure' each module. All input and output variable parameters within the simulator are stored within one of these structures, determined by their 'parent' module (module with which the parameter is associated). In addition to these module structures there is also a module 'label' parameter. This parameter is a string array containing a short piece of information describing the parameters, in order, within each structure. Each time a new parameter is added to a module structure, the module label is also updated. All new parameters and labels are appended to the end of the current structure/label list.

Modules incorporate both input and output parameters, which are subdivided in to the categories as set out below.

1. Input parameters: these are parameters to be supplied to a module in order for it to operate. The inputs required at each phase of operation

may be different depending on the module functionality and purpose:

   (a) User inputs – input parameters supplied by the user via the parameter files;
   (b) Module inputs – input parameters derived from hard coded data within the simulator;
   (c) System inputs – input parameters to one module, created by a previous module operation, within the same simulation.

2. Output parameters: these are parameters generated by module processes. Each module may output different parameters at each phase of operation. Subsequent modules may use these outputs as input parameters:
   (a) System outputs – output parameters which describe fixed (non-time varying) parameters within the observing system, e.g. optical transmission;
   (b) Timeline outputs – derived system parameter time lines, e.g. astronomical power time line;
   (c) Map outputs – output maps representing the sky as seen by the observing system, e.g. convolved sky maps.

Timeline output parameters can be of three kinds:

1. Command timelines: these are time-lines of commanded parameters, such as telescope or BSM position, which are available without error for the data analysis;

2. Hidden timelines: these are time-lines which are produced by the module corresponding to quantities which cannot in reality be directly available to the instrument user - an example is the actual telescope pointing timeline as opposed to the commanded timeline: the former is equivalent to the latter but with added noise, the details of which will never be available from the data stream;

3. Measured timelines: these are timelines of measured (sampled) science or housekeeping data.

These subcategories of timeline parameters are not explicitly separated within the simulator operation. These are important only to those users who wish to use only those parameters available from the physical system. The class of each time line is specified in the accompanying module documentation.

4.4.4 Data Volume

Each time line is a vector of $i = 1$ - n_{ticks} parameter values, corresponding to times from 0 to t_{tot} in steps of Δt_{clk} (the clock interval). There are approximately 300 detectors in total, each with four output timelines: astronomical power, noiseless detector voltage, noisy detector voltage, and sampled detector voltage. Therefore the total number of output timelines is $\sim$1200, meaning that the total number of data points needed for a full one-hour simulation is in the order of 3×10^8, based on the baseline master clock interval being 12 ms, producing 300,000 points per timeline for a 1-hr observation. In addition to these there will also be other memory requirements from other large arrays, e.g. input sky maps.

4.5 Coordinate Systems

The spacecraft and array coordinate system is as shown in Figure 4.2. The telescope boresight is the X direction, with the nominal Sun direction along the Z axis. The detector arrays are in the Y-Z plane. The three arrays overlap on the sky, ideally with no misalignment. In practice there will be some misalignment: the centre of the PSW array is defined to be the (0,0) position.

The chopping/nodding direction is along the Y-axis. For scanning observations, the telescope scan direction is defined with respect to the Z axis as shown.

Coordinates in the Y-Z plane can be expressed in arcseconds on the sky or mm in the focal plane with angle on the sky related to distance in the focal plane related by the plate scale equation. The telescope boresight position

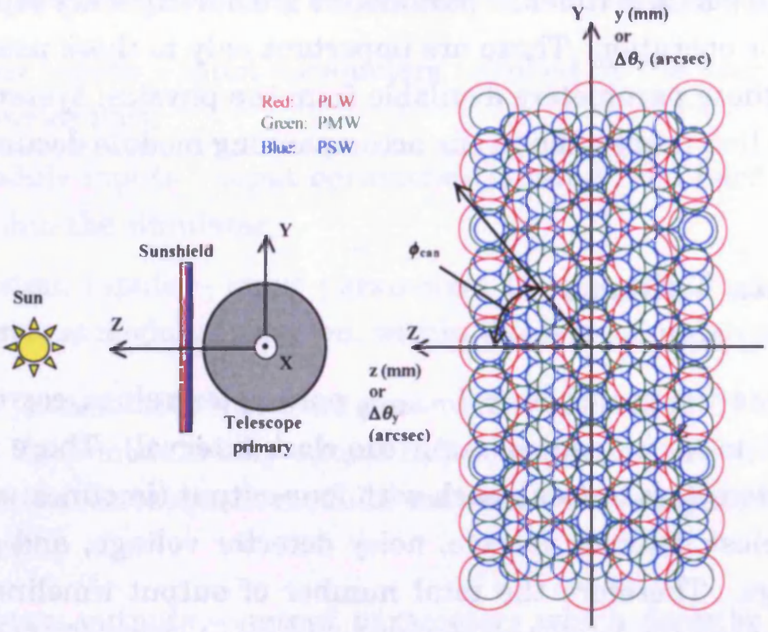

Figure 4.2: Space craft coordinate system, and the projection of this system on to the SPIRE photometer detector arrays.

$(\Delta\theta y, \Delta\theta z)$ is defined with respect to the centre of the PSW array (0,0).

4.6 Module Operations

4.6.1 Sky Simulator (Sky)

This module produces a simulation of an area of sky larger than the area to be observed. The output consists of three rectangular grids of sky positions with spacing significantly smaller than the 16″ FWHM at 250 μm. There is one sky map per SPIRE array each with the same size and resolution. The simulator can operate on any sky map produced in FITS format, where the sky image is contained within the primary data table.

The grid coordinate system is defined as follows, the lower left corner of the simulated area is designated as the (0,0) position on the spacecraft Z and

Y axes respectively (Figure 4.3). The grid units are in terms of the angle on the sky in the spacecraft Z-Y plane, as measured in arcseconds. The square grid has a spacing of nominal value 2″. Other integer pixel sizes up to 6″ are also supported. Each pixel represents a square area of sky, and has an associated value of flux density (Jy/pixel). To represent a point source, the delta-function is approximated by a single pixel with the appropriate flux density, superimposed on the representation of extended emission.

Once read in, the FITS file will produce a 2D array of arbitrary dimensions with an associated flux density per pixel at each array point. There are three files to be read in, each representing the same area of sky at different SPIRE photometer wavelengths. It is also required that the user specify the resolution of the input sky map. These maps will be a representation of the true sky, i.e. unconvolved with any instrument beams. The simulator can support the input of preconvolved skies via an informational switch set when inputting the simulation setup.

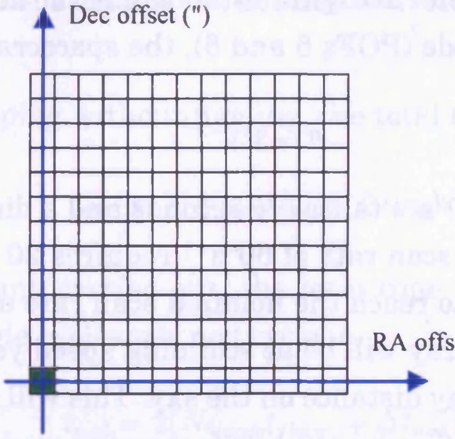

Figure 4.3: Coordinates system as seen on input sky grid

4.6.2 Observatory Function (Obsfun)

This module specifies the photometer observing mode to be simulated in terms of the appropriate Observatory Function and its parameters, as defined in the observing mode document (Swinyard and Griffin, 2002). The observing parameters corresponding to the chosen POF are set up and the telescope pointing timeline, including associated pointing errors computed.

Telescope Movement

Re-pointing: Section 5.12 of the Herschel/Planck Instrument Interface Document (A) specifies the requirement and goal for small slews executed during observations. The movement time, Δt_{motion}, is defined as the time between the start of the motion and the instant at which the new telescope position is deemed to have been reached, and depends on the angular distance according to the following formula:

$$\Delta t_{motion} = 10 + \sqrt{2\Delta\theta} \ (req.) \qquad \Delta t_{motion} = 5 + \sqrt{\Delta\theta} \ (goal) \tag{4.2}$$

where $\Delta\theta$ is in arcseconds.

Accelerating and decelerating: In establishing the desired scan speed for continuous scanning mode (POFs 5 and 6), the spacecraft scan acceleration will be fixed at a value:

$$\ddot{\theta} = 3''s^{-2} \tag{4.3}$$

To attain a scan rate of $\dot{\theta}''\text{s}^{-1}$ takes $\dot{\theta}/\ddot{\theta}$ seconds and a distance of $\dot{\theta}^2/2\ddot{\theta}''$. For example, the maximum scan rate of $60''\text{s}^{-1}$ requires 20 s and $10'$. However it should be noted that to reach the nominal scan rate of $30''\text{s}^{-1}$ requires 10 s and $2.5'$. Hence the array will be at scanning speed yet the array will not have travelled a full array distance on the sky. This will result in a region at the beginning and end of each scan line (assuming equivalent deceleration) where full spatial sampling may not be achieved. As a result an adjustment may be necessary when setting up the observation to ensure that the correct area of sky is properly observed.

Nodding: The nodding movement time, Δt_{nod}, is defined as the time between the start of nod motion and the instant at which the new telescope position is deemed to have been reached (assumed to be the same for both nod directions). This is shown schematically in Figure 4.4. Δt_{nod} is given by

Equation 4.4.

$$\Delta t_{nod} = 10 + \sqrt{2\Delta\theta_{chop}}\ (req.) \qquad \Delta t_{nod} = 5 + \sqrt{\Delta\theta_{chop}}\ (goal) \tag{4.4}$$

For example, with $\Delta\theta_{chop}$ = 126″, the nod time is 25 s (req.) or 16 s (goal).

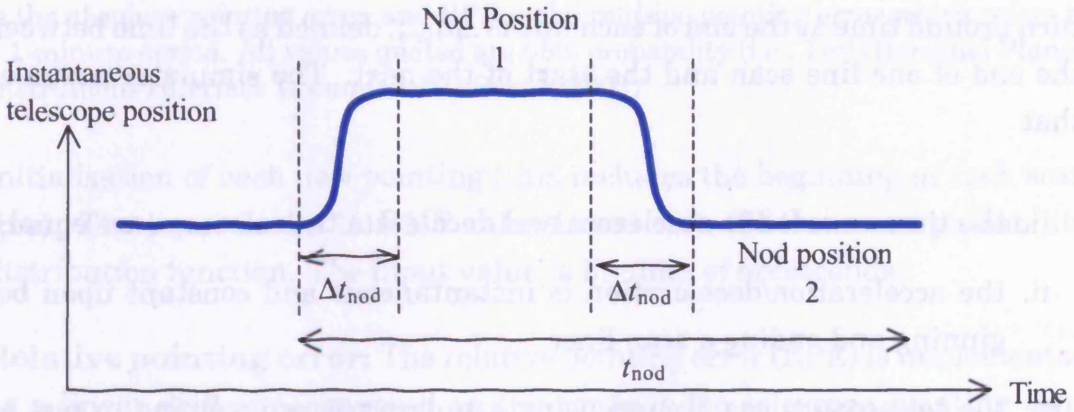

Figure 4.4: Telescope nod position as a function of time.

For the case of chopping without jiggling, the total time per nod cycle is

$$t_{nod} = 2(N_{chop}t_{chop} + \Delta t_{nod}). \tag{4.5}$$

When jiggling is being carried out, the total time for a complete nod cycle involving N_{jigcyc} jiggle cycles per nod cycle is

$$t_{nod} = 2(N_{jigcyc}t_{jigcyc} + \Delta t_{nod}) \tag{4.6}$$

The total number of nod cycles to be carried out in an observation is N_{nod}.

Rastering: A standard raster observation consists of N_{lines} lines with N_{steps} raster points per line. The raster movement times, Δt_{step} for repointing by $\Delta\theta_{step}$ along a line, or Δt_{line} for repointing by $\Delta\theta_{line}$ between lines, are also given by Equation 4.7. For a raster of 4 × 4 jiggle maps, the step could be 3.5′ (to provide some overlap between the sub-maps). The step time for each movement of the raster pattern is then ∼ 30 s (reg.) or ∼ 20 s (req.).

The total time spent in moving the telescope between raster positions is

$$\Delta t_{rast} = (N_{step} - 1)\Delta t_{step} + (N_{lines} - 1)\Delta t_{line}. \tag{4.7}$$

Scanning: A standard scanning observation consists of N_{lines} scans, each of length $\Delta\theta_{scan}$ with spacing $\Delta\theta_{line}$. A line scan is not deemed to have started until the telescope has attained the required scan speed, $\dot{\theta}$. The telescope turn around time at the end of each line is Δt_{turn}, defined as the time between the end of one line scan and the start of the next. The simulator assumes that

i. the times needed to accelerate and decelerate the telescope are equal;

ii. the acceleration/deceleration is instantaneous and constant upon beginning and ending a scan line;

iii. the telescope turns around using a square pattern, coming to rest at each corner.

The total turn-around time is then

$$\Delta t_{turn} = \frac{2\dot{\theta}}{\ddot{\theta}} \tag{4.8}$$

The total time for an observation is

$$t_{tot} = N_{lines}(\dot{\theta}\Delta\theta_{scan} + \Delta t_{turn}), \tag{4.9}$$

where we also assume a time $\Delta t_{turn}/2$ is needed both for the first acceleration at the start, and the last deceleration at the end of the observation.

Pointing Error

The pointing errors are defined in the Herschel Planck Instrument Interface Document IID PartA (2003) and shown in Table 4.1

Absolute pointing error: The absolute pointing error (APE) is implemented as a random positional offset in both the Z and Y direction upon the

APE ($''$)	=	$3.7 + 0.05\dot{\theta}$	req.
	=	$1.5 + 0.03\dot{\theta}$	goal
RPE ($''$)	=	0.03	Pointing
	=	1.2	req. scanning
	=	0.8	goal, scanning

Table 4.1: Summary of the Herschel pointing stability requirements and goals. APE is the absolute pointing error, and RPE is the relative pointing error which refers to a 1-minute period. All values quoted are 68% probability (i.e., 1-σ) (Herschel Planck Instrument Interface Document IID PartA, 2003)

initialisation of each new pointing (this includes the beginning of each scan line). The input is the 1σ RMS value based on a 2D Gaussian probability distribution function. The input value is in units of arcseconds.

Relative pointing error: The relative pointing error (RPE) is implemented as a linear drift superimposed on the commanded telescope pointing time line. This drift occurs for the full duration of the observation. The amplitude of the drift is derived from an input drift velocity variable. This variable defines the 2D Gaussian probability distribution from which the implemented drift velocity is derived, and is input in units of arcseconds per second. The direction of drift is derived via a random number generator.

This is only valid for short scans. Further work will be carried out and an improved version developed for future SPS releases.

Input Scanning Parameters

There are four important input parameters to be specified when performing an extended map observation (POFs 4, 5 or 6) in order to ensure the output map covers the region required. These are $centre_z$, $centre_y$, dir_{scan}, *scan rotation* (see Figure 4.5).

The start parameters define the centre of the scan map pattern and are defined with reference to the input sky. The lower left corner of the input sky is regarded as the (0,0) point. These parameters have the units of arcseconds. The input map resolution is used to scale these parameters to the input map

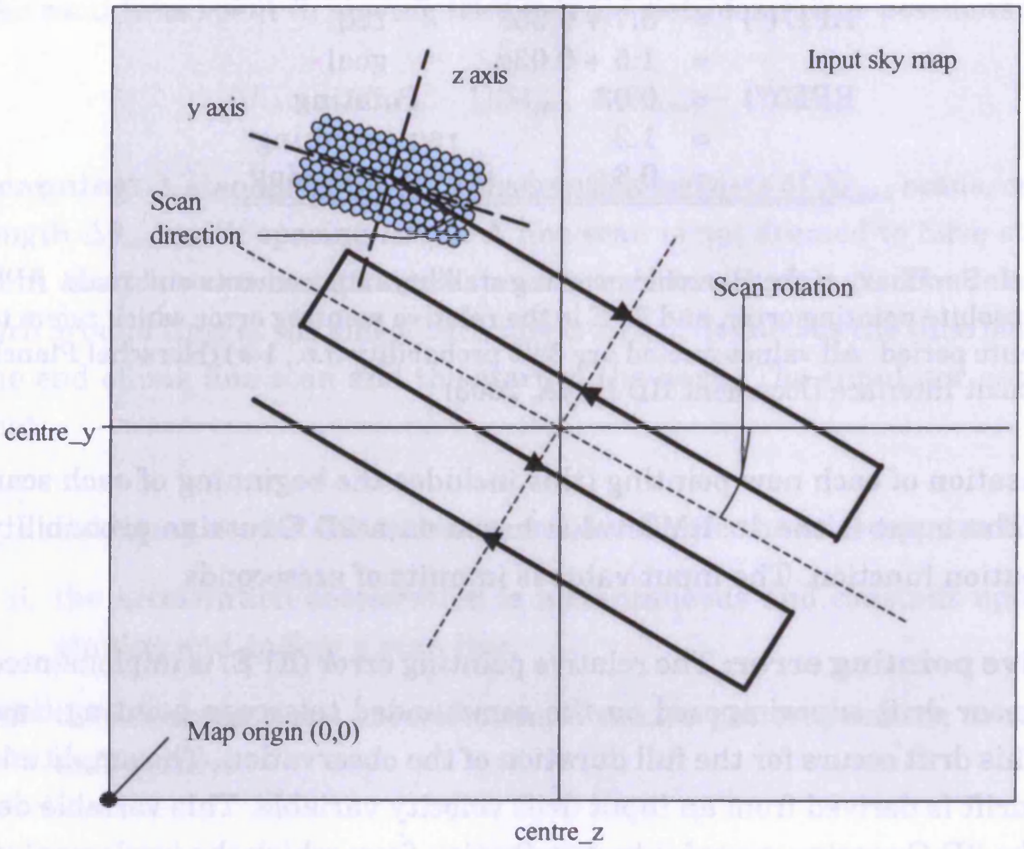

Figure 4.5: Schematic defining the SPS input scanning parameters.

pixelisation during the simulation.

The scan direction parameter defines the detector array orientation with respect to the satellite Y-Z axes. The angle is taken with reference to the Y-axis. This angle is the 'magic angle' required for fully sampled mapping.

The scan rotation parameter rotates the entire scan map about the centre point (the 'start' values). This allows for investigation of various interlinked scanning patterns etc.

4.6.3 Optics Module (Optics)

This module represents the main optical properties and parameters for the telescope and the SPIRE instrument optics, including the detector feedhorns. It computes the overall Relative Spectral Response Function (RSRF) for the three bands. The input sky maps are also convolved here with a modelled telescope beam (see below). Finally the selection of operational detector pixels is performed and their positional sky offsets calculated.

Telescope Properties: The telescope is characterised by its primary mirror diameter, 3.5 m, emissivity, $\sim$4%, focal ratio, 8.68, and obscuration factor, 0.872 (Griffin, 2004).

Mirror and filter properties: The optical properties of the mirrors and filters (transmission, emissivity) are characterised as a function of frequency. For simplicity, a discrete frequency vector is used, covering the range 3×10^{11} Hz (1 mm) to 3×10^{12} Hz (100 μm), with a spacing of 3×10^{9} Hz (a total of 901 points).

Each component in the optical chain is described by transmission (t) and emissivity (e) profiles for the component. The positions of the optical components are as indicated in Figure 3.1(b). This standard optical element numbering convention assigns each subsequent optical element a number referring to its position in the optical chain, with element 0 being the telescope primary.

Detector Arrays and Detector Positions

All detectors are defined by their Y and Z positional offsets with respect to the centre of the PSW array. The geometrical centre of the PSW array is defined to be coincident with the telescope pointing boresight. These Y and Z offsets are translated into pointing offsets on the sky via multiplication by the plate scale. It is these pointing offsets that are imposed onto the final telescope and BSM pointing timelines to provide individual pointing information for each detector. Each detector position parameter can be given a slight random scatter if manufacturing errors are required to be represented.

Each detector is assigned a number defined by its position within the array and shown in Figure 4.6. Numbers start at 0 and run to 138 in the case of the PSW array. Numbering begins at the bottom left of the array and increases as shown. Additional pixels such as dark pixels and thermometers are appended to the end of this number sequence.

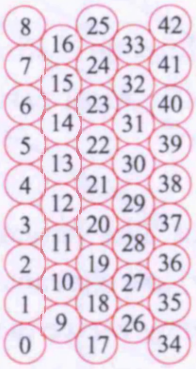

Figure 4.6: Diagram showing the indexing system used to specify individual detector pixels within the SPS.

Beam profiles: Each detector has a beam profile on the sky, represented by a modelled telescope beam, computed using a Hankel transformation. An example of the modelled beam used in the SPS is shown in Figure 4.7. In the current version, all detectors in a given array have the same beam profile. The module architecture allows the beam profiles to be specified independently for different detectors.

Feedhorn throughput: Since each feedhorn is single moded, the optical throughput ($A\Omega$) is nominally equal to λ^2 (Griffin et al., 2002a).

Spillover efficiency: This is the fraction, η_s, of the throughput from a detector that illuminates the telescope. A fraction 1-η_s is assumed to terminate on the walls of the level-1 enclosure. The value of η_s is assumed to be the same for all detectors in a given array.

Feedhorn/cavity efficiency: Each detector has an optical efficiency, η_{feed},

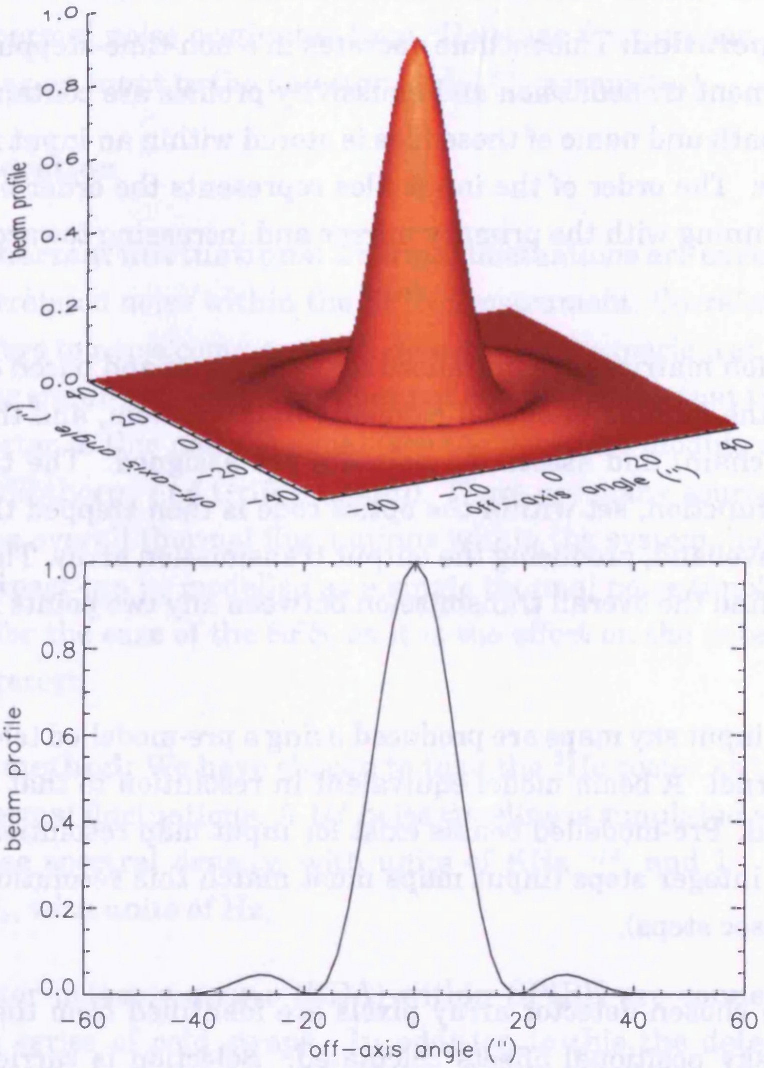

Figure 4.7: Sample modelled SPIRE PSW band beam profile as seen by a SPIRE photometer detector. This model is used in the SPS, shown in (a) 3D, and (b) cross-section. The side-lobe power is ~5% of the peak power.

equal to the fraction of the horn throughput ($A\Omega$) which is absorbed by the bolometer.

Cutoff wavelength: Each detector feedhorn has an output waveguide with diameter d_{wav}, which determines the cutoff wavelength.

Module operation: This module operates in a non-time-stepping mode. All optical element transmission and emissivity profiles are contained in input files. The path and name of these files is stored within an input file specified by the user. The order of the input files represents the order of the optical chain, beginning with the primary mirror and increasing towards the detector array.

Transmission matrices are initialised for each waveband based on the input data (e.g. the number of optical elements in the system, and their order in the optics chain) and associated pointers are assigned. The transmission calculator function, set within the optics code is then stepped through once for each waveband, producing the output transmission array. This array can be used to find the overall transmission between any two points in the optics chain.

Convolved input sky maps are produced using a pre-modelled telescope beam pattern kernel. A beam model equivalent in resolution to that of the input map is used. Pre-modelled beams exist for input map resolutions from 1 to 6″/pixel in integer steps (input maps must match this resolution, i.e. be in integer arcsec steps).

Finally the chosen detector array pixels are identified from the user input and their sky positional offsets calculated. Selection is carried out via a graphical user interface (*array-gui.pro*), which allows selection of individual detectors, or a choice of either full arrays or all co-aligned pixels. Opting to use less detector pixels results in a faster run time, however a minimum of one pixel must be selected in each array.

4.6.4 Thermal System (Thermal)

This module characterises the temperatures of all relevant elements and their time variations. A vector of temperature differences verses time describes thermal drifts of elements within the system for the timeline duration. The thermal noise originates from ^{3}He stage fluctuations. This timeline is used as an input to the detector model (T_o parameter).

Module operation

Origin of thermal fluctuations: Thermal fluctuations are expected to be a source of correlated noise within the SPIRE instrument. Correlated noise in this case refers to noise common to all detectors and experienced simultaneously, or near simultaneously. This does not however mean that the response of each detector to this noise is equal (see the detectors module documentation within Sibthorpe and Griffin (2006)). There are many sources that contribute to the overall thermal fluctuations within the system, however their resultant impact can be modelled as a single thermal noise timeline. This is reasonable for the case of the SPS, as it is the effect on the detector output that is of interest.

Modelling method: We have chosen to take the ^{3}He cooler as the primary source of thermal fluctuations. A $1/f$ noise timeline is simulated with a given thermal noise spectral density, with units of KHz$^{-1/2}$, and $1/f$ noise knee frequency, f_k, with units of Hz.

The bolometer detector arrays (BDA) within SPIRE are connected to the cooler via a series of cold straps. In addition to this the detector arrays themselves are directly coupled to a large thermal mass of the invar mount. As a consequence of this, any thermal fluctuations arising in the cooler are low-pass filtered by the time they reach the bolometers. This is modelled here using a first order low pass filter profile, with a different time constant, in seconds, for each array. The different time constants represent the different ways in which the thermal noise could manifest itself in each array. The input thermal noise timeline remains fixed for each array, but the filtering changes the thermal noise timeline seen by the three detector arrays.

Given the difficultly in accurately predicting the operational thermal environment of SPIRE, the nominal values to be used within the SPS are chosen so as to present a challenging task for data analysis systems. This will assist in the development of robust data analysis tools. Values for the thermal noise spectral density, $1/f$ noise knee frequency, and three time constants are required. The noise spectral density is be given a value higher than that expected from most ^{3}He fridges. This value should also be set so as to produce a noise timeline with large-scale deviations several times those arising from independent detector $1/f$ noise sources alone. It was found that a value of 50 μKHz$^{-1/2}$ works well.

To produce significant variation within a single scan line, a $1/f$ noise knee frequency of approximately 30 mHz is currently used. This allows for approximately four $1/f$ noise timescales to pass during a 1 degree scan line, scanning at the nominal rate of $30''\mathrm{s}^{-1}$. It also sets the thermal $1/f$ noise knee close to the detector $1/f$ noise knee, making the identification of one from the other a more challenging task.

Thermal time constants have been estimated from instrument test results. Values range from 70 - 130 s, with a nominal value of 100 s. From this the chosen nominal SPS values are currently 70, 100, and 130 s, for the photometer short, medium, and long wavelength arrays respectively.

Implementation: The initial $1/f$ noise time line is produced using the standard SPS $1/f$ noise timeline generator (see Sibthorpe and Griffin (2006) for information). The Fourier transform of this timeline is then performed, and the resultant frequency spectrum multiplied by the appropriate first order filter profile. The inverse transform is then performed to return the final thermal noise timeline.

This noise timeline is input to the bolometer model as an addition to the detector array base temperature, T_o.

Sample data: Figure 4.8 shows a sample detector output voltage timeline. This timeline shows the result of an input thermal drift, generated as outlined above (red line), with input parameters of 50 μKHz$^{-1/2}$ thermal stability, f_k = 30 mHz, and t = 70 s, for a single PSW detector. Significant thermal

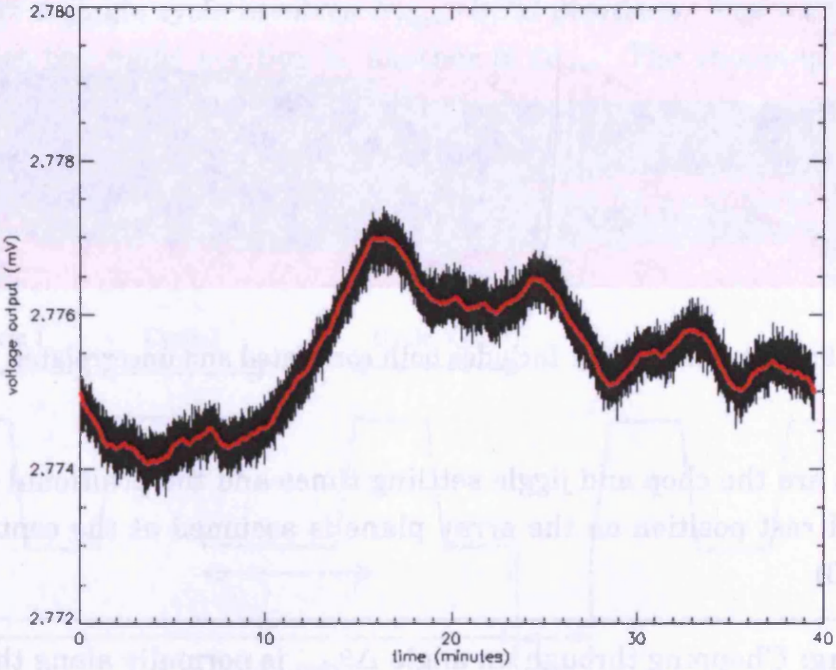

Figure 4.8: Sample detector output resulting from thermal drift.

drift can be seen on the scale of approximately two minutes. In addition, the final detector output timeline (before onboard low-pass filtering), including independent $1/f$ noise contribution from the detector electronics and read-outs, is shown in black. The amplitude of the independent non-thermal $1/f$ noise in this case is set to the nominal SPIRE values, with a $1/f$ noise knee frequency of 100 mHz.

Figure 4.9 illustrates the impact of the thermal drift seen in Figure 4.8 in the form of a map (PSW array). Large correlated thermal drifts, in addition to independent uncorrelated noise variations can be clearly seen. No data processing has been performed on these data beyond the low pass filtering imposed by the on-board 5-Hz filter.

4.6.5 Beam Steering Mirror (BSM)

This module simulates the required motion of the BSM and produces a time-line corresponding to the pointing modulation that it produces. The key pa-

Figure 4.9: Map of blank sky. Includes both correlated and uncorrelated 1/f noise.

rameters are the chop and jiggle settling times and the positional stability. The BSM rest position on the array plane is assumed at the centre of the array (0,0).

Chopping: Chopping through an angle $\Delta\theta_{chop}$ is normally along the Y-axis, and symmetrical about (0,0). The left beam is defined as the one on the negative side of the Y-axis and the right beam as the one on the positive side (Figure 4.10).

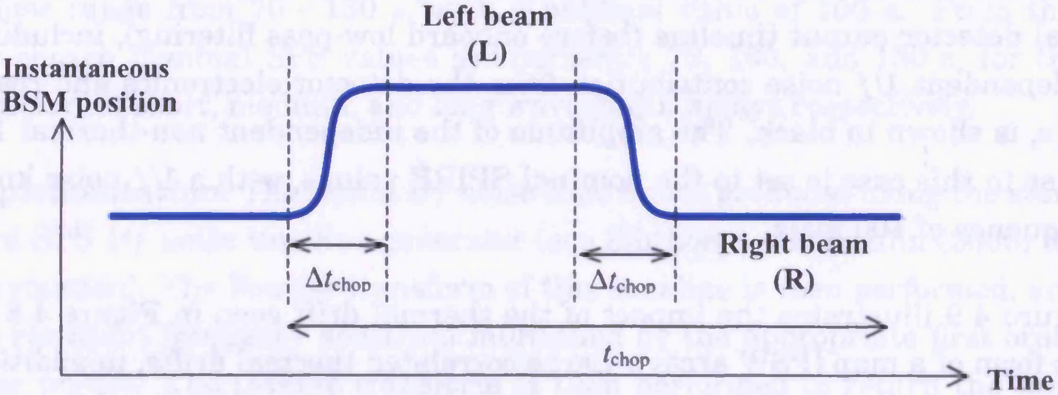

Figure 4.10: BSM chop position as a function of time.

The time for one complete chop cycle is t_{chop}. Δt_{chop} is the time between the start of chop position motion and the instant at which data are deemed valid (BSM sky position within 1″ of the required position). The total 'dead time' for one chop cycle is thus $2\Delta t_{chop}$. The nominal value of Δt_{chop} is 20 ms (Parr-Burman, 2003).

Jiggling: A jiggle cycle involves N_{jigpos} BSM positions. The time taken to move from one jiggle position to another is Δt_{jig}. The chopping motion is interrupted for a time Δt_{jig} while the jiggle axis moves to a new position (Figure 4.11), and then chopping is resumed. The nominal value of Δt_{jig} is 100 ms (Parr-Burman, 2003). The total time taken for a complete jiggle cycle of N_{jigpos} positions, involving $N_{jigpos} -$ jiggle position movements is,

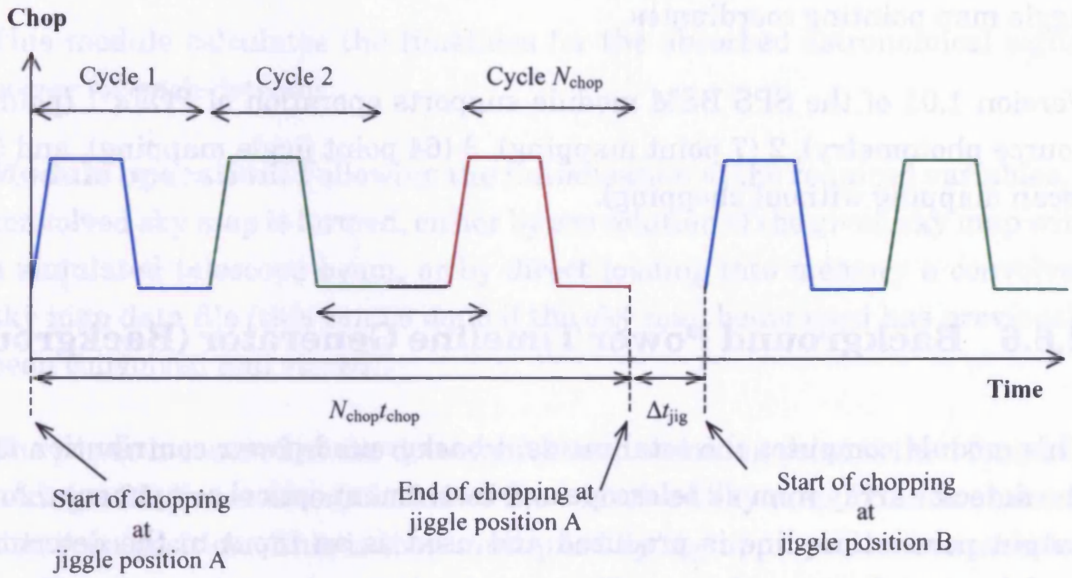

Figure 4.11: BSM jiggle position as a function of time

$$t_{jigcyc} = N_{jigpos}(N_{chop}t_{chop}) + (N_{jigpos} - 1)\Delta t_{jig} \tag{4.10}$$

Note that in the case of chopping without jiggling, t_{jigcyc} reduces to $N_{chop}t_{chop}$.

Module operation: In the current version of the SPS, BSM movement is assumed to occur instantaneously between consecutive pointings. These pointings are also assumed to contain no error. Time lags between pointing are planned for future versions of the simulator. The detector response to a BSM movement is dominated by the 5-Hz low pass filter. Therefore, the current model is sufficient for the first generation of simulator investigations.

In the case of no BSM operation (e.g. POF 5 scan map mode) scalar values of -1 are returned in the BSM pointing time line parameters. Computation of the BSM time-lines are performed independent of any telescope pointing time line generation.

When performing a 64 point jiggle map a set of normalised pointing positions are loaded from a file. System parameters are then used (detector array beam separation) in conjunction with these data to compute the full 64 point jiggle map pointing coordinates.

Version 1.01 of the SPS BSM module supports operation of POFs 1 (point source photometry), 2 (7 point mapping), 3 (64 point jiggle mapping), and 5 (scan mapping without chopping).

4.6.6 Background Power Timeline Generator (Background)

This module computes the total incident background power contribution at the detector array from all telescope and instrument optical components. An output power time line is produced and used as an input to the detector model.

Module operation: Required variables are derived from the optics module. All optical components are assumed to emit as greybodies. The integrated power is computed over the full SPS frequency range ($3 \times 10^{11} - 3 \times 10^{12}$ Hz) for each optical element, taking into account the emissivity and optical transmission profiles (equation 4.11). The output is then multiplied by the requisite efficiencies to produce a final background power for this element,

$$Q_{back} = A\Omega\eta_{feed} \int_{\nu_{lower}}^{\nu_{upper}} \epsilon(\nu)t(\nu)B(\nu,T)d\nu, \qquad (4.11)$$

where Q_{back} is the background power produced by a single optical element, A is the telescope area, Ω is the solid angle, η_{feed} is the feedhorn efficiency, ϵ is the emissivity of optical element, $t(\nu)$ is the optical transmission of optical element as seem by the detector, and $B(\nu,T)$ is the blackbody function.

This processes is stepped through for all optical elements in each waveband and finally summed to produce a single value for the total background power in each waveband. It is assumed that the incident background power is the same for each detector within an array is equal.

4.6.7 Astronomical Power Timeline Generator (Astropower)

This module calculates the timelines for the absorbed astronomical signal power for each detector.

Module operation: Following the initialisation of the required variables, a convolved sky map is formed, either by convolution of the given sky map with a simulated telescope beam, or by direct loading into memory a convolved sky map data file (this can be done if the sky map being used has previously been convolved and stored).

The power measured at the detector for each scanning point is then found by taking a 2D linear interpolation of the convolved sky map for each observation scan position. This is then multiplied by the appropriate transmission profile to give the power at the detector. These values are then integrated over the frequency range using Simpson's rule and multiplied by the necessary efficiency factors and constants resulting in an astronomical power value. The output is an array, for each waveband, of the total astronomical power at the detector for each scan point observed.

The total astronomical signal power falling on a detector in a single time step is given by,

$$Q_{sig} = A\Omega\eta_{feed}\eta_{tel}S_{\nu}10^{-26}\int_{\nu_{lower}}^{\nu_{upper}} t(\nu)d\nu, \tag{4.12}$$

where Q_{sig} is the astronomical power in W from a source, and S_{ν} is the flux received from the source in Jy.

4.6.8 Detector Voltage Timeline Generator (Detectors)

This module models the detector response to an input background and astronomical power via a full physical model of the system. The model used is based on the work of Sudiwala et al. (1992), and is implemented in order to generate realistic bolometer responses for the flight detector arrays. This includes the ability to generate a non-linear output in response to a sufficiently high power input. In addition, measured flight detector parameters can be input, thereby generating a unique response to any system variation, such as fluctuation in thermal environment, for each bolometer.

Bolometer response: The detector module requires initialisation before it can be used to begin an observation. This is due to the fact that in order to perform an observation, operating points on the bolometer load curves must first be defined and set into the common blocks used to store detector module parameters. Subsequent time steps compare new inputs with those from a previous time step in order to determine the level of change within the system, and hence the bolometer response, before computing a new output.

In cases where key parameters change, such as the detector array base plate temperature or background power, a recalculation of each bolometer operating point is required. The operating point is found using a Newton Raphson method to compute the correct bias parameter. A bias parameter is set and the associated bias voltage for that parameter found. This is then compared to the actual bias voltage set within the system. Once the bias voltage associated with the bias parameter is within some tolerance, the operating point is obtained. Each time a new operating point is calculated, new values for responsivity and detector time constant are derived, and used in the computation of the detector response.

In cases of high astronomical signal the detector response will become non-linear. A threshold is set for this condition, the value being set from tests or as a compromise for computational power. Up until this threshold is reached the previous operating point and associated parameters are assumed to be constant, and a linear response computed. In cases where the astronomical signal becomes greater than a small fraction of the nominal background power ($\sim$ 5%), the detector's operating point and parameters are recalculated, and the new operating point is compared to the previous voltage and taken as the new voltage change (dV). The time constant is taken to be the mean of the time constant at each operating point.

Noise: Noise spectral density estimates are made for each detector independently via a series of equations as formulated by Sudiwala et al. (1992). The noise estimate is made based on the initial bolometer parameters. Only one value of noise spectral density is computed for any individual detector. The noise estimates include contributions from photon noise arising from the primary and secondary mirrors (background power dominated), phonon noise, load resistor noise, Johnson, and amplifier noise. These replicate the noise sources specified in the SPIRE sensitivity document (Griffin, 2004).

These noise estimates are used as inputs to a noise time line generator. The noise generator uses this noise estimate along with a $1/f$ noise knee frequency to output a unique $1/f$ noise time line for each detector. The $1/f$ power spectrum is imposed in Fourier space via multiplication with a white noise time line. The white noise has a Gaussian probability distribution with the RMS value set to $e_n\sqrt{\Delta f}$, where e_n is the overall noise spectral density, and Δf is the frequency bandwidth corresponding to the specified simulator time step.

Bolometer parameters: There are two options when selecting the bolometer parameters to be used within the detector model. The first assumes that each detector is identical, giving every bolometer the same nominal bolometer parameters for a given array. The second option is to use the individual measured bolometer parameters. These are read in from a parameters file. The choice is made by selecting either to have the 'real bolometer parameters' on or off (1/0) in the detectors parameters file (*params-detectors.txt*).

Operating with the real bolometer parameters also provides the measured values of $1/f$ noise knee frequency for each detector. These values are used as a series of offset values from the SPIRE nominal detector knee frequency (0.1 Hz). For example, when the nominal knee frequency is set to 0.1 Hz, the realistic values are set. In the case where the knee frequency is set to 1 Hz, the same scatter will be seen but with 1 Hz added to each value.

4.6.9 Sampling System (Sampling)

This module low-pass filters and samples the output detector data time line. The data are sampled at the rate specified by the user. This system replicates the SPIRE on-board 5-Hz analogue filter within the physical system.

Module operation: Each detector voltage time line is filtered by multiplication in Fourier space with the 5-Hz filter profile.

The data are then sampled at a given frequency, where the sampling frequency is lower than the simulator step frequency. A linear interpolation is performed when a sampling point does not match an integer number of simulator time steps.

4.6.10 Simulator Operation

There are currently two modes of SPS operation, standard, and repeat. Standard is classed as operating mode 0. This setting will perform n number of simulations in full. Repeat mode (1) performs one full simulation. Once complete, new detector noise realisations and filtering is performed and imposed on the detector model output of the initial simulation. This is intended for fast generation of data sets in cases such as high redshift extra-galactic studies, where many maps of the same region will be required. The output from these simulations can not therefore include variations in system pointing or detector temperature. As a result these data have a lower order representation of the SPIRE system.

The current version runs a full simulation in mode 0 in approximately half the time of the real life observation, on a typical desktop computer (CPU speed $\sim$P4 2.7 GHz). The output file size varies depending on the output options selected, but a one square degree scan map simulation with two types of output time-line (e.g. sampled and noiseless data) will be $\sim$ 400 MB.

4.7 Chapter Summary

In this chapter, I have introduced the SPIRE photometer software simulator, and outlined its primary goals and operation. The SPS is a highly realistic software model of the SPIRE photometer, which in the current version, contains all of the primary photometer subsystems. It is capable of simulating the photometer system operation, and data characteristics. A brief description of the methods used to model each instrument subsystem, implemented in the form of a module, has also been presented. The limitations of the simulations have been noted, specifically, that results from simulation can only be representative, and not identical to, the final system output. This makes the simulator useful in understanding the impact of the known systematics on the data quality, but it cannot predict the final instrument performance until the system is in orbit.

Chapter 5

SPIRE Data Reduction and SPS Performance Verification

The SPIRE photometer simulator produces as its primary output three kinds of time ordered data (TOD) time-lines, the telescope pointing time-line, BSM position time-line, and detector voltage time-line. In order for the simulator to be useful, it is crucial that the system operation be verified. Correct operation can be assessed by comparing the output signal and noise levels for sample cases with the theoretical values. This in turn requires the reduction of the TOD to some useful form, such as a map. The data should also be cleaned of instrumental and astronomical characteristics which might introduce error which cannot be easily accounted for theoretically. This cleaning will represent the kind of processes performed in a pre-map-making data pipeline.

In this chapter an overview of the data cleaning methods, through which SPIRE data must be processed, are presented. A brief introduction to naïve and maximum likelihood map-making methods is also given. Following this, a robust method for the determination of the SNR of a point source, in a map containing uniform noise, is presented. This method is then used to derive the SNR of a source within a SPS output map. The SNR obtained is then used to validate the SPS operation, by comparison with the theoretically expected value, and by comparison with the SPIRE sensitivity model (Griffin, 2004). Finally, an aside on the SPIRE map-making selection exercise is presented.

5.1 Data Cleaning

Raw detector TOD contain a range of different artefacts which require cleaning before any data analysis can be performed. Cosmic rays hitting the detector array for example will cause a large signal spike, or 'glitch', in the signal timeline. It may take several time constants for the detector to return to a normal operating level following such a hit. Often these artefacts are dealt with by identifying the cosmic ray hit and flagging this section of data as 'bad' for a certain number of time constant after its detection. In many cases these missing data are then filled using some interpolation of the surrounding data, with the correct characteristic noise being input. This makes it possible to perform other data analysis processes, such as Fourier transforms, without the missing data resulting in new artifacts.

A clean telescope pointing solution must also be obtained from the raw TOD. Herschel has an absolute pointing error requirement of $3.7''$. An additional drift on this initial error will occur throughout an observation and is a function of time. It is expected that a pointing calibration will be performed at the beginning of each observation, and possibly during long observations, with the time period depending on the final telescope pointing stability. The calibration will be performed by the system using two star tracker cameras facing backwards on the Herschel service module. These cameras will also track the telescope throughout the observation, and their data telemetered to the ground. These data can be used for a posteriori pointing reconstruction. These data do not however, feedback to the telescope systems to correct any pointing drifts which might occur during an observation.

Common mode noise, i.e. correlated $1/f$ noise, will also be removed at at the data cleaning stage by the data reduction pipeline. The major source of common mode noise is expected to be long time scale thermal drifts, originating in the ^{3}He cooler, especially immediately after fridge recycle. These are passed on to the BDAs resulting in a corresponding drift detector output voltage (see Section 1.4). Due to the individual bolometer parameters associated with each detector, the resultant change in operation will vary from detector to detector. Data from the two thermometers located within each BDA can be used to monitor the thermal drifts, and used as an input to the bolometer thermal model of (Sudiwala et al., 1992). By working this model backwards, and applying the previously measured parameters for each detector, it is possible to remove the effects of the thermal drifts for each detector, to the accuracy of the thermometer measurement. In practice many of the common mode noise signals may contain a partial correlation across the detector array, caused by a temperature gradient. Therefore some phase lag may need to be introduced in the application of the thermometry data.

In addition to thermal drifts within the BDA, there may be drifts in the temperature, and therefore emission, of some cold optical components, thereby causing a variation in optical loading on the detectors. This will act as another source of common mode noise. It is drifts in the components in the Level-1 temperature stage (5-K) that will cause the significant error, especially to PLW observations, due to their high temperature.

Other optical components will also experience temperature fluctuations and thus will give rise to similar correlated noise. The scale of the variations will however again be small, and on long time scales. A particularly significant source of correlated noise from the optics system would be from variations in the telescope primary and secondary mirrors, were it not for the long thermal time constant of these components, expected to be significantly longer than the observing time of a typical observation.

Finally the data will require flat-fielding. The responsivity of each detector will be different, even when operating in a stable environment. As a result a different signal level will be measured by each detector when observing the same source. These differences must be calibrated out in order to co-add all of the detector timelines within an array, and produce an accurate flux calibration. This is done by multiplying each detector timeline by a gain factor, or flat-field. The flat-field is often derived from observations of a blank part of the sky, or the inside of a telescope dome. In the case of Herschel-SPIRE, the flat-field can be derived initially from measurements of the detector responsivity, and use of the bolometer thermal model and measured bolometer parameters, but will be verified and enhanced by observations of astronomical sources.

For SPIRE, it is not critical to deal with the removal of the detector response function. While the output data timeline will be a convolution of the astronomical sky signal with the detector (R-C style) response function, this is only a minor issue. The detector time constants are sufficiently fast, that the dominating factor in the response of a detector to a step change in signal, is the 5-Hz low pass filter.

Observations that involve chopping or nodding require a further stage of preprocessing, before a map can be made. Both the chop and nod cycles must be demodulated. In the simplest case, this can be done by integrating the total signal in one chop half, and subtracting it from the subsequent chop half. This gives the total change in signal between the on, and off source positions, i.e. the astronomical signal. The signal is then averaged over chop cycles. The error in this measurement can be taken as the standard deviation of the signal values. Telescope nodding can also be demodulated in a similar way.

Each one of these data processing techniques is likely to result in some loss of information, as no routine will be perfect. Also, it is highly likely that data from the in-flight system will contain various other, as yet unknown, systematic artefacts. These will also need to be dealt with at this stage of data processing.

There is a huge range of data analysis techniques which can be applied to perform these tasks, and many more being continually developed. The SPIRE data reduction pipeline is currently being designed to carry out these corrections. The SPS will be used to evaluate the efficiency and accuracy of this software. To date, however, simulations have been carried out assuming that such systematic effects can be successfully eliminated, in order to evaluate the basic observing modes, the effects of known noise contributions that will not be dealt with by the pipeline, and map making routines.

5.2 Calibration

In general, calibration of the data can be performed at any stage of data processing. If the detector system used has a linear response, a calibration constant, with units of Jy/V, can be derived, simply by observing a source of known flux. This constant can then be applied to the entire data set, converting the data from V to Jy. As well as the responsivity of the detector, this constant takes into account all gain factors between the detector and the output.

In the case of a bolometer, the responsivity is a function of detector operating temperature, bias, and radiant background, and therefore the calibration constant will only be correct for given conditions. If the temperature of the detectors is known, then it is possible to use a thermal model (Sudiwala et al., 1992) to calculate the corresponding responsivity.

In addition to these dependences, bolometers also have a non-linear response. At low signal levels the deviation from linearity is small and can be ignored; however at high signals it can become an issue. Given the appropriate parameters, this non-linear response can again be modelled, and an appropriate calibration applied (see Section 1.4).

Studies performed thus far with SPS data have not implemented thermal drifts. Therefore it has been possible to derive a calibration constant for the nominal detector operating conditions. In cases where a simulation contains a very bright source, a separate calibration curve has been used to calibrate the data. This calibration curve was produced using the simulator's response to a series of sources of known flux. The chosen fluxes ranged from the linear to the highly non-linear regime.

5.3 Map-Making

Once cleaned the data must be converted from TOD to a map. There is a range of map-making methods, the more complex of which are summarised in Tegmark (1997), that can be applied depending on the noise characteristics. The simplest form of map making can be achieved by binning the data into a grid, and assigning to each pixel a value equal to the mean of the samples falling within it. This is referred to as a 'naïve map'. In the presence of 1/*f* noise however, striping may be seen along the scan direction. Other map-making methods attempt, through a variety of techniques, to deal with this 1/*f* noise during the map-making process. In many cases the technique implemented is science case dependent, and thus requires that some assumption is made regarding the information contained within the data. In the case of point source studies, it is generally sufficient to high-pass filter the TOD to remove the 1/*f* noise drifts, as the majority of the information relating to this source type is contained at high frequencies.

In this section we will outline a commonly used maximum likelihood method, also referred to as the 'COBE' method, which attempts to deal with $1/f$ noise without the requirement to make assumptions about the underlaying data. This case is in essence a χ^2 minimisation given by:

$$\chi^2 = \sum_{i,i'}(d_i - \sum_p A_{i,p}m_p)N^{-1}_{i,i'}(d_{i'} - \sum_{p'} A_{i',p'}m_{p'}), \tag{5.1}$$

where d_i is the i^{th} data sample and m_p is value of the map pixel p. Note that m is being treated as a 1D vector. $N_{i,i'}$ is the time-time noise covariance matrix, given by $N_{i,i'} = \langle(d_i - \mu_i)(d_{i'} - \mu_{i'})\rangle$, where μ is the mean. This matrix effectively measures the noise correlation between sample i, and sample i'. $A_{i,p}$ is the pointing matrix and has dimensions of $n_{samples} \times n_{pixels}$. This is a sparse matrix, containing a value of 1 where there is a sample, and zero in all other locations. This matrix can be used to turn a map in to a timeline and vice-versa.

The minimisation of this expression can be represented as:

$$\begin{aligned} 0 &= \frac{\partial \chi^2}{\partial m_p} \\ &= \sum_{i,i'}(-A_{i,p})N^{-1}_{i,i'}(d_{i'} - \sum_{p'} A_{i',p'}m_p) \end{aligned}$$

$$
\begin{aligned}
&+\sum_{i,i'}(d_i - \sum_{p} A_{i,p}m_p)N^{-1}_{i,i'}(-A_{i',p}) \\
= \; &-2\sum_{i,i'} A_{i,p}N^{-1}_{i,i'}(x_{i'} - \sum_{p'} A_{i',p'}m_{p'}), \qquad (5.2)
\end{aligned}
$$

which when converted to matrix notation becomes:

$$
\begin{aligned}
&A^T N^{-1} A m = A^T N^{-1} d \\
\Rightarrow \;\; &m = (A^T N^{-1} A)^{-1} A^T N^{-1} d. \qquad (5.3)
\end{aligned}
$$

Solving this generalised least squares equation for m will produce the maximum likelihood map. However, this is not easy in practice. Even for maps of modest size, the memory and computational power required to store and invert the matrices involved is beyond that currently available. In order to generate a one square degree SPIRE scan map using this direct method, a matrix containing approximately three billion points would have to be stored and inverted. This matrix would be ~46 GB, and the inversion would not be possible. This problem has been tackled in a variety of ways. It is often assumed that the noise properties are stationary, i.e. that the noise level, and 1/*f* knee frequency is constant over some period of time. This, along with various other assumptions regarding the covariance matrix, such as the matrix being Toeplitz, can be used, simplifying the matrix inversion method. Almost all methods use some form of iterative scheme, generating at first a naïve map. This map is used to refine the covariance matrix, and a more accurate map is produced. This continues until either a fixed number of iterations has been performed, or some convergence criterion has been met. See Christopher (2002), and Crill and Netterfield (in prep.), for good reviews of implementation methods.

It should be noted that multiple observations of the same region of sky, with the region being revisited on a variety of time scales, is required to derive a maximum likelihood map in this way. This type of observation is known as cross-linking, and provides redundancy in the data. Random cross-linking provides the best results (Tegmark, 1997).

5.4 Simulator Performance Verification

Individual SPS modules and subsystems were independently verified during development. In addition, it was important to confirm that the entire system worked as predicted by theory. The modelled voltage response from the SPS bolometer module was compared to the SPIRE sensitivity model (Griffin, 2004) and found to agree well for a given source flux. Since the signal and noise time-lines are generated independently, the measurement of the SNR of a point source provides a robust test of the entire system. The noise equivalent flux density (NEFD) can be used to predict the SNR of a source of flux density S_ν, when observed for time t_{int}. The NEFD is defined as the source flux density that will provide a SNR of 1 in an integration time of 1/2 s, and for SPIRE is given by Equation 5.4.

$$NEFD = \frac{NEP}{\eta \eta_{filt} A_{tel} \Delta\nu}, \tag{5.4}$$

where NEP is the detector noise equivalent power, A_{tel} is the area of the telescope, η is the product of the system efficiency factors, e.g. feedhorn throughput, spill over efficiency, telescope obscuration factor etc., $\Delta\nu$ is the filter band width, and $\eta_{filt}(\nu)$ is transmission efficiency of the system optical components.

The test results from the simulator were compared to the standard SPIRE performance model (Griffin, 2004). The appropriate 5σ-1 hour sensitivity values when observing in scan map mode were used for comparison.

5.4.1 Point Source SNR Measurement

Consider here a telescope whose beam profile (response to a scan of a point source) is a Gaussian. The resultant map from such an observation would be a Gaussian embedded in a noisy map with a signal, in each pixel i, of S_i, and with a uniform pixel to pixel noise value of n across the map (measured by the standard deviation of the background pixel values). We would like to know the best estimate of the source signal, and also its SNR. To do this we must incorporate our knowledge of the telescope beam profile, which, when binned using the same pixel size as the map, is labelled b (Figure 5.1).

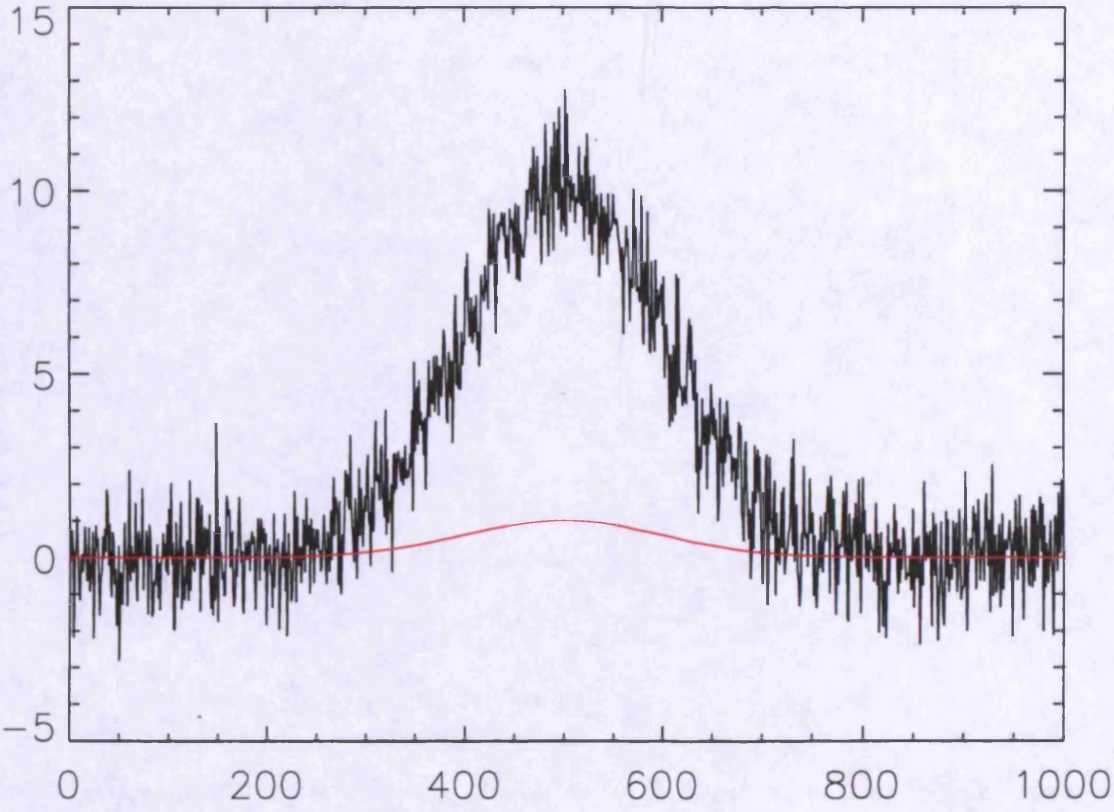

Figure 5.1: Plot of both the signal data, S_i, in black, and the beam function, b_i, in red.

Let us assume that the source has been fitted by the beam profile so that it has achieved a best fit. Now we need to find the signal and SNR of that fitted source.

In order to make sure that all of the information contained within the map is used, we need to make use of all pixels within the map. However, pixels in the wings of the beam will contain more noise relative to the amount of signal that they contain. Therefore we need to find an appropriate weighting function so that pixels near the centre of the beam contribute more than these noisy pixels. The inverse of the beam function, $(1/b)$ acts as an ideal weighting function, where the mean of S/b is the source signal value that we are interested in (Figure 5.2).

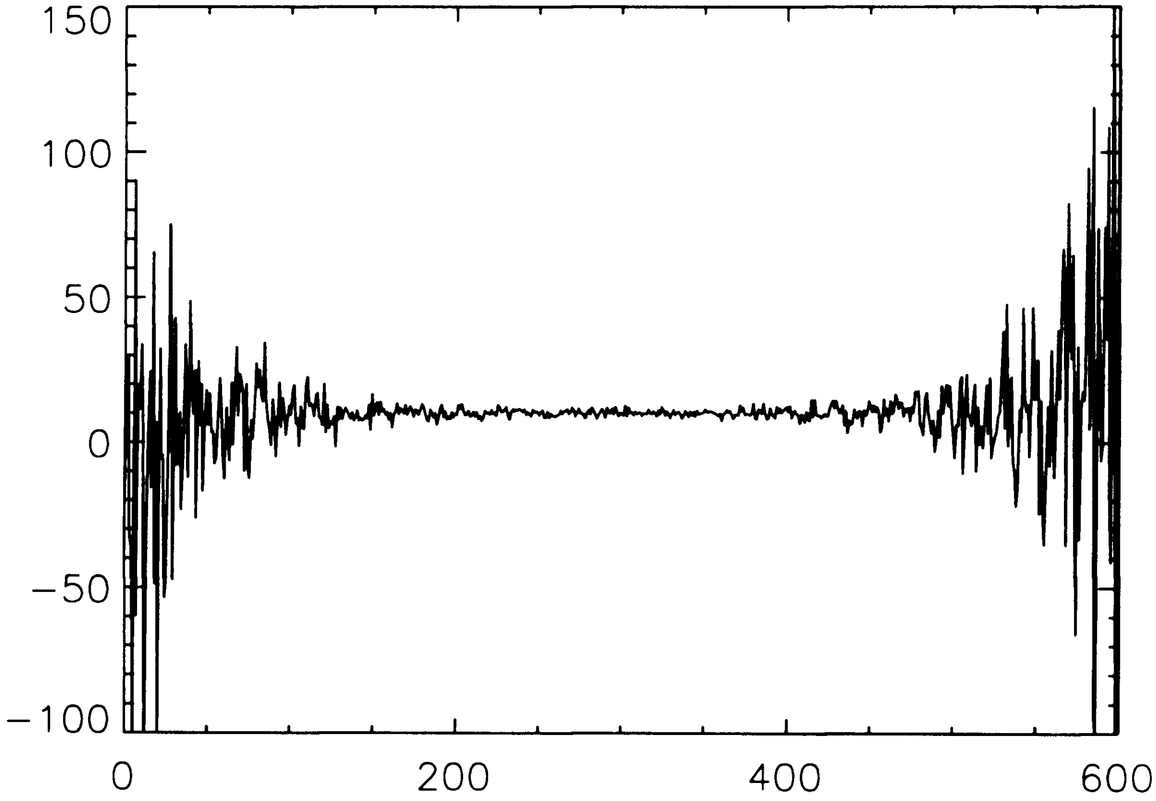

Figure 5.2: Plot of the effective weighting of S_i/b_i.

Now, the noise in each pixel is not constant any more but is instead n/b_i. The best estimate of S/b is obtained by weighting each measurement appropriately:

$$\frac{S}{b} = \frac{\sum_i^N \frac{S_i}{b_i}\omega_i}{\sum_i^N \omega_i}, \tag{5.5}$$

where $\omega_i = \frac{1}{\sigma_i^2}$ and $\sigma_i = \frac{n}{b_i}$, are the weights that optimise this equation giving the smallest final error, and N is the total number of pixels used in the calculation (within some aperture, for example).

Equation 5.5 leads to:

$$\frac{S}{b} = \frac{\sum_{i}^{N} \frac{S_i}{b_i} \frac{b_i^2}{n^2}}{\sum_{i}^{N} \frac{b_i^2}{n^2}}. \tag{5.6}$$

The final error in this measurement is then defined as

$$\frac{1}{\sigma_{best}^2} = \sum_{i}^{2} \frac{1}{\sigma_i^2} = \sum_{i}^{N} \omega_i \tag{5.7}$$

$$\Rightarrow \sigma_{best} = \frac{1}{\sqrt{\sum_{i}^{N} \omega_i}} = \frac{1}{\sqrt{\frac{1}{n^2} \sum_{i}^{N} b_i^2}} = \frac{n}{\sqrt{\sum_{i}^{N} b_i^2}}. \tag{5.8}$$

Thus the SNR is simply

$$SNR = \frac{\sum_{i}^{N} S_i b_i}{\sum_{i}^{N} b_i^2} \cdot \frac{\sqrt{\sum_{i}^{N} b_i^2}}{n} = \frac{\sum_{i}^{N} S_i b_i}{n \sqrt{\sum_{i}^{N} b_i^2}}. \tag{5.9}$$

This has two main advantages over other methods for calculating signal to noise. The first is that it produces an estimate that is independent of both the size of the pixel used in the map, and the size of the aperture placed around the source. The first point can be demonstrated by seeing how each term in the above expression varies with the pixel size.

If L is the pixel size then:

$$\begin{aligned} \sum_{i}^{N} S_i b_i &\propto \frac{1}{L^2}, \\ \sum_{i}^{N} b_i^2 &\propto \frac{1}{L^2}, \\ n &\propto \frac{1}{L}. \end{aligned} \tag{5.10}$$

Therefore:

$$SNR \propto \frac{\frac{1}{L^2}}{\frac{1}{L} \cdot \frac{1}{L}} = constant. \tag{5.11}$$

The second point can be seen by considering an annulus that is increased in size, beyond the extent of the beam profile. As the annulus increases in size the new pixels that are encompassed contain only noise and no signal. Therefore these pixels are weighted such that they contribute nothing to the final measurement, and so have no effect on the derived signal to noise ratio. The best signal to noise is then obtained by selecting an annulus that is big enough to contain all of the significant beam profile.

Additionally the beam profile does not need to be normalised so that it matches the amplitude of the signal. So long as it is centred on the position of the source, the final signal to noise ratio will be independent of the beam normalisation. To obtain the final source signal, the measurement in Equation 5.6 must be multiplied by the peak value of b.

These equations are only applicable when the noise in the map can be taken as uniform. In the case of non-uniform noise, such as $1/f$ noise, these expressions are only approximate. In this case we need to replace n with n_i in all the calculations. This results in an expression for the signal of:

$$\frac{S}{b} = \frac{\sum_i^N \frac{S_i b_i}{n_i^2}}{\sum_i^N \frac{b_i^2}{n_i^2}}, \tag{5.12}$$

and for the error in this measurement of

$$\sigma = \frac{1}{\sqrt{\sum_i^N \frac{b_i^2}{n_i^2}}}. \tag{5.13}$$

Combining these we have a signal to noise of

$$SNR = \frac{\sum_{i}^{N} \frac{S_i b_i}{n_i^2}}{\sqrt{\sum_{i}^{N} \frac{b_i^2}{n_i^2}}}. \tag{5.14}$$

In practice it is extremely difficult to derive a noise map that is applicable in this case to this method. If the data are correlated in any way, then the noise is not uniform, meaning that this method cannot be used. Such correlations can be due to 1/*f* noise, or filtering.

5.4.2 Measuring the SNR of a Point Noise in a Simulated Output Map

When comparing the SNR measurement obtained from the map with that expected from theory, two factors must be taken in to account. The first is the reduction in SNR caused by sharing the total integration time over many map pixels. The second is the improvement in SNR by adding up measurements from those same map pixels.

Since the three SPIRE arrays are all slightly different sizes, the effective integration time within a given map pixel will vary. In addition to the signal map, a counts map (e.g. Figure 5.3) which quantifies the number of data points contributing to any particular pixel, can also be generated in the map-making process. The mean number of counts per map pixel is obtained from an aperture placed within a uniform part of the counts map, as shown by the green box in Figure 5.3.

Each detector within an array is responsible for filling a particular area of the map during a scan, illustrated by the black rhombus in Figure 5.4. The circles in the figure represent the array feedhorns. Assuming a uniform map coverage (as is the case with the central section of our map) the sum of the counts within this region will give the effective integration time for the map. In other words, if a single detector were moved around inside this area for

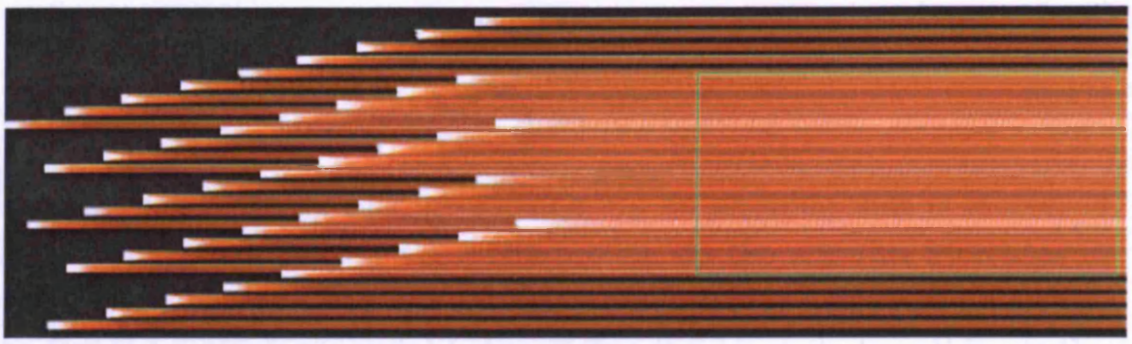

Figure 5.3: Sample integration time map for a single scan, with the SPIRE PLW array, starting from rest. The green box defines the region of uniform data taken when the telescope has achieved its proper scanning rate (i.e. it is no longer in the acceleration phase).

the effective integration time, then the average number of counts per pixel would match that of the final map. This effective integration time is different to the time it takes for the array to perform its scan.

The area of the rhombus above is simple to calculate if the separation, d, of the detectors is known (this is similar but not exactly equal to twice the FWHM of the beam for each array).

$$A = \frac{\sqrt{3}}{2}\frac{d^2}{l^2} \tag{5.15}$$

To convert this area from arcseconds to pixels the size of the pixels, l, must also be taken into account.

Finally, to get the effective integration time, we must multiply the mean number of counts per pixel by the time each count represents. This represents the mean integration time per pixel, t_{pix}. This is then multiplied by the number of pixels covered by each detector. In the case of the PLW array, each pixel has a mean of 8.8 counts per 2″ pixel. The integration time per count, set by the simulator time step, is 12 ms, and the area covered by each detector is 853.6 pixels. This gives a total integration time, t_{tot}, of $8.8 \times 12 \times 10^{-3} \times 853.6 = 90.1$ s.

A measurement of the noise in the map can be obtained by taking the standard deviation of the pixels in a blank region of the map, such as the green

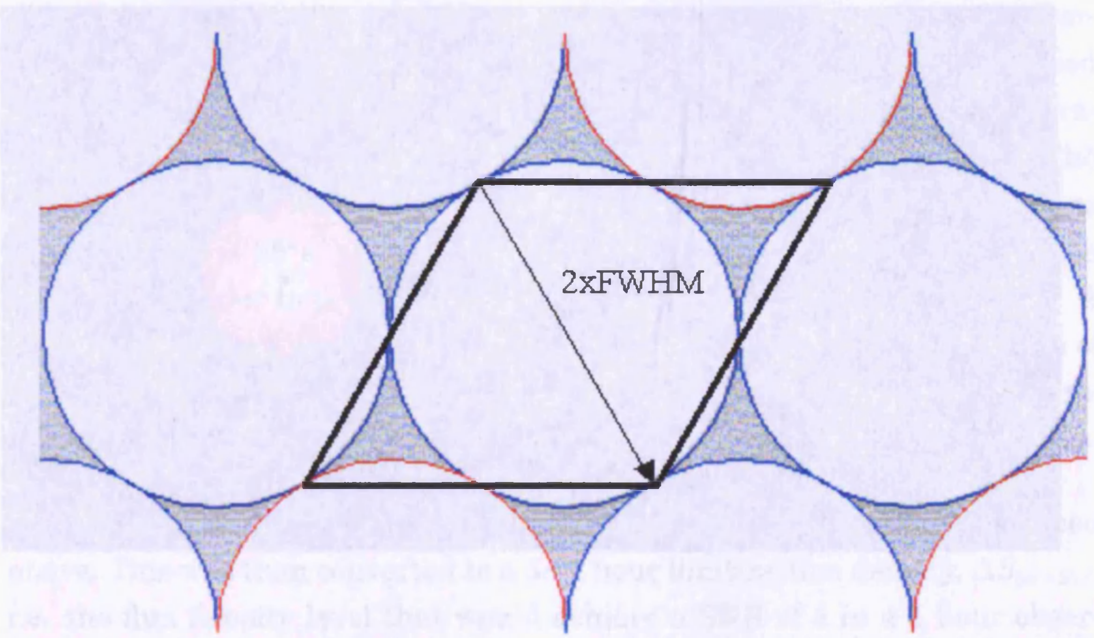

Figure 5.4: Schematic representation of the area of sky covered by a single pixel during a scan map observation.

box in Figure 5.5. In this particular example the noise value is 45.3 nV. Taking the peak source value of 1.21 μV, shown in here as a blue pixel, along with this noise measurement, the SNR_{peak} for this pixel is calculated to be 26.7.

This measurement uses only the peak signal. When applying the method outlined above, which uses the total source signal, weighted appropriately by the beam, we achieve a SNR of 342. This is an improvement by a factor of 12.81.

For a point source observation, the best possible SNR would be achieved by starring at the source for the full integration time. This cannot be the case however when performing a scan-map observation, as the integration time is spread over the map. The best SNR possible in this case would be the peak SNR, adjusted for the full integration time, i.e. $SNR_{max} = 26.7 \times \sqrt{t_{tot}/t_{pix}} = 778$. Therefore, the degradation in SNR in any given pixel from the theoretical maximum is $\sqrt{t_{tot}/t_{pix}} = 29.15$.

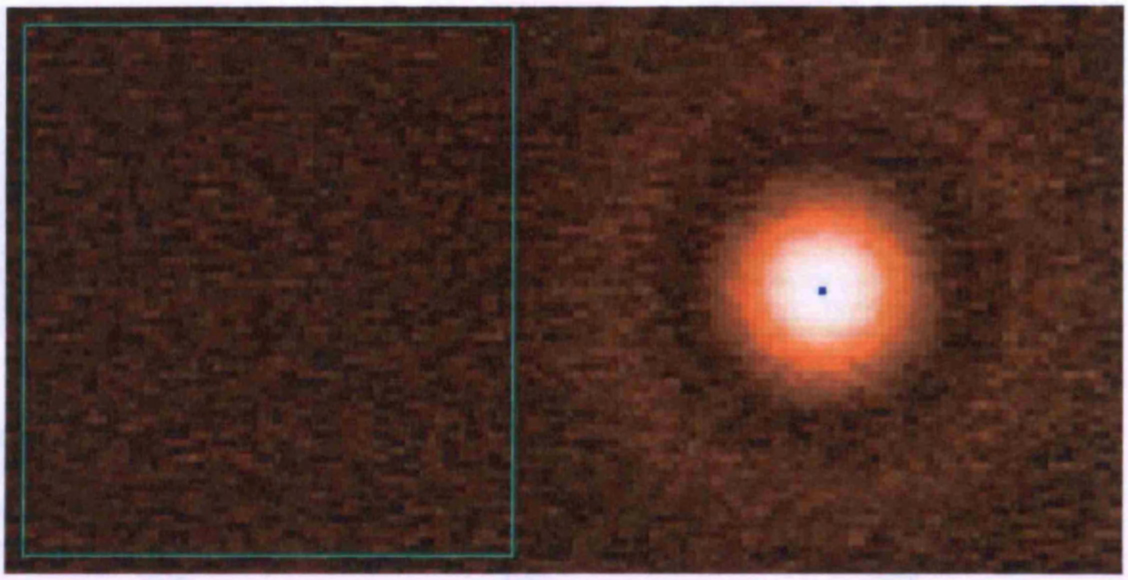

Figure 5.5: Sample simulated observation of a point source, observed in scan map mode. The blue dot is the peak signal value in this map, and the green box shows the region used to calculate the noise level in the map.

Therefore, when making a map, the SNR of a point source can only ever be a maximum of $12.81/29.15 = 342/778 = 0.44$ times that of the same source observed using point source photometry, when integrating for the same length of time. This factor is approximately the same for all three arrays (within the uncertainties of the measurement process) and is robust to changes in the pixel size of the maps and to the source flux. Taking the mean of the factors for the three arrays gives 0.43. This value is in good agreement the value stated by Griffin et al. (2002a).

Again, in the presence of correlated or non-stationary noise this treatment does not hold true. In the case of a variable white noise level, then a noise measurement obtained from the residuals of a model source subtracted map would be more appropriate than one made within a nearby blank region.

5.4.3 Simulator Verification

Verification tests performed on the simulator were done with a simplified, yet complete system. The data tested contained no $1/f$ noise, and were not filtered by the 5-Hz filter; any filtering being performed would introduce correlations in the data, meaning that the source detection method described above would not be valid. All detectors were also all assumed to be equivalent, thereby avoiding the need to flat-field the data. In order to perform the system verification a simple simulation was performed using 4 repeat scans at a scan rate of $25''\mathrm{s}^{-1}$, with a line separation of $2''$. This small separation was used in order to produce a map with extremely uniform integration. A 1.6 Jy point source was observed and a naïve map with a pixel resolution of $2''$ per pixel was made of the resulting data. The noise level within the simulation was as derived from theory within the simulator bolometer module.

A SNR measurement was made for the sources using the methods described above. This was then converted to a 5σ 1 hour limiting flux density, $\Delta S_{5\sigma-1hr}$, i.e. the flux density level that would achieve a SNR of 5 in a 1 hour observation. These values were then compared with those calculated from theory using the NEFD derived from the simulator input parameters. The results are summarised in Table 5.1.

Array	Effective Integration Time (s)	SNR (1.6 Jy)	$\Delta S_{5\sigma-1hr}$ (mJy)	
			Measured	Theoretical
PSW	80.4	416	2.87	2.88
PMW	85.0	352	3.49	3.34
PLW	90.1	342	3.70	3.74

Table 5.1: Summary of measured and theoretical simulator sensitivity results for scan-map mode.

These values were also compared to those found in the SPIRE sensitivity model document (Griffin, 2004), which represents the official sensitivity limits for the SPIRE instrument. The NEFD values were used for the comparison, but it was necessary however to make some adjustments to the sensitivity model before a direct comparison could be made. The input values for spill-over efficiency and operating detector temperature had to be altered in order to be in line with those of the simulator (0.7 and 0.3 K respectively). The NEFD values are displayed in Table 5.2.

The two values for SNR, one obtained theoretically, and the other by analysis of simulated data, are both in good agreement, with a maximum error of

Array	NEFD simulator ($\mathrm{mJyHz}^{-1/2}$)	NEFD sensitivity model ($\mathrm{mJyHz}^{-1/2}$)
PSW	18.9	19.0
PMW	21.2	21.9
PLW	23.9	24.5

Table 5.2: Comparison of NEFD values from both the simulator and SPIRE sensitivity model.

~4.5%. The comparison of NEFD values derived from the simulated map, with those in the sensitivity model document, also show good agreement, and provide external validation. In this case the greatest error was ~2%. Given the uncertainties in the measurement process, as well as the rounding error and slight differences in computational methods used by the simulator and sensitivity model, we consider these tests to have been passed, and the simulator operation validated.

5.5 The SPIRE Map-Making Algorithm

The SPS has recently been used to select the best map making routine to be used by the official SPIRE data reduction pipeline, when operating in scan map mode (POF 5). Simulated observations were provided by myself and the analysis and selection of these data was performed by SPIRE team members in Imperial Collage London, and IPAC in Pasadena.

More than one standard routine could be selected, with different routines being optimal for different source types. The routine selected is required to reconstruct an input sky image with high fidelity, in a reasonable amount of time, given commonly available computing power. The selected method must also not require any complicated observing strategy which might make the observation difficult, and must work well for point and extended sources.

To achieve this task, a series of simulations was produced using the SPS. Various source types, from point sources, to large scale extended structure, were used as input sky models. An individual metric for assessment of the performance of each science case was defined.

Two simulations of each input sky were performed using the nominal scan map parameters (see Chapter 6). The two simulations were performed at different scan angles to provide cross-linking. At the map-making stage it is assumed that the data have been cleaned, and contain no glitches, correlated noise, or differences in detector response. Therefore the key issue to be tackled by these routines is uncorrelated $1/f$ noise individual to each detector.

Six map-making routines were compared. The first was a naïve mapping method, which was used as a reference. The second method again used a naïve mapping routine, but pre-filtered the data using Fourier methods. An adapted version of the Spitzer MOsaicking and Point source EXtraction (MOPEX) mapping routine was also used (Makovoz and Khan, 2005). This filtered the data and constructed the map in a similar way to the previous method. The map making routine used for the BOLOCAM instrument on the Caltech Submillimetre Observatory was used (Haig et al., 2004), which works by performing an iterative principle component analysis (PCA). The final two methods attempt to produce a maximum likelihood map by solving Equation 5.3. The first method, called Constrained Mapmaker (CM), uses an iterative approach (Crill and Netterfield, in prep.), while the second method, MADmap, solves the equation by making several assumptions about the stationarity of the noise, i.e. the stability of the noise properties, and inverting the covariance matrix directly (Christopher, 2002).

Different input maps were used to test each map-making algorithgm's ability to deal with various science cases. Figures 5.6–5.11 contain examples of one particular input map case for each of the six mapping methods used. The specific example is the observation of a simple simulated input source with an exponential radial flux density profile. The exponential source is truncated at a particular radius resulting in the step seen in the figures. Some of the methods requiring filtering (Figures 5.8 and 5.9) show clear dark lobes either side of the source in the scan direction, characteristic of this type of method. A distortion in the source shape can also be seen with the MOPEX method (Figure 5.8). Clear striping can be seen in the naïve, filtered and

BOLOCAM methods (Figures 5.6, 5.7, and 5.9). Both of the maximum likelihood map-making routines (Figures 5.10 and 5.11) perform well, with minimal striping visible when cross-linking (cross scanning), required for these methods to operate optimally, is performed. When cross-linking is not performed, these methods are essentially reduced to a naïve map makers.

The finding of the selection board was that CM and MADmap were the two strongest mapping routines in terms of data quality. The two forms of naïve mapping produce an intermediate result, and so were discounted. While the BOLOCAM code does well with point sources, it is optimised for ground based observations and does not do well at recovering extended emission.

MADmap was finally chosen over CM for the following reasons:

- it performs better than CM on extended sources;
- it is more robust (CM is still in the development stages);
- it is competitive with just a single iteration;
- it is relatively simple to incorporate into the current pipeline;
- as a maximum likelihood method, it has the scope for improved performance with increased cross-linking.

The full results of this investigation can be found in the official report by Clements et al. (2006). It is intended that this work be published in the near future.

5.6 Chapter Summary

This Chapter has outlined some of the major data processing tasks required to convert raw instrument timeline data into a useable format for astronomy, in this case a map. It highlights various data cleaning process, including removal of cosmic ray detections, correlated noise, and flat-fielding. Where

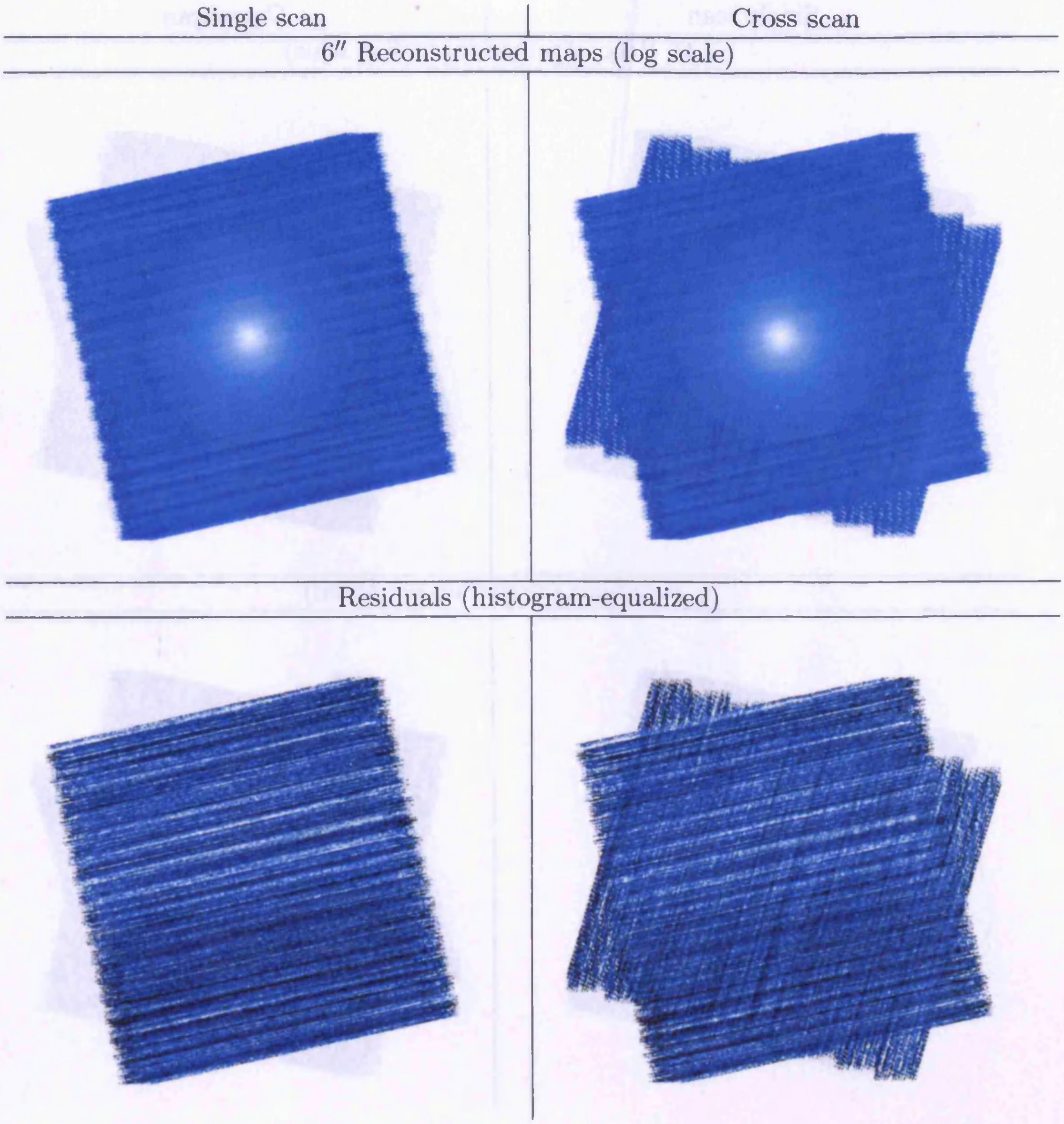

Figure 5.6: Naïve map reconstructions derived from a simulated observations of source with an exponential radial profile. Single scan and cross-scan maps are presented, along with the map residuals (Clements et al., 2006).

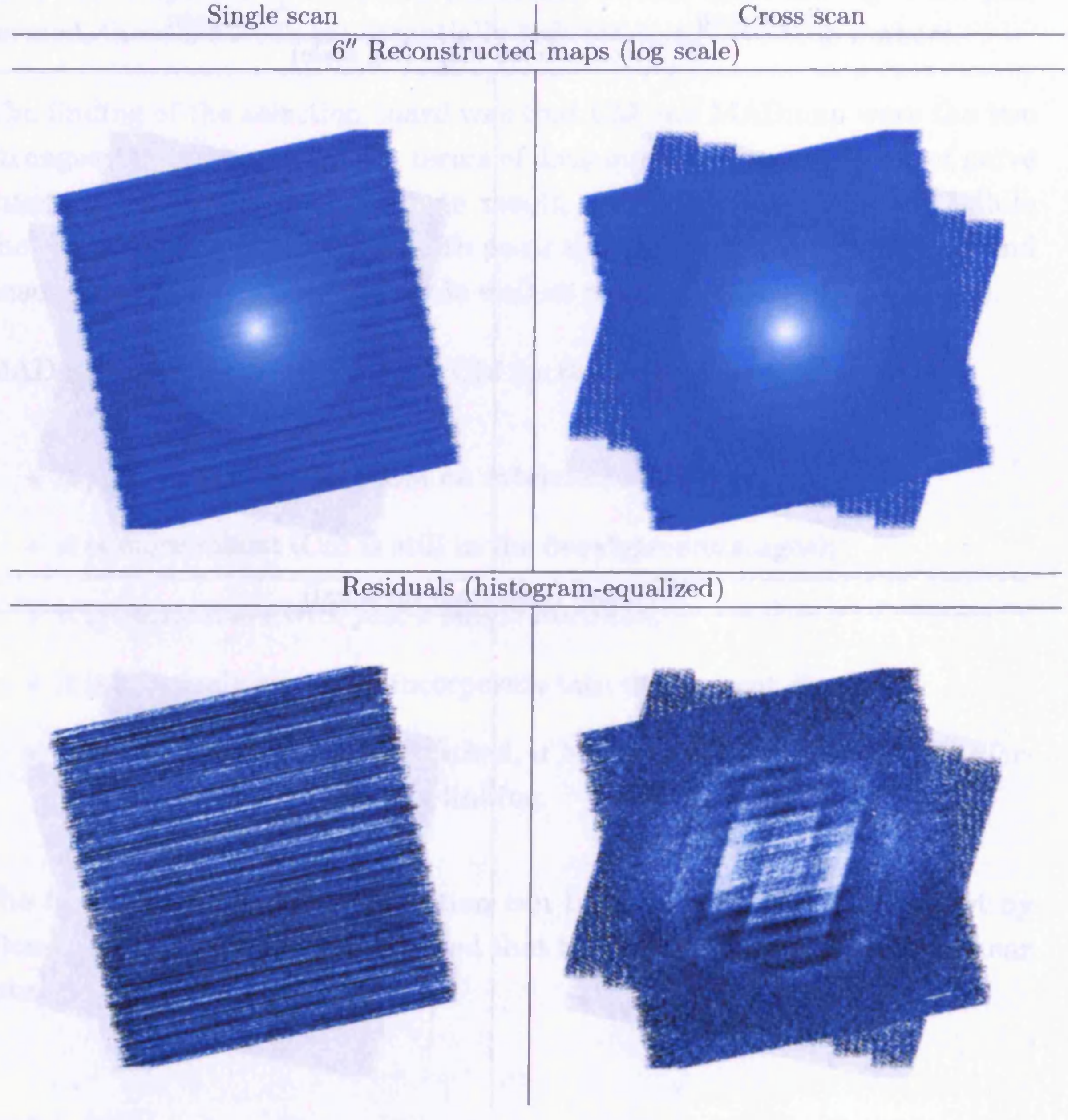

Figure 5.7: Fourier filtered map reconstructions derived from a simulated observations of source with an exponential radial profile. Single scan and cross-scan maps are presented, along with the map residuals (Clements et al., 2006).

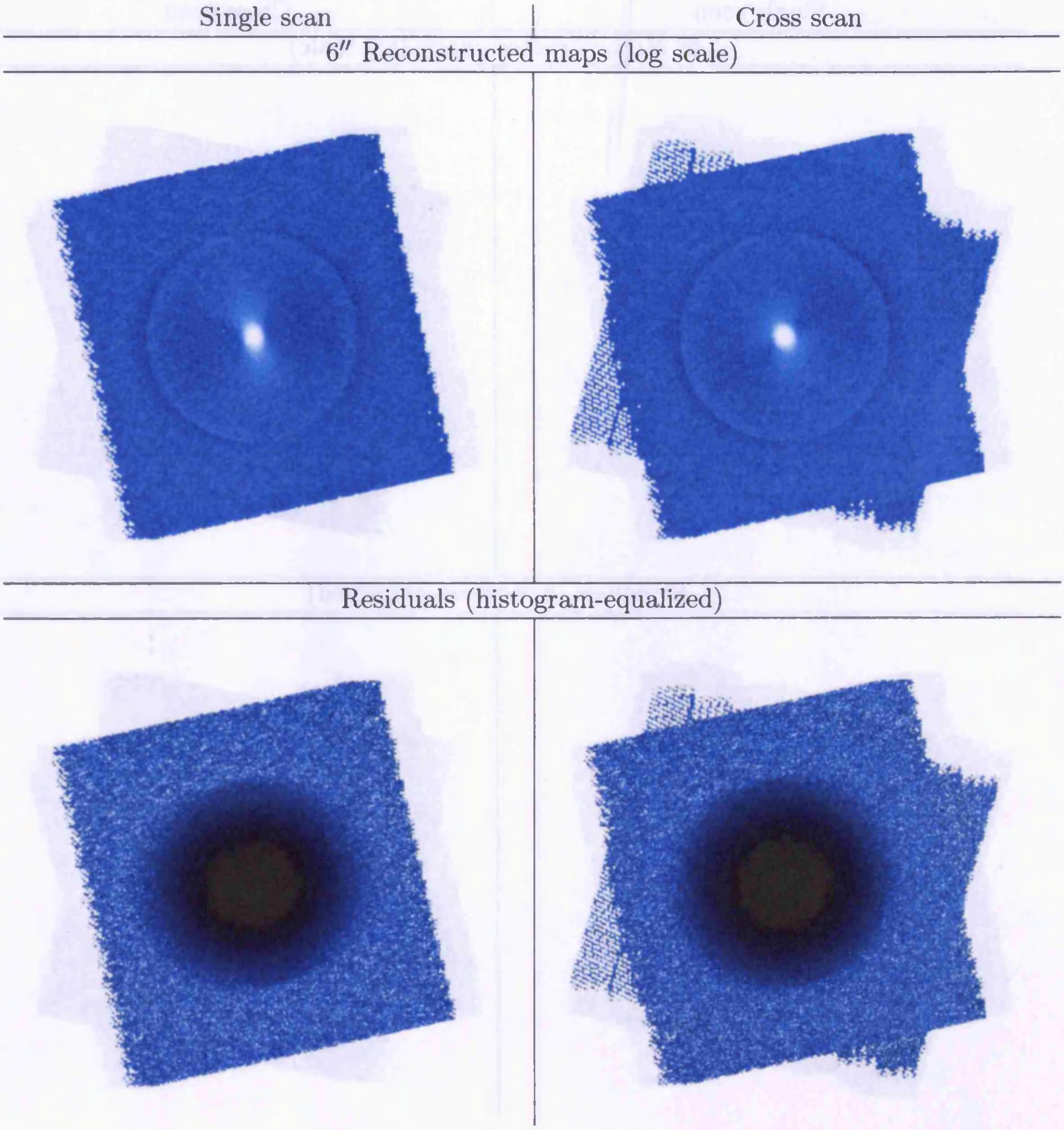

Figure 5.8: MOPEX map reconstructions derived from a simulated observations of source with an exponential radial profile. Single scan and cross-scan maps are presented, along with the map residuals (Clements et al., 2006).

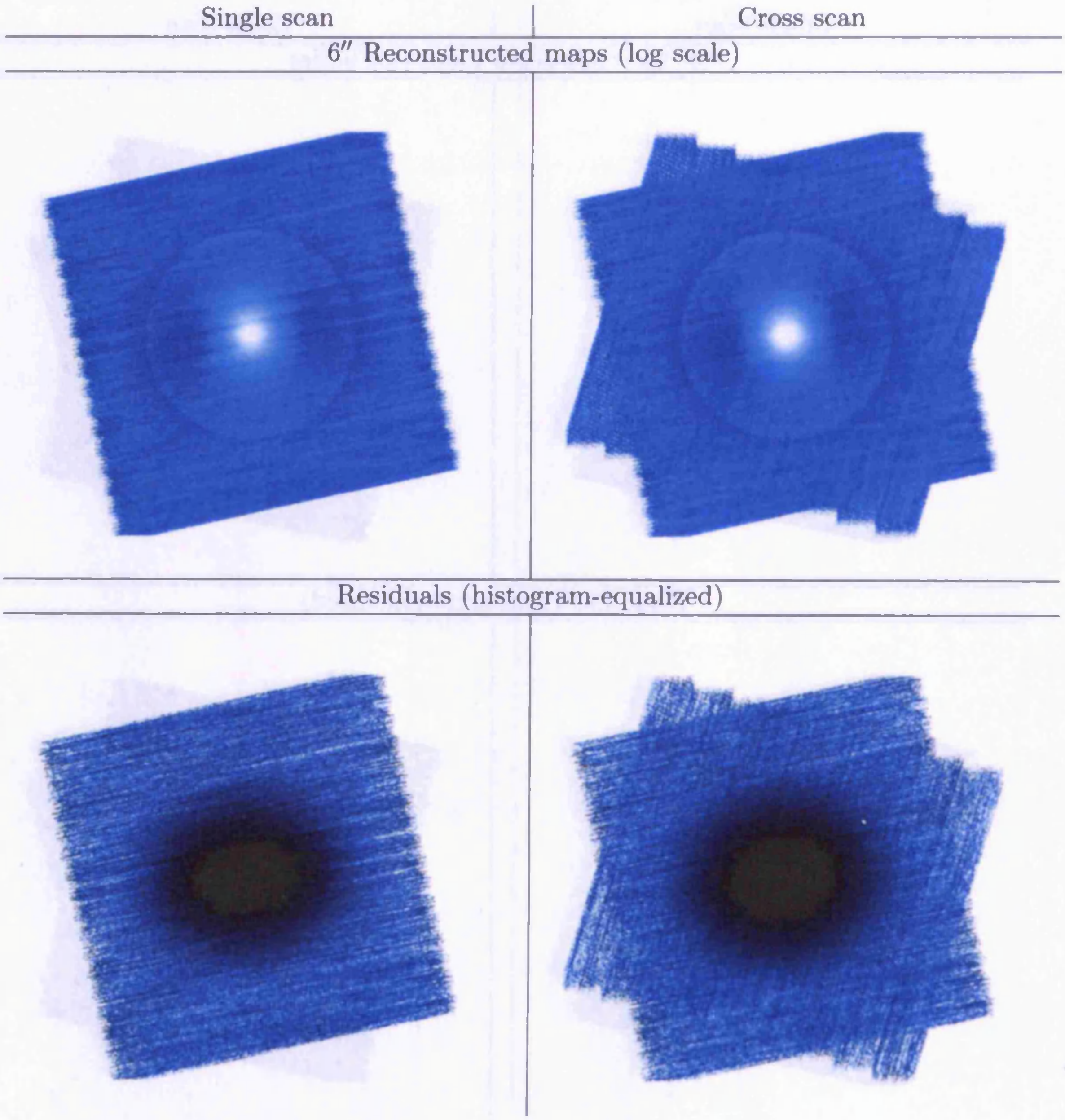

Figure 5.9: BOLOCAM method map reconstructions derived from a simulated observations of source with an exponential radial profile. Single scan and cross-scan maps are presented, along with the map residuals (Clements et al., 2006).

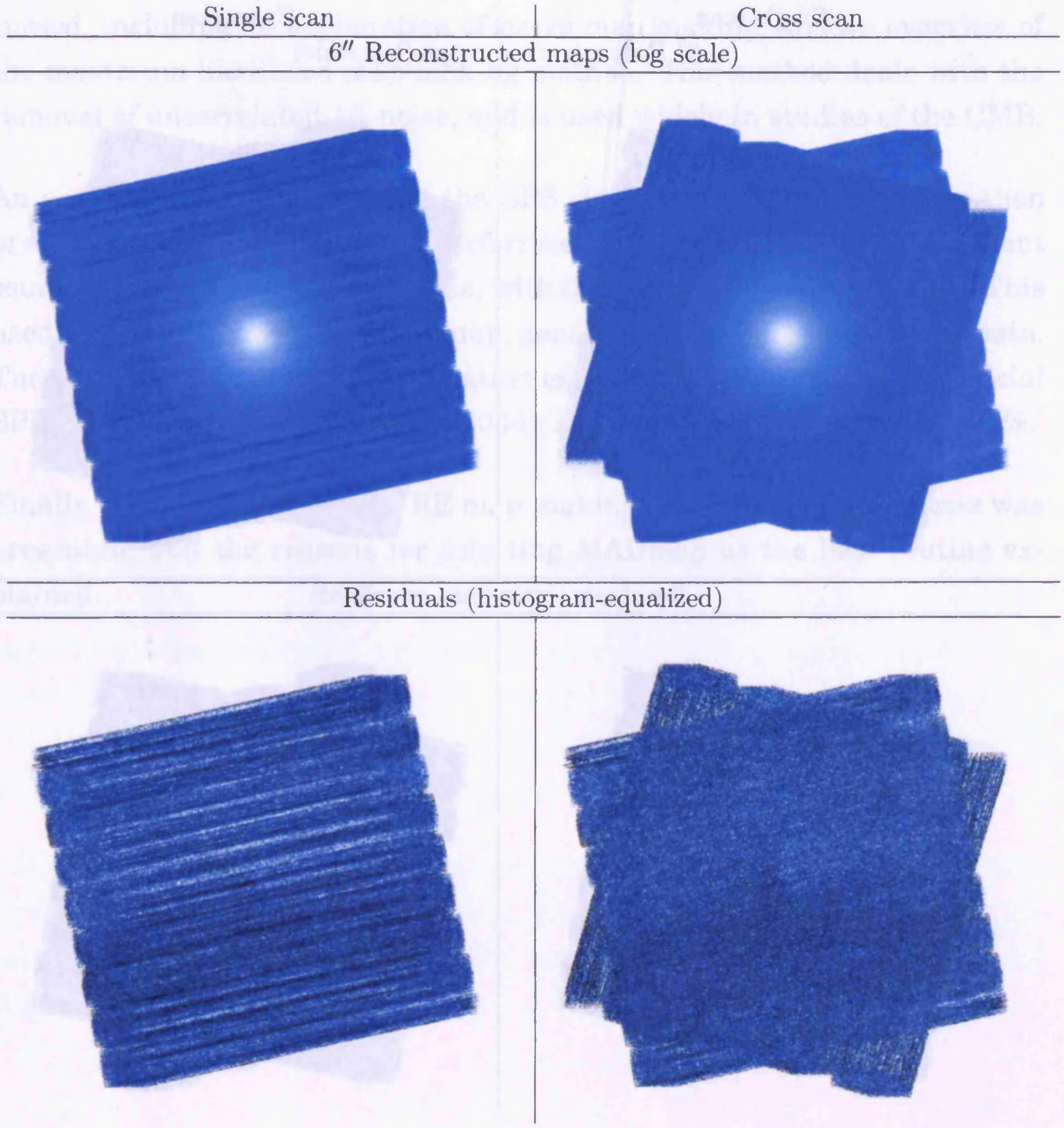

Figure 5.10: CM map reconstructions derived from a simulated observations of source with an exponential radial profile. Single scan and cross-scan maps are presented, along with the map residuals (Clements et al., 2006).

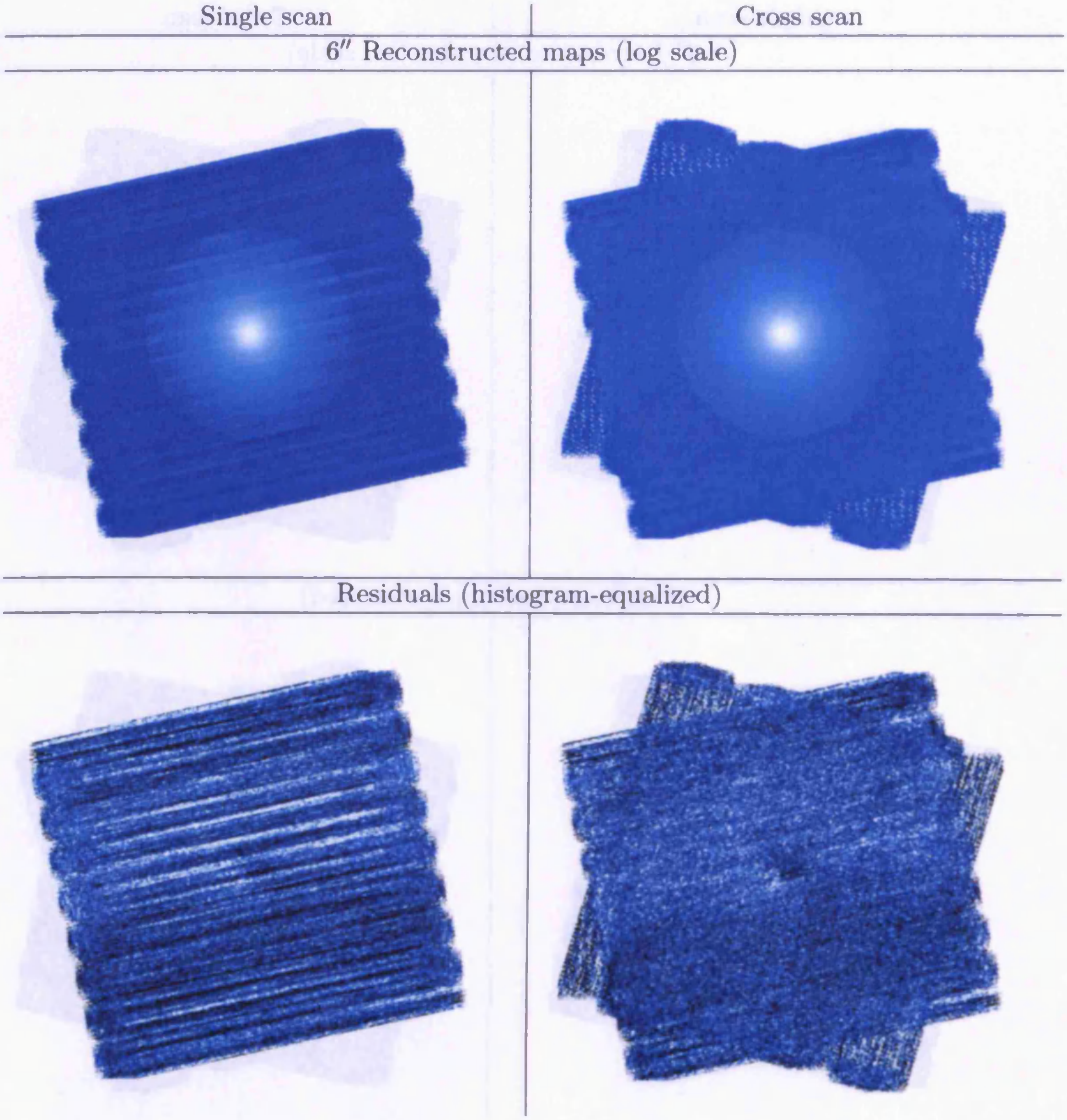

Figure 5.11: MADmap map reconstructions derived from a simulated observations of source with an exponential radial profile. Single scan and cross-scan maps are presented, along with the map residuals (Clements et al., 2006).

necessary, an explanation of these methods, as applied to SPS data, was also given.

The issues involved with making maps from the processed data were discussed, including an explanation of naïve map making, and an overview of the maximum likelihood map-making method. This method deals with the removal of uncorrelated $1/f$ noise, and is used widely in studies of the CMB.

An account of the validation of the SPS signal and noise output was then presented. This validation was performed by comparing the SNR of a point source, observed in scan-map mode, with the theoretical SNR expected. This used data in the form of a naïve map, generated by unfiltered detector data. The NEFD obtained in this verification exercise was compared to the official SPIRE sensitivity model (Griffin, 2004), and found to agree to within $\sim 2\%$.

Finally, an overview of the SPIRE map-making routine selection process was presented, and the reasons for selecting MADmap as the best routine explained.

Chapter 6

Observing Mode Optimisation

With the overall cost of Herschel being approximately €1 million per day, the efficient use of observing time is essential. Therefore, the optimisation of the photometer observing modes, outlined in Section 3.2, is an essential part of the SPIRE pre-flight planning. Not only must the modes be efficient, they must also return a high quality of data. Since a significant fraction of the SPIRE observing time will be in the form of large scale photometric survey programmes, it is particularly important that the scan-map mode be carefully optimised in terms of efficiency and data quality.

This chapter describes the use of the simulator in the optimisation of the SPIRE photometer observatory functions. The key parameters for each observing mode are described, and the use of the SPS in the determination their optimal value is presented.

6.1 Point Source Photometry

The parameters available for optimisation within the point source photometry observing modes are chop frequency, f_{chop}, chop throw, Δ_{chop}, chop direction, nod frequency, f_{nod}, and nod throw. Most of these parameters are actually fixed or constrained by the design of the instrument. For example the chop throw parameter is set at 126″ by the requirement for the co-aligned pixels (Figure 6.1) to perform pixel–pixel chopping. In this case, when one set of pixels is off source, the other is on source, thus ensuring that the target is continually observed. The optimum sets to use for chopped photometry are sets 1 and 2 in Figure 6.1, as this minimises the BSM power dissipation by chopping symmetrically about the rest position with the smallest possible angular deviation. Sets 2 and 3, or their equivalents on the opposite side are also usable but with higher BSM power dissipation. Hence a nominal chop throw of 126″ is defined. This also sets the telescope nod throw. In order for the off source position in nod location '*A*', to become the on source position in nod location '*B*', the nod throw must be equal to the chop throw.

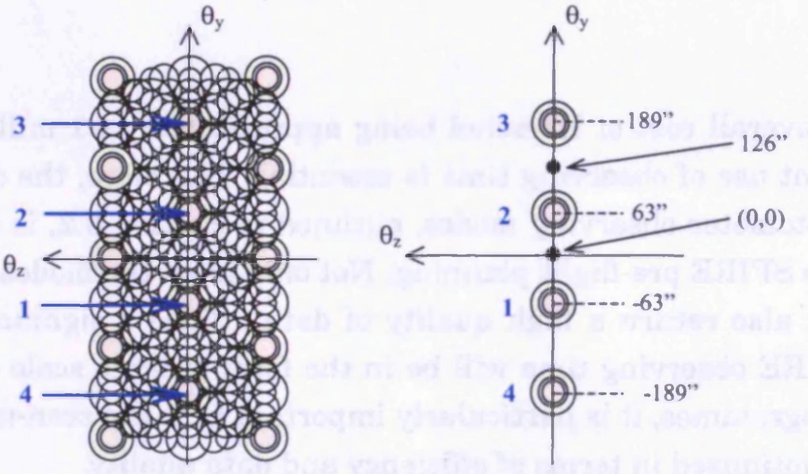

Figure 6.1: Sets of detectors (shaded) for which there is simultaneous overlap in all three bands (left), and the sets of overlapping detectors on the Y axis shown separately with their angular distance from the boresight as indicated (right).

POF 2 has the additional observing parameter, the angular offset for the 7-point, $\Delta\theta_7$. This defines the separation of the 7 jiggle positions implemented by this mode (see Figure 3.6). The optimum value of this parameter will vary with beam size, thus a compromise is required. In order to achieve the optimum flux recovery, $\Delta\theta_7$, should be set equal to 0 (requiring precise pointing). In this case a POF 1 observation is performed. A POF 2 observation may be implemented if the source position is not well known, or the telescope pointing error are significant. Therefore a significant nonzero value must be used to ensure that the source is not missed. However, as $\Delta\theta_7$, and consequently the map size, is increased, the total SNR for the observation decreases (Griffin et al., 2002a), decreasing the accuracy of the measurement. Conversely as the map size increases, the contrast between the map positions increases, thereby allowing a more accurate measurement of the source position. This occurs up until a point, beyond which the decrease in overall SNR outweighs this improvement.

A series of simulations was performed to evaluate the recovery of the peak flux and position of a point source, as a function of $\Delta\theta_7$. A symmetric Gaussian telescope beam was assumed in this case. The error on the measurement of these data was assessed as a function of $\Delta\theta_7$ and pointing error, Δ. Simulations were performed for sources with a worst case SNR = 3, and an ideal case SNR = 10 (Figure 6.2).

An optimum value for $\Delta\theta_7$ of 0.3 beam FWHM was derived (Sibthorpe et al., 2005), corresponding to ~5, 7, and 10$''$ for the PSW, PMW, and PLW bands respectively. The PSW value works well for all bands, despite the variation in beams, as a high pointing error is still relatively small as a fraction of the larger beam sizes. This also allows the longer wavelength bands to benefit from the advantages seen when using a smaller map, i.e. better peak flux recovery. For a modest SNR of ~10, and pointing error of ~0.2-0.3 PSW beam FWHM, a typical peak flux error of ~7 %, and positional error of ~7 % of the beam FWHM can be expected.

Herschel has an absolute pointing error requirement of 3.7$''$(although a value of 2$''$ is expected to be achieved). The SPIRE team has decided that 7-point photometry (POF 2) will be adopted as the standard observing mode for point sources, with a nominal separation of 6$''$. This will ensure a good fit to both source position and flux.

6.2 Field Mapping

A POF 3 (jiggle map) observation is constructed from a series of independent POF 1 (point source photometry) observations. As a result, many of the relevant optimum parameter values are as for POF 1. In this case however,

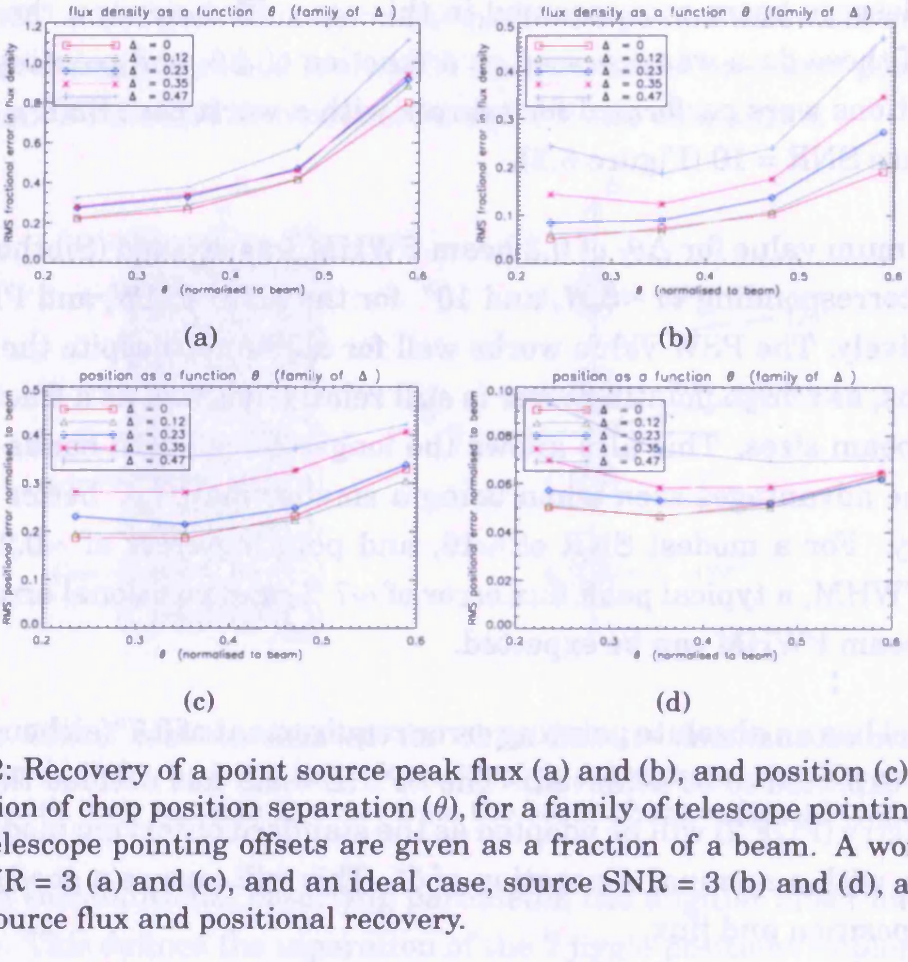

(a) (b)

(c) (d)

Figure 6.2: Recovery of a point source peak flux (a) and (b), and position (c) and (d), as a function of chop position separation (θ), for a family of telescope pointing offsets Δ. The telescope pointing offsets are given as a fraction of a beam. A worst case, source SNR = 3 (a) and (c), and an ideal case, source SNR = 3 (b) and (d), are given for both source flux and positional recovery.

since the source is assumed to be extended, a larger chop throw of 4′ is used. As in POF 2, it is the separation of the chop positions that is important here, $\Delta\theta_{64}$. A jiggle map containing 16 chop positions will be Nyquist sampled in any one array, however, in order to achieve full sampling in all three arrays at the same time, a 64 point map is required. An example pattern is shown in Figure 6.3. The telescope may also be required to nod. In order to minimise telescope movement overheads, two nod cycles will be performed, by visiting some nod positions A and B, in the following sequence, A, B, B, A.

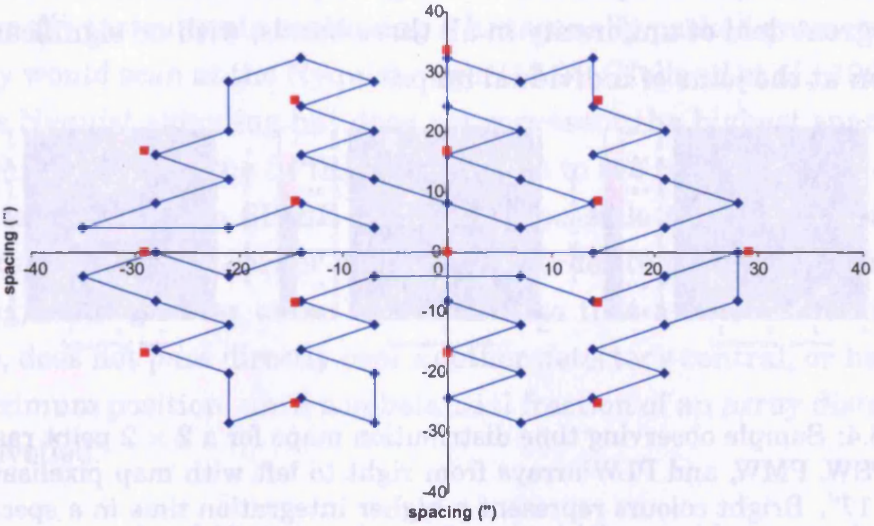

Figure 6.3: Schematic showing a 64 point jiggle map. Also included is the 16 point map required from full sampling in the PLW array, shown by the red squares.

The separation of the detectors as projected on the sky is $\sim 2\times$ FWHM. To achieve Nyquist sampling, a chop position separation of $\frac{1}{2}$ FWHM is necessary. This gives a nominal value of $\Delta\theta_{64} = 8.1''$, defined by the PSW array beam size. The 16 points required to fully sample the PLW array are shown in Figure 6.3. The small offsets seen are due to small array geometry effects. These errors are only a small fraction of a beam and are unimportant in practice. In the case of the 64 point jiggle, both the PLW and PMW bands benefit from being over sampled.

POF 4 (raster mapping) performs a series of jiggle maps (POF 3) at regular points in a raster pattern. Thus the optimised parameters derived for POF 3 are also applicable in this case. In addition to these parameters, the raster point separation in both the Y and Z directions, $\Delta_{rasterz}$ and $\Delta_{rastery}$, must be defined. Since the fully mapped area is strictly defined by the $4' \times 4'$ field of view, individual POF 3 observations have neat straight edges. Consequently no fitting of the array geometry is required. As a result, a separation of $4'$ in both directions would be expected, as defined by the field of view. However, it is still possible to combine the two maps in an optimal way by accurately aligning the edges of the individual jiggle maps. The optimal values derived for these parameters are $\Delta_{rasterz} = 245''$, and $\Delta_{rastery} = 236''$. Figure 6.4 shows the distribution of integration time for a 2×2 ($8' \times 8'$) raster map in each band. These maps were performed using the parameters defined above, and show a great deal of uniformity in all three bands, with no significant variation seen at the joins of individual maps.

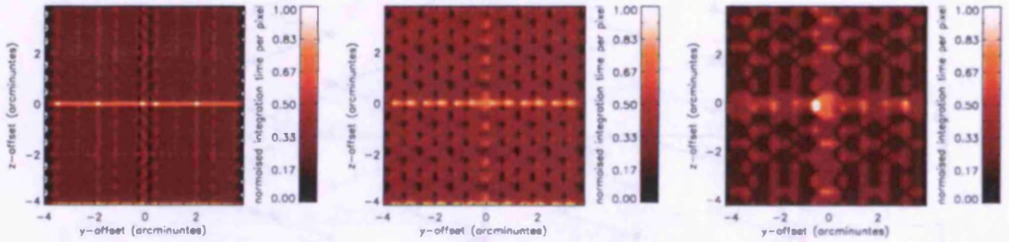

Figure 6.4: Sample observing time distribution maps for a 2×2 point raster map, in the PSW, PMW, and PLW arrays from right to left with map pixelisation of 9, 12, and $17''$. Bright colours represent a higher integration time in a specific pixel. Optimal raster point spacing is set as defined above.

6.3 Scan Mapping

POF 5, scan mapping without chopping, is expected to be the most commonly used observing mode. This mode will be used to perform large area observations for many of the 'key programmes'.

The principle parameters for this mode are the scan angle, ϕ_{angle} (shown in Figure 3.8), telescope scan rate, $\dot{\theta}$, and scan line separation, d. In addition to these parameters, the telescope acceleration rate and velocity settling times are important in dictating the observation overheads.

The scan angle, ϕ_{angle} is defined as the angular separation between the detector array long axis (Y-axis in spacecraft coordinates) and the array's direction of motion (Figure 3.8). Since the array is hexagonal packed it has six-fold symmetry. Therefore, for every scan angle there are 2 other angles which can produce the same result, with each angle having an opposite counterpart. These angles are illustrated in Figure 6.5. The three different options are referred to as scanning in the long, short, and diagonal directions, where 'long' refers to scanning along the long axis of the array, 'short' refers to scanning along the short axis of the array, and 'diagonal' refers to scanning angle the intermediate angle of the array.

Traditionally instruments containing a hexagonally packed geometry detector array would scan at the Nyquist angle (13.9°) (Holland et al., 1999). This provides Nyquist sampling but does not represent the highest spatial sampling achievable with the SPIRE arrays. Due to the relatively high number of detectors within the SPIRE arrays it is possible to rely on trailing detectors to follow up on earlier detectors. In order to achieve higher spatial sampling, an angle was taken which ensures that a detector, as far as is possible, does not pass directly over another detector's central, or half width half maximum position, until a substantial fraction of an array distance has been travelled.

An optimum angle of 12.4° has been found which provides scan data sufficient to produce maps with $\frac{1}{4}$ FWHM sized map pixels (i.e. double Nyquist sampling) in all three bands when scanning in the long direction. This pixel size chosen is independent of beam size, but the choice of a pixel size greater than $\frac{1}{2}$ a beam would result in a degradation of spatial information within the data. The high spatial sampling at 12.4° results in a high degree of uniformity in the map's signal to noise coverage (Figure 6.6(a)). Such uniformity will be particularly important for the large-scale deep survey programs. This increased uniformity is gained at the expense of some redundancy. However, redundancy is present in each scan with several strips of sky being visited by more than one detector (albeit fewer strips than when scanning at the Nyquist angle).

Gaps (map pixels containing no data) do appear in the PLW maps for scans in the diagonal and short directions, and also for the PMW array when scanning close to the short axis, as there are insufficient detectors in this di-

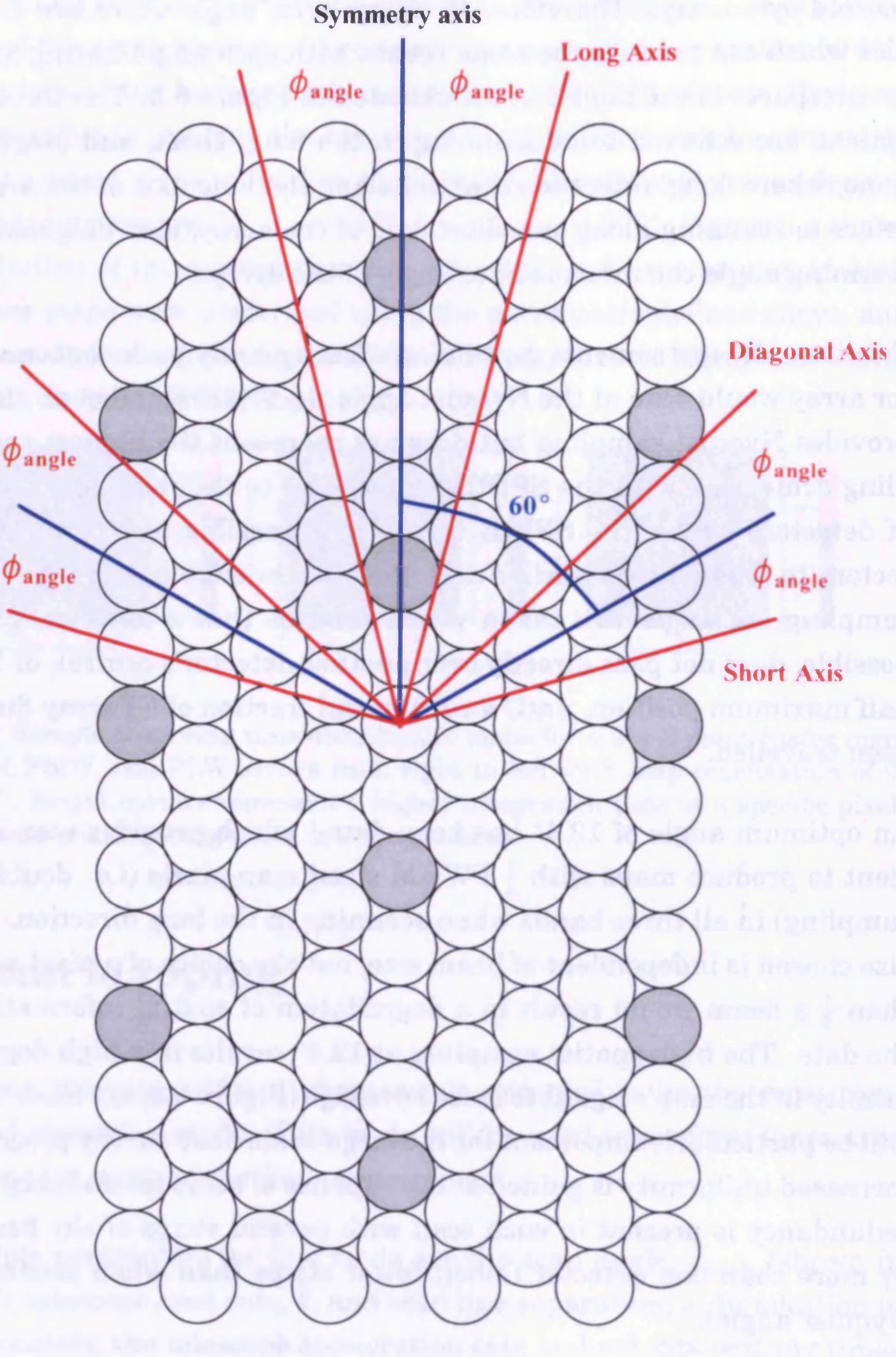

Figure 6.5: Illustration of the photometer detector array symmetry, and possible scan map scanning angles.

rection to perform a fully sampled observation. In these cases, the double Nyquist sampling (1/4 beam spacing) cannot be maintained. Using larger pixels alleviates this problem, and the sampling is still at least as good as in the Nyquist sampled case and are often better, i.e. pixel sizes remain $\leq \frac{1}{2}$ FWHM. Full sampling, meaning that there are no gaps in the maps for a chosen pixel size, for the PLW array is achieved with pixel size of 14″ for diagonal and short scanning; full sampling for the PMW array is achieved with a pixel size of 9″ for short axis scanning. The main disadvantage of this strategy is lower redundancy – that is, fewer points of the sky are visited by more than one pixel in a single scan leg.

In this analysis we have assumed 100% detector yield. While at present the number of dead detectors is very low (~5%); this may not be the case once in flight. Dead detectors could lead to gaps in the maps, but scanning close to the long axis will reduce this problem since there are more trailing detectors to fill in the gaps. Therefore, it is recommended that the nominal scanning direction be along the long axis. A disadvantage to this strategy however is higher overhead time required during telescope turnaround, because the array has to travel further before the entire array has passed over the required map area. For large maps this will be a minor fraction, but for smaller maps it may be better to scan close to the short axis. Dithering of repeated maps can then be used to fill in any holes within the map if necessary.

Since the PSW array is always fully sampled, with $\frac{1}{4}$ beam FWHM pixels, when scanning at 12.4°, even for diagonal and short axis scanning, the need for larger than $\frac{1}{4}$ FWHM pixels in the other two arrays can in some cases be offset. For example, source extraction can still be performed on the PSW array using the smaller pixels with the associated higher spatial sampling. This will support the source extraction in the other two bands by giving an improved source position. If it is necessary to scan along either the diagonal or short axes (due to scheduling constraints or cross-linking requirements) then this angle still provides a good compromise between uniformity and redundancy. In any case, Nyquist scanning requires larger map pixels than double Nyquist scanning in all situations. Therefore, a scanning angle of 12.4° is recommended, regardless of which axis the scanning direction is closest to.

For large square maps it is generally recommended that scans be made in the diagonal direction. Using the two counterpart diagonal options, it is possible to perform two almost orthogonal ($\sim$95.2°) scans maps. This provides a great deal of cross-linking in the data, providing redundancy and more importantly, the ability to implement the maximum likelihood map-making routines outlined in Section 5.3. The choice of these angles means that an equal amount of integration time is spent on each map section within a single scan. Scanning along the short, and then long axis, would produce a map with greater integration in time, per map area, being performed in short axis scan, than the long axis scan. The same integration time could be achieved in two scans along the long axis, but this would require scheduling the observations months apart in order for the telescope orbit to rotate the array and make the observations possible. This is not necessary for the diagonal scan option.

Small ($> 10'$), or irregularly shaped maps, e.g. scans of long thin structures, will not benefit much from scanning with these two angles. This is because the overheads required to repoint the telescope may be greater than the time to perform a single scan map. Here, the cross scan may not be more efficient than simply performing another scan in the same direction. In this case, the observation would scan along the long axis, thus recovering the $\frac{1}{4}$ FWHM pixel size performance in all bands. The use of the cross scan is also not beneficial for long thin maps, as they would only cross at one small point. Again, repeat maps in the same direction would be more efficient.

The optimum angular line separation, d, is the distance between successive scan lines that ensures the map is uniform in terms of distribution of integration time, both along, and perpendicular to, the scan line direction. In order to achieve this, it is necessary to derive a separation which will allow each scan line to fit perfectly into place with the previous line's observation, thereby creating a scan equivalent to one made with a single array with an effective size of n scan lines (Figure 6.6(b)).

This optimum scan separation depends on the particular array geometry, and hence is slightly different for each array. The optimum value of d for a

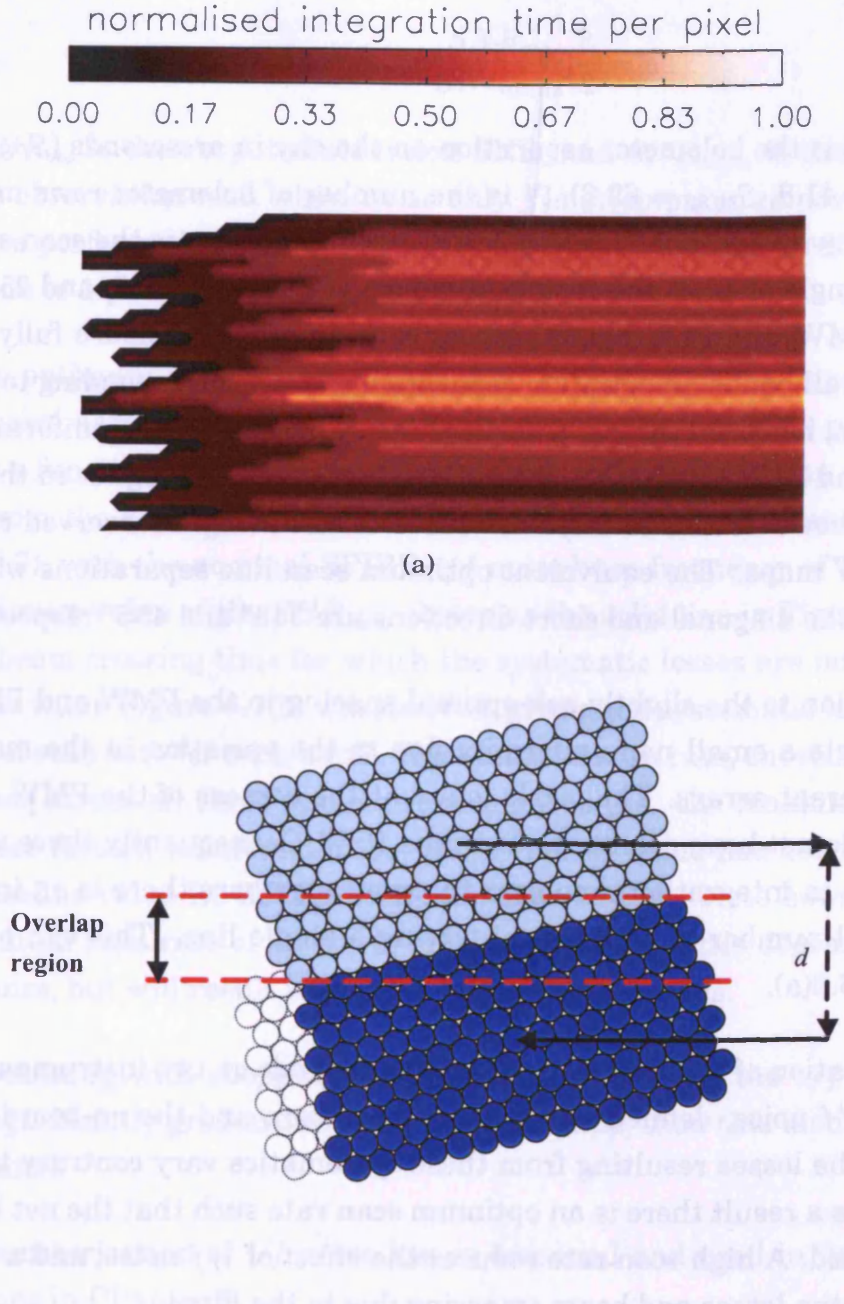

Figure 6.6: (a) Sample integration maps for the PSW (top) and PLW (bottom) arrays for two scan lines separated by 235″; (b) Illustration of optimum scan line separation with the scan performed along the long axis. Optimum line separation results in perfect interlinking between separate scan lines, thus giving a uniform integration map.

given scan angle, scanning along the short axis, is given by Equation 6.1,

$$d = \frac{S}{2}(N\sqrt{3}\cos(\phi_{scan}) - \sin(\phi_{scan})), \tag{6.1}$$

where S is the bolometer separation on the sky in arcseconds (S_{PSW} = 31.4, S_{PMW} = 41.8, S_{PLW} = 62.8), N is the number of bolometer rows making up each array (N_{PSW} = 9, N_{PMW} = 7, N_{PLW} = 5), and ϕ_{scan} is the scan angle. For a scan angle of 12.4° the resultant values of d are 235, 243, and 258″ for the PSW, PMW, and PLW bands respectively. In order to ensure fully sampled maps in all bands an optimum separation of 235″, corresponding to the PSW optimum, has been chosen. This does result in some loss in uniformity in the PMW and PLW, where the integration time is slightly higher in the overlap region, however this is more favorable than having unobserved regions in the PSW maps. The equivalent optimum scan line separations when scanning in the diagonal and short directions are 348″ and 455″ respectively.

In addition to the slightly sub-optimal spacing in the PMW and PLW, there also exists a small non-uniformity due to the variation in the make up of the different arrays. The pixels found at the corners of the PMW and PLW arrays do not have counterparts in the PSW. Consequently there is a slight increase in integration time near the overlap, where there is an increase in the total number of detectors observing a single line. This can be seen in Figure 6.6(a).

Optimisation of the scan rate parameter depends on two instrument systematics: $1/f$ noise, defined by the knee frequency, and the on-board low-pass filter. The losses resulting from these systematics vary contrary to one another. As a result there is an optimum scan rate such that the net losses are minimised. A high scan rate reduces the effect of $1/f$ noise, and a slow rate reduces the losses and beam smearing due to the filter.

A series of simulations was performed in order to assess the impact of $1/f$ noise on our ability to recover a point source during a single scan observation. This impact was quantified by comparison of the output SNR with an identical observation, performed with only white noise (Equation 6.2). This is referred to as the SNR loss factor, SNR_{loss}.

$$SNR_{loss} = \frac{SNR_{obs}}{SNR_{white}}, \tag{6.2}$$

where SNR_{obs} is the output observation SNR, and SNR_{white} is the SNR for the same observation with white noise only. No attempts to remove the $1/f$ noise were performed. A SNR_{loss} value of unity would be the ideal case, i.e. no loss due to $1/f$ noise.

Since the optimum scan rate will vary with convolved source size scale, a more general parameter to use is the beam crossing time τ. This parameter varies as a function of the convolved source size scale and the scan rate. The results from the simulations performed are thus plotted as a function of τ (Figure 6.7), with the nominal SPIRE $1/f$ noise knee frequency of 100 mHz. The maximum value of the SNR_{loss}, shown as the solid line in Figure 6.7(a), give the beam crossing time for which the systematic losses are minimised. Using this value Figure 6.7(b) was derived, giving the systematic losses as a function of scan rate for each band. The optimum scan rate, chosen such the total losses across all three bands are minimised (i.e. the maximum value of SNR loss factor), was found to be $\sim 30'' \mathrm{s}^{-1}$. This value has been adopted as the baseline value for SPIRE scan-map observations. Note however that the maximum scan rate of $60'' \mathrm{s}^{-1}$ is useable with very little degradation in performance, but will result in greater telescope overheads.

POF 6, scanning with chopping, is an auxiliary mode. If the $1/f$ noise in orbit is significantly greater than the nominal value, then this mode may be implemented.

This parameterisation of $1/f$ noise loss is extended and used in further investigations in Chapter 8.

6.4 Observing Mode Selection

A comparison of the efficiency of the raster and scan map modes was carried out. The basic jiggle map figure of merit, against which scan map observa-

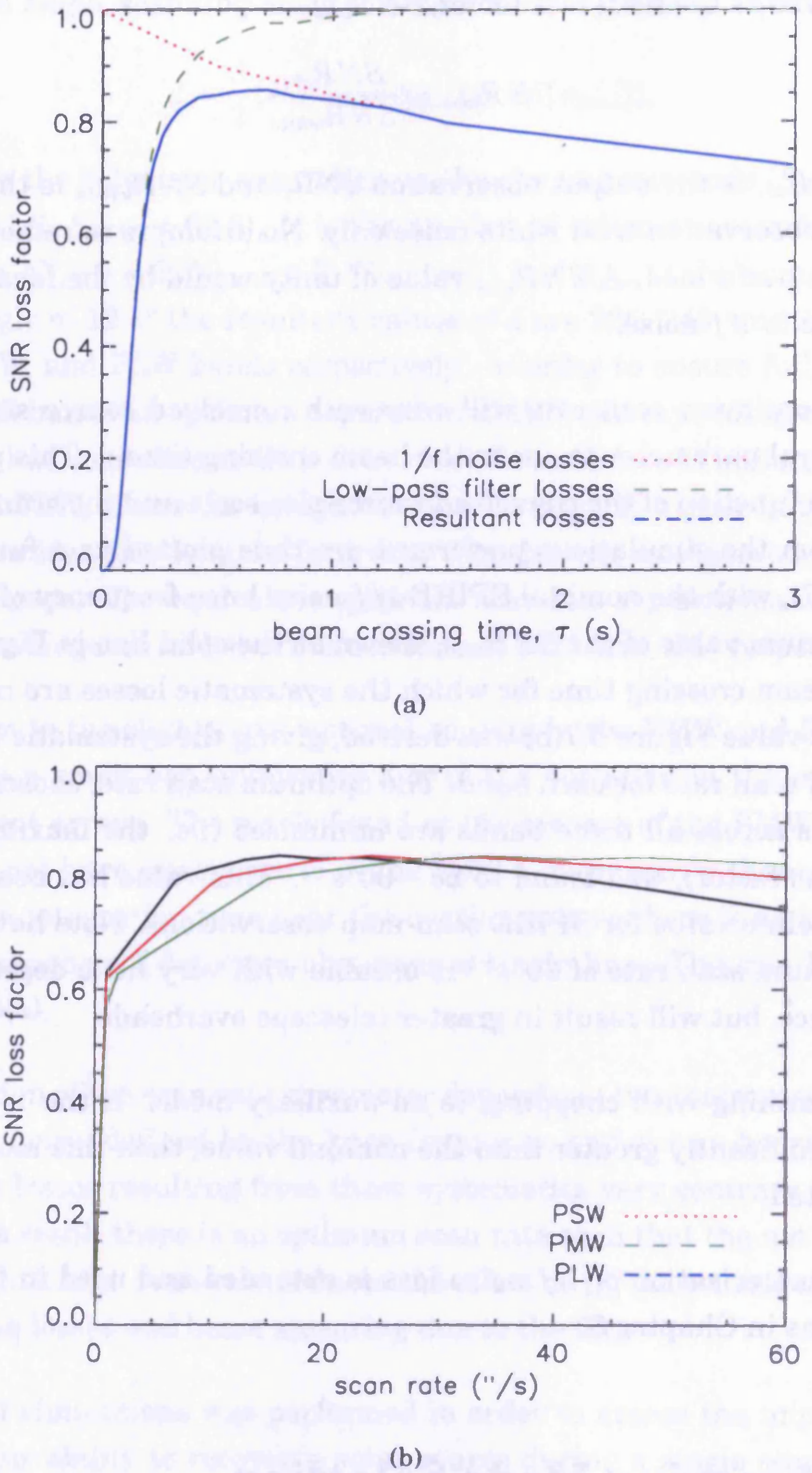

Figure 6.7: (a) SNR loss factor as a function of beam crossing time for $1/f$ noise (dotted line) and low pass filter (dashed line) systematics. Also shown is the combined losses (solid line). (b) SNR loss factor as a function of scan rate, derived from both $1/f$ and low pass filter systematics, for each of the SPIRE bands. The data in both Figures are for the nominal detector $1/f$ noise knee frequency of 100 mHz

tions are compared, is the point source sensitivity achieved by a single jiggle map using 12 chop cycles. The total integration time for an observation of this type is 768 s (and a total observation time of 848 s) (Swinyard and Griffin, 2002). The point source 1σ detection limit for this map would be $\Delta S_{1\sigma}$ = 5.0 mJy.

The assumption is made that a single jiggle map has an area of $3.6' \times 3.6'$. The actual map will be slightly larger than this (more like 4′) but this assumption allows for trimming of bad signal-to-noise areas, and compensates for overlaps of tiled maps for larger areas. To map an equivalent area using scan map mode we must perform two scan lines. Measures were taken to ensure that the area observed is uniform and did not suffer from edge effects. All scan map parameters were the nominal values derived above. Note how the actual scan map area scanned is slightly larger than that of the jiggle map. This is because the separation between subsequent scan lines is (Δ_{line}) 3.9′ rather than 3.6′. This does of course mean that there is a great deal of extra data covered in the scan map, particularly when the acceleration phases are taken into account. Although the quality of these data cannot be assured, it is expected that they will be significantly useful and so constitute a potential bonus. To obtain the same sensitivity as the 12 chop cycle jiggle map requires 19 map repeats (giving an ultimate sensitivity of $\Delta S_{1\sigma}$ = 4.90 mJy). Several size raster maps were studied. The results are summarised in Table 6.1.

Raster map geometry (WxH)	Total raster map time (s)	Total scan map time (s)	Raster/Scan map
1 × 1 (4′ × 4′)	848	2373	0.36
2 × 2 (8′ × 8′)	3392	4416	0.77
3 × 3 (12′ × 12′)	7632	6090	1.25
2 × 1 (8′ × 4′)	1696	2646	0.64
3 × 1 (12′ × 4′)	2544	2920	0.87
3 × 2 (12′ × 8′)	5088	4878	1.04

Table 6.1: Comparison of scan-map and raster-map efficiencies for small maps.

These results show that in general, for maps ~$8' \times 8'$ and greater, scanning is more efficient then jiggling. For this reason scan map mode is preferred for all maps except a single 4′× 4′ field. This is because the majority of the scan map overheads are composed of the acceleration and deceleration at the beginning and end of each scan line. The scan map efficiency is in general higher as it has a field of view twice that of the raster map. These overheads are dependant on scan rate and not map size. Thus for large maps, scan map will always be more efficient.

Several other factors need to be taken into consideration if simple observing efficiency is not the primary concern. Because it involves chopping, raster mapping is immune to $1/f$ noise so this may be attractive in some cases. However, it also removes large scale structure, in which case scanning may be preferable. The additional data around the edges of a small scan map may be useful albeit of lower quality than the main map area.

Since this analysis was carried out, the telescope movement overheads have been increased. The impact of this change on the results of the jiggle map verses scan map study is currently under investigation. The situation regarding the final telescope overheads is currently being assessed by the SPIRE and Herschel science centre (HSC) teams.

6.5 Chapter Summary

In this chapter the main observing modes for SPIRE have been assessed, and the baseline optimum parameters derived. POF 2, 7 point mapping, will be used as the nominal point source photometry mode, with a jiggle position spacing, $\Delta\theta_7$, of 6″. This mode is chosen over a single pointing observation (POF 1) as it guarantees source flux and position recovery, within the Herschel pointing accuracy and reasonable source position errors, with only a small reduction in SNR.

The optimum spacing required within the jiggle map pattern (Figure 6.3), in order to fully sample all arrays, is 8.1″. The spacing between consecutive jiggle maps when raster mapping, was found to be 245, and 236″ in the Z and Y telescope coordinates respectively. This ensures that the observation remains fully sampled at the join between jiggle maps, and that the distribution of integration time remains even.

The optimum scan map mode parameters were found to be a scan rate of $30''\mathrm{s}^{-1}$, and scan angle of 12.4°. Perpendicular scans in the diagonal directions are optimal for large maps, as they provide cross-linked data, suitable for use with a maximum likelihood map-maker. Small and irregular maps however are more efficiently performed by scanning along the long axis. The optimum scan line separation for the diagonal and long axis scan directions are 235 and $348''$ respectively. These parameters minimise the losses due to $1/f$ noise and low pass filter systematics, provide full sampling down to $\frac{1}{4}$ FWHM, and provide a uniform distribution of integration time across the map.

Scan map mode was found to be more efficient than raster mapping for maps greater than $4' \times 4'$. In addition to the shorter total observation time, it provides a more uniform integration time map, as well as significant bonus data in the surrounding map regions. As a result this will be the nominal mode for all but single field jiggle maps ($4' \times 4'$). This result is currently being reassessed due to new information regarding telescope movement overheads.

The optimum observing parameters for each of the SPIRE observing modes are summarised in Table 6.2. These parameters are adopted as the nominal operational values. Specific science cases may require a variation on some parameters, however these nominal values will be used for the majority of observations.

Many of the conclusions derived here are applicable to other observing systems, particularly those with a hexagonally packed detector array.

For further reading and a more detailed description of the optimisation of the SPIRE photometer observatory functions see Sibthorpe et al. (2005), Sibthorpe et al. (2006), and Sibthorpe and Waskett (2006).

POF	Parameter	Symbol	Nominal value
POF 1,2,3,4	Chop frequency	f_{chop}	2 Hz
POF 1,2,4	Chop throw	Δ_{throw}	$126''$
POF 2	7 point chop separation	$\Delta\theta_7$	$6''$
POF 4	raster point separation z axis	$\Delta_{rasterz}$	$245''$
POF 4	raster point separation y axis	$\Delta_{rastery}$	$236''$
POF 5	Scan rate	$\dot{\theta}$	$30''s^{-1}$
POF 5,6	Scan angle	ϕ_{angle}	12.4, 47.6, 72.4°
POF 5,6	Scan line separation	Δ_{line}	$235, 348, 455''$

Table 6.2: Summary of optimised POF parameters. POF 5 parameters refer to scanning in the long, diagonal, and short directions respectively where appropriate.

Chapter 7

BLAST Observations of the Cassiopeia A Supernova Remnant

7.1 Introduction

In this chapter we present results from recent BLAST observations of the supernova remnant Cassiopeia A (Cas A), and discuss their contribution towards the on-going argument about whether significant amounts of dust are formed in supernovae (SNe). I performed the analysis of these data, which will be submitted to the Astrophysical Journal by Hargrave et al. (In Prep.). The reduction and calibration of the BLAST data from timelines to maps was performed by external members of the BLAST consortium.

7.2 The Cassiopeia A Supernova Remnant

Cas A is the remnant of a type II supernova (Raymond, 1984) approximately $4'$ in diameter, at right ascension (RA) 23 h 23.4 m, and declination $+58^\circ\ 50'$(J2000). The progenitor star is believed to have had a mass greater than 20 $M_\odot$ (Pérez-

Rendón et al., 2002). It is at a distance of approximately 3.4 kpc and is in the region of 320 years old (Thorstensen et al., 2001; Fesen et al., 2006). It emits over a wide range of the electromagnetic spectrum, with particularly strong emission in the X-ray and radio. With the exception of the Sun, it is the brightest radio source in the sky, with a flux density of 2720 Jy at 1 GHz (Green, 2006).

Figure 7.1 is a composite image composed of X-ray, optical, and infrared data. The expanding shock can be clearly seen in all bands, along with extended filamentary structure. The outer shock is visible only in the X-ray image as a thin blue ring. The remains of the progenitor star can also be seen in the X-ray image as a small green dot near the centre of the image.

Figure 7.1: Composite image of Cas A composed of Chandra data acquired using broadband X-rays (low to high energies) (blue); Chandra data correspond to intermediate energy X-rays (green); Hubble data taken using a 900 nanometer-wavelength filter (yellow), and Spitzer data from the telescope's 24-micron MIPS camera (red) (Krause, 2005).

Several emission processes contribute to the Cas A spectrum in the 1–1000 μm wavelength range. These include free-free, synchrotron, and line emission (Dwek et al., 1987), in addition to the thermal radiation.

In an analysis by Dwek et al. (1987), the flux density contribution from free-free emission is assumed to be wavelength independent, and was defined as

$S_\nu(Jy) \approx 0.068 n_e M_{ion} g_{ff}/T^{1/2}$, for a source at a distance of 1 kpc. Here, n_e is the electron density, M_{ion} is the mass of ionised gas, $g_{ff}(\approx 10)$ is the Gaunt factor, and T is the temperature (Spitzer, 1978). This equates to a flux density of $\sim 7M_{ion}(M_\odot)$ Jy, assuming an electron density of 10^4 cm^{-3} and temperature of 15,000 K. Since the total mass of the knots in Cas A are thought to be between 0.016 and $\sim$ 0.25 $M_\odot$ (Peimbert and van den Bergh, 1971), and only a small fraction of this will be emitting free-free radiation, the contribution from free-free emission was concluded to be negligible within this wavelength range.

Relativistic electrons spiraling in the strong magnetic field of Cas A means that there is a significant contribution to the Cas A SED from synchrotron radiation. Millimetre and radio data show this emission to exhibit a constant power law behavior of the form, $S_\nu \propto \nu^\alpha$, where α = -0.72 (Baars et al., 1977; Wright et al., 1999; Reichart and Stephens, 2000).

Finally, there are several strong emission lines associated with Cas A which should be noted. Figure 7.2 shows the mid-infrared spectrum of the northern knot in Cas A. The data are obtained from observations made with ISO-CAM, and ISO-SWS, the camera and short wavelength spectrometer respectively, on board ISO. The ISOCAM observations have a spectral resolution of $\lambda/\Delta\lambda \simeq 40$.

Line emission due to [ArII] (7 μm), [ArIII] (9 μm), [SIV] (10.5 μm), NeII (12.8 μm), NeV (14.3 μm, very weak), [NeIII] (15.5 μm), [OIII] (25.9 μm), can clearly be seen in Figure 7.2(b) (Douvion et al., 2001b). These contributions only constitute a significant flux density contribution to the total SED at short wavelengths ($\lambda \lesssim 25$ μm) when compared to the Planck black-body emission.

7.3 Dust Creation in SNe

Understanding the origin of cosmic dust is fundamental to our understanding of many astronomical processes, including star formation and galaxy

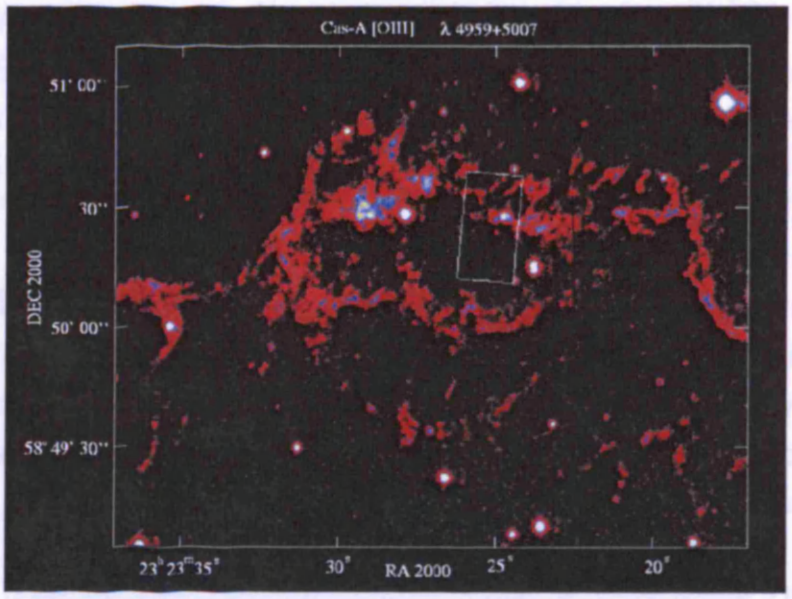

(a) Optical image of the northern part of the Cas A SN remnant

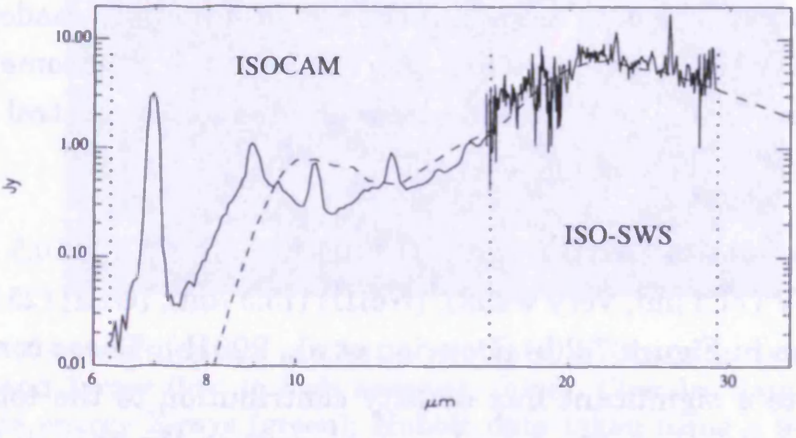

(b) Mid-infrared spectrum of the Cas A SN remnant

Figure 7.2: (a) Optical image of the northern part of the Cas A SN remnant in the [OIII] lines at 4959 and 5007 Å; (b) Mid-infrared spectrum of the region outlined in part (a), taken with ISOCAM (6–16μm) and ISO- SWS (16–29μm) (Douvion et al., 2001b).

evolution. Traditionally, the main source of dust production within a galaxy is assumed to be due to the stellar winds of stars on the asymptotic giant branch (AGB) of the Hertzsprung-Russell (HR) diagram (see Section 2.2). These stars are in the latter stages of their evolution. Recent observations have, however, cast doubt doubt on this theory. Galaxies (Dunne et al., 2003b; Hughes et al., 1998; Smail et al., 1997) and quasars (Bertoldi et al., 2003; Archibald et al., 2001) at high redshift have been found which contain large amounts of dust ($> 10^8$ $M_\odot$), at a time when the universe was only $\sim 1/10^{th}$ of its present age. Stars would not have been able to form and reach the AGB of the HR diagram in the available time. Therefore, another mechanism for the formation of dust is required to explain these observations (see Section 2.2.2).

For several years, models have predicted that significant amounts of dust (0.2–4 $M_\odot$) could be produced within supernova explosions (Todini and Ferrara, 2001; Clayton et al., 1999; Woosley and Weaver, 1995; Kozasa et al., 1991). The life cycle of high mass stars (> 8 $M_\odot$), the progenitors of SNe, is sufficiently fast for SNe to occur within the timescales constrained by the observations. As a result SNe have been proposed as a possible solution to the origin of the excess dust seen at high redshift.

The first supporting evidence for this theory came from observations of Cas A by Dunne et al. (2003a), which found ~2–4 $M_\odot$ of cold (~18 K) dust (Figure 7.3). Previous observations made with ISO and IRAS (6–170 μm) did not extend to longer wavelengths, and therefore had only detected the hot dust component, which indicated a mass of 10^{-7}–10^{-3} $M_\odot$.

This detection was followed shortly afterwards by a detection of cold dust in Kepler's SN remnant (Morgan et al., 2003). Here the dust mass detected was ~1 $M_\odot$, 1000 times greater than previous measurements. Both of these SN remnants are sufficiently young for the dust observed to be associated with the remnant, rather than being material swept up from the ISM by the shockwave.

The data for these measurements were taken using SCUBA in 'scan-map' mode (Holland et al., 1999). Note, this method is different to the scan-map mode employed by SPIRE. The observation was performed while chopping,

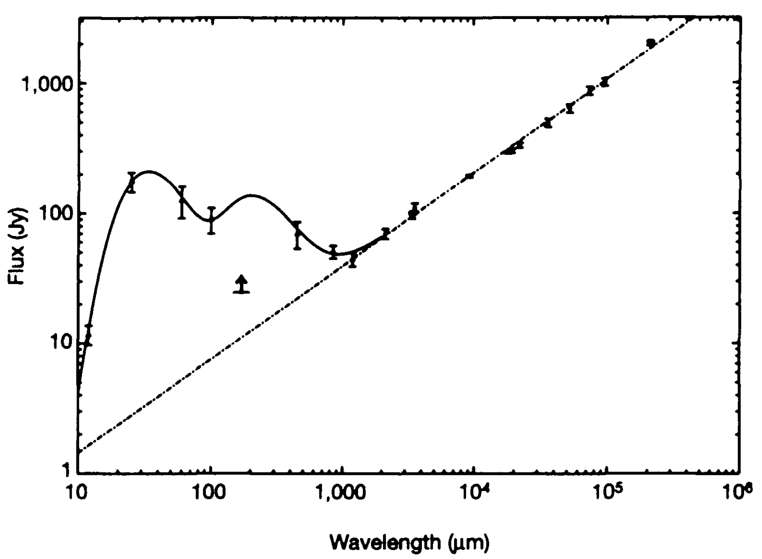

Figure 7.3: SED of Cas A from Dunne et al. (2003a) derived using IRAS, ISO, and SCUBA data. The SED shows both a hot (~ 112 K) and cold (~12 K) dust component. Also shown is the synchrotron emission fit as a power law $S_\nu \propto \nu^\alpha$, where $\alpha = -0.72$.

raising the possibility of spurious large-scale structure. Observations at the SCUBA wavelengths also contain a great deal of contaminating synchrotron radiation.

More recently Krause et al. (2004) have argued that the dust observed in Cas A, is in fact associated with a molecular cloud, located between Earth and the SN remnant. Using observations of molecular gas, the presence of such large scale foreground structure has been confirmed. Consequently Krause et al. (2004) estimate the dust yield within Cas A to be an order of magnitude lower than that found by Dunne et al. (2003a), thereby weakening the argument that SNe could be a significant source of interstellar dust.

The evidence for dust in Kepler's SN remnant has similar issues. While the foreground cloud contribution is lower for Kelper than that of Cas A, it is still high enough to be regarded as significant (Krause et al., 2004; Arendt, 1989)). Therefore the result from Kepler is not sufficient alone to create a compelling case for dust formation in SNe.

Despite the argument of Krause et al. (2004), there remains an interesting relation between the structure of the Cas A SN remnant, and the emission from the foreground cloud, which suggests that there could still be cold dust associated with the remnant.

7.4 Observations of Cas A with BLAST

Neither the SCUBA nor Spitzer observations sample the cold dust component seen towards Cas A particularly well. The SCUBA 450 μm and 850 μm observations provide measurements longward of the peak cold dust emission (Figure 7.3), while Spitzer data are only available at shorter wavelengths (3.6 – 160 μm). In addition, the Spitzer 160 μm band data are poorly sampled, with large holes in the map. The BLAST bands span this missing wavelength range well, providing three valuable additional measurements within the cold dust region of the SED. BLAST is also, like Spitzer (and SPIRE in scan-map mode), a direct measurement system, and therefore does not need to chop. As a result, these data will not be susceptible to the spurious large scale structure issues that plague the SCUBA observations. The high mapping speed of BLAST means that in addition to Cas A, it is possible to map a large area (30′) surrounding the SN remnant, giving data for the foreground cloud structure.

Here I describe the BLAST observations performed, and the analysis of these data. I derive an SED for both the cloud, and SN remnant sources within the maps, and discuss the implications of these results in terms of the possible cold dust associated with Cas A.

7.4.1 The Data

BLAST performed a ‘cap’ observation of Cas A during the first LDB flight in July 2005. In this observing mode the telescope slews backwards and forwards in azimuth while slowly, and at a constant rate, increasing in altitude. The slew is varied such that a circular region of sky is observed (see Figure 7.4). At the start of the scan the azimuth scan is below the minimum angular scale, resulting in the flattened regions seen at the top and bottom (beginning and end) of the scan pattern shown.

A slew rate of $6's^{-1}$ and altitude scan rate of 3.25′ per scan line (1/2 an array) were used to perform the observation. Due to flight time limitation, it was only possible to perform 1.25 scan maps. The maps were ~40′ × 60′ in size.

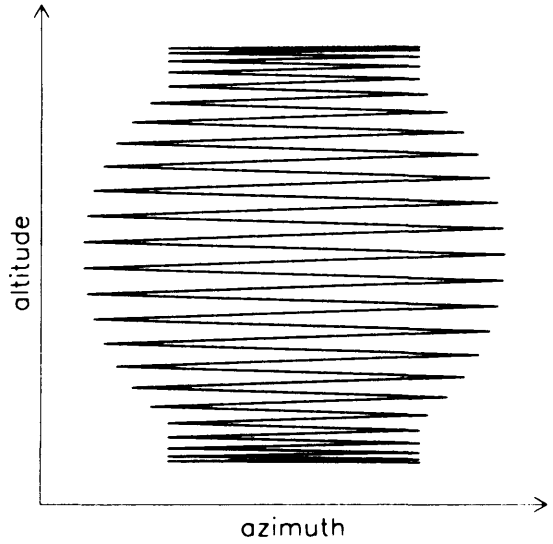

Figure 7.4: Schematic diagram of a typical BLAST 'cap' scanning pattern.

Early in the flight it was found that the telescope was not correctly focused. Modelling of the distortion suggests that this could have been due to the secondary mirror being several centimetres from its designed location. When the telescope was recovered, part of the secondary support structure was damaged. This could have happened in launch or during landing. If this fault developed during the launch, then this could explain the focusing error. The result of this was a distortion of the telescope beam in the three wavelength bands, as shown in Figure 7.5.

The beam deformation resulted in a severely degraded angular resolution in all bands. Using Figure 7.5 it can be seen that the beam sizes for all three bands are ~3-4′, rather than the nominal values of 30, 41, and 59″ for the PSW, PMW, and PLW bands respectively. Consequently it was not possible to resolve structure within the 4′ diameter SN remnant. I were therefore unable to determine if there was significant cloud structure on scales smaller

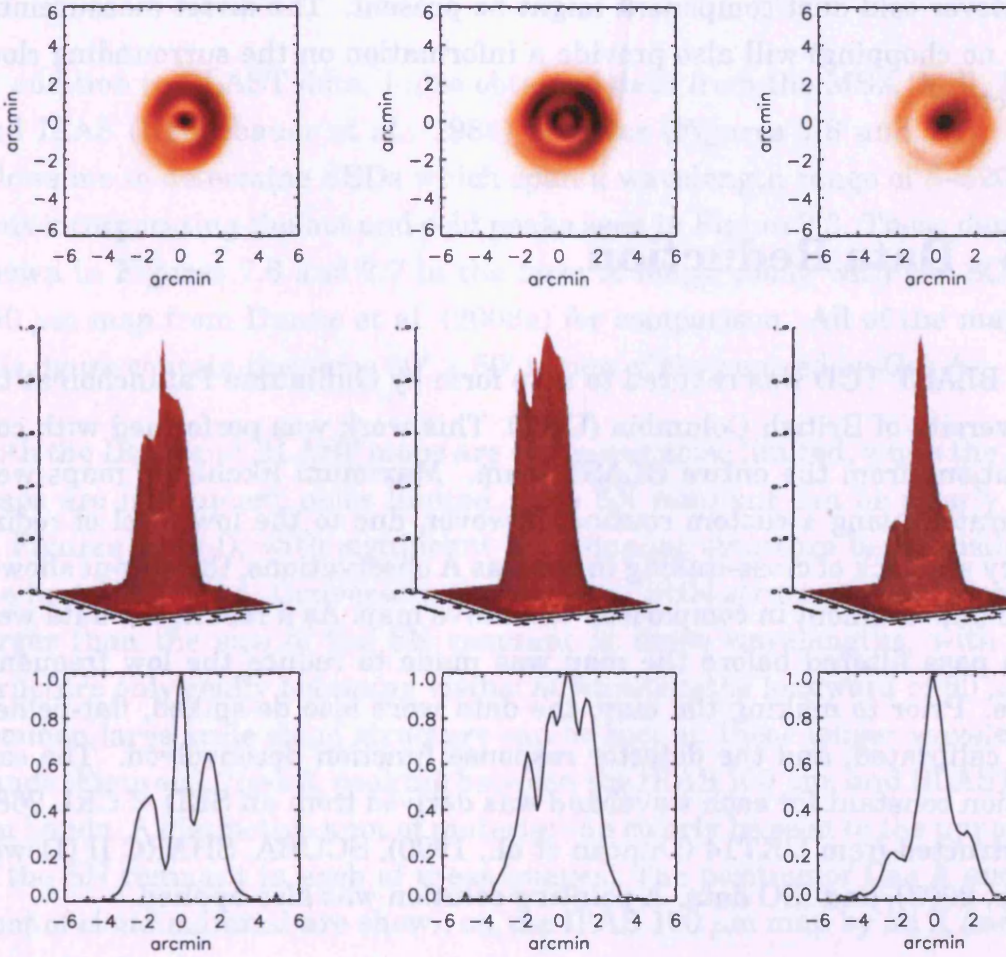

Figure 7.5: Modelled BLAST beam patterns from the 2005 LDB flight. A beam image, surface plot, and cross-section is shown in columns, for each of band, with the PSW, PMW, and PLW bands being in the left, central, and right hand columns respectively. These modelled beams were generated by Edward Chapin and Marie Rex, from a series of stacked beams, derived from all detectors observing a point source.

than that of the SN remnant.

The BLAST data are still useful however, despite the focusing problem. With these data I am able to measure the flux density of both the SN remnant and the surrounding cloud in all three bands, and hence further constrain whatever cold dust component might be present. The direct measurement (i.e. no chopping) will also provide a information on the surrounding cloud structure.

7.5 Data Reduction

The BLAST TOD was reduced to map form by Guillaume Patanchon at the University of British Columbia (UBC). This work was performed with contributions from the entire BLAST team. Maximum likelihood maps were generated using a custom routine, however, due to the low level of redundancy and lack of cross-linking in the Cas A observations, the output showed little improvement in comparison to a naïve map. As a result, the data were high pass filtered before the map was made to reduce the low frequency noise. Prior to making the map, the data were also de-spiked, flat-fielded, and calibrated, and the detector response function deconvolved. The calibration constant for each waveband was derived from an SED of CRL 2688, constructed from UKT14 (Duncan et al., 1990), SCUBA, SHARC II (Dowell et al., 2003), and ISO data. A pointing solution was also applied.

7.6 Data Analysis and Results

The aim of our analysis was to derive two SEDs, one in the direction of the foreground cloud (SED_{cloud}), and the other in the direction of Cas A (SED_{CasA}). This second SED would contain contributions from both the SN remnant and the cloud combined. We would then be able to compare the SED of the cloud, with the cold component seen in the SED of Cas A. A similar SED for both the cloud and cold SN remnant component would suggest that the measured dust was most likely associated with the cloud, and not the SN remant.

7.6.1 Maps

In addition to BLAST data, I also obtained data from the MSX (Mill, 1994) and IRAS (Neugebauer et al., 1984) archives (Figures 7.6 and 7.7). This allows me to determine SEDs which span a wavelength range of 8–520 μm, thus incorporating the hot and cold peaks seen in Figure 7.3. These data are shown in Figures 7.6 and 7.7 in the form of maps, along with the SCUBA 850 μm map from Dunne et al. (2003a) for comparison. All of the maps in this figure contain the same $50' \times 50'$ region of sky centred on Cas A.

Both the IRAS and BLAST maps are confusion noise limited, while the MSX maps are instrument noise limited. The SN remnant can be clearly seen in Figures 7.6(a-f), with significant SN remnant structure being visible in the first MSX band. Conversely, there is very little structure seen on scales larger than the size of the SN remnant at these wavelengths, with such structure only really becoming visible at wavelengths longward of 60 μm. A common large scale cloud structure can be seen in these longer wavelength bands (Figures 7.7(g-k)), peaking between the IRAS 100 μm, and BLAST 250 μm bands. A distinctive knot of material can clearly be seen to the upper left of the SN remnant in each of these images. The position of Cas A and the knot of cloud material are shown on the IRAS 100 μm map by an X and a Δ respectively.

Due to the focusing problem mentioned above, the BLAST maps have insufficient resolution to identify any sub-remnant scale structure in the foreground cloud. It is therefore difficult to assess the influence such structure might have had on the reliability of the SCUBA measurements. However, using the limited extent of the SCUBA map as a guide to the chop throw, and the BLAST 520 μm map as representative of the surrounding cloud structure, it is possible to assess the credibility of the chopped observing function used by SCUBA, given the large scale cloud structure. The large variation seen in cloud structure immediately adjacent to the edge of the SCUBA

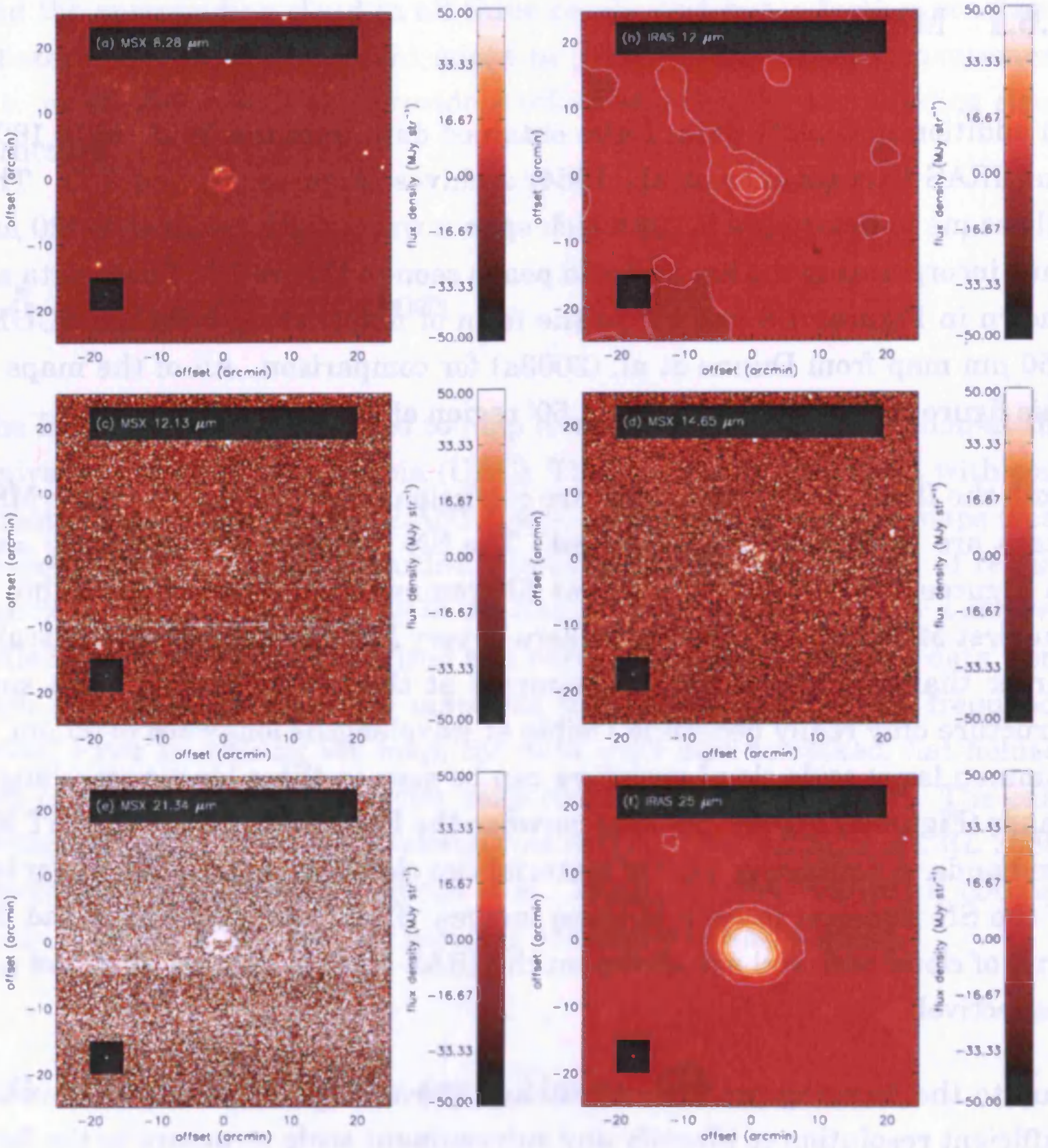

Figure 7.6: Data from MSX (a,c-e) and IRAS (b,f), used in the analysis presented in this chapter. All images are centred on Cas A and are 50′ × 50′ square.

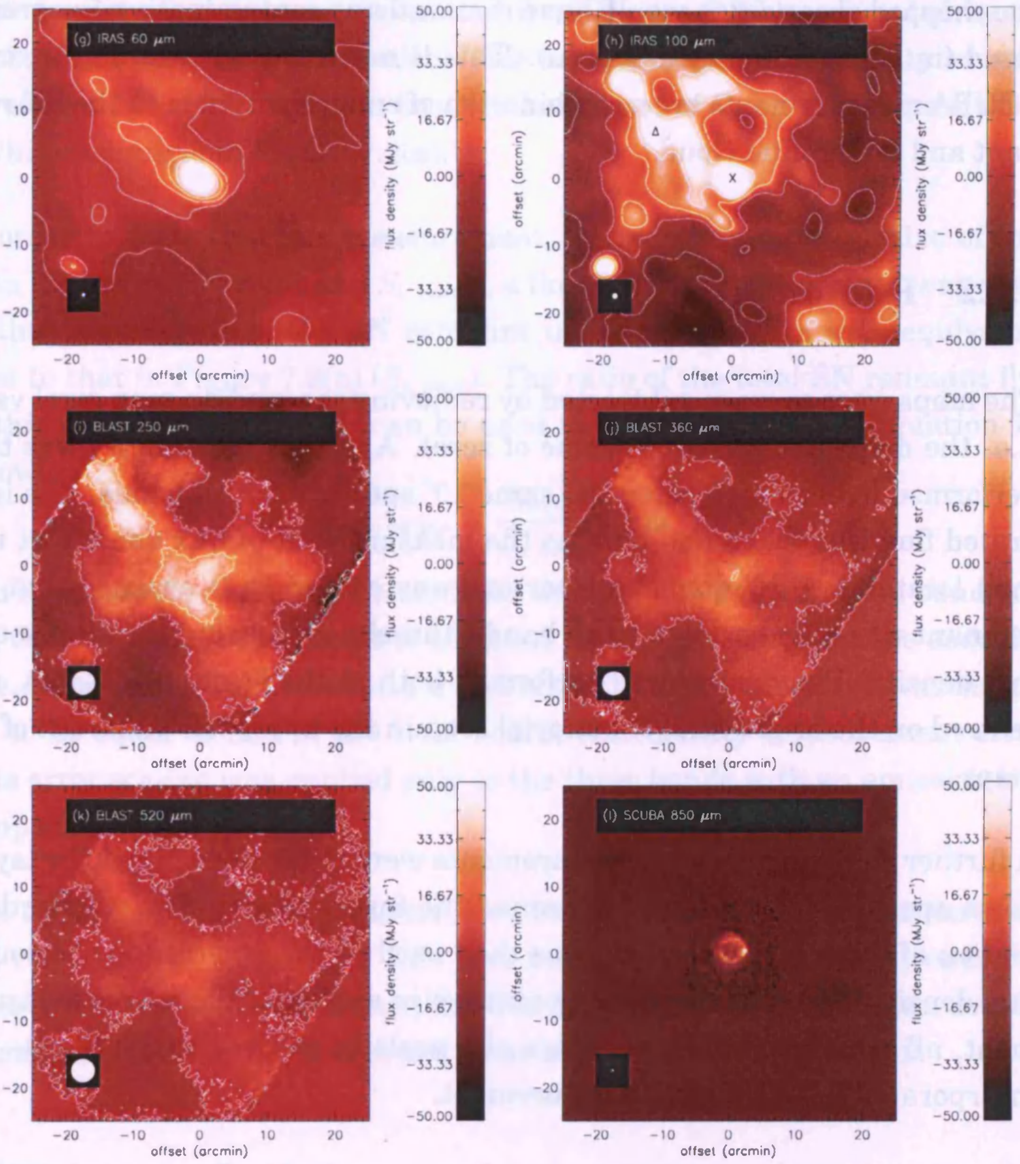

Figure 7.7: Data from IRAS (g-h), and BLAST (i-k), used in the analysis presented in this chapter. All images are centred on Cas A and are $50' \times 50'$ square. The SCUBA 850 μm data (l) from Dunne et al. (2003a) is also shown for comparison. The position of Cas A and the knot of cloud material are shown on the IRAS 100 μm map by an X and a Δ respectively.

maps means that the SCUBA observations were certainly influenced by the presence of the cloud. Had the cloud been uniform over an angular scale greater than a chop throw from the edge of the map, then the differencing of the chopped observation would have removed any contaminating foreground cloud (in addition to sky emission). This is not the case, meaning that the SCUBA measurements are a combination of emission from both the SN remnant and foreground cloud.

7.6.2 Photometry

The maps were average subtracted by removing the median map pixel value (i.e. the maps had a median value of zero). Aperture photometry was then performed in each map using the same $10'$ aperture for all bands. The integrated flux was taken and used as the measurement of flux density at that map location. A $10'$ diameter aperture was chosen as it ensured that the remnant was fully enclosed in all bands, thereby measuring the total source flux density. Photometry was performed both at the location of Cas A, and centred on the bright knot of material seen in the upper left quadrant of the maps.

A further 8–10 flux density measurements were made in each map by laying down apertures of $10'$ diameter around the target region. The standard deviation of these measurements was then used as the 1σ error on the source flux density. By using the same aperture size as that of the source measurement, all noise correlations on this size scale in the various data sets are incorporated into this error measurement.

The same synchrotron emission power law, as applied by Dunne et al. (2003a) (see Section 7.2), was then used to derive the synchrotron contribution within each band. These estimates were then subtracted from the flux measurements made at the location of Cas A. The synchrotron emission is associated with the SN remnant only, hence no equivalent adjustment was made to measurements of the cloud.

The short wavelength observations (8–25 μm) also contain significant contributions to their flux from emission line and other chemical features (Figure 7.2(b)). The 8.28 μm MSX data are a particularly good example of this, with the band containing strong [Ar II] and [Ar III] lines. The area under the emission line features was estimated from Figure 7.2(b) and scaled by the appropriate observing bandwidth. This represents the flux density as measured in a 14″ × 27″ region in the Northern knot of Cas A ($S_{\nu\ line}$), shown as a white rectangle in Figure 7.2(a).

In order to scale this flux measurement, so as to be representative of that from the entire SN remnant, $S_{\nu\ totline}$, a flux density measurement was made in the same region of the SN remnant using an aperture with equivalent area to that in Figure 7.2(a) ($S_{\nu\ knot}$). The ratio of the total SN remnant flux to this derived value could then be used to scale $S_{\nu\ line}$, using Equation 7.1 below:

$$S_{\nu\ totline} = \frac{S_{\nu\ tot}}{S_{\nu\ knot}} S_{\nu\ line} \tag{7.1}$$

Crude estimates could only be made for the 8.28, 12, and 12.13 μm bands using this method. It is difficult to estimate an accurate error for the emission line contribution with the data available. Therefore the error was simply set to be equal to half of the total source flux density measurement error. This error scaling was applied only to the three bands with an emission line component.

The estimated flux contributions from both synchrotron and line emission are contained in Table 7.1. This also contains the thermal dust emission measurements used to construct the Cas A SED. The equivalent flux density measurements, for the foreground cloud are contained in Table 7.2.

7.6.3 SED Determination

The value of flux density derived in each band is plotted in Figure 7.8, for both the SN remnant, and the cloud. Any measurement with a S/N below 3σ was classed as a non-detection, and plotted as a 3σ upper limit (downwards pointing arrows). This applied to the short wavelength measurements (<60 μm) of the cloud only. The absence of flux from the cloud in these bands can

Wavelength (μm)	Emission Component (Jy)			Total Flux Density (Jy)
	Synchrotron	Emission Lines	Thermal Dust	
8.28	1.3	10.9	0.90	13.1 ± 3.7
12	1.7	6.6	28.0	36.3 ± 8.0
12.13	1.7	6.6	30.6	28.9 ± 10
14.65	2.0	...	35.2	37.2 ± 13
21.34	2.6	...	143	146 ± 37
25	2.9	...	226	228 ± 11
60	5.4	...	196	202 ± 37
100	7.9	...	268	276 ± 73
250	15.2	...	180	195 ± 31
360	19.7	...	83.9	103 ± 23
520	25.8	...	35.8	61.6 ± 12

Table 7.1: Flux density emission components from the Cas A SN remnant.

Wavelength (μm)	Flux Density (Jy)	Detection (S/N $\geq 3\sigma$)
8.28	1.48 ± 3.7	No
12	13.2 ± 10	No
12.13	6.26 ± 13	No
14.65	55.3 ± 37	No
21.34	21.5 ± 8.0	No
25	31.7 ± 11	No
60	89.6 ± 28	Yes
100	300 ± 73	Yes
250	184 ± 31	Yes
360	84.3 ± 23	Yes
520	46.6 ± 12	Yes

Table 7.2: Flux density measurements of the foreground cloud.

be seen visually in Figures 7.6(a–f).

These data were fit, using a least squares method, with a modified blackbody curve, denoted as a "greybody" (Equation 7.2):

$$S_\lambda = \Omega\lambda^\beta B(\lambda, T), \tag{7.2}$$

where Ω is a normalisation term depending on the source mass, and $B(\lambda, T)$ is the Planck blackbody function.

The greybody does not assume a source emissivity (ϵ) of 1, as is the case with a blackbody. Here a frequency dependant emissivity is used which follows a power law of the form $\epsilon \propto \lambda^\beta$.

Whilst a good fit could be made to the measurements of the cloud ($\chi^2 < 3$) using a single temperature greybody, it was not possible to achieve an equivalent fit to the Cas A data. This was remedied by performing a two temperature greybody fit, using Equation 7.3 below.

$$S_\lambda = \Omega_h\lambda^\beta B(\lambda, T_h) + \Omega_c\lambda^\beta B(\lambda, T_c) \tag{7.3}$$

where the subscripts h and c denote the hot and cold component parameters respectively. In order to minimise the number of free parameters the same value of β was used for both SEDs, across the full wavelength range. Strickly β would be expected to increase from 1 below 200 μm, to 2 above 200 μm (Hildebrand, 1983), however this variation will be small over the wavelength range used here, and any error should be small in comparison with the current flux density measurement errors. This also replicates the method used by Dunne et al. (2003a) and Morgan et al. (2003) in their analysis.

The final parameters used for the greybody fits are contained in Table 7.3. These fits are shown separately for Cas A, and the cloud, in Figure 7.8.

The temperature of the cold dust component seen in the SED of the Cas A region (Figure 7.8(a), 26.2 ± 3.6 K) is similar to that found by Dunne et al. (2003a) ($18^{+2.6}_{-4.6}$ K). The two temperature component greybody fit also agrees well with the original flux density measurements made by Dunne et al. (2003a), as well as the re-reduced 850 μm measurement of Loinard et al. (2003) (Figure 7.9).

β	SED$_{Cloud}$		SED$_{CasA}$			
	T (K)	χ^2	T_h (K)	T_c (K)	χ^2	Ω_c/Ω_h
0.95 ± 0.48	27.9 ± 2.36	0.5	111 ± 12.9	26.2 ± 3.6	2.1	377

Table 7.3: One and two temperature component greybody fit parameters for the foreground cloud and Cas A respectively.

7.6.4 Mass Estimation

The mass of dust can be derived from the SEDs found in the previous section using Equation 2.12 (Hildebrand, 1983), outlined in Section 2.4.2. The largest uncertainty in a dust mass, derived via this equation, is introduced by the uncertainty in the value of κ. Not only is it difficult to directly measure, it has also been seen to vary with physical environment. The 'typical' value of κ at 850 μm, for dust in the ISM, is often regarded as 0.07 (James et al., 2002). Higher values (0.2–0.8) have been found in regions where the dust may not have experienced a great deal of processing, such as reflection nebulae and dark clouds (Rowan-Robinson et al., 1986; Sopka et al., 1985). Laboratory measurements suggest still higher values, ranging from 0.6–1.1, again at 850 μm (Agladze et al., 1996). This has lead to the supposition that newly formed, or coagulated dust, would have a value of κ higher than that seen in the ISM (Dunne et al., 2003a).

In the dust mass measurements of Cas A made by Dunne et al. (2003a), and also by Morgan et al. (2003) for Kepler's SN remnant, three values of κ were used, 0.76, 0.3, and 0.073. These are mean values at 850 μm, derived from the literature, and represent three measurement cases outlined above. We too have used these values, scaled to the correct frequency by using the value of β derived above, to determine our mass estimates (Table 7.4).

The masses contained in Table 7.4 agree well with those of Dunne et al. (2003a) (0.2–4 $M_{\odot}$). The total dust mass in the direction of Cas A, is approx-

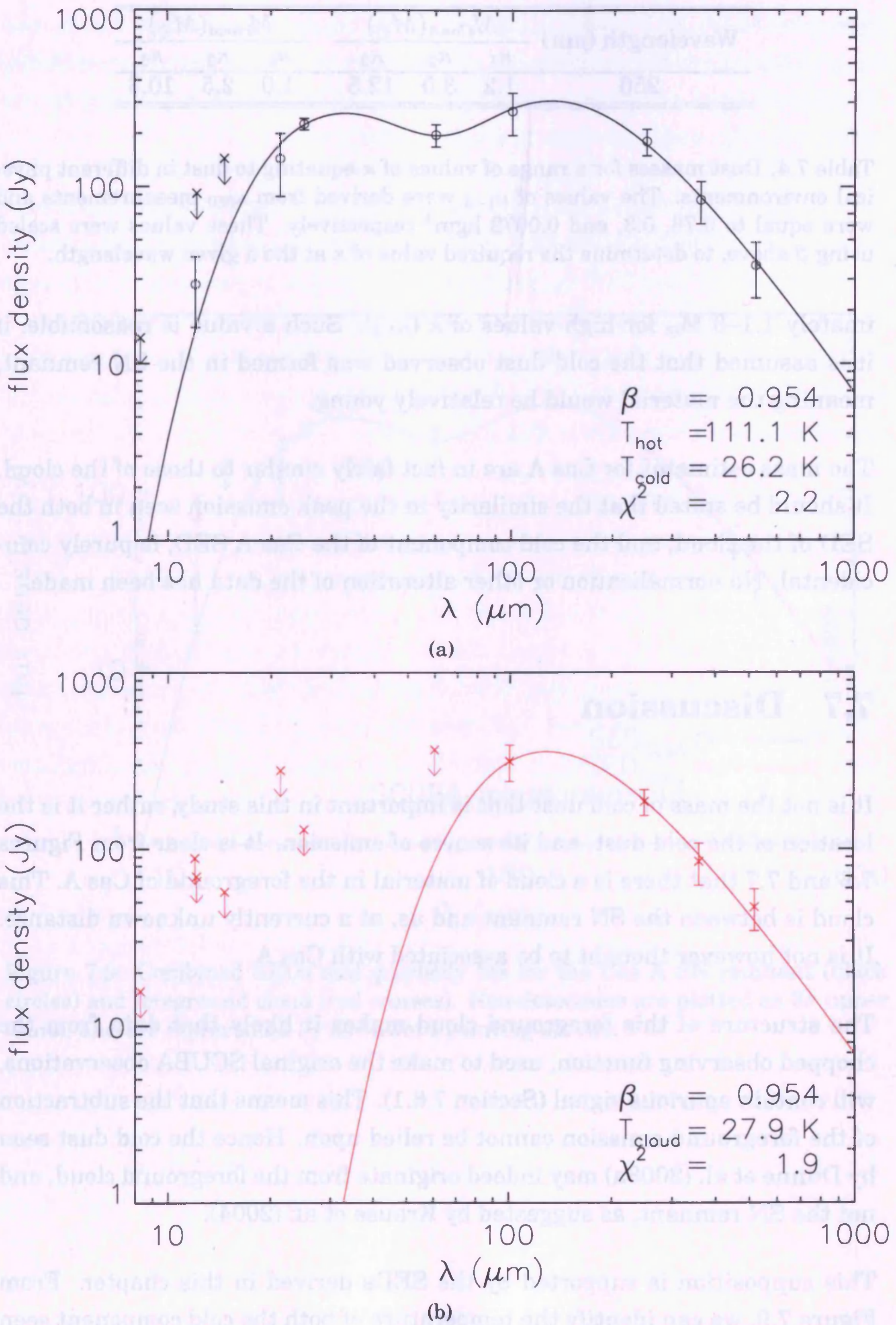

(a)

(b)

Figure 7.8: Derived SED and associated greybody fits for (a) the Cas A SN remnant and (b) the foreground cloud. Non-detections are plotted as 3σ upper limits, and are represented by downward pointing arrows.

Wavelength (μm)	$M_{CasA}(M_\odot)$			$M_{cloud}(M_\odot)$		
	κ_1	κ_2	κ_3	κ_1	κ_2	κ_3
250	1.2	3.0	12.5	1.0	2.5	10.3

Table 7.4: Dust masses for a range of values of κ equating to dust in different physical environments. The values of κ_{1-3} were derived from κ_{850} measurements and were equal to 0.76, 0.3, and 0.0072 kgm^2 respectively. These values were scaled using β above, to determine the required value of κ at the a given wavelength.

imately 1.1–3 M$_\odot$ for high values of κ ($\kappa_{1,2}$). Such a value is reasonable, if it is assumed that the cold dust observed was formed in the SN remnant, meaning the material would be relatively young.

The mass estimates for Cas A are in fact fairly similar to those of the cloud. It should be stated that the similarity in the peak emission seen in both the SED of the cloud, and the cold component of the Cas A SED, is purely coincidental. No normalisation or other alteration of the data has been made.

7.7 Discussion

It is not the mass of cold dust that is important in this study, rather it is the location of the cold dust, and its source of emission. It is clear from Figures 7.6 and 7.7 that there is a cloud of material in the foreground of Cas A. This cloud is between the SN remnant and us, at a currently unknown distance. It is not however thought to be associated with Cas A.

The structure of this foreground cloud makes it likely that data from the chopped observing function, used to make the original SCUBA observations, will contain spurious signal (Section 7.6.1). This means that the subtraction of the foreground emission cannot be relied upon. Hence the cold dust seen by Dunne et al. (2003a) may indeed originate from the foreground cloud, and not the SN remnant, as suggested by Krause et al. (2004).

This supposition is supported by the SEDs derived in this chapter. From Figure 7.9, we can identify the temperature of both the cold component seen

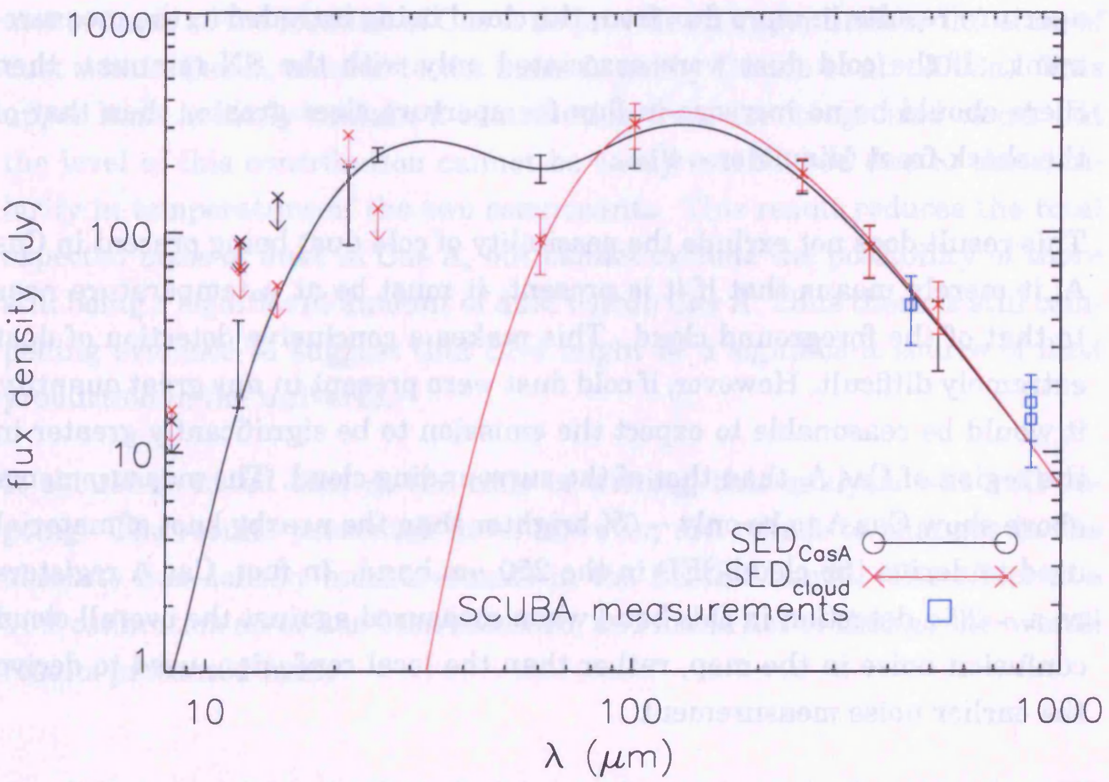

Figure 7.9: Combined SEDs and greybody fits for the Cas A SN remnant (black circles) and foreground cloud (red crosses). Non-detections are plotted as 3σ upper limits, and are represented by downward pointing arrows.

towards Cas A, 27.9±2.4 K, and that of the cloud, well away from the remnant, 26.2±3.6 K. The agreement of these two values strongly suggests that the detection of significant quantities of cold dust in Cas A was due to contamination by emission from the foreground cloud.

The peak of the derived Cas A SED is also greater than that seen by Dunne et al. (2003a) (Figure 7.3). This is a consequence of using a larger aperture than Dunne et al. (2003a), when performing the photometry. The larger aperture results in more flux from the cloud being included in the measurement. If the cold dust were associated only with the SN remnant, then there should be no increase in flux for aperture sizes greater than that of the shock-front (diameter $\sim 4'$).

This result does not exclude the possibility of cold dust being present in Cas A; it merely means that if it is present, it must be at a temperature near to that of the foreground cloud. This makes a conclusive detection of dust extremely difficult. However, if cold dust were present in any great quantity, it would be reasonable to expect the emission to be significantly greater in the region of Cas A, than that of the surrounding cloud. The measurements above show Cas A to be only $\sim$ 6% brighter than the nearby knot of material used to derive the cloud SED in the 250 μm band. In fact, Cas A registers as a $\sim 2.5\sigma$ detection in this band when measured against the overall cloud confusion noise in the map, rather than the local confusion, used to derive the earlier noise measurement.

The presence of a large knot of material, directly at the location of Cas A, would be required to explain these observations, assuming that there is no cold dust in Cas A. It would seem to be extremely improbable that this knot of material should contain the peak emission in the map, exactly at the position of Cas A, and have no contribution from the SN remnant.

Further observations are needed of more SN remnants in order to resolve this issue. Observations with higher angular resolution, such as those achievable with SPIRE and PACS on Herschel, and SCUBA 2 on the JCMT, will allow us to resolve the SN remnants and their foreground structure. This will enable us to further disentangle the two emission sources. SPIRE and PACS observations of SNRs, including Cas A, are currently planned within the SPIRE SAG 6 programme. In addition to improved angular resolution, these instruments will be more sensitive to large and diffuse structure, and will provide data across peak of the cold dust emission.

From these results alone it is difficult to draw a firm conclusion as to absolute mass of dust in Cas A. The main conclusion that can be made, however, is that the temperature of the cloud in the foreground of Cas A is similar to that of any possible cold dust within the remnant. The flux density measurements made at the location of Cas A do provide an upper limit to the mass of dust within Cas A, similar to the mass found by Dunne et al. (2003a). This upper limit is likely contain a contribution from the foreground cloud, but the level of this contribution cannot be easily established due to the similarity in temperature of the two components. This result reduces the total expected mass of dust in Cas A, but cannot exclude the possibility of there still being a significant amount of dust within Cas A. Thus there is still compelling evidence to suggest that SNe might be a significant source of dust production in the universe.

It should be noted that at the time of writing, this analysis was still ongoing. The results presented here, however, are robust to changes in the absolute flux density measurements in the BLAST bands. The effect of a 50% calibration error has been assessed, and found not to change the overall results presented here.

7.8 Chapter Summary

This chapter presented the analysis of observations of the Cas A SN remnant, and surrounding interstellar cloud structure, using all MSX, IRAS, and BLAST bands. Two SEDs were derived, one centred at the location of Cas A, and the other on a knot of material well outside the SN remnant shock front. This knot was assumed to be representative of a molecular cloud in front of the remnant. The Cas A SED was fitted by a two temperature greybody, and the knot SED with a single greybody. The temperature of the Cas A cold component was found to be extremely close to the temperature of the knot, and thus the surrounding dust. Evidence for a substantial quantity of cold dust being present in Cas A has been presented by Dunne et al. (2003a), with the conclusion that this might indicate SNe to be a significant source of cosmic dust. The results presented in this chapter imply that this dust mass measurement may be an upper limit. This is because some of the previously detected material may be associated with the foreground molecular cloud, and not the SN remnant. More samples of other young SN remnants are required to settle this question. Such observations are currently being planned by the SPIRE consortium.

Chapter 8

Simulations of SPIRE Galactic Field Observations

A particularly difficult observational challenge for scanning instruments, such as the SPIRE photometer, is the accurate recovery of the sky brightness distribution on large spatial scales. This is largely due to 1/*f* noise, which has greater power at low frequencies, resulting in long time-scale noise drifts, which ultimately increase the resultant noise level in an observation. Instrumental noise is the limiting source of error within a SPIRE observation, with other instrumental artefacts, such as detector hysteresis and resultant beam smearing, responsivity variation from detector to detector, and on-board filtering being characterised and removed by the data processing pipeline. This can be easily seen by performing a simulated observation with, and without noise. Figure 8.1 contains output maps from such simulations. The maps in the top two panels are the same, and represent the input sky used for both simulations. Once the simulator output had been generated, it was passed through the data pipeline to remove the instrument systematics. The data timelines were then converted to maps, which are shown in the middle two panels in Figure 8.1. The difference between the input and output maps, i.e. the residuals, for both cases are presented in the bottom two panels. It is clear from these maps that the instrumental noise dominates over any residual instrumental artefact. The standard deviation of the residuals in this specific case for the noisy map was found to be three orders of magnitude greater than those of the noiseless map. It is therefore critical that we understand and characterise the nature of the instrumental noise, assess how it might impact observations in terms of the SNR we can expect.

In order to approach the untimate white nosie sensitivity of an instrument, the $1/f$ must be address and where possible removed. Chopping can be used to encode all signal information at a single frequency, and can thus be used to eliminate degradation in sensitivity due to $1/f$ noise by choosing a high enough chop frequency. However this is at the cost of reduced observing efficiency and chopping out of large-scale structure.

In pure scanning observations, sky structure on different spatial scales is encoded at different electrical frequencies in the detector output, with larger scales corresponding to lower frequencies. Such scales are more vulnerable to $1/f$ fluctuations, which impose long-timescale fluctuations on the detector output timelines. In principle, it is desirable to be able to characterise structure on arbitrarily large scales; in practice there will be some limit on the size-scale imposed by the overall $1/f$ noise and the scan rate. Targets with such large scale structure include diffuse emission from galactic star forming clouds, circumstellar dust shells, and cirrus clouds.

In the case of ground-based instruments, such faint extended emission is difficult to measure due to a high level of atmospheric fluctuations and the consequent need to chop. Space-borne observatories such as those on Herschel and Planck will have a natural advantage in this respect, in addition to their superior sensitivity and wavelength coverage. However they will still be limited in their ability to measure large-scale emission by an inevitable level of low frequency noise associated with the detectors and other elements within the observing system. Planck minimses these errors by spinning the telescope while observing. This means that the same point of sky is revisited by Planck on a time scale of about a minute. This is below the $1/f$ noise timescale of the instruments, therefore any drift from the mean sky value can be removed.

It is important to understand the limitations on the recovery of the sky brightness distribution imposed by $1/f$ noise, to ensure that the observing

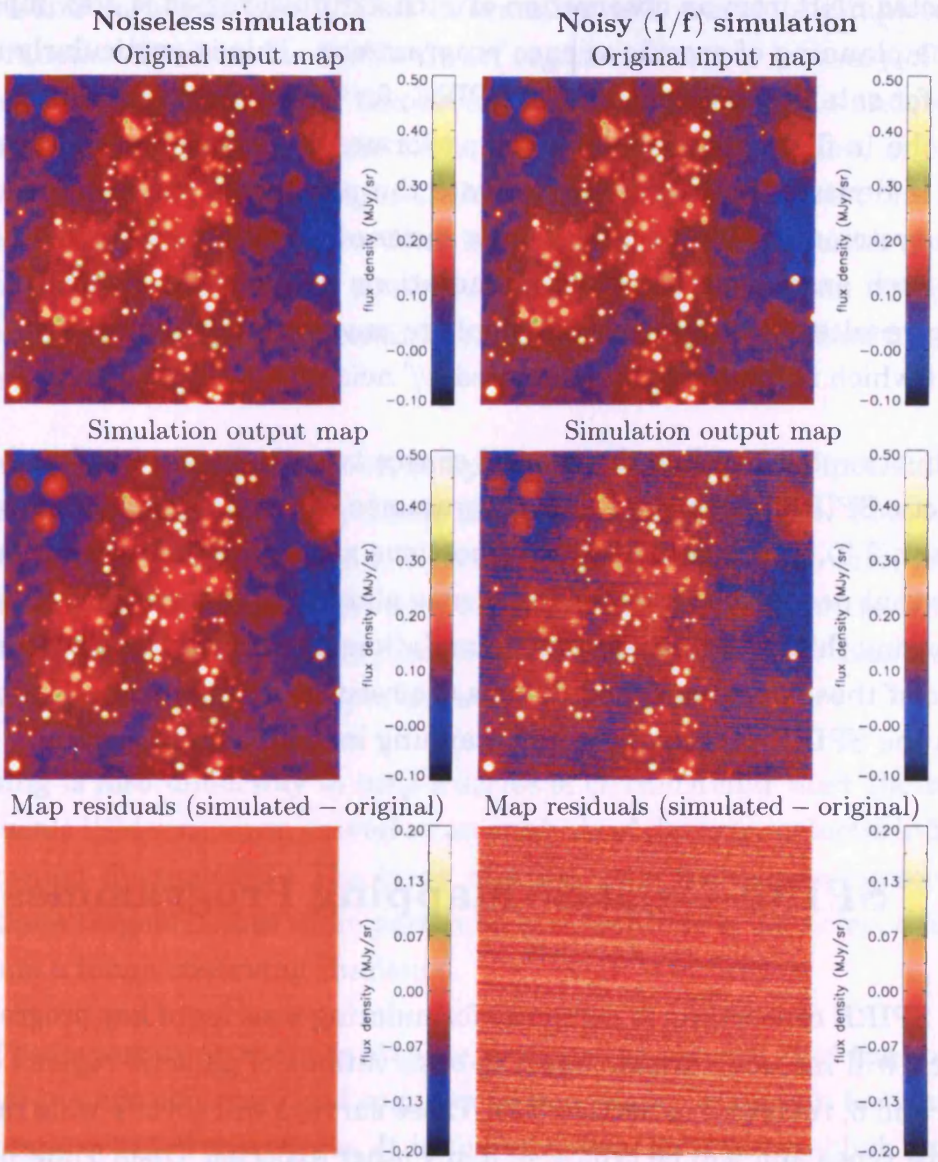

Noiseless simulation

Noisy (1/f) simulation

Original input map

Original input map

Simulation output map

Simulation output map

Map residuals (simulated – original)

Map residuals (simulated – original)

Figure 8.1: Sample noiseless (left) and noisy (right) simulated galactic field observations. Simulated output maps are shown in the middle panals, and the residuals of the input-output maps are shown in the bottom panals. Note, the cut levels in first four panels have been set such that they show large and small scale structure. Consequently the scale shown does not represent the full range of flux density. As a result some compact sources are saturated in this image. The brightest source in the image is ~10 MJy/sr.

modes and integration times are optimised, and that the analysis methods to be used are well matched to the data. A thorough understanding of the expected SNR from an observation of such a diffuse region is also important in the planning of specific science programmes. This is particularly important for satellite instruments like SPIRE, for which observing time is costly and the in-flight time available for performance verification and optimisation is limited. In order to investigate the parameter space influenced by such systematics, I have carried out a series of investigations using the SPS. Although some aspects of these simulations are particular to SPIRE, the main results of this analysis will apply to any scanning photometric instrument which is limited by uncorrelated 1/*f* noise.

In this chapter I outline the general source types to be observed within the galactic SPIRE guaranteed time programmes (SAGs 3, 4, and 6, reviewed in Section 3.3), and identify the key questions relating to instrument systematics that need to be answered in order to plan these observations efficiently. Following this, I outline a series of simulations performed in order to answer some of these questions, and discuss the results, and their implications for both the SPIRE programmes, and scanning instruments in general.

8.1 SPIRE Galactic Mapping Programmes

The SPIRE consortium is currently formulating a series of key programmes which will include various mapping observations of galactic regions (SAGs 3, 4, and 6, reviewed in Section 3.3). These surveys will cover a wide range of source types and will be typical of many other expected 'Open Time' observing programmes. The varied scientific goals will require accurate recovery of point-like or compact sources, such as embedded objects and star-forming cores, more extended sources such as circumstellar dust shells and supernova remnants, and the very extended structure in molecular clouds. The latter will pose the greatest challenge for the recovery of large-scale brightness structure.

As part of the SAG 3 investigation into the early stages of star formation, a census of prestellar condensations and young Class 0 protostars, down to a mass limit of 0.01 $M_\odot$ will be made in nearby molecular cloud complexes (André and Saraceno, 2005). This information will provide a complete core mass function down to the brown dwarf regime. Accurate recovery of these sources over the full range of flux levels is essential in order to understand the mechanisms involved in the earliest stages of star formation, in particular to understanding the origin of the stellar initial mass function (IMF). Current data for the core mass function shows it to have a similar slope to that of the IMF (Motte et al., 2001; Nutter and Ward-Thompson, 2007), and hence is important in the determination of the early stages of cloud fragmentation and collapse.

In addition to the need to extract compact sources, it is also of interest to be able to recover the radial brightness profiles of prestellar cores. This can be used to obtain the density and temperature profiles within the core, providing information to test current core collapse models. The limit to which a radial profile can be accurately recovered, in the presence of $1/f$ noise, and a confused environment, is not yet known.

Planning is also underway to map a series of circumstellar dust shells and large-scale ISM structure, as well as an analysis of the extragalactic infrared background fluctuations. The large angular scale fluctuations associated with these targets makes them particularly susceptible to $1/f$ noise, and this presents a tough observing challenge.

It will be important in the case of these, and similar surveys, that the goals of both large scale structure and compact source science cases can be achieved in a single set of observations. It is therefore essential to establish the impact of telescope and instrument systematics on each case and optimise the final observing strategy accordingly. To this end I have identified the following set of key questions relating specifically to the observation of galactic targets:

1. What are the limitations and effects of $1/f$ noise on the accuracy of recovery of large-scale structure?
2. How does the simultaneous presence of $1/f$ noise and diffuse cirrus

limit the detection of compact sources?

3. What is the impact of 1/*f* noise on our ability to reconstruct the radial profiles of compact cores?

8.2 Simulations

A series of simulations was performed in order to address the questions set out above. The initial set of simulations was aimed at answering the first question: to assess, in a general way, the effect of 1/*f* noise on the ability to recover structure of an arbitrary scale. These simulations were first performed in a simple one dimensional case, followed by a more realistic 2D study of simple Gaussian sources. The next stage dealt with noise-only maps, which represent a real life observing situation with no prior source information. These results were then applied to the case of compact sources in the presence of a diffuse cirrus cloud structure, in order to address the second key question. A final set of simulated observations, was then created, and the recovery of an input radial core profile assessed. These simulations tackle the last key question.

The SPIRE scan-map mode without chopping (POF 5, see Section 3.2) was used for all simulations. In order to establish the fundamental limits on data quality imposed by unavoidable 1/*f* noise from the detectors themselves, various simplifications were introduced: no common mode noise or pointing errors were included; the detectors in a given array were taken to be identical (perfect flat-fielding); and there were no correlated thermal drifts, cross-talk or glitches. Whilst these conditions are not fully representative of the real system performance, they do allow us to investigate the consequence of 1/*f* noise alone. Other noise effects may also reduce the data quality, but these will act as a scaling upon the results presented here.

The noise timeline imposed on each detector was unique, but generated using the same noise spectrum (noise voltage spectral density, e_n, and 1/*f* noise knee frequency, f_k). This represents uncorrelated noise within each detector channel arising from independent detectors and their readouts.

The simulated time ordered data were converted to a map using a simple flux binning method to produce a 'naïve' map. This method assigns a value to a map pixel equal to the mean value of all data counts falling within that pixel (see Section 5.3). This was used to provide a baseline result, against which the improvement resulting from more sophisticated data analysis methods could be compared.

To quantify the effect of 1/*f* noise, the achieved SNR for a source in the presence of 1/*f* noise is quoted as a fraction of the SNR from an equivalent white noise observation. This is referred to as the SNR loss factor (SNR_{lf}) and is given in Equation 8.1. This method of evaluation is like that used in Chapter 6.

$$SNR\,loss\,factor = \frac{SNR_{1/f}}{SNR_{white}}, \tag{8.1}$$

where $SNR_{1/f}$ is the SNR in an observation containing 1/*f* noise, and SNR_{white} is the SNR of the same observation in the white noise case. This allows us to quantify the sensitivity degradation due to 1/*f* noise, independent of the integration time and source flux density.

The degradation of SNR in the presence of 1/*f* depends on the 1/*f* noise knee frequency, f_k, the telescope scan rate, $\dot{\theta}$, and the beam-convolved source size scale, λ. Together, f_k and $\dot{\theta}$ determine the spatial frequency scale in the map corresponding to the 1/*f* knee frequency ($f_s = f_k/\dot{\theta}$). The equivalent angular size scale is $\lambda_s = 1/f_s$. Crudely, the SNR of a source close to or greater than this scale, observed in the presence of 1/*f* noise, will be significantly reduced.

It is convenient to define a new variable, ψ, in the following way:

$$\psi = \frac{f_k}{\dot{\theta}}\sqrt{\lambda}. \tag{8.2}$$

This combines all the information from the three related variables into a single parameter. The impact of 1/*f* noise is influenced by all three parameters and identical results can be achieved for a range of source scales and scan rates for a given 1/*f* noise knee frequency. A single scalable plot can be derived which is capable of representing any combination of the dependent parameters. The form of Equation 8.2 is explained in Section 8.4 below, in which a general analysis is presented (applicable to any scanning instrument which is affected by uncorrelated 1/f noise). In this analysis, the sensitivity is characterised as a function of the parameter ψ, and the results can be used to determine the effective sensitivity as a function of any one of the key parameters, keeping the other parameters constant.

8.2.1 1D Simulations

In order to characterise the influence of 1/f noise on observations of large-scale structure in the most general case, an initial simple one dimensional study was performed. Here a single detector was scanned once across a 1D Gaussian source characterised by its width and brightness. A 1/f noise timeline was then added to the resulting detector voltage time series. Three Gaussian source sizes were explored varying from a beam convolved width equal to 1, 1.5, and 2.0 times the beam FWHM. The SPIRE 250 μm band with a size of 16.2$''$ was used for this study, but the results can be parameterised in a straightforward way to an arbitrary beam size (see Equation 8.2).

For computational convenience, the scan rate was kept constant at 25$''$s^{-1}, and a range of 1/f knee frequencies from 0 Hz (white) to 2 Hz was explored. Five hundred simulations were performed for each value of f_k, and a Gaussian fit made to each. For the amplitude of the Gaussian, the ideal (noiseless) result is for the fitted amplitude to be equal to the amplitude of the beam-convolved source. The reciprocal of the standard deviation of the input:output amplitude ratio from unity is adopted as a measure of the SNR.

In addition to a variety of knee frequencies and source sizes, various baseline lengths were also used in the fitting of the Gaussian curve. Thus an optimum baseline was found for a given value of f_k.

8.2.2 2D Simulations

The 1-D simulations were then extended to the case of two dimensional maps. As with the 1-D case, the input skies used in the simulations were a set of simple 2D 'toy' skies containing isolated Gaussian sources of varying full width half maximum (FWHM) with zero background. A range of Gaussian sources with beam-convolved sizes up to 10 beam FWHM was used. These represent astronomical signals spanning a range of spatial scales, and allowed for a straightforward evaluation of the ability of any scanning system to extract extended source structure in the presence of $1/f$ noise. The simplicity of this input sky provides a representative general result applicable to all science cases.

Five hundred maps were again created for each λ and f_k combination. The data from each detector time series were then used to produce a naïve map as described in Chapter 5. The same assessment of the data as in the 1-D case was carried out, this time fitting a Gaussian surface.

8.2.3 Noise Map Simulations

Next, a series of tests was performed using a blank input sky. Noise maps were produced with a range of pixel sizes. The reciprocal of the standard deviation of the map pixels was then taken as the SNR for sources of that pixel size. This was then compared with the white noise case to obtain a SNR loss factor as before.

To make this analysis equivalent to the 2D case above, the source scale, defined by the map pixel size, must be scaled by a factor of $1/\sqrt{2}$. This results in a scale size which contains 1/2 of the total pixel flux, equivalent to the FWHM scaling used in the 2D case.

8.2.4 Radial Profile Simulations

Finally, the SPS was used to simulate eight observations of a synthetic sky, populated with 36 critical BESs (Section 2.3.3), with a FWHM size of 5 PSW beams. Two scans were performed for each simulation with perpendicular scan angles, as defined in Chapter 6. Each simulation contained a different value of f_k, ranging from 0 (white) to 2 Hz (severe $1/f$).

It is likely that cores with a wide range of widths will be observed, from point-like to many beams in scale. The width of the spheres used in these simulations is representative of a realistic BES located at the distance of the Orion nebula.

The radial profile extraction routine 'ELPROF' by Currie and Berry (2001) was used to construct the radial profiles from the simulated output maps. The program bins the pixels in a map into a series of concentric elliptical or circular annuli. The mean pixel value in each annulus is then returned, giving the radial profile. It was assumed that the source location was known perfectly, and that the source was circular.

A χ^2 test, used to measure how well a particular hypothesis matches the data, in this case how well the radial profile data match the input model, was used to assess the results. The χ^2 statistic with k free parameters has the following distribution,

$$\chi^2 = \sum_{i=0}^{k} \left(\frac{X_i - \mu_i}{\sigma_i} \right)^2, \tag{8.3}$$

where X_i are the data, μ_i is the mean value of X_i, and σ is the standard deviation of the data. A certain value of the reduced χ^2 relates to a specific probability that the data match the model, given a certain number of free parameters (measurements).

The output χ^2 values were normalised with respect to the white noise case, and a χ^2 gain factor, χ^2_{gf}, was deduced for each value of f_k. This is the factor by which χ^2 is increased with respect to χ^2 value obtained in an observation containing only white noise.

8.3 Results

8.3.1 1D Simulations

The simple 1-D case represents the highest achievable sensitivity for a given integration time as the signal is concentrated in one timeline. No co-addition of multiple independent detector timelines is required, which would degrade the SNR in proportion to the square root of the number of scans. Figure 8.2 shows the SNR loss factor as a function of f_k and ψ. As expected the SNR loss gets worse (i.e. the value of SNR_{lf} decreases) with increasing f_k. Figure 8.2(a) also illustrates the increased degradation in SNR as a function of λ. Figure 8.2(b) shows the same data scaled and plotted against the ψ parameter. All three cases are now described by a single curve. To avoid a loss of SNR (compared to the white noise case) of more than 30 %, ψ must be made less than about 0.04 Hz$^{1/2}$. For example, this would equate to a maximum convolved source size of 144$''$ when observed with the nominal SPIRE scan rate and f_k of 30$''$/s and 100 mHz respectively ($\lambda_s = 300''$).

8.3.2 2D Simulations

Initial tests showed there to be no significant variation in SNR when the map size, analogous to the baseline in the 1D case, was varied. This is because while in the 1D case the baseline was determined using a single correlated timeline, and thus was affected by long-term 1/f drifts, the 2D case uses multiple time series, across which (perpendicular to the scan direction) these fluctuations are averaged out.

As in the 1D case, the results demonstrate increased losses when observing sources with greater values of f_k or source scale, as shown in Figure 8.3(a). This figure plots the SNR loss factor as a function of f_k for a variety of source size scales. Figure 8.3(b) shows these results plotted as a function of ψ, with all cases now described by a single curve as in the 1D case. This represents a general result, applicable to any combination of f_k, λ and $\dot{\theta}$.

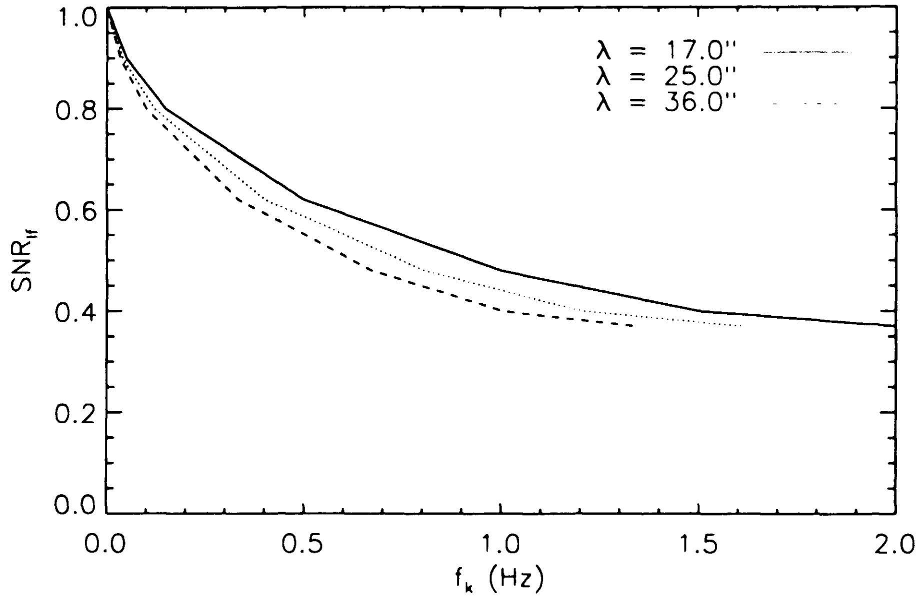

(a)

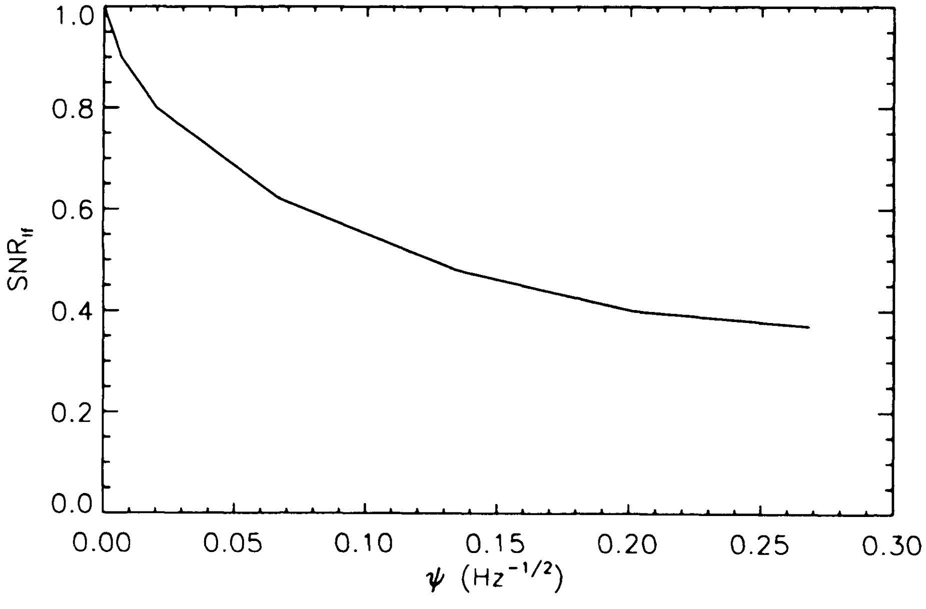

(b)

Figure 8.2: (a) SNR loss factor as a function of f_k (Hz) – 1D case; (b) SNR loss factor as a function of the ψ parameter – 1D case

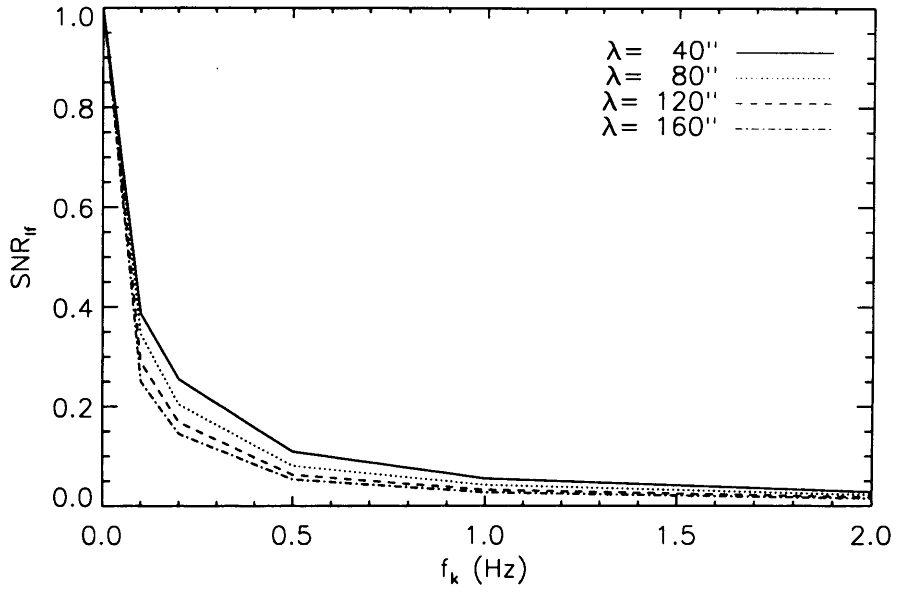

(a)

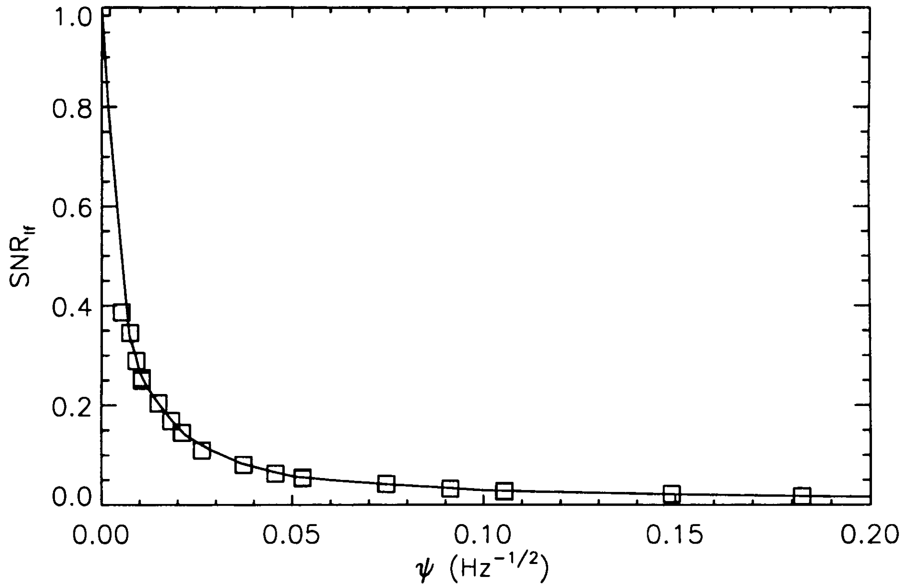

(b)

Figure 8.3: (a) SNR loss factor as a function of f_k for a variety of source size scales, with a fixed scan rate of 30″/s; (b) SNR loss factor as a function of ψ.

Figure 8.3(b) shows significantly increased losses compared with the 1D case. For example, using the same nominal SPIRE value for λ_s as in the 1D case, and the criterion of no more than 30% loss in sensitivity with respect to the white noise case ($\psi \leq 4 \times 10^{-3}$ Hz^{-1}), the maximum observable convolved source scale is 1.4″. This corresponds to a scale significantly smaller than the beam, meaning that not even a point source can be observed without significant degradation due to 1/*f* noise. The increased losses occur due to the added noise arising from the combination and fitting to multiple uncorrelated detector noise timelines.

8.3.3 Noise Map Simulations

The results of investigations carried out using a blank input sky (noise maps) are shown in Figure 8.4 and agree well with those seen in the 2D study. The output maps in this case, as in the previous 2D case, are simple naïve maps. No baseline adjustments have been made, nor have the data been altered in any other way. This analysis is unbiased in that it does not assume any prior information regarding the source shape or structure. The agreement between this and the previous 2D case is sufficient to validate the earlier simplified investigations as useful in a real-world situation.

8.3.4 Radial Profile Simulations

The χ^2 gain factor as a function of ψ for radial profile fitting to a prestellar core is shown in Figure 8.5. The gain factor increases with increased ψ, meaning that the hypothesis becomes less certain. Therefore, at the nominal SPIRE scan rate of $30''s^{-1}$, with the nominal detector f_k of 100 mHz, and observing a source of 4 PSW beams in width (i.e. $\psi \simeq 0.025$), the χ^2 gain factor will be $\sim$ 10. So for a sample radial profile measurement with 5 free parameters and a χ^2 value of 0.55, this equates to a drop in the probability of the data matching the model, of $\sim$ 60%, dropping from 0.99, to ~0.4. However, scanning at a rate of $60''s^{-1}$ would reduce the decrease in probability to only $\sim$ 9%, from 0.99 to 0.9.

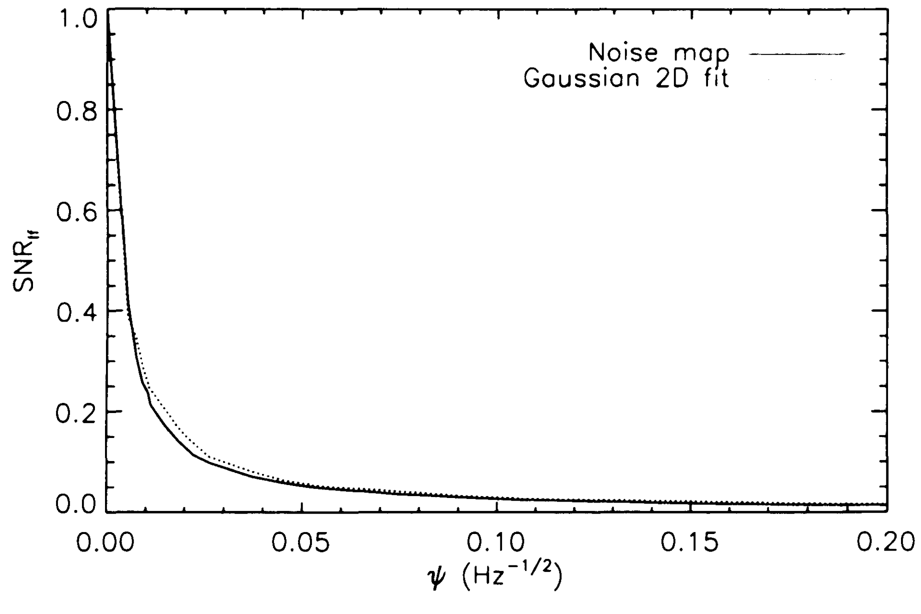

Figure 8.4: SNR loss factor as a function of ψ, as derived using noise maps containing various levels of $1/f$ noise and map pixelisation. Also shown for comparison is the equivalent curve for the 2D Gaussian fitting case.

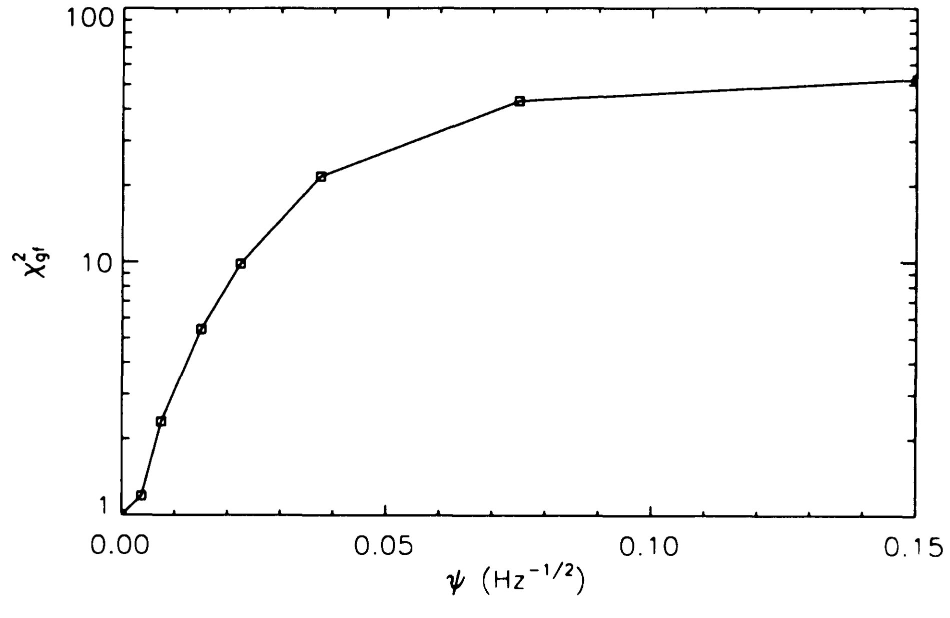

Figure 8.5: χ^2 gain factor as a function of ψ, for radial profile fitting to a prestellar core. In this specific case the model used was a critical BES.

8.4 Discussion

8.4.1 Large Scale Structure

A series of many simulations was used to derive the noise level in the above tests requiring many repeat observations of the source. This is generally not possible in real life, and in many cases the noise is simply derived from the standard deviation of some empty region of the map, and assumed to be constant throughout. However, this method is only applicable in the presence of white noise. Also, in doing this it is implicitly assumed that there is no dependence of SNR_{lf} with source scale, which is not true. Correlations within the 1/*f* noise result in the $\sqrt{\lambda}$ dependence seen in Equation 8.2. Any form of correlation (including those introduced in many instruments by on-board filters) will result in a source size dependence, and will generally cause an over-estimate of the SNR. An example of this can be seen in Figure 8.6, which shows SNR_{lf} curves derived using the above Monte Carlo Gaussian fitting method, and from the matched filtering method described in Chapter 5, which assumes white noise. The matched filtering method uses knowledge of the source shape in order to weight the data, and thus derive the optimal SNR. These curves were generated using the data set from the 2D study above. The figure contains four curves, representing different source scales, for each method. The overlap of the curves in the matched filtering case demonstrates the apparent, and erroneous scale independence of the white noise assumption method.

The increased losses in SNR seen in the 2D cases over the 1D case are large; however it is possible to improve significantly on these losses by applying various data reduction methods during the map-making stages. Adjustments can be made in an attempt to reduce the effects of 1/*f* noise drifts, such as median filtering, high-pass filtering, and baseline subtraction. All such filtering methods destroy some information in their implementation, and require assumptions to be made regarding the maximum source scale present in the data. Consequently these methods are of limited use when measuring large-scale structure, but they can be effective when the target source is known to be point-like or small, i.e. a source with relatively little

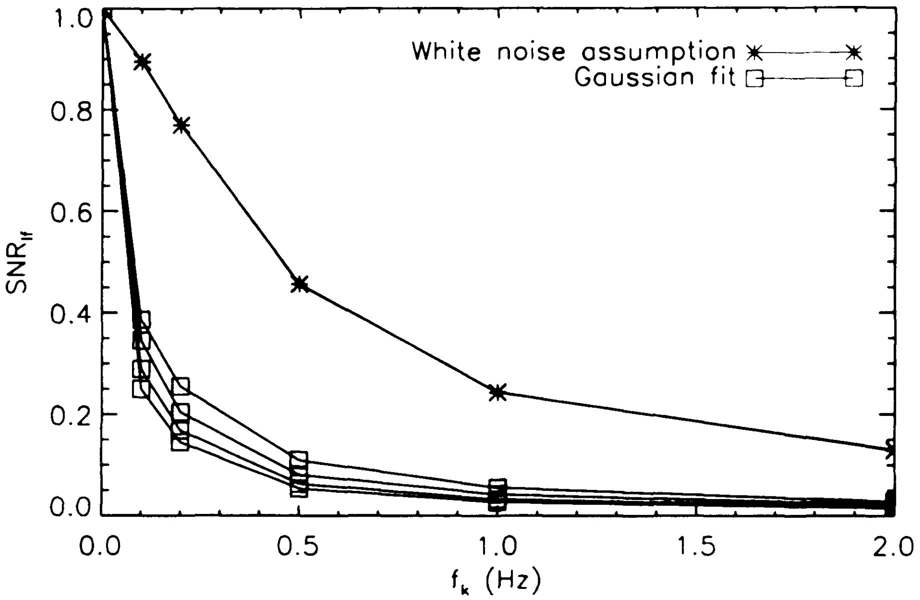

Figure 8.6: SNR_{lf} as a function of f_k for a range of values of λ, as calculated using two different SNR methods. The first fits a Gaussian to the map as discussed in Section 8.3.2 (open boxes); the second assumes Gaussian white noise and uses a matched filter approach (stars), as described in Section 5.4.1. The results from all four sources sizes are plotted for both methods, but overlap in the case of the second method.

low frequency structure (Haig et al., 2004; Waskett et al., 2006). Examples of naïve maps, and the equivalent high-pass filtered maps are shown in Figures 8.7 and 8.8. The degradation in the peak signal can be seen in the filtered maps in comparison with that of the naïve maps.

Another technique to reduce the effects of 1/*f* noise is based on establishing the power spectrum of the 1/*f* noise within an observation. This information is then used to estimate and remove the noise correlations in the output map (see Section 5.3). This method is widely used by cosmic microwave background (CMB) experimenters (Poutanen et al., 2006; Tegmark, 1997), who are interested in a wide range of scales on the sky. It produces a maximum likelihood map and does not require any prior assumptions about the data. This method also does not result in the ringing artefacts, often seen when using the previous filtering techniques.

Both approaches are often used in data reduction. In order to assess the relative improvement presented by each method, the 2D tests were repeated using high-pass filtered, and maximum likelihood maps as inputs.

A high-pass filter with a four PSW beam ($\sim 65''$) cut-off was applied to the time ordered data, filtering the data in the scan direction. The maximum likelihood maps were generated by directly solving the generalised least squares formula, Equation 5.3 (Section 5.3). In order to employ this method a cross-linked observation is required. The performance of this method is a function of the scan pattern implemented; a greater level of cross-linking will improve its ability to remove 1/*f* drifts. In these simulations, two perpendicular Boustrophedon scan patterns were implemented (Figure 3.8). A small 30×30 pixel map was produced using one detector for computational efficiency. The corresponding data redundancy is representative of the typical level of cross-linking available when observing with an observatory such as Herschel, which does not have scope for complicated scanning patterns due to telescope control limitations. As before, the noise was kept stationary for these tests. A model noise covariance matrix was derived from the mean of many independently generated matrices. An inferior noise covariance matrix will result in a greater rate of SNR loss with increasing ψ. This may occur if there are limited data from which to derive the matrix. Conversely, greater cross-linking within the observation may reduce the rate of SNR loss with increasing ψ. The result presented by this analysis shows the improvement in data quality achieved with this method, even in this simple example. Examples of the maps produced by both methods are shown, in comparison with their naïve map equivalents, containing various levels of f_k, in Figures 8.7, 8.8, 8.9 and 8.10.

The results from these treatments of the data, along with the naïve 2D case are shown in a generalised plot in Figure 8.11. In addition, the 1D result is shown for comparison. The maximum likelihood results are clearly superior to both the naïve and filtered cases.

Using again the criterion of no more than 30% loss of sensitivity with respect to the white noise case, and a λ_s of 300″, the maximum convolved source size scales for the naïve, filtered, and maximum likelihood maps are 1.4″, 9″, and 110″ respectively. It should be noted that any frequency dependent system component, such as a filter, must be considered in conjunction with these results. Some systems for example include a high-pass filter, which will suppress both 1/*f* noise and large scale signals. In this case these results will be less applicable.

8.4.2 Limiting Source Flux in a Confused Environment

Every astronomical survey has a limiting sensitivity, below which sources cannot be readily identified. This limiting sensitivity relates to a limiting SNR within the map. Often this level is set with respect to the confusion noise (see Section 2.4.3) level within the region; e.g., for a survey with a minimum source detection threshold of 10σ, the limiting SNR would be 10 times the confusion noise level. In practice however, it is not possible to reach this level as there will always be some residual instrumental noise in the data. The results from Section 8.4.1 have been used to investigate the limiting SNR achievable with a survey, given a range of f_k, $\dot{\theta}$, λ, and confusion noise level (σ_{conf}) parameters.

Initially, the limiting flux was derived for a white noise survey over a range

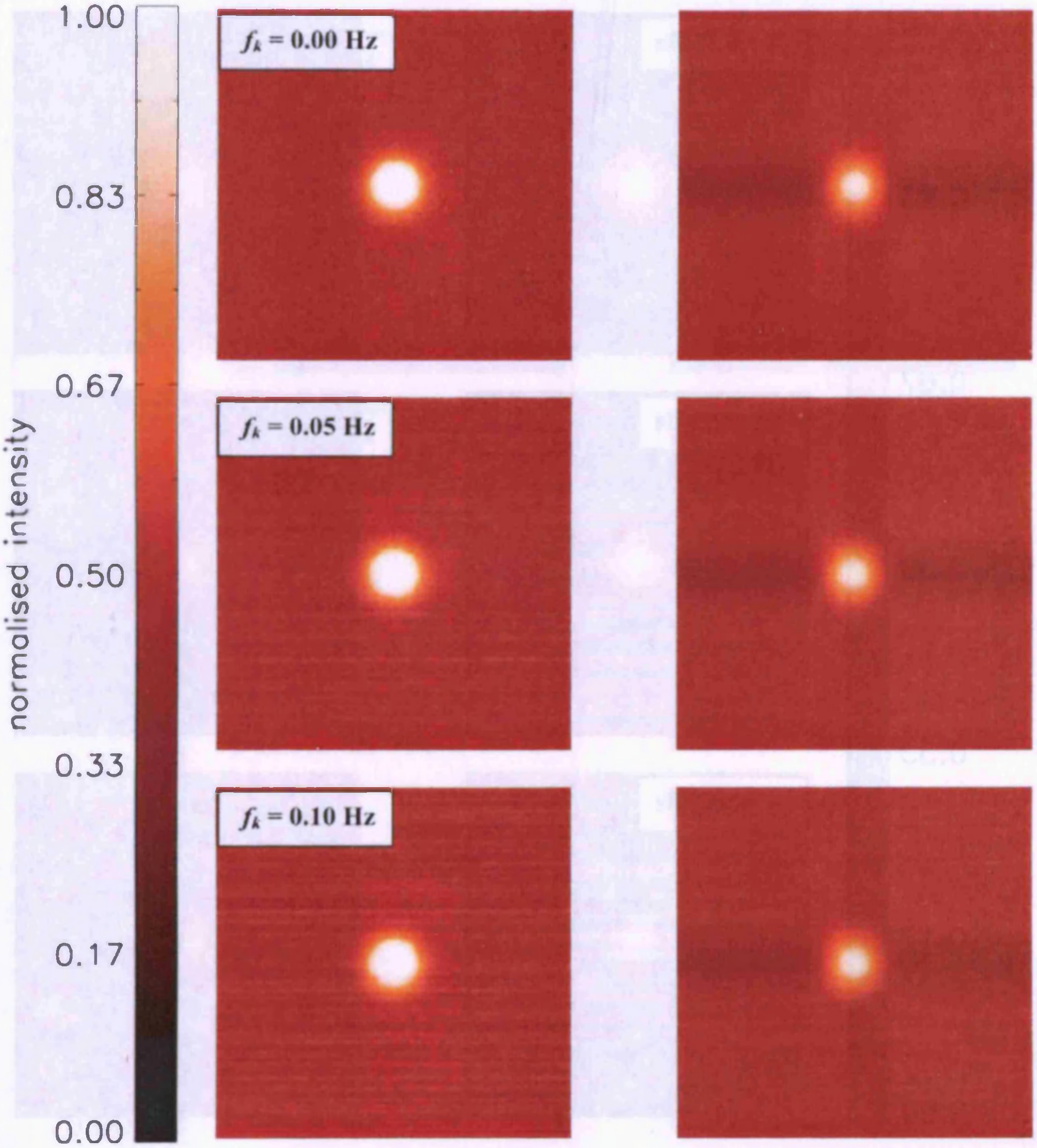

Figure 8.7: Sample simulations of a single Gaussian source, observed with $f_k = 0.0$–0.1. Naïve maps, left, and simple high-pass filtered maps are shown for comparison. All maps are equally scaled.

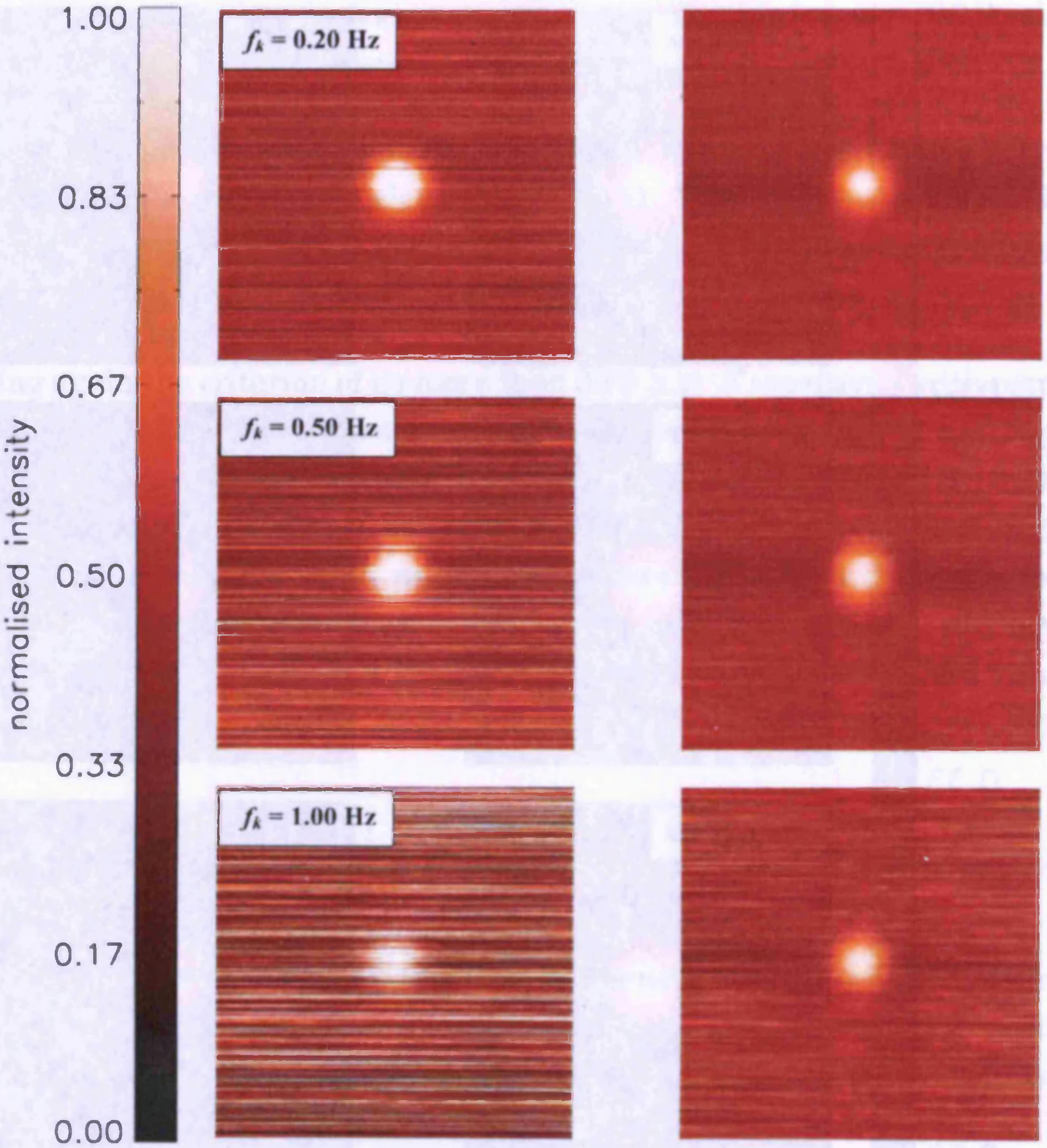

Figure 8.8: Sample simulations of a single Gaussian source, observed with f_k = 0.2–1.0. Naive maps, left, and maximum likelihood maps are shown for comparison. All maps are equally scaled.

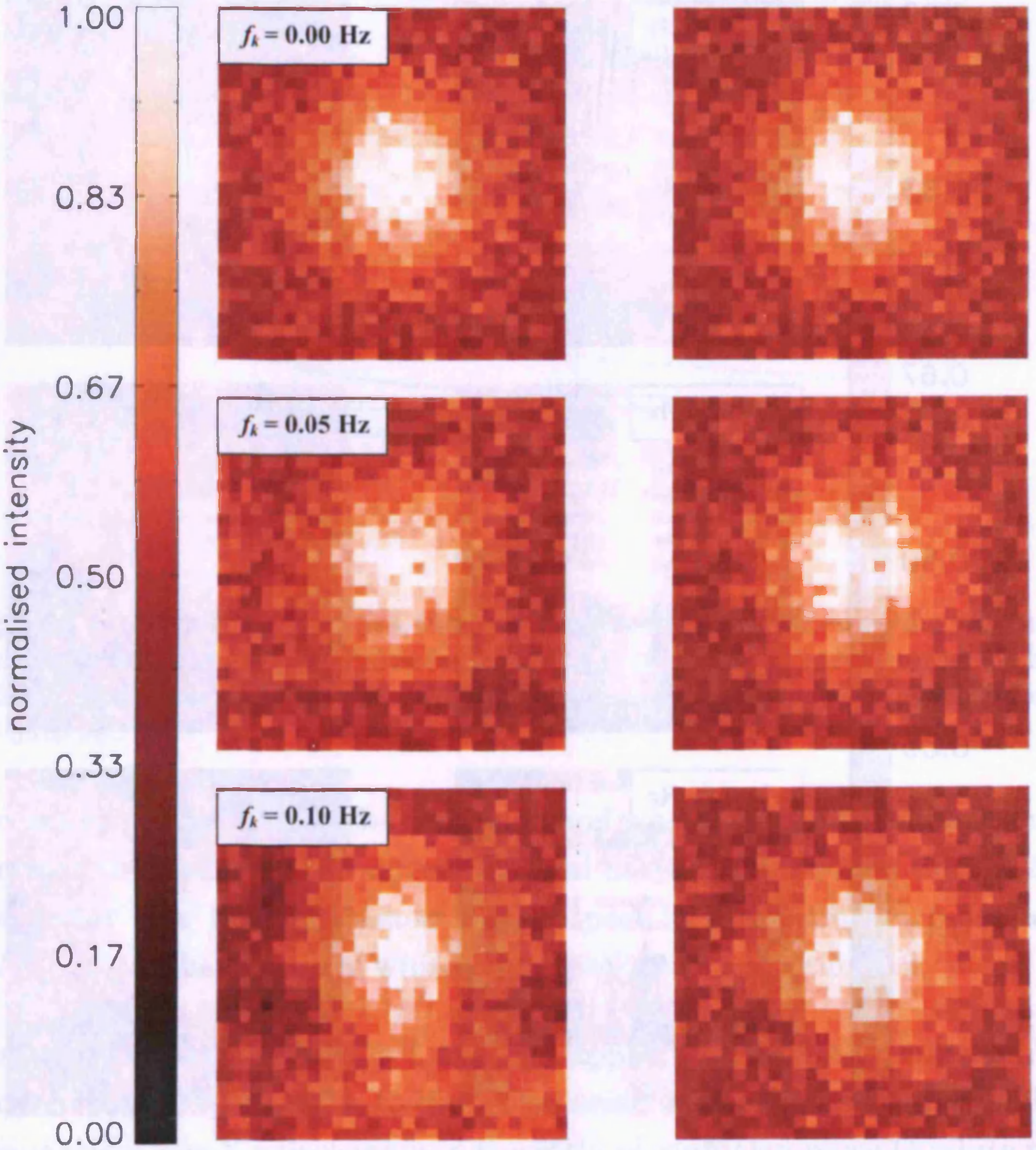

Figure 8.9: Sample simulations of a single Gaussian source, observed with $f_k = 0.2$–1.0. Naïve maps, left, and simple high-pass filtered maps are shown for comparison. All maps are equally scaled.

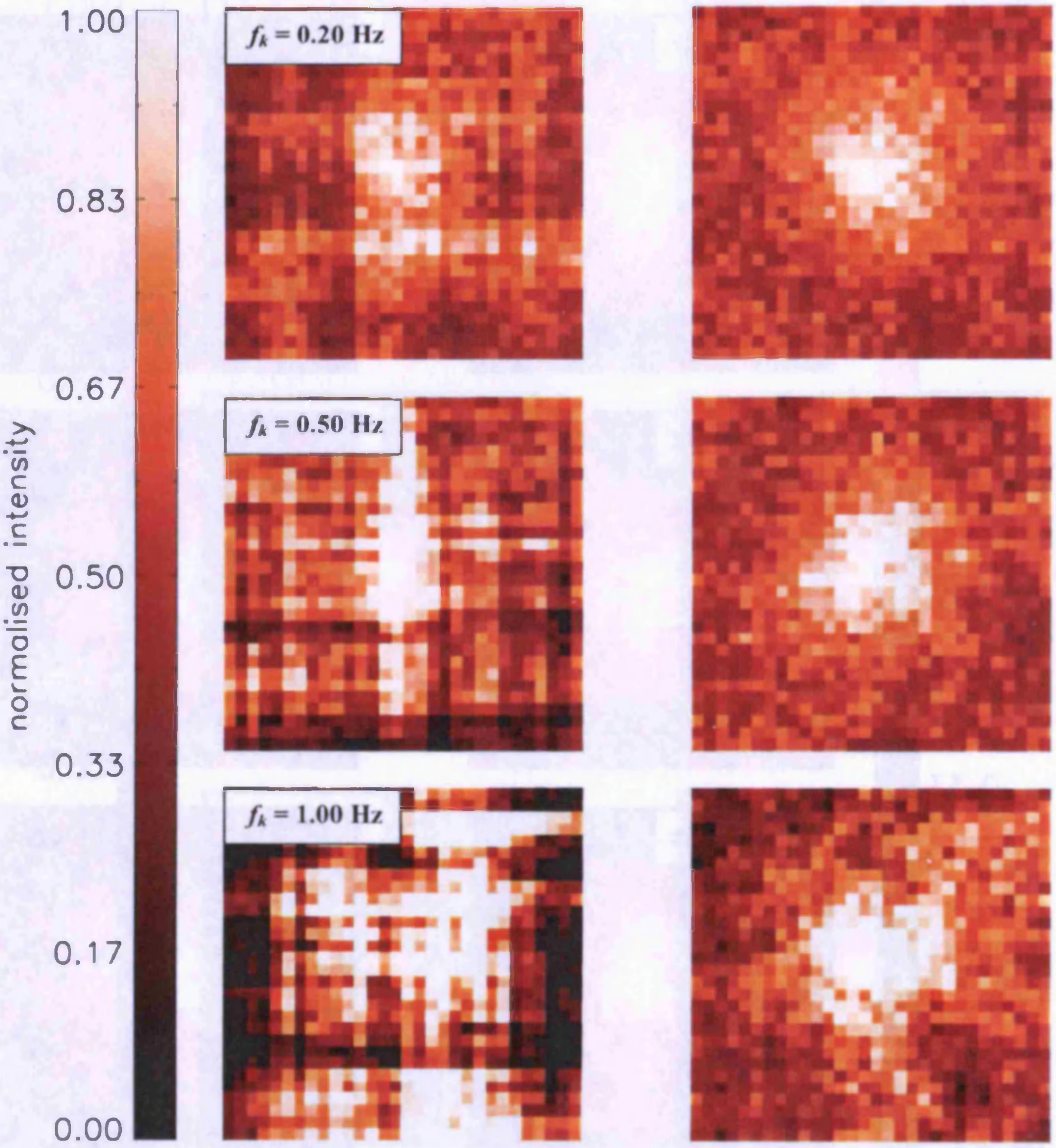

Figure 8.10: Sample simulations of a single Gaussian source, observed with $f_k = 0.2 - 1.0$. Naïve maps, left, and simple high-pass filtered maps are shown for comparison. All maps are equally scaled.

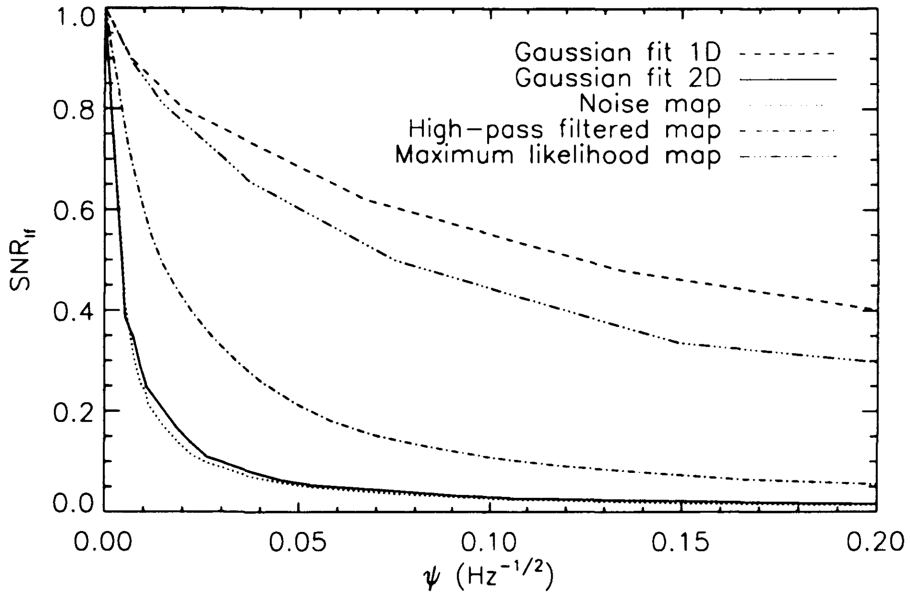

Figure 8.11: SNR loss factor as a function of ψ for data generated in the 2D and 1D studies above. Results from naïve (standard 2D result), high-pass filtered (10 beam cut-off), and maximum likelihood map treatments of the data are presented for the 2D data set.

of confusion noise levels. The confusion and white instrumental noises were summed in quadrature to derive the total noise in the observation. A SNR loss factor was then calculated with respect to the confusion noise level, $SNR_{lf\ conf}$, rather than the white noise level used in Section 8.2.

The losses derived in Section 8.4.1 were applied, using the maximum likelihood method (Figure 8.11), to the white noise values for a range of 1/*f* knee frequencies. The X-axis remained the ratio of confusion noise to white noise level (Figure 8.12). The Y-axis in Figure 8.12 effectively represents the decrease in sensitivity due to instrumental white and 1/*f* noise as compared to the confusion noise alone.

Many observations are planned to achieve an instrumental white noise level equivalent to the confusion noise ($\sigma_{conf}/\sigma_{inst} = 1$). This is referred to as a confusion noise limited observation, and is represented in Figure 8.12 by

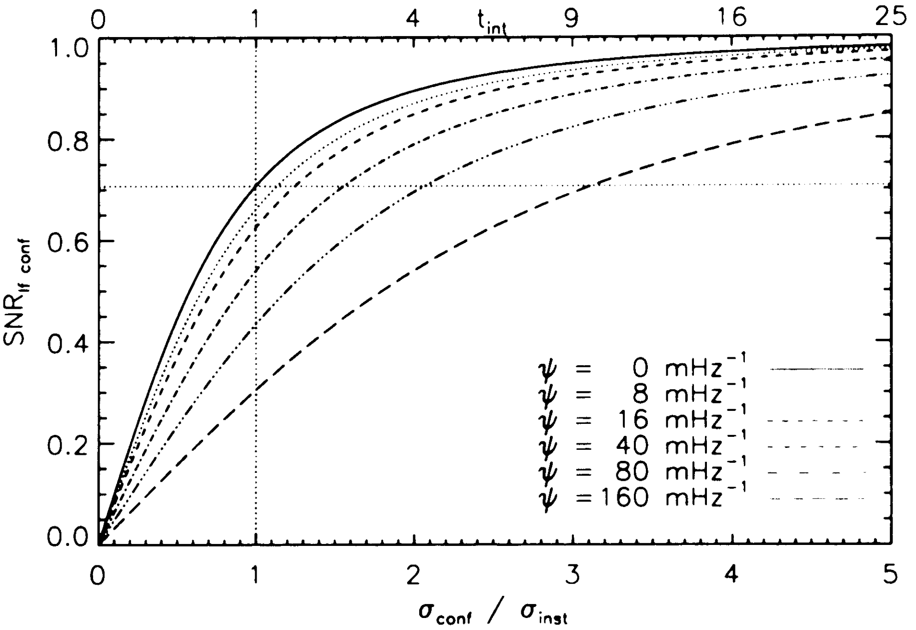

Figure 8.12: SNR loss factor as a function of the confusion noise (σ_{conf}), normalised to the instrumental white noise (σ_{inst}), for a range of values of ψ. The dotted lines shown cross at the loss factor value for white noise, when the instrumental white noise is equal to the confusion noise. A second x-axis is also shown giving the integration time (t_{int}) normalised to the $\sigma_{conf}/\sigma_{inst} = 1$ case.

the vertical dotted line. The solid line in Figure 8.12 represents the white noise case. The value of the Y-axis at the point where the solid line, and the vertical dotted line intersect, represents the decrease in sensitivity; in this white noise case the loss factor is ~0.71. In this example, a source measured at the 10σ confidence level in an observation containing only confusion noise, will only be a $\sim 7.1\sigma$ detection in the presence of confusion and instrumental white noise combined. In theory it is never possible to achieve a limiting level, set with respect to the confusion noise, as there will always remain some instrumental noise component. However, in practice, given sufficient observing time, it is possible to minimise the instrumental component to the point where it becomes a negligible contribution.

Using Figure 8.12, it is possible to derive the loss in sensitivity for a range of values of ψ, in the case where the confusion noise is equal to the instrumental white noise ($\sigma_{conf}/\sigma_{inst} = 1$). This is done by inspecting the value of the y-axis where the line associated with a particular value of ψ, intersects the dotted vertical line. For example, by locating where the $\psi = 80$ mHz$^{-1/2}$ curve meets the vertical dotted line, we can obtain the sensitivity degradation for that value of ψ – in this case the detection significance would fall to 0.4 of that which might be achieved in a confusion noise only observation. Thus, for a 10σ limit defined with respect to the confusion noise level, the final detection would actually be 4σ.

In order to achieve a detection limit equivalent to that of the white noise case, in the presence of 1/*f* noise, an increased integration time will be required to lower the instrumental noise level. This can be quantified by locating the point at which the curve of interest crosses the horizontal dotted line, and reading off the value on the upper X-axis. Taking again as an example the case of $\psi = 80$ mHz$^{-1/2}$, to achieve a $SNR_{lf\ conf}$ equivalent to that of the white noise case ($\sim$ 0.71) the integration time must be increased by approximately a factor of four.

The improvement in limiting SNR resulting from faster scanning can also be easily derived from this figure. Doubling the scanning rate will halve the value of ψ for a fixed λ and f_k due to the inverse relation of ψ with $\dot{\theta}$ (Equation 8.2). Consequently the loss factor would improve from 0.4 to 0.53 when the confusion to instrumental white noise level ratio is equal to unity. Also, the extra integration time required to achieve the equivalent detection limit to that of a white noise observation would decrease from a factor of $\sim$4 to $\sim$3.

8.4.3 Radial Profile Fitting

The data in Figure 8.5 demonstrate that, as is the case with the other tests, the data quality rapidly degrades with increased values of ψ. Therefore, our ability to ascertain the correct radial profile and fit it to a specific model is affected equivalently. The rapid increase in gain factor at low values of ψ ($\sim$0.02) means that high scanning rates are preferable, giving an overall factorial improvement in χ^2 of 2.2 when scanning at $60''\mathrm{s}^{-1}$ as opposed to

$30''\mathrm{s}^{-1}$. Since any source for which a radial profile is being sought must be greater than the beam size, the signal response, even at a high scan rate, will not approach the low-pass filter cut off, and so will not impose a limiting factor in the case of SPIRE. Therefore, the fastest scanning rate possible is advised. However, this must be balanced with the increased overheads associated with a fast scanning rate, in order to derive the optimal observing strategy.

The test performed here used naïve maps only. It is reasonable to expect the χ^2 gain factor to be reduced by a similar factor to that seen in the large scale structure tests. Until a maximum likelihood map-maker capable of dealing with full scale simulations is available, however, it will not be possible to test this supposition. For now these results can be used as a worst case scenario, i.e. an upper limit to the χ^2 gain factor for a specific value of ψ.

The results of these tests focus on the extraction of prestellar cores, but are however applicable to observations of nearby galaxies too. Similar methods are employed to determine the luminosity profiles of galaxies, in order to determine their morphology.

8.5 Chapter Summary

This chapter has described a series of investigations of the impact of uncorrelated $1/f$ noise when observing with a DC coupled scanning instrument, as a function of $1/f$ knee frequency, scanning rate, and convolved source size scale. The results represent the realistic limits to the sensitivity of a scanning instrument when observing sources of an arbitrary scale. While there are many other possible systematic effects, it is likely that these will act merely as a scaling on the normalised SNR, or can be modelled independently and considered in conjunction with these results. High-pass filtered and maximum likelihood maps were generated in order to provide a realistic example of how the data might be treated, and to assess how these methods can reduce the degradation in sensitivity caused by $1/f$ noise.

The losses due to 1/*f* noise were found to increase linearly with knee frequency, as the square root of convolved source size scale, and inversely with scanning rate. A parameterisation of these three variables was presented (see Equation 8.2) in order to provide a curve which is scalable to a general system using any combination of these factors. Generation of a maximum likelihood map was found to significantly reduce the impact of 1/*f* noise compared with a naïve approach or high-pass filtering.

The results from this investigation were also applied to the case of a confused observation in order to ascertain the impact of 1/*f* noise on the accurate determination of the detection level within a survey. It was found that an increase in scanning rate can substantially reduce the added integration time required to overcome the degradation due to 1/*f* noise. However, the anti-aliasing filter contained within most real-life systems will degrade any signal beyond its cut-off frequency. The improvement resulting from a high scan rate must be coupled with the losses experienced due to the filter. In addition, operational constraints such as telescope overheads may limit the scan rate.

The final test performed analysed how telescope scan rate, 1/*f* noise knee frequency, and source size scale, affect our ability to recover, and identify, the radial profile of a prestellar core. They show that in general, the quality of the fit degrades quickly at low values of ψ. However, a high scan rate will result in a decreased value of ψ, which corresponds to a significant improvement to the χ^2 value, and therefore a more confident correlation with a specific model.

The results outlined are important in the planning of large scale observing programmes in which both extended and compact sources are required to be observed simultaneously. They allow for an informed selection of scanning strategy to ensure that the source scales of interest are observed efficiently. They also provide information on the integration times required to ensure that the desired detection limits are reached.

This study also illustrates how the often used method of determining noise in a map, by measuring the pixel-to-pixel standard deviation within a blank region of the map, is misleading when dealing with correlated noise. The invalid assumption of scale invariance will result in an incorrect determination of SNR, and its dependence on size scale in the map.

Chapter 9

Conclusions and Future Work

This thesis has focused on the development of a sophisticated Herschel-SPIRE software instrument simulator, and its use in the investigation of instrumental effects on observational data in the FIR-submm. Of particular interest was the optimisation of the SPIRE observing modes and observations of galactic sources, specifically the recovery of structure on arbitrary scales. It has also included analysis of observations of the Cas A SNR made using BLAST, with the aim of determining if SNe are a significant source of dust production in the universe.

Chapter one introduced and summarised FIR/submm astronomy, and the techniques by which it is performed. Overviews of the Herschel and BLAST projects were also given, including details of the PACS and HIFI instruments on board Herschel. Finally, a qualitative review of bolometer operation was presented.

The following chapter reviewed a range of processes in which dust plays a major role in the ISM. It highlighted the important role played by cosmic dust, from chemical processing, to the formation of stars, as well as the cycle through which dust passes, from birth to destruction. Particular attention was paid to a review of the accepted dust formation mechanism in the universe – formation in the atmospheres of evolved (AGB) stars. The overall injection rates were then compared with those required to generate the dust fraction seen in the galaxy today. This identified a deficit in the overall production rate of dust from stars, meaning that another source of dust must be found to explain the observed levels. The need for a new mechanism of dust formation is further supported by the detection of dusty galaxies in the early universe. This dust could not have been formed by AGB stars, as they would not have had time to reach the necessary evolutionary stage. The current evidence for SNe as the missing source was then introduced.

A summary of the SPIRE instrument was presented in chapter three. This included a review of the instrument hardware, observing modes, and scientific capabilities, illustrated by a description of the SPIRE consortium's proposed guaranteed time science programmes.

Chapter four described the SPIRE photometer software simulator, and outlined its primary goals and operation. The SPS is a highly realistic software model of the SPIRE photometer, which contains all of the primary photometer subsystems. It is capable of simulating the photometer system operation, and data characteristics. The system contains models of each subsystem, to varying levels of sophistication. A brief description of the methods used to model each instrument subsystem, implemented in the form of a module, has also been presented. The limitations of the simulations have been noted, specifically, that results from simulation can only be representative, and not identical to, the final system output. This makes the simulator useful in understanding the impact of the known systematics on the data quality, but it cannot predict the final instrument performance until the system is in orbit.

The issue of processing instrument data from raw timelines, to a useable format for astronomy, in this case a map, was addressed in Chapter five. The various data cleaning processes, including removal of cosmic ray detections, correlated noise, and flat-fielding were discussed, and where necessary, an explanation of these methods, as applied to SPS data, was given. The issues involved with making maps from the processed data were also described, including an explanation of naïve map making, and an overview of the maximum likelihood map-making method. This method deals with the removal of uncorrelated $1/f$ noise, and is used widely in studies of the CMB.

This chapter also provided an account of the validation of the SPS signal and noise output. This validation was performed by comparing the SNR of a point source, observed in scan-map mode, with the theoretical SNR expected. This used data in the form of a naïve map, generated by unfiltered detector data. The NEFD obtained in this verification exercise was compared to the official SPIRE sensitivity model (Griffin, 2004), and found to agree to within $\sim 2\%$. Finally, an overview of the SPIRE map-making routine selection process was presented, and the reasons for selecting MADmap as the best routine explained.

In Chapter six, the main observing modes for the SPIRE photometer were assessed, and the baseline optimum parameters derived. POF 2 (7-point mapping) will be used as the nominal point source photometry mode, with a jiggle position spacing, $\Delta\theta_7$, of $6''$. This mode is chosen over a single pointing observation (POF 1) as it guarantees source flux and position recovery, within the Herschel pointing accuracy and reasonable source position errors, with only a small reduction in SNR.

The optimum spacing required within the jiggle map pattern, in order to fully sample all arrays, is $8.1''$. The best spacings between consecutive jiggle maps when raster mapping, was found to be 245, and $236''$ in the Z and Y telescope coordinates respectively. This ensures that the observation remains fully sampled at the join between jiggle maps, and that the distribution of integration time remains even.

The optimum scan map mode parameters were found to be a scan rate of $30''\mathrm{s}^{-1}$, and scan angle of 12.4°. Perpendicular scans in the diagonal directions are optimal for large maps, as provide cross-linked data, suitable for use with a maximum likelihood map-maker. Small and irregular maps however are more efficiently performed by scanning along the long axis. The optimum scan line separation for the diagonal and long axis scan directions are 235 and $348''$ respectively. These parameters minimise the losses due to $1/f$ noise and low pass filter systematics, provide full sampling down to $\frac{1}{4}$ FWHM, and provide a uniform distribution of integration time across the map.

Scan map mode was found to be more efficient than raster mapping for maps greater than $4' \times 4'$. In addition to the shorter total observation time, it provides a more uniform integration time map, as well as significant bonus data in the surrounding map regions. As a result this is currently the nominal mode for all but single field jiggle maps ($4' \times 4'$). Note that this result is now being reassessed due to new information regarding telescope movement overheads.

The optimum observing parameters for each of the SPIRE observing modes are summarised in Table 6.2. Specific science cases may require a variation on some parameters, however these nominal values will be used for the majority of observations.

Many of the conclusions derived in this chapter are applicable to other observing systems, particularly those with a hexagonally packed detector array.

Chapter seven presented the analysis of observations of the Cas A SN remnant, and surrounding interstellar cloud structure, using all MSX, IRAS, and BLAST bands. Two SEDs were derived, one centred at the location of Cas A, and the other on a knot of material well outside the SN remnant shock front. This knot was assumed to be representative of a molecular cloud in front of the remnant. The Cas A SED was fitted by a two temperature greybody, and the knot SED with a single greybody. The temperature of the Cas A cold component was found to be extremely close to the temperature of the knot, and thus the surrounding dust. Evidence for a substantial quantity of cold dust being present in Cas A has been presented by Dunne et al. (2003a), with the conclusion that this might indicate SNe to be a significant source of cosmic dust. The results presented in this chapter imply that this dust mass measurement may be an upper limit. This is because some of the previously detected material may be associated with the foreground molecular cloud, and not the SN remnant. More samples of other young SN remnants are required to settle this question.

Finally, Chapter eight reports a series of investigations performed on the impact of uncorrelated $1/f$ noise when observing with a DC coupled scanning instrument, as a function of $1/f$ knee frequency, scanning rate, and convolved source size scale. The results represent the realistic limits to the sensitivity of a scanning instrument when observing sources of an arbitrary scale.

While there are many other possible systematic effects, it is likely that these will act merely as a scaling on the normalised SNR, or can be modelled independently and considered in conjunction with these results. High-pass filtered and maximum likelihood maps were generated in order to provide a realistic example of how the data might be treated, and to assess how these methods can reduce the degradation in sensitivity caused by 1/*f* noise.

The losses due to 1/*f* noise were found to increase linearly with knee frequency, as the square root of convolved source size scale, and inversely with scanning rate. A parameterisation of these three variables was performed (see Equation 8.2) in order to provide a curve which is scalable to a general system using any combination of these factors. Generation of a maximum likelihood map was found to reduce significantly the impact of 1/*f* noise compared with a naïve approach or high-pass filtering.

The results from this investigation were also applied to the case of a confused observation in order to ascertain the impact of 1/*f* noise on the accurate determination of the detection level within a survey. It was found that an increase in scanning rate can substantially reduce the added integration time required to overcome the degradation due to 1/*f* noise. However, the anti-aliasing filter contained within most real-life systems will degrade any signal beyond its cut off frequency. The improvement resulting from a high scan rate must be coupled with the losses experienced due to the filter.

The final test performed analysed how telescope scan rate, 1/*f* noise knee frequency, and source size scale, effect our ability to recover, and identify, the radial profile of a prestellar core. They show that in general, the quality of the fit degrades quickly at low values of ψ. However, a high scan rate can provide a significant improvement to the χ^2 value, and therefore a more confident correlation with a specific model.

The results outlined are important in the planning of large scale observing programmes in which both extended and compact sources are required to be observed simultaneously. They allow for an informed selection of scanning speed to ensure that the source scales of interest are observed efficiently. They also provide information on the integration times required to ensure that the desired detection limits are reached.

This study also illustrates how the often used method of determining noise in a map, by measuring the pixel-to-pixel standard deviation within a blank region of the map, is misleading when dealing with correlated noise. The invalid assumption of scale invariance will result in an incorrect determination of SNR, and its dependence on size scale in the map.

9.1 Future Work

The SPIRE photometer simulator has many uses beyond the tasks outlined in this thesis, and is already a working tool within the Instrument Control Centre team. I intend to upgrade and enhance the simulator compared to the current version, for further use. Detailed modelling of the on-board electronics and sampling system is planned within this upgrade. This will allow me to study the way in which the system deals with an observation with a high dynamic range, such as a scan across the galactic plane. This type of observation may saturate the electronic readout unless special steps are taken, such as changing the detector bias. Simulation of this effect will allow me to assess and investigate various methods to overcome this problem. Other minor updates and corrections, such as inclusion of measured beam profiles will also be included.

An interface is also planned which will allow the SPIRE pipeline to use simulator data as an input. This will allow the simulator to be used in testing the SPIRE data reduction pipeline modules as they are developed. A measure of the ability of the data processing pipeline to remove instrument artefacts will allow us to assess more accurately the instrument performance and quality of SPIRE photometer data.

In addition to the upgrades outlined above, there are still various studies that need to be carried out using the simulator. The effects of pointing jitter and correlated noise are still to be investigated. Also, I need to study the effect of modelling each bolometer individually, using the bolometer parameters measured during instrument level testing. More detailed simulations of the large guaranteed time survey programmes will also be performed using the final observing strategies, in order to assess their performance, and to measure in a more realistic way their data quality.

I plan to compare results from the simulations described in this thesis with data from the recent Antarctic BLAST LBD flight (December 2006). These BLAST data can be used to further validate accuracy of the SPS, and as an input for preparation for the SPIRE guaranteed time programmes. An assessment of the cirrus confusion can be made at the SPIRE wavelength for example, helping in the planning of the SAG 3 Gould Belt survey.

Finally, I intend to exploit data from the Antarctic BLAST flight, including new observations of SNe. I will use these data to investigate further the possibility of SNe as a significant source of dust in the universe.

In addition to these tasks, I expect the simulator to play a large role in the preparation and planning of other key programmes, both in guaranteed and open time, which require the use of the SPIRE photometer.

9.2 Closing Remarks

I have developed and tested a detailed SPIRE photometer software simulator. This software is sufficiently flexible in its architecture for it to be easily adapted to simulate any astronomical photometer system. I have optimised the SPIRE photometer observing modes, and found a highly efficient mode of performing scan map observations.

The work contained in this thesis also provides, for the first time, the ability to quantify in a general way, the sensitivity of a DC coupled scanning instrument to source of arbitrary scale, in the presence of uncorrelated $1/f$ noise. This general result can be extended and applied to a variety of cases, including observations performed in a confused environment, as demonstrated in Chapter 8.

Finally, I have analysed new data from BLAST, and investigated the quantity of dust in the Cas A SNR. In addition to generating an SED at the position of the SNR, I also measured the SNR of the cloud structure in the foreground of the SNR for the first time. This study concludes that there is no significant quantity of cold dust in Cas A, contributing to the search for a new significant source of dust in the universe.

Bibliography

Abbott, D. C. and Conti, P. S.: 1987, ARA&A **25**, 113

Agladze, N. I., Sievers, A. J., Jones, S. A., Burlitch, J. M., and Beckwith, S. W.: 1996, **462**, 1026

Amure, M.: 2002, *Ph.D. thesis*, Cardiff University

André, P.: 1993, in T. Montmorle, C. J. Lada, I. F. Mirabel, and J. Tran Thanh Van (eds.), *The cold universe*

André, P. and Saraceno, P.: 2005, in A. Wilson (ed.), *The Dusty and Molecular Universe: A Prelude to Herschel and ALMA*, pp 179–184

Archibald, E. N., Dunlop, J. S., Hughes, D. H., Rawlings, S., Eales, S. A., and Ivison, R. J.: 2001, MNRAS **323**, 417

Arendt, R. G.: 1989, ApJS **70**, 181

Audley, M. D., Holland, W. S., Atkinson, D., Cliffe, M., Ellis, M., Gao, X., Gostick, D. C., Hodson, T., Kelly, D., Macintosh, M. J., McGregor, H., Robson, I., Smith, I., Irwin, K. D., Duncan, W. D., Doriese, W. B., Hilton, G. C., Reintsema, C. D., and Bastien, P.: 2003, in *Bulletin of the American Astronomical Society*, p. 1267

Baars, J. W. M., Genzel, R., Pauliny-Toth, I. I. K., and Witzel, A.: 1977, A&A **61**, 99

Basu, S. and Mouschovias, T. C.: 1994, ApJ **432**, 720

Bertoldi, F., Carilli, C. L., Cox, P., Fan, X., Strauss, M. A., Beelen, A., Omont, A., and Zylka, R.: 2003, A&A **406**, L55

Bhattal, A. S., Francis, N., Watkins, S. J., and Whitworth, A. P.: 1998, MNRAS **297**, 435

Bianchi, S., Alton, P. B., Davies, J. I., and Trewhella, M.: 1998, MNRAS **298**, L49

Bode, M. F.: 1988, in M. E. Bailey and D. A. Williams (eds.), *Dust in the Universe*, pp 73–102

Bonnor, W. B.: 1956, MNRAS **116**, 351

Boulanger, F., Abergel, A., Bernard, J.-P., Burton, W. B., Desert, F.-X., Hartmann, D., Lagache, G., and Puget, J.-L.: 1996, A&A **312**, 256

Cameron, R. M.: 1976, S&T **52**, 327

Chandrasekhar, S.: 1939, *Ciel et Terre* **55**, 412

Christopher, C.: 2002, *MADmap: A Fast Parallel Maximum Likelihood CMB Map Making Code*, `http://crd.lbl.gov/~cmc/MADmap/doc`

Clayton, D. D., Liu, W., and Dalgarno, A.: 1999, *Science* **283**, 1290

Clements, D., Bendo, G., Chanial, P., Laurent, G., Schulz, B., Sibthorpe, B., Waskett, T., and Xu, K.: 2006, *Internal SPIRE review document*

Currie, M. and Berry, D.: 2001, *Kappa - kernel application userss manual - starlink user note 95.19*

Curry, C. L. and Stahler, S. W.: 2000, in F. Favata, A. Kaas, and A. Wilson (eds.), *ESA SP-445: Star Formation from the Small to the Large Scale*, p. 351

de Graauw, T., Caux, E., Guesten, R., Helmich, F., Pearson, J., Phillips, T. G., Schieder, R., Tielens, X., Saraceno, P., Stutzki, J., Wafelbakker, C. K., and Whyborn, N. D.: 2005, in *Bulletin of the American Astronomical Society*, p. 1219

de Jong, T.: 1984, *The Messenger* **37**, 26

Devlin, M. J., Ade, P. A. R., Aretxaga, I., Bock, J. J., Chung, J., Chapin, E., Dicker, S. R., Griffin, M., Gundersen, J., Halpern, M., Hargrave, P., Hughes, D., Klein, J., Marsden, G., Martin, P., Mauskopf, P. D., Netterfield, B., Olmi, L., Pascale, E., Rex, M., Scott, D., Semisch, C., Truch, M., Tucker, C., Tucker, G., Turner, A. D., and Weibe, D.: 2004, in *Astronomical Structures and Mechanisms Technology. Edited by Antebi, Joseph; Lemke, Dietrich. Proceedings of the SPIE, Volume 5498, pp. 42-54 (2004).*, pp 42–54

Dole, H., Lagache, G., Puget, J.-L., Caputi, K. I., Fernández-Conde, N., Le Floc'h, E., Papovich, C., Pérez-González, P. G., Rieke, G. H., and Blaylock, M.: 2006, A&A **451**, 417

Dominik, C., Sedlmayr, E., and Gail, H.-P.: 1993, A&A **277**, 578

Douvion, T., Lagage, P. O., Cesarsky, C. J., and Dwek, E.: 2001a, A&A **373**, 281

Douvion, T., Lagage, P. O., and Pantin, E.: 2001b, A&A **369**, 589

Dowell, C. D., Allen, C. A., Babu, R. S., Freund, M. M., Gardner, M., Groseth, J., Jhabvala, M. D., Kovacs, A., Lis, D. C., Moseley, Jr., S. H., Phillips, T. G., Silverberg, R. F., Voellmer, G. M., and Yoshida, H.: 2003, in T. G. Phillips and J. Zmuidzinas (eds.), *Millimeter and Submillimeter Detectors for Astronomy. Edited by Phillips, Thomas G.; Zmuidzinas, Jonas. Proceedings of the SPIE, Volume 4855, pp. 73-87 (2003).*, pp 73–87

Draine, B. T. and Lee, H. M.: 1984, ApJ **285**, 89

Duband, J.: 1997, *Proc. of ESA symposium on The Far Infrared and Submillimetre Universe* 401

Duncan, W. D., Sandell, G., Robson, E. I., Ade, P. A. R., and Griffin, M. J.: 1990, MNRAS **243**, 126

Dunne, L., Eales, S., Ivison, R., Morgan, H., and Edmunds, M.: 2003a, Nature **424**, 285

Dunne, L., Eales, S. A., and Edmunds, M. G.: 2003b, MNRAS **341**, 589

Dwek, E., Hauser, M. G., Dinerstein, H. L., Gillett, F. C., and Rice, W. L.: 1987, ApJ **315**, 571

Dwek, E., Moseley, S. H., Glaccum, W., Graham, J. R., Loewenstein, R. F., Silverberg, R. F., and Smith, R. K.: 1992, ApJ **389**, L21

Ebert, R.: 1955, *Zeitschrift fur Astrophysik* **37**, 217

Evans, A.: 1994, *The Dusty Universe*, Ellis Horwood

Ferrara, A.: 2003, in A. N. Whittet, G. C. Clayton, and B. T. Draine (eds.), *Astrophysics of Dust*, Vol. 209, pp 355–372

Fesen, R. A., Hammell, M. C., Morse, J., Chevalier, R. A., Borkowski, K. J., Dopita, M. A., Gerardy, C. L., Lawrence, S. S., Raymond, J. C., and van den Bergh, S.: 2006, ApJ **645**, 283

Foster, P. N. and Chevalier, R. A.: 1993, ApJ **416**, 303

Gail, H.-P. and Sedlmayr, E.: 1999, A&A **347**, 594

Gautier, T. N., Boulanger, F., Perault, M., and Puget, J. L.: 1992, *aj* **103**, 1313

Gilman, R. C.: 1969, ApJ **155**, L185+

Goldsmith, P. F. and Langer, W. D.: 1978, ApJ **222**, 881

Green, D. A.: 2006, *A Catalogue of Galactic Supernova Remnants (2006 April version)*, Astrophysics Group, Cavendish Laboratory, Cambridge, United Kingdom (available at `http://www.mrao.cam.ac.uk/surveys/snrs/`)

Griffin, D., Griffin, M. J., and Swinyard, B. M.: 2003, *SPIRE-RAL-PRJ-000620*

Griffin, M., Abergel, A., Ade, P., and Wright, G.: 2006, *Proc. SPIE 6265, Florida*

Griffin, M. J., *priv. comm.*

Griffin, M. J.: 2004, *SPIRE-QMW-NOT-000642*

Griffin, M. J., Bock, J. J., and Gear, W. K.: 2002a, *Applied Optics* **41**, 6543

Griffin, M. J., Swinyard, B. M., and Vigroux, L.: 2002b, *Proc Symposium 'The Promise of the Herschel Space Observatory*

Guiderdoni, B., Bouchet, F. R., Puget, J.-L., Lagache, G., and Hivon, E.: 1997, Nature **390**, 257

Guiderdoni, B., Hivon, E., Bouchet, F. R., and Maffei, B.: 1998, MNRAS **295**, 877

Haig, D. J., Ade, P. A. R., Aguirre, J. E., Bock, J. J., Edgington, S. F., Enoch, M. L., Glenn, J., Goldin, A., Golwala, S., Heng, K., Laurent, G., Maloney, P. R., Mauskopf, P. D., Rossinot, P., Sayers, J., Stover, P., and Tucker, C.: 2004, *SPIE* **4598**, 78

Hargrave, P. C., Bock, J., Brockley-Blatt, C., Coker, J., Duband, L., Goizel, A., Griffin, D., Swinyard, B., and B., W.: 2006, pp 17–22

Hargrave, P. C., Sibthorpe, B., Mauskopf, P. M., and the BLAST consortium: In Prep., ApJ

Harwit, M.: 2001, *Kluwer Academic Publishers* pp 301–330

Hayton, D.: 2004, `http://cfa-www.harvard.edu/HITRAN/`

Helou, G. and Beichman, C. A.: 1990, in B. Kaldeich (ed.), *Liege International Astrophysical Colloquia*, pp 117–123

Herschel Planck Instrument Interface Document IID PartA: 2003, *SCI-PT-IIDA-04624*

Hildebrand, R. H.: 1983, QJRAS **24**, 267

Holland, W. S., Robson, E. I., Gear, W. K., Cunningham, C. R., Lightfoot, J. F., Jenness, T., Ivison, R. J., Stevens, J. A., Ade, P. A. R., Griffin, M. J., Duncan, W. D., Murphy, J. A., and Naylor, D. A.: 1999, MNRAS **303**, 659

Hoyle, F. and Wickramasinghe, N. C.: 1962, MNRAS **124**, 417

Hughes, D. H., Serjeant, S., Dunlop, J., Rowan-Robinson, M., Blain, A., Mann, R. G., Ivison, R., Peacock, J., Efstathiou, A., Gear, W., Oliver, S., Lawrence, A., Longair, M., Goldschmidt, P., and Jenness, T.: 1998, Nature **394**, 241

James, A., Dunne, L., Eales, S., and Edmunds, M. G.: 2002, MNRAS **335**, 753

Jeans, J. H.: 1920, *The Observatory* **43**, 389

Jones, A. P., Tielens, A. G. G. M., Hollenbach, D. J., and McKee, C. F.: 1994, ApJ **433**, 797

Jones, A. P., Tielens, A. G. G. M., Hollenbach, D. J., and McKee, C. F.: 1997, in T. J. Bernatowicz and E. Zinner (eds.), *American Institute of Physics Conference Series*, p. 595

Jura, M. and Kleinmann, S. G.: 1990, ApJS **73**, 769

Kamijo, F.: 1963, PASJ **15**, 440

Kessler, M. F., Steinz, J. A., Anderegg, M. E., Clavel, J., Drechsel, G., Estaria, P., Faelker, J., Riedinger, J. R., Robson, A., Taylor, B. G., and Ximenez de Ferran, S.: 1996, A&A **315**, L27

Kirk, J.: 2002, *Ph.D. thesis*, Cardiff University

Kiss, C., Ábrahám, P., Klaas, U., Juvela, M., and Lemke, D.: 2001, A&A **379**, 1161

Kiss, C., Klaas, U., and Lemke, D.: 2005, A&A **430**, 343

Knapp, G. R.: 1985, ApJ **293**, 273

Kozasa, T., Hasegawa, H., and Nomoto, K.: 1991, A&A **249**, 474

Kraus, J. D.: 1966, *Radio Astronomy*, McGraw-Hill

Krause, O.: 2005, *Cassiopeia A: Death Becomes Her*, `http://www.spitzer.caltech.edu/Media/releases/ssc2005-14/ssc2005-14c.shtml`

Krause, O., Birkmann, S. M., Rieke, G. H., Lemke, D., Klaas, U., Hines, D. C., and Gordon, K. D.: 2004, Nature **432**, 596

Kreysa, E., Bertoldi, F., Gemuend, H.-P., Menten, K. M., Muders, D., Reichertz, L. A., Schilke, P., Chini, R., Lemke, R., May, T., Meyer, H.-G., and Zakosarenko, V.: 2003, in T. G. Phillips and J. Zmuidzinas (eds.), *Millimeter and Submillimeter Detectors for Astronomy. Edited by Phillips, Thomas G.; Zmuidzinas, Jonas. Proceedings of the SPIE, Volume 4855, pp. 41-48 (2003).*, pp 41–48

Lamarre, J. M., Puget, J. L., Bouchet, F., Ade, P. A. R., Benoit, A., Bernard, J. P., Bock, J., de Bernardis, P., Charra, J., Couchot, F., Delabrouille, J., and Efstathiou, G.: 2003, *New Astronomy Review* **47**, 1017

Lindner, J., Naylor, D., and Swinyard, B. M.: 2004, *Proc. SPIE 5847, Glasgow*

Loinard, L., Lequeux, J., Tilanus, R. P. T., and Lagage, P. O.: 2003, in J. Arthur and W. J. Henney (eds.), *Revista Mexicana de Astronomia y Astrofisica Conference Series*, pp 267–269

Low, F. J., Young, E., Beintema, D. A., Gautier, T. N., Beichman, C. A., Aumann, H. H., Gillett, F. C., Neugebauer, G., Boggess, N., and Emerson, J. P.: 1984, ApJ **278**, L19

Lucy, L. B., Danziger, I. J., Gouiffes, C., and Bouchet, P.: 1991, in S. E. Woosley (ed.), *Supernovae. The Tenth Santa Cruz Workshop in Astronomy and Astrophysics, held July 9-21, 1989, Lick Observatory. Editor, S.E. Woosley; Publisher, Springer-Verlag, New York, 1991. LC # QB856 .S26 1989. ISBN # 0387970711. P. 82, 1991*, p. 82

Maciel, W. J.: 1981, A&A **98**, 406

Maeder, A.: 1992, A&A **264**, 105

Makovoz, D. and Khan, I.: 2005, in P. Shopbell, M. Britton, and R. Ebert (eds.), *ASP Conf. Ser. 347: Astronomical Data Analysis Software and Systems XIV*, p. 81

Mather, J. C.: 1982, Appl. Opt. **21**, 1125

Mauskopf, P. D., Gerecht, E., and Rownd, B. K.: 2000, in J. G. Mangum and S. J. E. Radford (eds.), *ASP Conf. Ser. 217: Imaging at Radio through Submillimeter Wavelengths*, p. 115

McKee, C. F.: 1989, ApJ **345**, 782

Mestel, L. and Spitzer, Jr., L.: 1956, MNRAS **116**, 503

Mill, J. D.: 1994, in I. Kadar and V. Libby (eds.), *Proc. SPIE Vol. 2232, p. 200-216, Signal Processing, Sensor Fusion, and Target Recognition III, Ivan Kadar; Vibeke Libby; Eds.*, pp 200–216

Morgan, H.: 2004, *Ph.D. thesis*, Cardiff University

Morgan, H. L., Dunne, L., Eales, S. A., Ivison, R. J., and Edmunds, M. G.: 2003, ApJ **597**, L33

Motte, F., André, P., Ward-Thompson, D., and Bontemps, S.: 2001, A&A **372**, L41

Mouschovias, T. C.: 1976, ApJ **206**, 753

Myers, P. C.: 1983, ApJ **270**, 105

Neugebauer, G., Habing, H. J., van Duinen, R., Aumann, H. H., Baud, B., Beichman, C. A., Beintema, D. A., Boggess, N., Clegg, P. E., de Jong, T., Emerson, J. P., Gautier, T. N., Gillett, F. C., Harris, S., Hauser, M. G., Houck, J. R., Jennings, R. E., Low, F. J., Marsden, P. L., Miley, G., Olnon, F. M., Pottasch, S. R., Raimond, E., Rowan-Robinson, M., Soifer, B. T., Walker, R. G., Wesselius, P. R., and Young, E.: 1984, ApJ **278**, L1

Nutter, D. and Ward-Thompson, D.: 2007, MNRAS **374**, 1413

Oliver, S. and Todd, N.: 2000, *Presentation at SPIRE Detector Array Selection Meeting, Rutherford Appleton Laboratory*

Olofsson, H., Eriksson, K., Gustafsson, B., and Carlstrom, U.: 1993, ApJS **87**, 267

Parr-Burman, P.: 2003, *SPIRE-ATC-PRJ-000460*

Peimbert, M. and van den Bergh, S.: 1971, ApJ **167**, 223

Pérez-Rendón, B., García-Segura, G., and Langer, N.: 2002, in W. J. Henney, J. Franco, and M. Martos (eds.), *Revista Mexicana de Astronomia y Astrofisica Conference Series*, pp 94–94

Pilbratt, G. L.: 2005, in *The Dusty and Molecular Universe: A Prelude to Herschel and ALMA*, pp 3–10

Poglitsch, A., Waelkens, C., Bauer, O. H., Cepa, J., Henning, T., van Hoof, C., Feuchtgruber, H., Kerschbaum, F., Lemke, D., Renotte, E., Rodriguez, L., Royer, P., and Saraceno, P.: 2005, *American Astronomical Society Meeting Abstracts* **207**, 35.02

Poutanen, T., de Gasperis, G., Hivon, E., Kurki-Suonio, H., Balbi, A., Borrill, J., Cantalupo, C., Doré, O., Keihänen, E., Lawrence, C. R., Maino, D., Natoli, P., Prunet, S., Stompor, R., and Teyssier, R.: 2006, A&A **449**, 1311

Raymond, J. C.: 1984, ARA&A **22**, 75

Reichart, D. E. and Stephens, A. W.: 2000, ApJ **537**, 904

Reynoso, E. M. and Mangum, J. G.: 2001, AJ **121**, 347

Richards, P. L.: 1994, *Journal of Applied Physics* **76**, 1

Rowan-Robinson, M., Lock, T. D., Walker, D. W., and Harris, S.: 1986, MNRAS **222**, 273

SAG 1 GT proposal: 2004, *SPIRE SAG 1 stage 3 proposal*

SAG 1 GT proposal: 2005, *SPIRE SAG 1 stage 3 proposal*

SAG 2 GT proposal: 2005a, *SPIRE SAG 2 stage 3 proposal*

SAG 2 GT proposal: 2005b, *SPIRE SAG 2 stage 3 proposal*

SAG 3 GT proposal: 2006a, *SPIRE SAG 3 stage 3 proposal*

SAG 3 GT proposal: 2006b, *SPIRE SAG 3 stage 3 proposal*

SAG 4 GT proposal: 2006, *SPIRE SAG 4 stage 3 proposal*

SAG 5 GT proposal: 2004, *SPIRE SAG 5 stage 3 proposal*

SAG 6 GT proposal: 2006a, *SPIRE SAG 6 stage 3 proposal*

SAG 6 GT proposal: 2006b, *SPIRE SAG 6 stage 3 proposal*

Salpeter, E. E.: 1974, ApJ **193**, 579

Scalo, J. M. and Pumphrey, W. A.: 1982, ApJ **258**, L29

Shu, F. H.: 1977, ApJ **214**, 488

Sibthorpe, B. and Griffin, M. J.: 2006, *SPS Document*

Sibthorpe, B. and Waskett, T. J.: 2006, *SPIRE-UCF-NOT-002315*

Sibthorpe, B., Waskett, T. J., and Griffin, M. J.: 2005, *SPIRE-UCF-NOT-002315*

Sibthorpe, B., Waskett, T. J., and Griffin, M. J.: 2006, in *Observatory Operations: Strategies, Processes, and Systems. Edited by Silva, David R.; Doxsey, Rodger E.. Proceedings of the SPIE, Volume 6270, pp. 627019 (2006).*

Smail, I., Ivison, R. J., and Blain, A. W.: 1997, ApJ **490**, L5+

Sodroski, T. J., Odegard, N., Arendt, R. G., Dwek, E., Weiland, J. L., Hauser, M. G., and Kelsall, T.: 1997, ApJ **480**, 173

Sopka, R. J., Hildebrand, R., Jaffe, D. T., Gatley, I., Roellig, T., Werner, M., Jura, M., and Zuckerman, B.: 1985, ApJ **294**, 242

Spitzer, L.: 1978, *Physical processes in the interstellar medium*, New York Wiley-Interscience, 1978. 333 p.

Stahler, S. W., Palla, F., and Ho, P. T. P.: 2000, *Protostars and Planets IV* p. 327

Sudiwala, R. V., Griffin, M. J., and Woodcraft, A. L.: 1992, *International journal of Infrared and Millimeter Waves*

Swinyard, B. M. and Griffin, M. J.: 2002, *SPIRE-RAL-PRJ-000320*

Tauber, J. A.: 2005, in A. N. Lasenby and A. Wilkinson (eds.), *IAU Symposium*, p. 86

Tegmark, M.: 1997, *Physical Review D* **56**, 4514

Thorstensen, J. R., Fesen, R. A., and van den Bergh, S.: 2001, AJ **122**, 297

Thronson, Jr., H. A., Latter, W. B., Black, J. H., Bally, J., and Hacking, P.: 1987, ApJ **322**, 770

Todini, P. and Ferrara, A.: 2001, MNRAS **325**, 726

Turner, A. D., Bock, J. J., Beeman, J. W., Glenn, J., Hargrave, P. C., Hristov, V. V., Nguyen, H. T., Rahman, F., Sethuraman, S., and Woodcraft, A. L.: 2001, *Applied Optics* **40**, 4921

Väisänen, P., Tollestrup, E. V., and Fazio, G. G.: 2001, MNRAS **325**, 1241

Vazquez-Semadeni, E., Ostriker, E. C., Passot, T., Gammie, C. F., and Stone, J. M.: 2000, *Protostars and Planets IV* p. 3

Waskett, T. J., Sibthorpe, B., and Griffin, M. J.: 2006, in V. Charmandaris and D. Rigopoulou (eds.), *Studying Galaxy Evolution with Spitzer and Herschel*

Werner, M. W.: 2006, in *Space Telescopes and Instrumentation I: Optical, Infrared, and Millimeter. Edited by Mather, John C.; MacEwen, Howard A.; de Graauw, Mattheus W. M.. Proceedings of the SPIE, Volume 6265, pp. (2006).*

Whittet, D. C. B. (ed.): 2003, *Dust in the galactic environment*, Bristol: Institute of Physics (IOP) Publishing

Whitworth, A. P., Bhattal, A. S., Francis, N., and Watkins, S. J.: 1996, MNRAS **283**, 1061

Wolfire, M. G. and Cassinelli, J. P.: 1987, ApJ **319**, 850

Woosley, S. E. and Weaver, T. A.: 1995, ApJS **101**, 181

Wright, M., Dickel, J., Koralesky, B., and Rudnick, L.: 1999, ApJ **518**, 284

Appendix A

The SPIRE Photometer Simulator V1.01

Contents

Introduction

This document describes the design of the SPIRE Photometer Simulator (SPS), and attempts to outline the basic system and module operation. It does not constitute users manual. This document should also be considered a working version and any questions or comments should be directed towards the lead author stated above.

The ultimate purpose of the simulator is to produce simulated SPIRE photometer data (both science and housekeeping) timelines, derived from a realistic physical model of the instrument which "observes" a simulated astronomical sky using any of the allowed photometer observing functions (POFs). The sensitivity results should be compatible with the photometer sensitivity model (implemented in MATHCAD), but the instrument simulator will constitute a much more sophisticated and versatile tool for evaluating the photometer performance. The simulated data can be analysed using a range of data reduction software and the results compared with the input sky.

Simulator development plan

Building up the full simulator is expected to take some time, and will require input and participation from various members of the SPIRE consortium. A first version has been produced at Cardiff, implementing basic forms of most modules. The modular architecture is implemented, allowing the initial version to be updated and enhanced.

A similar code will need to be developed for the FTS - while that is beyond the scope of this exercise, it is envisaged that a similar modular structure can be adopted, and that a number of the modules can be shared or straightforwardly adapted.

Revision History

Version 1.0 release 08 February 2006
Version 1.01 release 24 April 2006

- User SPS path and temp_path now defined as a system variable (`!SPS_path`)
- New lines to be added to the users startup file. Allows SPS to be called from any local under UNIX / LINUX
- Corrected array rotation problem when scanning at various angles
- Map now specified by a centre point, rather than the start point
- Corrected float conversion error in detectors module
- Updated thermal fluctuations model, now uses first order low pass filter with a range of time constants

List of relevant documents

Document	Ref.	Comments
Operating Modes for the SPIRE Instrument (Chap. 5) Abbreviation: OMD	SPIRE-RAL-PRJ-000320; Issue 3.0, 4 Jan.. 2002	Describes the basic operations of chopping and nodding, and outlines the different observing modes and their parameters.
SPIRE Sensitivity Models	SPIRE-QMW-NOT-000642; Issue 3.0, 6 June 2003	Presents detailed calculations of the instrument sensitivity in various observing modes, and summarises the values of various telescope and instrument parameters. Simulator results should be basically compatible with it.
Herschel/Planck Instrument Interface	SCI-PT-IIDA-04624 Issue 3, 1 July 2002	Provides information on Herschel pointing and slewing capabilities and parameters in

Document Part A		Section 5.12
Herschel Pointing Modes	SCI-PT-RS-07725; Issue 3.0, 24 May 2002	Describes the Herschel pointing modes. Note: this doc. Is also Annex 4 of the IID-A
Herschel/SPIRE Detector Control Unit Design Document	SAp-SPIRE-FP-0063-02; Issue 0.3, 18 Feb. 2003	Describes how the bolometer signals are processed and digitised by the DCU electronics
SPIRE Filter Specification Document	SPIRE-QMW-PRJ-000454 Issue: 2.2, 29 Oct. 2002	Summarises the location of and requirements for the filters and dichroics.
Relative performance of filled and feedhorn-coupled focal plane architectures	Griffin, Bock, and Gear, *Applied Optics* 41, 6543, 2002.	Presents a general treatment of the performance of feedhorn-coupled detector arrays.

Installing and operating the SPS

The SPS is comprised of a variety of files, all contained within a single zip file. These files should be extracted to a specific SPS folder. In case of a Windows platform installation, the path to this folder must be input to the path section of the preferences menu. The coyoteprograms and IDL astro libraries (included with SPS) will need to be accessible within the IDL session path. These must be installed and set up.

The user's IDL startup file must be edited to include the SPS folder path, and SPS temporary directory path (see below). The required lines are stated below and must be copied to the users startup file. These lines can also be found in startup.pro within the SPS_V1_01_code folder. This code is valid for both UNIX and Windows operating systems.

```
;Primary location of SPS directories - EDIT THIS ON INSTALLATION
DEFSYSV, '!SPS_path',     'Z:\Simulator\SPS_V1-01\'
;Location of SPS temporary folder    - EDIT THIS ON INSTALLATION
DEFSYSV, '!SPS_temp_path','C:\harddisk_simulator_datafiles\temp\'
op = STRUPCASE(!VERSION.OS_FAMILY)
IF op EQ 'WINDOWS' THEN spacer = ';' ELSE spacer = ':'
!path = EXPAND_PATH('+'+!SPS_path,/ALL_DIRS) + spacer + !path
```

During SPS operation a series of files will be generated. By default they will be stored in the working directory. These files may be large arrays (n detectors by n time steps) and will be written and read several times within a simulation. It is important that the SPS temporary directory be stored on the computer performing the simulation. Failure to do this will require large amounts of data to be transferred backward and forwards across the network, potentially resulting in a significantly great run time. The temporary path must be specified in the IDL startup file.

The SPS can be called in two ways, either via a command line interface, or via a graphical user interface (GUI).

All user input parameters are defined within a series of parameter files. There is a parameters file associated with each simulator module. These files contain the parameters associated with the subsystem the module represents, e.g. file `params_optics.txt` contains parameters such as the feed horn efficiency, telescope focal ratio etc. The parameter labels contained within the files include the nominal parameter value, where appropriate, in brackets.

1.1 Command line

Command line operation requires the parameter files to be edited before a run is initiated. Selection of operational detector pixels is still made by calling a simple GUI program (`array_gui.pro`). The files must be edited and the values set for the required simulation. Following this the main SPS program (`SPS.pro`) may be called without passing any addition parameters.

```
IDL> SPS
```

All input parameters will be read from the parameters files.

1.2 Graphical User Interface - GUI

A simpler mode of operation is to use the GUI interface. This allows the parameter files to be edited and the initialisation of the SPS from one simple interface. The GUI is called from the command line in the following way.

```
IDL> GUI1
```

1.3 Simulator operating modes

There are currently two modes of SPS operation, standard, and repeat. Standard is classed as operating mode 0. This setting will perform *n* number of simulations in full. Repeat mode (1) performs one full simulation. Once complete, new detector noise realisations and filtering is performed and imposed on the detector model output of the initial simulation. This is intended for fast generation of data sets in cases such as high red-shift extra-galactic studies, where many maps of the same region will be required. The output from these maps cannot however include variations in system pointing, e.g. pointing noise and field rotation. Nor can they include thermal variations. As a result these data have a lower order representation of the SPIRE system.

1.4 Output options

There are two available output formats, IDL save file, and FITS file, specified as output modes 0 and 1 respectively. Both have the ability to output all input and output parameters to a single file.
The IDL save file is aimed at users who plan to use IDL to analyse their data. This output is a fast efficient way to access the data. The structures containing the simulator parameters are restored to their original parameter names (equal to the module to which they belong).

FITS file output is available as a general user output. IDL is not required to access the data in this format. Simulator parameters are stored in a series of FITS file extensions. Each extension contains the input and output parameters from one module. A simulator FITS file to Interactive Analysis (IA) converter is planned for future development.

In addition to the output mode, certain parameters may be selected for exclusion from the output file.

1.5 Understanding your output file

The simulator will output a file in either IDL save format (*.xdr) of FITS format, depending on the user selection. These files contain the structures used within the simulator (see documentation for information). When restored all parameters used within the simulator should be available. Each parameter will be stored within it associated module structure, e.g. telescope pointing is in the *obsfun* module, detector offsets are in the optics module, BSM pointing is in the BSM module etc. For a simple way to read in simulator output in to IDL use read_SPS_data.pro contained within the 'OtherPros' folder. Once restored, the structures, and parameters contained therein, can be accessed in the normal way, e.g. to plot the telescope pointing time line you would require the *DirZ* and *DirY* parameters:

```
IDL> plot, obsfun.DirZ, obsfun.DirY
```

Simulator architecture

The simulator is made up of modules representing instrument systems or subsystems, called as required to generate timeline data for key instrument and system parameters.

The modules are defined with specific inputs and outputs in such a way that the manner in which the module operates internally (e.g., in physically representing the system or subsystem) can be modified without affecting other modules. In addition to the detector science data timelines, the timelines (actual and sampled) for various other parameters can be accessed (e.g., detector array temperatures, BSM position, etc.)

Timeline generators will be based on a single master clock. All samples and the start of all mechanism movements are at clock ticks. This clock will always run at a frequency greater than or equal to the SPIRE photometer sampling frequency to allow processes acting on time scales shorter than the sampling time scale to be included within the system.

1.6 Parameters

There exists an independent 'structure' parameter for each module. All input and output variable parameters within the simulator are contained within one of these structures determined by their 'parent' module (module with which the parameter is associated). In addition to these module structures there is also a module label parameter. This parameter is a string array containing a short piece of information describing the parameter to with which it is associated. Each time a new parameter is added to a module structure, that module label must also be updated. All new parameters and labels are appended to the end of the current structure/label list.

Each module incorporates both input and output parameters, each of which is subdivided in to the categories as set out below.

(i) **Input parameters**: these are defined parameters to be supplied to a module in order to operate. The inputs required at each phase of operation may be different depending on the module functionality and purpose.
   a. **User inputs** – Input parameters supplied by the user via the parameter files
   b. **Module inputs** – Input parameters derived from hard coded data within the simulator
   c. **System input** – Input parameters whose origin is an output from a previous module operation

(ii) **Output parameters**: these are parameters obtained via module processes. Each module may output different parameters at each phase of operation. Subsequent modules may use these outputs as a *simulator input* parameters.
   a. **System outputs** – Output parameters which describe fixed (non-time varying) parameters within the observing system, e.g. optical transmission.
   b. **Timeline outputs** – Derived system parameter time lines, e.g. astronomical power time line.
   c. **Map outputs** – Output maps representing the sky as seen by the observing system, e.g. convolved sky maps

Timeline output parameters can be considered to be one of three kinds:

(i) **Command timelines**: these are time-lines of commanded parameters, such as telescope or BSM position, which are available without error for the data analysis;

(ii) **Hidden timelines**: these are time-lines which are produced by the module corresponding to quantities which cannot in reality be directly available to the instrument user - an example is the actual telescope pointing timeline as opposed to the commanded timeline: the former is equivalent to the latter but with added noise, the details of which will never be available from the data stream;

(iii) **Measured timelines**: these are timelines of measured (sampled) science or housekeeping data.

These subcategories of time line parameters are not explicitly separated within the simulator operation. These are important only to those users who wish use only those parameters available from the physical system. The class of each time line is specified in the accompanying module documentation.

SPS architecture and operation

The SPS runs via a four-phase process. These processes are as follows:

(i) **Input** – parameter input phase, set up of module structures with input parameters
(ii) **Initialisation** – module initialisation and run of non-time step (static) operation modules
(iii) **Time step** – time stepped operation phase, each module is called once each time step
(iv) **After run** – finalisation and post processing of time step time lines, e.g. sampling

There is the opportunity for each module to run at each stage depending on its functionality and operating processes. In most cases a module will perform it's primary task in only one operation phase.

Each phase in initiated via the central SPS control program file (SPS.pro).

1.7 SPS control

The control program progresses through each operation phase in order, as shown in Figure 1. Correspondingly there are four calling sequences for each module, one for each phase. These sequences call a routine specific to the current phase of operation for a specific module and pass the required structure parameters. The parameters within the structures are then converted as required in to a useable form before being passed to the central module code. This code contains the modelled subsystem, which once complete outputs its required data back to the module phase routine. These data are then appended to the modules own parameter structure, and the associated module label parameters updated, before returning to the control program. The module phase routines (file names) contain the suffix *input*, *init*, *step*, or *afterrun*, depending on the specific phase of operation they refer to. The modules are called in sequence according to their module number, as specified in Table 1, within a single phase.

1.8 Master clock

All timeline parameters must be simulated with a time step sufficiently small compared to the data sampling time. The nominal sampling interval for the photometer detectors is one-third the instrument-sampling rate. Time line output parameters created by modules in the initialisation phase must be created with a sampling time step equivalent to that performed in the time step phase.

The maximum telescope scan rate is 60 arcsec s^{-1}, so the time to cross 1/10th of a beam at 250 μm (approx 2 arcsec, the nominal input map resolution) is 1/30 sec. To ensure that all quantities are sufficiently finely sampled, a master clock step of no more than ~30 ms is required. A nominal step size of 12 ms is preferred for a system sampling rate of ~28 Hz. The total number of master clock ticks in an observation timeline is given by

$$n_{\text{ticks}} = \frac{t_{\text{tot}}}{\Delta t_{\text{clk}}}. \qquad (1)$$

Each time line is a vector of $i = 1 - n_{\text{ticks}}$ parameter values, corresponding to times from 0 to t_{tot} in steps of Δt_{clk}. With a master clock interval of 12 ms., the total number of points per timeline for a 1-hr observation is then 300,000. The total number of timelines to be simulated will be approximately 300 (270 detector channels and various others). So the total number of data points needed for a full one-hour simulation is on the order of 10^8 for one output data time line.

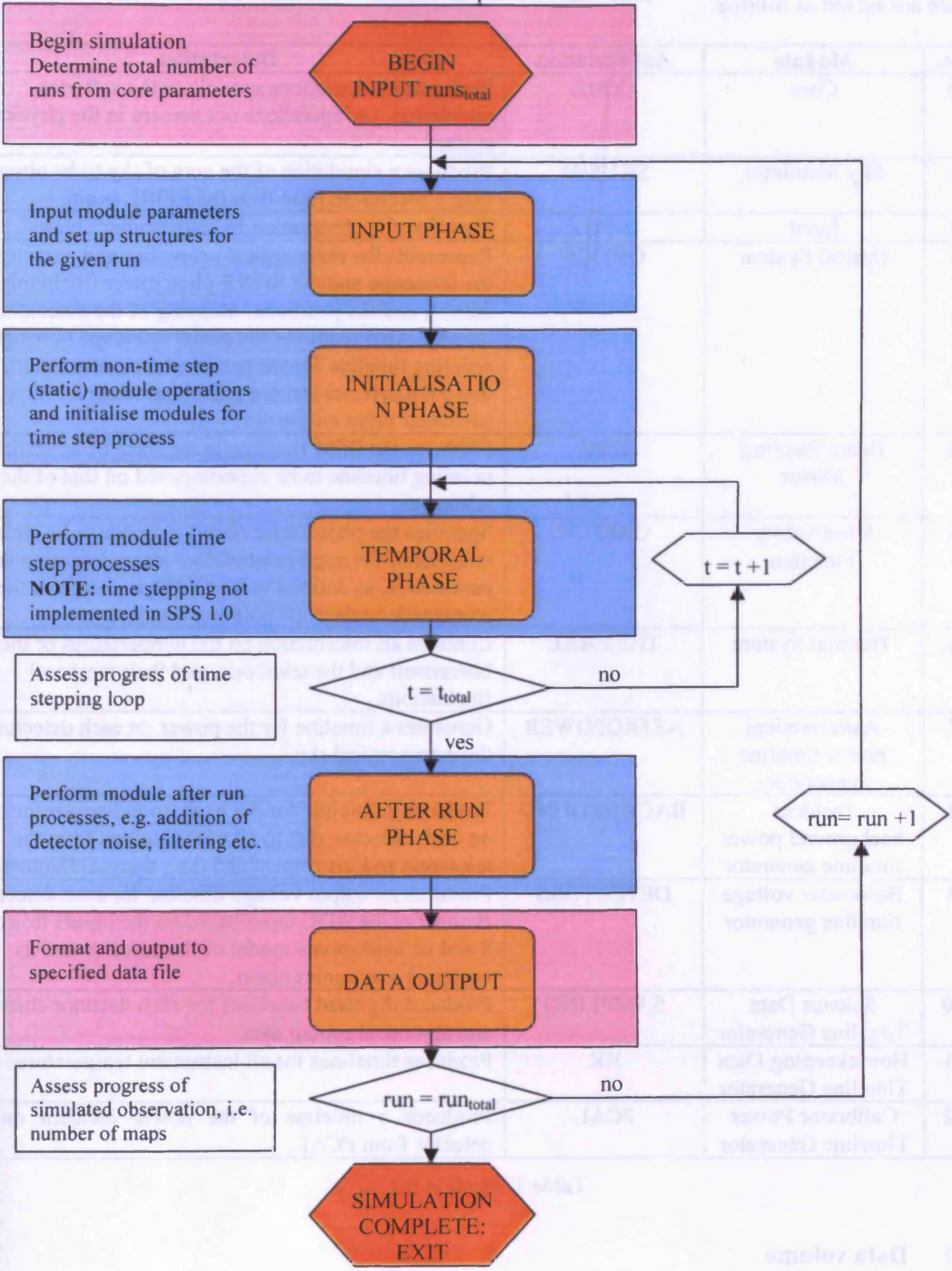

Figure 1: SPS operation flow chart

1.9 Module Summary

A module represents each operational process or system within the Herschel/SPIRE observing system. These are set out as follows:

No.	Module	Abbreviation	Description
0	Core	CORE	Performs all operations specific to the software simulation, i.e. operations not present in the physical system
1	Sky Simulator	SKYSIM	Produces a simulation of the area of sky to be observed, with a resolution finer than the SPIRE beam.
2	Input	INPUT	Specifies the observation in "astronomer's terms"
3	Optical System	OPTICS	Represents the main optical properties and parameters of the telescope and the SPIRE photometer (including the filters), and the positional mapping of the detectors on the sky. Also produces the actual telescope boresight pointing timeline for the period of the observation, so that each detector sample can be associated with a particular point on the sky.
4	Beam Steering Mirror	BSM	Produces the BSM timeline in the form of an additional pointing timeline to be superimposed on that of the telescope.
5	Observatory Function	OBSFUN	Specifies the photometer observing node to be simulated in terms of the appropriate Observatory Function and its parameters, as defined in the OMD, and defines the commanded telescope pointing timeline.
6	Thermal System	THERMAL	Contains all information on the temperatures of the instrument and the telescope, and their temporal fluctuations.
7	Astronomical power timeline generator	ASTROPOWER	Generates a timeline for the power on each detector from the astronomical sky
8	Incident background power timeline generator	BACKGROUND	Produces a timeline for the background power incident on each detector, due to all contributions from the telescope and instrument and their thermal fluctuations.
9	Bolometer voltage timeline generator	DETECTORS	Produces an output voltage timeline for each detector channel at the ADC input based on the inputs from 7 and 8 and an appropriate model of the detector and its analogue electronics chain.
10	Science Data Timeline Generator	SAMPLING	Produces digitised timelines for each detector channel and all housekeeping data
11	Housekeeping Data Timeline Generator	HK	Produces timelines for all instrument temperatures
12	Calibrator Power Timeline Generator	PCAL	Produces a timeline of the power incident on each detector from PCAL.

Table 1: Module list

1.10 Data volume

The total number of timelines to be simulated will be approximately 1200 (4 versions {astronomical power, noiseless voltage, noisy voltage, filtered and sampled voltage} of ~300 detector channels). Therefore the total number of data points needed for a full one-hour simulation is on the order of 3×10^8 (as discussed in Section 1.8), based on the baseline master clock interval being 12 ms, producing 300,000 points per timeline for a 1-hr observation. In addition to these there will also be other memory requirements from other large arrays, e.g. input sky maps.

Coordinate systems

The spacecraft and array coordinate system is as shown below. The telescope boresight is the X direction, with the nominal Sun direction along the Z axis. The detector arrays are in the Y-Z plane. The three arrays overlap on the sky, ideally with no misalignment. In practice there will be some misalignment: the centre of the PSW array is defined to be the (0,0) position.

The chopping/nodding direction is along the Y-axis. For scanning observations, the telescope scan direction ϕ_{scan} is defined with respect to the Y axis as shown.

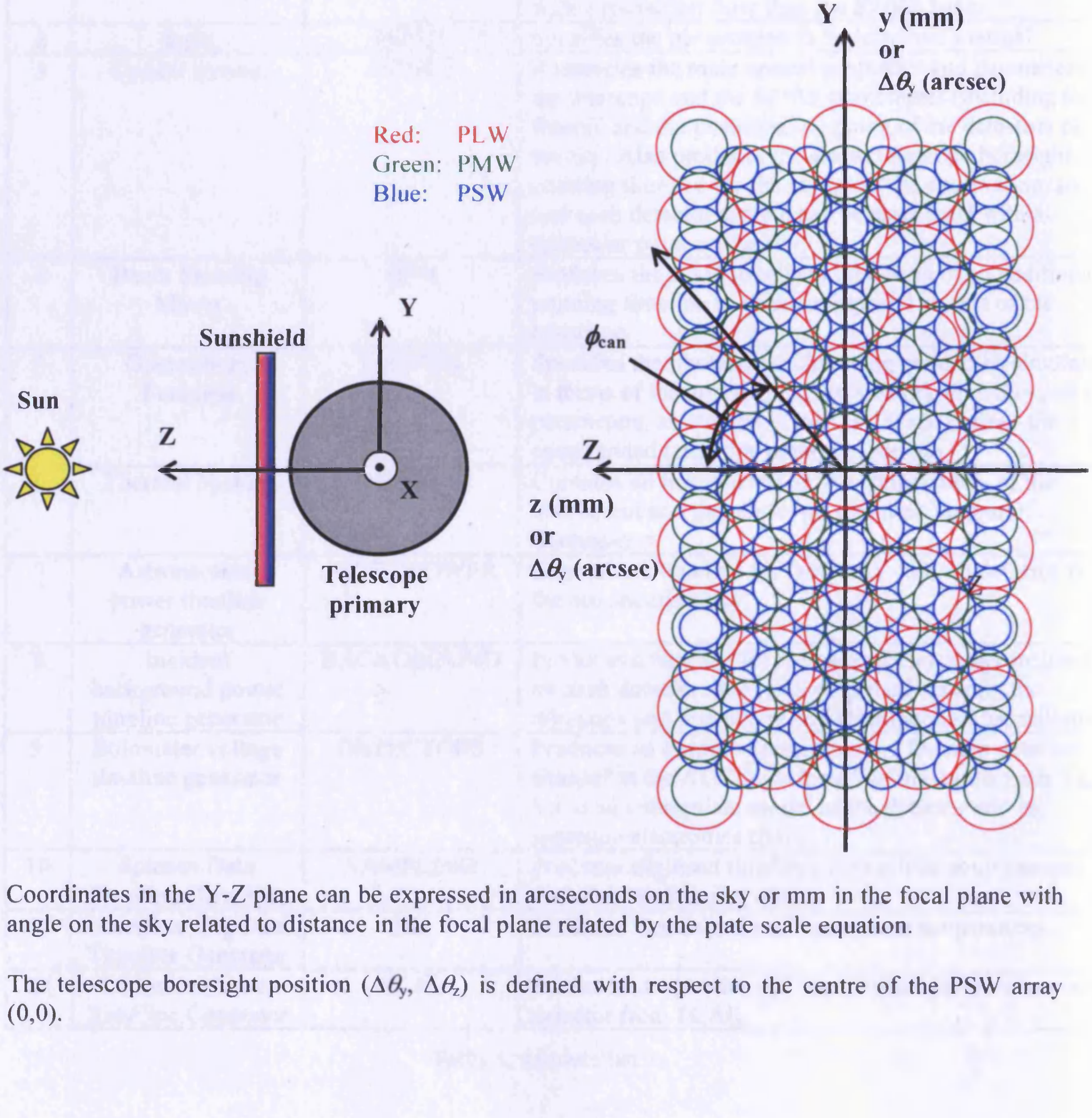

Coordinates in the Y-Z plane can be expressed in arcseconds on the sky or mm in the focal plane with angle on the sky related to distance in the focal plane related by the plate scale equation.

The telescope boresight position ($\Delta\theta_y$, $\Delta\theta_z$) is defined with respect to the centre of the PSW array (0,0).

Herschel/SPIRE Observing modes

The telescope and BSM motions involved in the various observing modes (chopping, nodding, scanning, rastering) are described in the *Herschel Pointing Modes* document and in the OMD. A quick summary of possible observing modes is given here for quick reference.

1.11 Observing modes

There are nine POFs, six relating to scientific observations, and three to instrument calibration and setup as summarized in the Table 2. The six scientific observing modes can be split into one of three main categories, point source photometry, field mapping, and scan mapping.

Observation	Observatory Function	Name	Comments
Point source photometry	POF1	Chop without jiggling	Accurate pointing and source position
	POF2	Seven-point jiggle map	In-accurate pointing or source position
Field mapping	POF3	Jiggle mapping	Field mapping
	POF4	Raster map	Extended field mapping
Scan mapping	POF5	Scan map without chopping	Large-area mapping
	POF6	Scan map with chopping	Large-area mapping
Peak-up	POF7	Photometer peak-up	Determination of pointing offsets
Calibrate	POF8	Photometer calibrate	Detector responsivity tracking
Engineering modes	POF9	Special engineering/ commissioning modes	

Table2: Summary of SPIRE photometer observing modes

POF commands are split into two categories, Observatory Functions and Instrument Functions. Observatory functions are carried out by the telescope (primarily pointing, scanning and nodding). Instrument functions are carried out by the SPIRE instrument hardware, such as control of the BSM to produce beam chopping and the sampling of the detectors. Combinations of these two commanded timelines produce all POFs specified above.

1.11.1 Point source photometry (POFs 1 & 2)

Point source photometry (POF 1) is used for observing isolated compact objects and is identical to the standard observing mode used on ground-based submillimetre telescopes. Observations can be made by simply chopping the source while pointing the telescope precisely and nodding if required. If telescope pointing is not sufficiently accurate however, or the source position is not well defined, then a seven-point jiggle map may be used (POF 2). This is constituted by seven individual POF 1 observations carried out in a symmetrical pattern centered on the source, with the BSM being offset by some angle θ for each point.

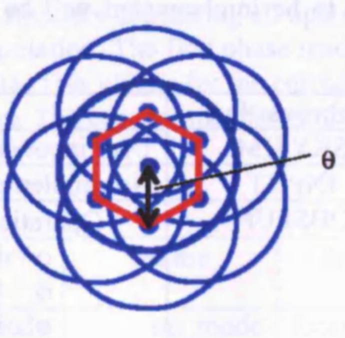

Seven-point hexagonal jiggle pattern.

1.11.2 Field mapping

POF 3 (field mapping) is for mapping of relatively small objects or regions, no greater than a few arcminutes in size. Implementation is identical to that of POF 1 but with a number of chop positions. In order to achieve full sampling in all wavebands 64 jiggle points must be used. POF 4 field mapping carries out a POF 3 observation at each point in a raster scan and can therefore be used to scan areas larger than the SPIRE field of view.

1.11.3 Scan mapping

Scan mapping (POF 5) is used in order to for large area maps – much bigger than the SPIRE field of view. In this configuration all three arrays observe simultaneously while the telescope scans across the sky at a rate of up to 1 arcminute per second. However should 1/f noise be significant, additional chopping motion can be added to introduce a higher frequency signal modulation. To achieve full spatial sampling with each of the hexagonally packed arrays the telescope scan angle must have a particular value of 77.6° with respect to the z-axis of the array.

1.12 Summary of total observation time for different cases

POF	Chop	Jiggle	Nod	Scan	N_{jig}	N_{nod}	Raster	Observation time
1	Yes	No	No	No	1	0	No	$t_{tot} = N_{chop} t_{chop}$
2	Yes	No	Yes	No	1	> 0	No	$t_{tot} = N_{nod} t_{nod}$
3	Yes	Yes	No	No	> 1	0	No	$t_{tot} = N_{jigcyc} t_{jigcyc}$
4	Yes	Yes	Yes	No	> 1	> 0	No	$t_{tot} = N_{nod} t_{nod}$
1 - 4							Yes	As above + Δt_{rast}
5	No	No	No	Yes	0	0	No	$t_{tot} = N_{lines} \left(\dot{\theta}_{line} \Delta\theta_{scan} + \Delta t_{turn} \right)$
6	Yes	No	No	Yes	0	0	No	As above

First version of the simulator

The first version of the simulator to be implemented will be a reduced version with the following features:

No.	Module	Abbreviation	Description
0	Sky Simulator	SKYSIM	User input sky files in FITS format (Jy/pixel)
1	Input	INPUT	Not implemented
2	Observatory Function	OBSFUN	• Operational observing modes: o POF 1 (point source photometry) o POF 2 (seven point mapping) o POF 3 (64 point jiggle mapping) o POF 5 (scan mapping without chopping) • Telescope pointing error with APE and linear

			drift implemented
3	Optical System	OPTICS	- Top-hat filter transmission. - Three modelled telescope beams, one for each detector array (no hexapod), i.e. beam is assumed to be equal in all detector within a single array - Detector selection options. - Convolution of input map with modelled beam
4	Thermal System	THERMAL	1/f thermal noise variations imposed on nominal stage temperatures. Input values not well known, for testing only.
6	Beam Steering Mirror	BSM	- 1, 7 and 64 point chopping operational - No noise added to commanded timeline - No power dissipation - Instantaneous BSM position switching
7	Incident background power timeline generator	BACKGROUND	- Background power based on emission from all optical elements - Optical elements assumed to be a constant temperature - All elements assumed to emit as a blackbody
8	Astronomical power timeline generator	ASTROPOWER	Astronomical power derived from pointing at convolved input sky map (output from optics module)
9	Bolometer voltage timeline generator	DETECTORS	- Output for all modules including option for non-linear operation beyond a set threshold - Option to use measure bolometer parameters as in input - Noise calculation performed based on calculated parameters - Choice of white or 1/f noise addition
10	Science Data Timeline Generator	SAMPLING	- Voltage data timeline filtering using measured filter profile - Data sampling at given input frequency
11	Housekeeping Data Timeline Generator	HK	Not implemented.
12	Calibrator Power Timeline Generator	PCAL	Not implemented.

Simulator Set-up (*Core*)

The simulator operating parameters, e.g. simulator time step, output mode etc., are initialised in the same way as other modules. The *core* structure containing all operating parameters receives two *input* phases in the first of a multiple run simulation. The first phase reads in the number of runs to perform, and the second reads the remaining data. This allows for the correct output file name to be given to subsequent runs in a multi-run situation. The core routine contains no input parameters.

Core parameters

Output category	Parent Module	Parameter	Name	Type	Units	Values	Description / comments
User	Core	Operating mode	op_mode	Integer		0,1	0 – single opertion 1 – repeat

							mode
User	Core	Number of runs	n_runs	Integer			
User	Core	Simulator time step	step_size	Float	s	Nom=0.012	
User	Core	Output file path	outputfile_path	String			
User	Core	Output file name	output_file	String			File name without file extension
User	Core	Output data mode	output_mode	Integer		0,1	0 – IDL 1 – FITS
User	Core	Output maps switch	output_maps	Integer		0/1	
User	Core	Output astronomical power switch	output_Qsig	Integer		0/1	
User	Core	Output voltage switch	output_Vout	Integer		0/1	
User	Core	Output noisy voltage signal switch	output_nsig	Integer		0/1	
User	Core	Output filtered signal switch	output_signal	Integer		0/1	

1.13 Sky Simulator (*sky*)

This module produces a simulation of an area of sky larger than the area to be observed. The output consists of three rectangular grids of sky positions with spacing significantly smaller than the 17" FWHM at 250 µm. There is one sky map per SPIRE array each with the same size and resolution. The intention is to use simulations produced by other groups where possible. Input files would be in FITS format and follow where possible the parameters outlined below.

Grid coordinate system: The lower left corner of the simulated area shall be designated as the (0,0) position on the spacecraft z and y axes respectively.

Grid units: angle on the sky in the spacecraft z-y plane, as measured in arcseconds

Grid spacing: square grid spacing of nominal value 2", corresponding to around 1/10th of a the narrowest SPIRE beam FWHM of 17". Other pixel integer pixel sizes up to 6" are also supported. Each pixel represents a square area of sky, and has an associated value of flux density (Jy/pixel).

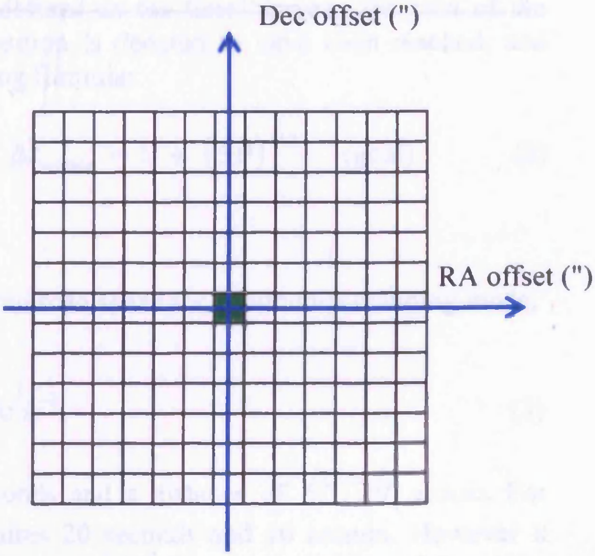

Representation of point sources: The delta-function of a point source is approximated by a single pixel with the appropriate flux density, superimposed on the representation of extended emission.

Once read in the FITS file will produce a 2D array of arbitrary dimensions with an associated flux density per pixel at each array point. There are three files to be read in, each representing the same area of sky at a different SPIRE photometer wavelengths. It is also required that the user input the sky resoluiton for the input map. These maps will be a representation of the true sky, i.e. unconvolved with any beam modelled. The simulator can support the input of preconvolved skies via an informational swtich set when inputting the simulation setup.

1.13.1 Module parameters

Input parameters

Input category	Parent Module	Parameter	Name	Type	Units	Values	Description / comments
User	Sky	PSW sky file	skyfilePSW	string			
User	Sky	PMW sky file	skyfilePMW	sting			
User	Sky	PLW Sky file	skyfilePLW	string			
User	Sky	Convolution requirement switch	needcon	integer		1/0	Allows the user to bypass the internal convolution routine
User	Sky	Sky resolution	pixel_size	float	arcsec	2	

Output parameters

Output category	Parent Module	Parameter	Name	Type	Units	Values	Description / comments
Map	Sky	PSW sky map	skyfilePSW	2D float array	Jy / pixel		
Map	Sky	PMW sky map	skyfilePMW	2D float array	Jy / pixel		
Map	Sky	PLW Sky map	skyfilePLW	2D float array	Jy / pixel		

1.14 Observatory Function (*obsfun*)

This module specifies the photometer observing mode to be simulated in terms of the appropriate Observatory Function and its parameters, as defined in the OMD. The observing parameters corresponding to the chosen POF are set up and the telescope pointing timeline, including associated pointing errors computed.

1.14.1 Telescope Movement

Re-pointing: The IID-A Section 5.12 specifies the requirement and goal for small slews executed during observations. The movement time, Δt_{motion}, is defined as the time between the start of the motion and the instant at which the new telescope position is deemed to have been reached, and depends on the angular distance according to the following formula:

$$\Delta t_{\text{motion}} = 10 + (2\Delta\theta)^{1/2} \quad \text{(req.)} \qquad \Delta t_{\text{motion}} = 5 + (\Delta\theta)^{1/2} \quad \text{(goal)} \qquad (2)$$

where $\Delta\theta$ is in arcseconds.

Accelerating and decelerating: In establishing the desired scan speed for continuous scanning mode, the spacecraft scan acceleration will be fixed at a value

$$\ddot{\theta} = 3 \quad \text{arcsec s}^{-2} \qquad (3)$$

To attain a scan rate of $\dot{\theta}$ arcsec s^{-1} takes $\dot{\theta}/\ddot{\theta}$ seconds and a distance of $\dot{\theta}^2/2\ddot{\theta}$ arcsec. For example, the maximum scan rate of 60 arcsec s^{-1} requires 20 seconds and 10 arcmin. However it should be noted that to reach the nominal scan rate of 30 arcsec s^{-1} requires 10 seconds and 2.5 arcmin. Hence the array will be at scanning speed yet the array will not have travelled a full array distance on the sky. This will result in a region at the beginning and end of each scan line (assuming equivalent deceleration) where full spatial sampling may not be achieved. As a result an adjustment may be necessary when setting up the observation to ensure that the correct area of sky is properly observed.

Nodding

The nodding movement time, Δt_{nod}, is defined as the time between the start of nod motion and the instant at which the new telescope position is deemed to have been reached (assumed to be the same for both nod directions). Δt_{nod} is given by Equation (2).

$$\Delta t_{\text{nod}} = 10 + (2\Delta\theta_{\text{chop}})^{1/2} \quad \text{(req.)} \qquad \Delta t_{\text{nod}} = 5 + (\Delta\theta_{\text{chop}})^{1/2} \quad \text{(goal).} \qquad (4)$$

For example, with θ_{chop} = 126 arcseconds, the nod time is 25 sec. (req.) or 16 sec. (goal).

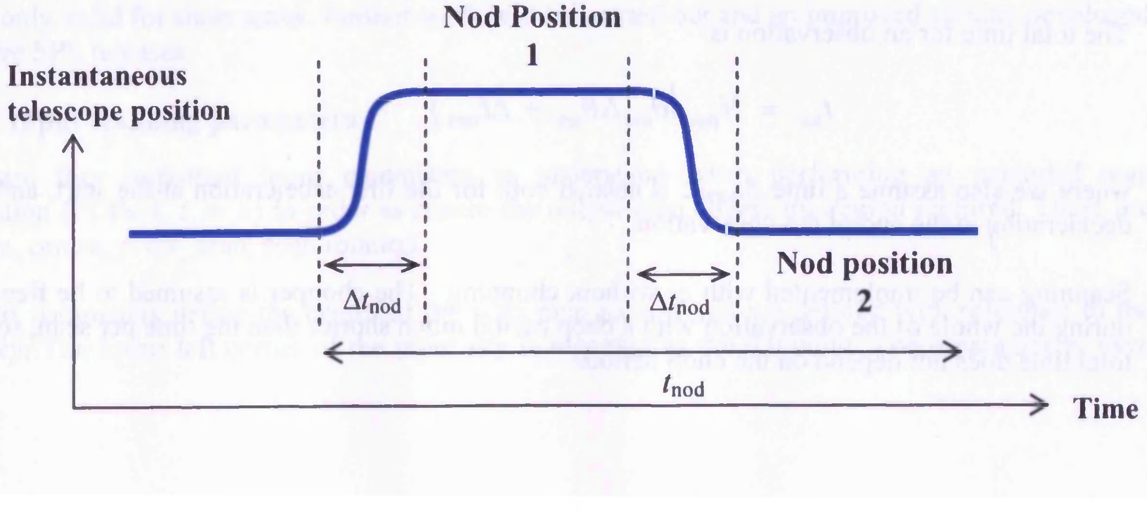

For the case of chopping without jiggling, the total time per nod cycle is

$$t_{\text{nod}} = 2\left(N_{chop}t_{chop} + \Delta t_{\text{nod}}\right). \qquad (5)$$

When jiggling is being carried out, the total time for a complete nod cycle involving N_{jigcyc} jiggle cycles per nod cycle is

$$t_{\text{nod}} = 2\left(N_{jigcyc}t_{jigcyc} + \Delta t_{\text{nod}}\right). \qquad (6)$$

The total number of nod cycles to be carried out in an observation is N_{nod}.

Rastering
A standard raster observation consists of N_{lines} lines with N_{steps} raster points per line. The raster movement times, Δt_{step} for repointing by $\Delta\theta_{\text{step}}$ along a line, or Δt_{line} for repointing by $\Delta\theta_{\text{line}}$ between lines, are also given by equation (1). For a raster of 4 x 4 arcminute jiggle maps, the step could be 3.5 arcmin (to provide some overlap between the sub-maps). The step time for each movement of the raster pattern is then ~ 30 sec. (reg.) or ~ 20 sec. (req.).

The total time spent in moving the telescope between raster positions is

$$\Delta t_{\text{rast}} = \left(N_{step} - 1\right)\Delta t_{step} + \left(N_{lines} - 1\right)\Delta t_{line}. \qquad (7)$$

Scanning
A standard scanning observation consists of N_{lines} scans, each of length $\Delta\theta_{\text{scan}}$ with spacing $\Delta\theta_{\text{line}}$. A line scan is not deemed to have started until the telescope has attained the required scan speed, $\dot{\theta}_{\text{line}}$. The telescope turn around time at the end of each line is Δt_{turn}, defined as the time between the end of one line scan and the start of the next. We assume that

(i) The times needed to accelerate and decelerate the telescope are equal
(ii) The acceleration/deceleration is instantaneous and constant upon beginning and ending a scan line
(iii) The telescope turns around using a square pattern, coming to rest as each corner

The total turn-around time is then then

$$\Delta t_{turn} = 2\dot{\theta}_{line} / \ddot{\theta}. \qquad (8)$$

The total time for an observation is

$$t_{\text{tot}} = N_{lines}\left(\dot{\theta}_{\text{line}}\Delta\theta_{\text{scan}} + \Delta t_{\text{turn}}\right) \qquad (9)$$

where we also assume a time $\Delta t_{\text{turn}}/2$ is needed both for the first acceleration at the start, and the last deceleration at the end of the observation.

Scanning can be implemented with or without chopping. The chopper is assumed to be free running during the whole of the observation with a chop period much shorter than the time per scan, so that the total time does not depend on the chop period.

1.14.2 Pointing error

Pointing noise characteristics

The pointing errors are defined and summarised in the IID-A Section 5.12 as follows:

$$\begin{aligned} APE\,[arc\sec] &= 3.7 + 0.05\dot{\theta} && \mathrm{Re}q. \\ &= 1.5 + 0.03\dot{\theta} && Goal \end{aligned}$$

$$\begin{aligned} AME\,[arc\sec] &= 3.1 + 0.03\dot{\theta} && \mathrm{Re}q. \\ &= 1.52 + 0.02\dot{\theta} && Goal \end{aligned}$$

where $\dot{\theta}$ is in arcsec s^{-1}.

$$\begin{aligned} RPE\,[arc\sec] &= 0.03 && Po\,\mathrm{int}\,ing \\ &= 1.2 && \mathrm{Re}q.\ scanning \\ &= 0.8 && Goal\ scanning \end{aligned}$$

Note: RPE refers to a 1-minute period
All values quoted are 68% probability (i.e., 1-σ)

All information pertaining to pointing errors is subject frequent change and thus these values should only be used as a guide.

Absolute pointing error
The absolute pointing error (APE) is implemented as a random positional offset in both the z and y direction upon the initialisation of each new pointing (this includes the beginning of each scan line). The input is the 1 sigma RMS value based on a 2D Gaussian probability distribution function. The input value is in units of arcseconds.

Relative pointing error
The relative pointing error is implemented as a linear drift superimposed on the commanded telescope pointing time line. This drift occurs for the full duration of the observation. The amplitude of the drift is derived from an input drift velocity variable. This variable defines the 2D Gaussian probability distribution from which the implemented drift velocity is derived. This input as the units of arcseconds per second. The direction of drift is derived via a random number generator.

This is only valid for short scans. Further work will be carried out and an improved version developed for future SPS releases.

1.14.3 Input scanning parameters

There are four important input parameters to understand when performing an extended map observation (POFs 4, 5 or 6) in order to ensure the output map covers the region required. These are centre_z, centre_y, dir_scan, scan rotation.

The start parameters define the centre of the scan map pattern and are defined with reference to the input sky. The lower left corner of the input sky is regarded as the 0,0 point. These parameters have the units of arcseconds. The input map resolution is used to scale these parameters to the input map pixelisation during the simulation.

The scan direction parameter defines the detector array orientation with respect to the satellite Y-Z axes. The angle is taken with reference to the z-axis. This angle is the 'magic angle' required for fully sampled mapping.

The scan rotation parameter rotates the entire scan map about the centre point (the 'start' values), i.e. represents the rotation of the scan pattern and sky coordinate systems. This allows for investigation of cross-linking etc.

All rotations are performed in a clockwise, i.e. right turning, direction.

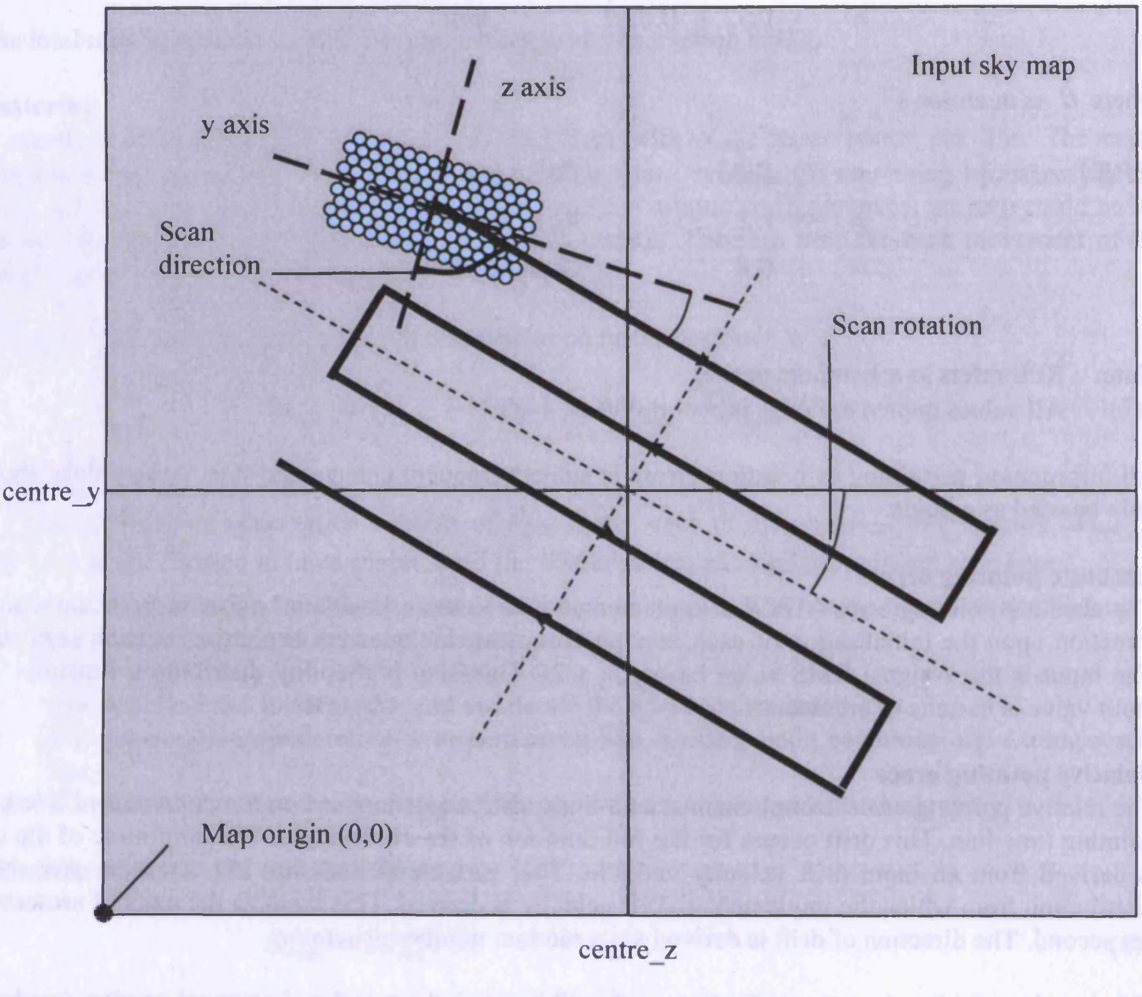

1.14.4 Module parameters

Input parameters

Input category	Parent Module	Parameter	Name	Type	Units	Values	Description/comments
User	obsfun	Scan start position (one parameter per axis)	centre_z centre_y	float	arcsec.		z-y axis offsets wrt the sky map (0,0) position of the only or initial telescope position for the observation = source position (POF 1, 2, 8) = map corner (POF3) = centre of first raster point (POF4)
User	obsfun	Chosen POF	POF	Integer		1 - 8	
User	obsfun	Absolute pointing error	APE	float	1 sigma rms value in arcsec	3.7	
User	obsfun	Relative pointing error	v_drift_rms	float	1 sigma rms value in arcsec	??	In the first version this is implemented as a linear drift

POF specific user input parameters

Parameter	Name	Units	POF								Values Description / comments	
			1	2	3	4	5	6	7	8		
Chopping ON	Chop		●	●	●	●	●	●	●	●	1 or 0	= 1 for all POFs except 3, 6, 8.
Chop Frequency	fchop	Hz	●	●	●	●		●	●		0.5, 1 . . . 5 Nom = 2	
Chop direction	chopdirn	Deg	●	●	●	●		●	●		0, 1 . . . 30 Nom = 0	Chop angle wrt S/C frame Y axis
Chop throw	Chop_throw	arcsec	●	●	●	●		●	●		0, 1 . . .180 Nom = 126 or 240	
Number of chop cycles per position.	n_chop		●	●	●	●		●	●		1, 2 . . . Nom > 5	
Nodding ON or OFF	Nod		●	●	●	●					1 or 0 Nom = 0	
Number of nod cycles/raster posn.	N_{nod}		●	●	●						0, 1, 2 ...	

Angle defining rotation of raster pattern axes wrt array Y axes	ϕ_{rast}	Deg.									0 - 180	0.1 deg. resolution
No. of telescope raster pointings per raster line	N_{steps}					●					1 - 32	= 1 except for POF 4
Number of lines for scan or raster	Nlines					●	●	●	●		1 - 32	= 1 except for POF 4
Angular distance between points on a raster line	$\Delta\theta_{step}$	arcsec				●					2 - 480	0.5 arcsec resolution Equivalent to d_1 in the HPM doc.
Angular distance between raster or scan lines	LineSep	arcsec				●	●	●			2 - 480 or 0	0.5 arcsec resolution Equivalent to d_2 in the HPM doc.
Scan angle	Dir_scan	deg					●	●			0 - 90 14.5 nom=12.4	Angle with respect to the y axis
Scan rate	ScanRate	Arcsec/s					●	●			0.1 - 60 Nom = 30	0.1 arcsec resolution
Angular length of each scan line	LineLength	arcsec					●	●			20" - 20 deg.	5 arcsec. resolution Equivalent to D_1 in the HPM doc.
Telescope acceleration	Telescope_a	Arcsec/s^2					●				3”/s^2	
Line separation	Linesep	arcsec					●	●			235”	
Scan rotation	Scan_rot	deg					●	●				Map rotation about centre of the map

Generated command timeline: Commanded telescope position vs. time

Output category	Defining Module	Parameter	Name	Type	Units	Values	Description/comments
Timeline	Obsfun	Telescope Pointing, z	DirZ	1D float array	arcsec		True array of scanned z-coordinate positions on sky map vs. time
Timeline	Obsfun	Telescope Pointing, y	DirY	1D float array	arcsec		True array of scanned y-coordinate positions on sky map vs. time
Timeline	Obsfun	Sampled telescope pointing, z	DirZsamp	1D float array	arcsec		Sampled version of DirZ
Timeline	Obsfun	Sampled telescope pointing, y	DirYsamp	1D float array	arcsec		Sampled version of DirY

1.15 Optical System (*optics*)

This module represents the main optical properties and parameters for the telescope and the SPIRE instrument optics, including the detector feedhorns. It computes the overall Relative Spectral Response Function (RSRF) the three bands. Also the input sky maps are convolved here with a modelled telescope beam. Finally the selection of operational detector pixels is performed and their positional sky offsets calculated.

1.15.1 Telescope properties

The telescope is characterised by its used diameter, emissivity, focal ratio and obscuration factor.

1.15.2 Mirror and filter properties

The optical properties of the mirrors and filters (transmission, emissivity) are characterised as a function of frequency over a vector of frequencies ν_j to allow various parameters to be integrated over the bandwidth of the filter or the ISRF.

For simplicity, the same frequency vector shall be used to cover all of the components, and will cover the range 3 x 10^{11} Hz (1 mm) to 3 x 10^{12} Hz (100 μm), with a spacing of 3 x 10^{9} Hz (a total of 901 points).

Each component in the optical chain is described by the following parameters:

Index corresponding to positional order of the component in the optical train	i
Transmission profile for the component	t_PxW
Emissivity profile for the component	e

Note: the optical parameters of the mirrors will be assumed to be independent of frequency over a given band.

The positions of the instrument components are as indicated in the diagram below (from *SPIRE Filter Specification Document*) and summarised in the following table. This standard optical element numbering convention assigns each subsequent optical element a number referring to its position in the optical chain, with elements 0 being the telescope primary.

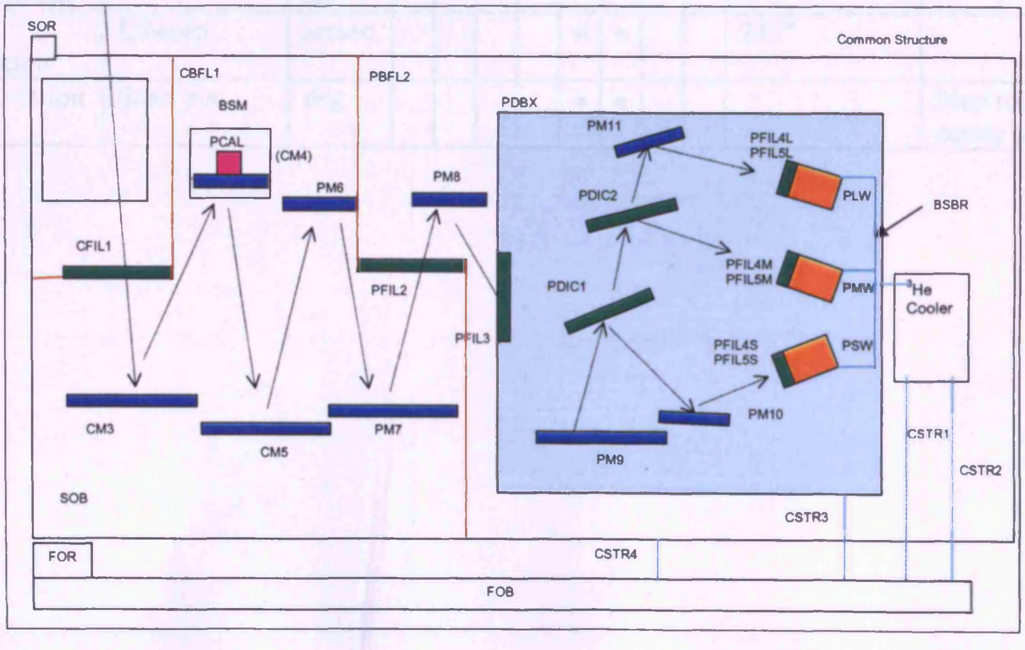

c	Component			Temp. Level	Description
0	M1			1	Telescope primary
1	M2			1	Telescope secondary
2	CFIL1			1	Input filter
3	CM3			1	Input mirror
4	CM4			1	BSM
5	CM5			1	Reimaging mirror
6	PM6			1	Field
7	PM7			1	First Offner relay mirror
8	PFIL2			1	Thermal blocker at baffle between PM 7 and PM8
9	PM8			1	Second Offner relay mirror
10	PFIL3			0	Thermal blocker at 2-K cold stop
11	PM9			0	Third Offner relay mirror
12	PDIC1			0	First dichroic
	PLW	**PMW**	**PLW**		
13	PM10				Flat in front of PSW array
14	PFIL4S			He-3	300-mK filter over PSW array
15	PFIL5S			He-3	300-mK filter over PSW array
16		PDIC2	PDIC2	He-3	Second dichroic
17		PFIL4M		He-3	300-mK filter over PMW array
18		PFIL5M		He-3	300-mK filter over PMW array *
19			PM11	He-3	Flat in front of PLW array
20			PFIL4L	He-3	300-mK filter over PLW array
21			PFIL5L	He-3	300-mK filter over PLW array *

* Baseline: not implemented – but provision should be made in the simulator

1.15.3 Detector arrays and detector positions

All detectors are defined by their y and z positional offsets with respect to the centre of the PSW array. The geometrical centre of the PSW array is defined to be coincident with the telescope pointing boresight. These y and z offsets are translated into pointing offsets on the sky by multiplication with the plate scale. It is these pointing offsets that are imposed onto the final telescope and BSM pointing timelines to provide individual pointing information for each detector. Each detector position parameter can be given a slight random scatter if manufacturing errors are required to be represented.

Each detector is assigned a number defined by its position within the array. Numbers start at 0 and run to 138 in the case of the PSW array. Numbering begins at the bottom left of the array and increases as shown. Addition pixels such as dark pixels and thermometers are appended to the end of this number sequence. The full comparison with the JPL pixel specification scheme can be found in Appendix I.

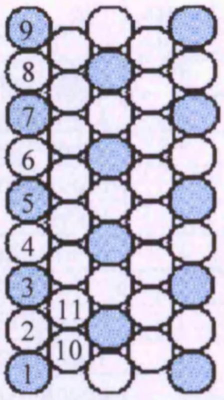

Beam profiles: Each detector has a beam profile on the sky, represented by a modelled telescope beam, computed using a Hankel transformation. Each beam is characterised by its FWHM. Errors in each beam could also be incorporated to mimic the unique errors that may occur during feedhorn manufacture. Such errors are planned for future simulator development and are not included at the current time. This includes implementation of beam vignetting.

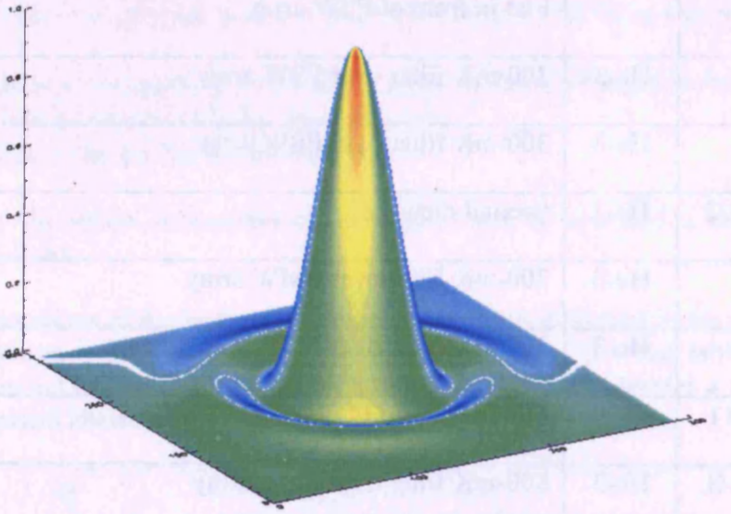

In general, beam errors could be different for different detectors in an array. In the first instance however, it will be assumed that all detector beams are identical for a given array.

Feedhorn throughput: Each detector has an optical throughput (*AΩ*), nominally equal to λ^2.

Spillover efficiency: A fraction ηs of the throughput from each detector illuminated the telescope pupil (and a fraction 1 - ηs is assumed to terminate on the walls of the level-1 enclosure. The value of ηs is assumed to be the same for all detectors in a given array.

Feedhorn/cavity efficiency: Each detector has an optical efficiency, $\eta feed$, equal to the fraction of the horn throughput (*AΩ*) which is absorbed by the bolometer.

Diffraction loss: Each detector has associated with it a value for the diffraction loss introduced by the optical system, $\eta diff$.

Cutoff wavelength: Each detector feedhorn has a diameter *dwav*, which determines the cutoff wavelength.

1.15.4 Module operation

This module operates in a non-time-stepping mode. All optical element transmission and emissivity profiles are contained within input files. The path and name of these files is stored within an input file specified by the user. The order of the input files represents the order of the optical chain, beginning with the primary mirror and increasing towards the detector array.

Transmission matrices are initialised for each waveband based on the input data (*MirrorNo* and *OrderPxW*) and associated pointers are assigned. The transmission calculator function, set within the *optics* code is then stepped through once for each waveband, producing the output transmission array.

The output arrays are 2D arrays of dimensions *frequency array length* columns, by *MirrorNo* rows. Each row represents the effective transmission profile after passing through optical elements 0 – row number. Production of different optical configuration transmission arrays can be simulated by input of different optical chain order inputs (*OrderPxW*) to the transmission calculator function.

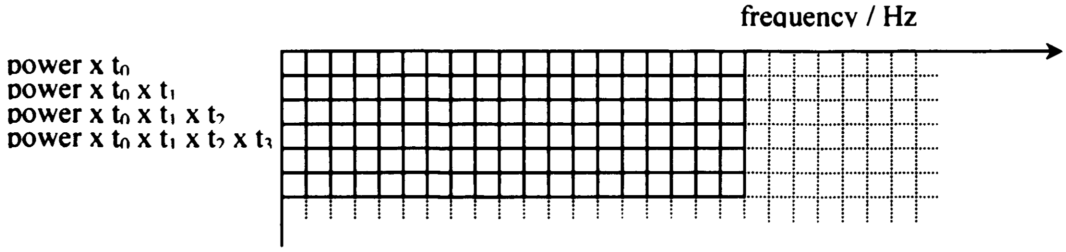

Convolved input sky maps are produced using a pre-modelled telescope beam pattern kernel. A beam model equivalent in resolution to that of the input map is used. Pre-modelled beams exist for input map resolutions from 1 to 6"/pixel in integer steps (input maps must match this resolution, i.e. be in integer arcsec steps).

Finally the chosen detector array pixels are identified from the user input and their sky positional offsets calculated. Selection is carried out via a graphical user interface (array_gui.pro), which allows selection of individual detectors, or a choice of either full arrays or all co-aligned pixels. Opting to use less detector pixels results in a faster run time, however a minimum of one pixel must be selected in each array.

1.15.5 Module parameters

Input Parameters

Input category	Parent Module	Parameter	Name	Type	Units	Values	Description/comments
User	Optics	Telescope obscuration factor	eta_obsc	Float		0.872	
User	Optics	Telescope focal ratio	F_{tel}	Float		8.68	
User	Optics	Array focal ratio	Ffin	Float		5.0	
User	Optics	Filter data file	filterdatafile	string			File containing file names + paths of files containing filter transmission profiles. List follows optical element numbering convention order.
User	Optics	Filter temperature file	filtertempfile	string			File containing optical element temperatures. List follows optical element numbering convention order. Implemented in v1.0, i.e. no temperature fluctuation with time.
User	Optics	Emissivity data file	emissivitydata	string			File containing file names + paths of files containing filter emissivity profiles. List follows optical element numbering convention order.
User	Optics	Gaussian	FWHM	Float	arcsec	17, 25,	Nominally

		beam profile				36	assumed to be the same for all detectors
User	Optics	Feedhorn / cavity efficiencies	eta_feed	Float		0.7	Nominally identical for all detectors in an array (maybe include some spread)
User	Optics	Feedhorn throughputs for each detector in the three arrays	eta_tel	Float		0.7	Nominally identical for all detectors in an array
User	Optics	Observing wavelength	PSWlambda PMWlambda PLWlambda	Float	microns	250, 363, 517	
User	Optics	Operating detectors	detectorPSW detectorPSW detectorPSW	1D float array			Array detuning which number detector operates during an observation
User	Optics	Telescope effective diameter	Dtel	Float	m^2	3.285	
User	Optics	Optical chain order x3, one for each band	OrderPSW OrderPMW OrderPLW	1D integer array			Optical chain order for specified waveband, e.g. for PLW, (1, 2, 3, 4, 5, 6, 7, 8, 9, 10, 11, 12, 16, 19, 20, 21).
User	Optics	Telescope emissivity vs. frequency	e	1x900 flaoting point array		TBD formula	Derived from input data file
User	Optics	Index for positional order of each component	i	Integer		1 - 23	
User	Optics	Transmission profile for each component	t	1x900 flaoting point array			Derived from input data file
User	Optics	Emissivity profile for each component	e	1x900 flaoting point array			Derived from input data file

User	Optics	Number of mirrors	MirrorNo	integer		22	Number of mirrors in optical entire system (telescope + instrument)
User	Optics	Detector positions	PSWz_pos PSWy_pos PMWz_pos PMWy_pos PLWz_pos PLWy_pos	1D float array	arcsec		Arrays defining detector positions on the sky wrt the PSW central pixel
System	Sky	Input sky map	SkymapPSW SkymapPMW SkymapPLW	2d float array	Jy/pixel^2		
System	Sky	Convolution requirement switch	needcon	integer		1/0	Allows the user to bypass the internal convolution routine

Derived parameters

Output category	**Parent Module**	**Parameter**	**Name**	**Type**	**Units**	**Values**	**Description/comments**
Map	Optics	Convolved sky maps	*ConskyPSW* *ConskyPMW* *ConskyPLW*	2D float array	Jy		Maps at each wavelength of the input astronomical sky convolved with the appropriate telescope beam
System	Optics	Instrument spectral response function. In-band transmission from each optical element to each detector array	t_PSW t_PMW t_PLW	2D float array		t_1 x t_2 x … x t_n where t_x is the xth optical element transmission profile	Overall spectral response of the complete system (telescope + instrument) to the detector +

System	Optics	Detector pixel sky offsets	PSWz_pos PSWy_pos PMWz_pos PMWy_pos PLWz_pos PLWy_pos	1D float array	arcsec		Pointing offsets for operational detector array pixels.

1.16 Thermal System (*thermal*)

This module characterises the temperatures of all relevant elements and their time variations. A vector of temperature deltas vs. time describes thermal drifts of elements within the system for the timeline duration. The thermal noise originates from ^{3}He stage fluctuations. This time line is used as an input to the detector model (To parameter).

1.16.1 Module operation

1.16.1.1 Origin of thermal fluctuations

Thermal fluctuations are expected to be a primary source of correlated noise within the SPIRE instrument. Correlated noise in this case refers to noise common to all detectors and experienced simultaneously, or near simultaneously. This does not however mean that the response of each detector to this noise is equal (see the detectors module documentation within the SPS document for more information). There are many sources that add to the overall thermal fluctuations within the system, however their resultant impact can be modelled as a single thermal noise timeline. This is reasonable for the case of the SPS, as it is the effect on the detector output that is of interest.

1.16.1.2 Modelling method

We have chosen to take the ^{3}He cooler as our primary source of thermal fluctuations. A 1/f noise timeline is simulated with a given thermal noise spectral density, with units of KHz$^{-1/2}$, and 1/f noise knee frequency, f_k, with units of Hz.

The bolometer detector arrays (BDA) within SPIRE are connected to this cooler via a series of cold fingers. In addition to this the detector arrays themselves are directly coupled to a large thermal mass. As a consequence of this, any thermal fluctuations arising in the cooler are low-pass filtered by the time they reach the bolometers. This is modelled here using a first order low pass filter profile, with a different time constant, in seconds, for each array. The different time constants represent the different ways in which the thermal noise will manifest itself in each array. The original input noise timeline remains fixed for each array; only the filtering changes the thermal noise timeline seen by the three detector arrays.

1.16.1.3 Input Values

Given the difficultly in accurately measuring or predicting the operational thermal environment of SPIRE, the nominal values to be used within the SPS are chosen, so as to present a challenging task for data analysis systems. This will allow for the development of robust data analysis tools.

Values for the noise spectral density, 1/f noise knee frequency, and three time constants are required. In order that the noise represents many sources of thermal fluctuation, in addition to that of the cooler, the noise spectral density will be given a value higher than that expected from most ^{3}He fridges. This value should also be set so as to produce a noise timeline with large-scale deviations several times those arising from independent detector 1/f noise sources alone. We have found a value of 50 μKHz$^{-1/2}$ works well.

To ensure significant variation within a single scan line, a 1/f noise knee frequency of approximately 30 mHz will be used. This allows for approximately 4 1/f noise timescales to pass during a 1 degree scan line, scanning at the nominal rate of 30"/s. It also sets the thermal 1/f noise knee close to the detector 1/f noise knee, making the identification of one from the other a more difficult task.

Thermal time constants can be estimated from current data. Values are expected to range from 70 – 130 s, with a nominal value of 100 s. From this the chosen nominal SPS values to be 70, 100, and 130 s, for the photometer short, medium, and long wavelength arrays respectively.

1.16.1.4 Implementation

The initial 1/f noise time line is produced using the standard SPS 1/f noise timeline generator (see SPS documentation for information). The Fourier transform of this timeline is then performed, and the resultant frequency spectrum multiplied by the appropriate first order filter profile. The inverse transform is then performed to return the final thermal noise timeline.

This noise timeline is input to the bolometer model as the detector array base temperature, T_o.

1.16.1.5 Sample data

Figure 2 shows a sample detector output voltage timeline. This timeline shows the result of an input thermal drift, generated as outlined above (red line), with input parameters of 50 $\mu KHz^{-1/2}$ thermal stability, f_k = 30 mHz, and τ = 70 s, for a single PSW detector. Significant thermal drift can be seen on the scale of approximately 2 minutes. In addition, the final detector output timeline (before onboard low-pass filtering), including independent 1/f noise contribution from the detector electronics and readouts, is shown in black. The amplitude of the independent non-thermal 1/f noise in this case is set to the nominal SPIRE values, with a 1/f noise knee frequency of 100 mHz.

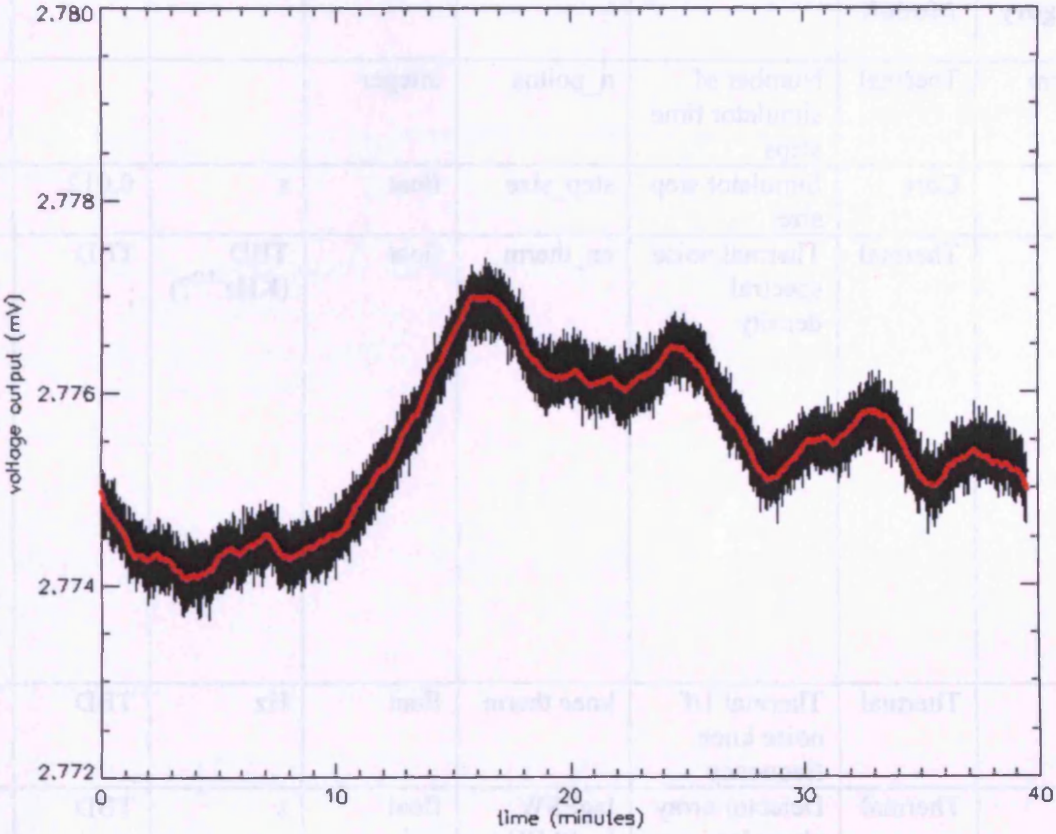

Figure 2: Sample detector output resulting from thermal drift

Figure 3 shows the impact of the thermal drift seen in **Figure 2** in the form of a map (PSW array). Large correlated thermal drifts, in addition to independent uncorrelated noise variations can be clearly seen. No data processing has been performed on these data beyond the low pass filtering imposed by the on-board 5 Hz filter.

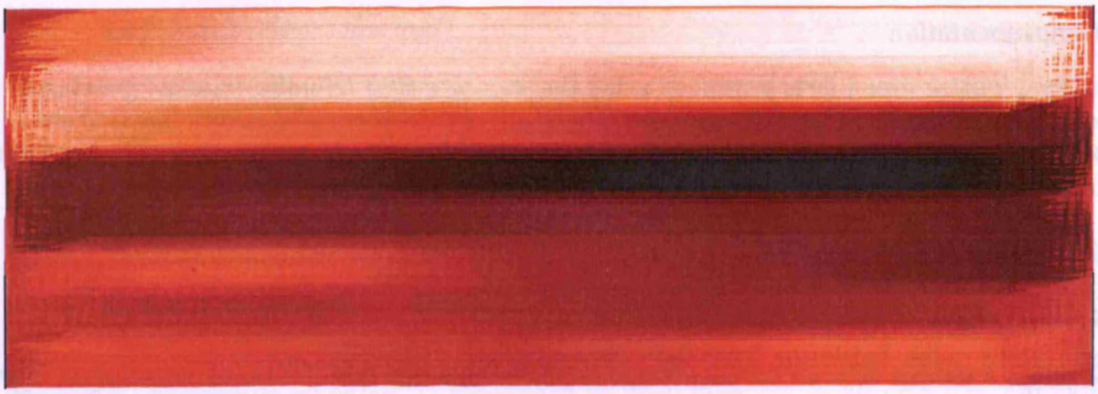

Figure 3: Map of blank sky. Includes both correlated and uncorrelated 1/f noise.

1.16.2 Module parameters

Input Parameters

Input category	Parent Module	Parameter	Name	Type	Units	Values	Description/comments
System	Thermal	Number of simulator time steps	n_poitns	integer			
User	Core	Simulator step size	step_size	float	s	0.012	
User	Thermal	Thermal noise spectral density	en_therm	float	TBD (KHz$^{-1/2}$?)	TBD	Value unknown. If set to large could cause non-physical response e.g. negative temperature
User	Thermal	Thermal 1/f noise knee frequency	knee therm	float	Hz	TBD	
User	Thermal	Detector array phase lag	lagPSW lagPMW lagPLW	float	s	TBD	
User	Thermal	Nominal base plate temperature	T0_nom	float	K	0.3	

Output parameters

Output category	Parent Module	Parameter	Name	Type	Units	Values	Description/comments

Time line	Thermal	Thermal noise time line	T0_PSW T0_PMW T0_PLW	1D float array	K		Early model only. May introduce cooler recycle variations. Primary source of common mode noise

1.17 Beam Steering Mirror (*bsm*)

This module simulates the required motion of the BSM and produces a timeline corresponding to the pointing modulation that it produces.

1.17.1 BSM properties

The main BSM properties and requirements are summarised in the BSM SSSD. The key parameters for the simulator are the chop and jiggle settling times and the positional stability.

Assumption: the BSM rest position on the array plane is assumed to be (0,0)

1.17.2 Definition of chopping parameters and times

1.17.3 Chopping

Chopping through an angle $\Delta\theta_{\text{chop}}$ is normally along the Y-axis, and normally symmetrical about (0,0). The left beam is defined as the one on the negative side of the Y-axis and the right beam as the one on the positive side.

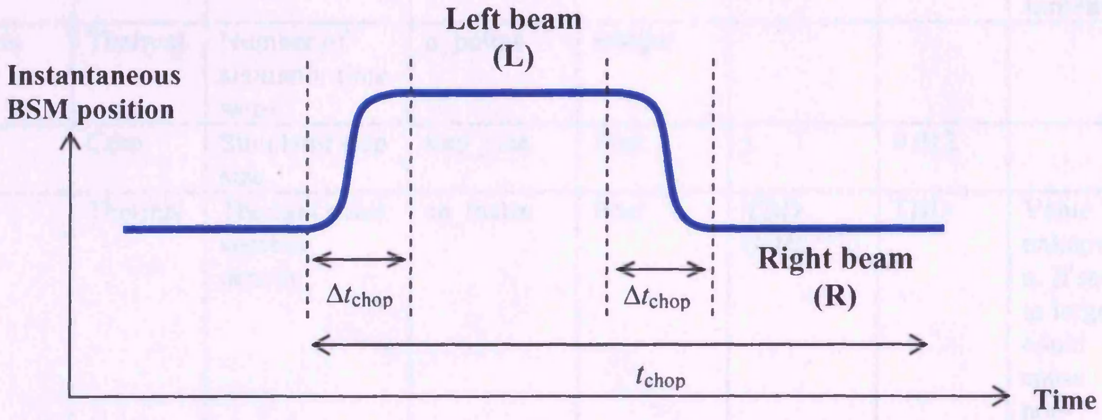

The time for one complete chop cycle is t_{chop}. Δt_{chop} is the time between the start of chop position motion and the instant at which data are deemed valid (BSM sky position within 1" of the required position). The total "dead time" for one chop cycle is thus $2\Delta t_{\text{chop}}$. The nominal value of Δt_{chop} is 20 ms (BSM SSSD).

1.17.4 Jiggling

A jiggle cycle involves N_{jigpos} BSM positions. The time taken to move from one jiggle position to another is Δt_{jig}. The chopping motion is interrupted for a time Δt_{jig} while the jiggle axis moves to an new position, and then chopping is resumed. The nominal value of Δt_{jig} is 100 ms (BSM SSSD).

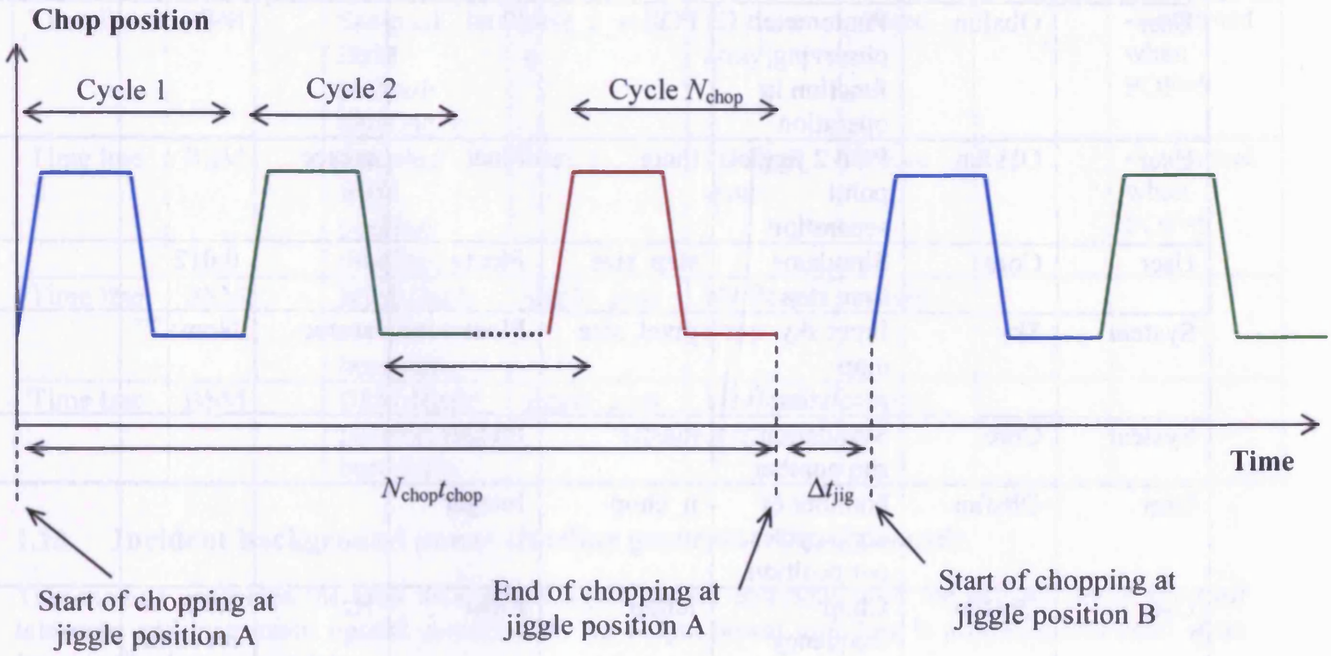

The total time taken for a complete jiggle cycle of N_{jigpos} positions, involving $N_{\text{jigpos}} - 1$ jiggle position movements is

$$t_{\text{jigcyc}} = N_{\text{jigpos}}\left(N_{\text{chop}}t_{\text{chop}}\right) + \left(N_{\text{jigpos}} - 1\right)\left(\Delta t_{\text{jig}}\right) \qquad (10)$$

Note that in the case of chopping without jiggling, t_{jigcyc} reduces to $N_{\text{chop}}t_{\text{chop}}$.

1.17.5 Module operation

BSM movement is assumed in the current version of the simulator to move instantaneously between consecutive pointings. These pointings are also assumed to contain no error. Time lags between pointing are planned for future versions of the simulator and will follow the plan set out above.

In the case of no BSM operation (e.g. POF 5 scan map mode) scalar values of –1 are returned in the BSM pointing time line parameters. Computation of the BSM time lines are performed independent of any telescope pointing time line generation.

When performing a 64 point jiggle map a set of normalised pointing positions are restored from file *'jiggle_64pt.xdr'*. System parameters are used (detector array beam separation) in conjunction with these data to compute a the full 64 point jiggle map pointing coordinate.

Version 1 of the SPS supports operation of POFs 1 (point source photometry), 2 (7 point mapping), 3 (64 point jiggle mapping), and 5 (scan mapping without chopping).

1.17.6 Module parameters

Input Parameters

Input category	Defining Module	Parameter	Name	Type	Units	Values	Description/comment

							s
User	Obsfun	Photometer observing function in operation	POF	Float		1-8	
User	Obsfun	POF 2 jiggle point separation	theta	Float	arcsec		
User	Core	Simulator time step	step_size	Float	s	0.012	
System	Sky	Input sky map resolution	pixel_size	Float	arcsec	Nom=2”	
System	Core	Simulation run number	master	Integer			
User	Obsfun	Number of chop cycles per position	n_chop	Integer			
User	Obsfun	Chop frequency	fchop	Float	Hz	1.98 recommended, Nom=2	
System	BSM	Detector pixel on sky separation	pixel_separation	Float	arcsec		Defined for PLW array
User	Obsfun	Chop throw	chopthrow	Float	arcsec		
User	Obsfun	Chop direction	chopdirn	Float	degrees		
User	Sampling	Sampling time step	sampstep	Float	s	0.036	

Output parameters

Output category	Defining Module	Parameter	Name	Type	Units	Values	Description/comments
Time line	BSM	Commanded BSM position timeline, z	bsm_zcom	1D float array	arcsec		Not active in SPS V1
Time line	BSM	Commanded BSM position timeline, y	bsm_ycom	1D flaot array	arcsec		Not active in SPS V1
Time line	BSM	BSM position timeline, z	bsm_z	1D float array	arcsec		-1 returned when POF=5
Time line	BSM	BSM position timeline, y	bsm_y	1D float array	arcsec		-1 returned when POF=5
Time line	BSM	BSM chop flag	bsm_flag	1D float array		1/0	
Time line	BSM	Sampled BSM chop	bsm_flag_samp	1D float array		1/0	

		flag					
Time line	BSM	Sampled BSM position timeline, z	bsm_z_samp	1D float array	arcsec		-1 returned when POF=5
Time line	BSM	Sampled BSM position timeline, y	bsm_y	1D float array	arcsec		-1 returned when POF=5
Time line	BSM	BSM Jiggle position wrt boresight	jiggle_posz	1D float array	arcsec		
Time line	BSM	BSM Jiggle position wrt boresight	jiggle_posy	1D float array	arcsec		

1.18 Incident background power timeline generator (*background*)

This module computes the total incident background flux contribution at the detector array from all telescope and instrument optical components. An output power time line is produced and used as an input to the detector model.

1.18.1 Module operation

Required variables are derived from the optics module. All optical components are assumed to emit as a blackbody. The integrated power is then computed over the full SPS frequency range ($3\text{x}10^{11}$ – $3\text{x}10^{12}$ Hz) for each optical element, taking in to account the emissivity and optical transmission profiles (as shown below). The output is then multiplied by the requisite efficiencies to produce a final background power for this element. This processes is stepped through for all optical elements in each waveband and finally summed to produce a single value for the total background power in each waveband.

$$Q_{background} = A\Omega\eta\int_{3\times10^{11}}^{3\times10^{12}}\varepsilon(\nu)t(\nu)B(\nu,T)d\nu$$

$Q_{background}$ – background power produced by a single optical element
A – telescope area
Ω – solid angle
η – feedhorn efficiency
ε – emissivity of optical element
$t(\nu)$ – optical transmission of optical element as seem by the detector
$B(\nu,T)$ – blackbody radiation as a function of frequency ν, and temperature T

It is assumed that the incident background power on each detector within an array is equal.

Input Parameters

Input category	Parent Module	Parameter	Name	Type	Units	Values	Description/ comments
System	Optics	Transmission profile for each component	t_PSW t_PMW t_PLW	2D float array			
User	Optics	Total number of optical	MirrorNo	Integer		22	

		system components					
System	Optics	Optical chain for three arrays	OrderPSW OrderPMW OrderPLW	1D integer array			
System	Obsfun	Z axis telescope pointing array	DirZ	1D float array	arcsec		Used to determine total number of samples with the observation
System	Optics	Optics emissivity	e	2D float array			
System	Optics	Optics temperatures	temp	1D float array	K		
User	Optics	Feedhorn efficiencies	eta_feed	float		0.7	
User	Optics	Spillover efficiency	eta_spill	float		0.7	
User	Optics	Central band wavelengths	lambda	1D float array	m	250e-3 363e-3 517e-3	
User	Optics	Number of row in frequency vector	rows	integer		900	

Output parameters

Output category	Defining Module	Parameter	Name	Type	Units	Values	Description/comments
Time line	Background	Nominal static background power level absorbed by each detector	QbackPSW QbackPMW QbackPLW	1D float array	W		Total background power from each optical element.

1.19 Astronomical power timeline generator (*astropower*)

This module calculates the timelines for the absorbed astronomical signal power for each detector.

1.19.1 Module operation

Following the initialisation of the required variables, a convolved sky map is formed, either by convolution of the given sky map with a simulated telescope beam, or by direct loading into memory a convolved sky map data file (this can be done if the sky map being used has previously been convolved and stored).

The flux density measured at the detector for each scanning point is then found by taking a 2D linear interpolation of the convolved sky map for each observation scan position. This is then multiplied by the appropriate transmission profile to give the flux density at the detector. These values are then integrated over the frequency range using the Simpson integration method and multiplied by the necessary efficiency factors and constants resulting in an astronomical power value. The output is an array in each waveband of the total astronomical power at the detector for each scan point observed.

The total astronomical signal power falling on a detector in a single time step is given by below.

$$Q_{signal} = A\Omega\eta_{feed}\eta_{tel}S_{\nu}10^{-26}\int_{3\times10^{11}}^{3\times10^{12}} t(\nu)d\nu \qquad (11)$$

Q_{signal} – signal power / W
A – telescope area
Ω – telescope solid angle
η_{feed} – feedhorn efficiency
η_{tel} – feedhorn point source coupling efficiency
$t(\nu)$ – optical transmission of optical element as seem by the detector
S_ν – central waveband frequency ($\nu \sim 1.2, 0.8, 0.6$ THz) flux density / Jy

Signal power in integrated over the range of the specified frequency vector ($3\text{x}10^{11} - 3\text{x}10^{12}$ Hz).

1.19.2 Module Parameters

Input Parameters

Input category	Parent Module	Parameter	Name	Type	Units	Values	Description/comments
System	Optics	Instrument optical transmission matrices for each array	t_PSW t_PMW t_PLW	array			Transmission matrices containing data for transmission of full optical chain
System	Optics	Convolved sky maps	conskyPSW conskyPMW conskyPLW	2D float array	Jy/pixel		Array containing sky map convolved with telescope beam.
System	Obsfun	Telescope pointing timeline	DirZ DirY	array	arcsec		x and y sky position pointing coordinates

System	Optics	Detector pixel sky offsets	PSWz_pos PSWy_pos PMWz_pos PMWy_pos PLWz_pos PLWy_pos	1D float array	arcsec		Pointing offsets for operational detector array pixels.
System	BSM	BSM pointing timeline	bsm_z bsm_y	1D float array	arcsec		
User	Optics	Feedhorn efficiencies	eta_feed	float		0.7	
User	Optics	Aperture efficiency	eta_A	float		0.7	
User		Obscuration factor	eta_obsc	float		0.872	
User		Telescope effective diameter	Dtel	float	m	3.285	
System	Core	Simulation run number	master	Integer			
User	Sky	Pixel size		float	arcsec	Nom=2”	

Output Parameters

Output category	**Parent Module**	**Parameter**	**Name**	**Type**	**Units**	**Values**	**Description/comments**
Time line	Astro-power	Absorbed astronomical power timeline for each detector	QPSW QPMW QPLW	2D float array	W		Astronomical power at each pointing position.

1.20 Detector voltage timeline generator (*detectors*)

This module models the detector response to an input background and astronomical power via a full physical model of the system. The model used is based on the work by Sudiwala et al. (2002), and is implemented in order to generate realistic bolometer response for the flight detector arrays. This includes the ability to generate a non-linear output in response to a sufficiently high power input. In addition, measured flight detector parameters can be input, thereby generating a unique response to any system variation, such as fluctuation in thermal environment, for each bolometer.

1.20.1 Module operation

1.20.1.1 Bolometer Response

The bolometer module is relatively complex in its operation and should not be altered without the input from the author or a member of the SPIRE instrument team familiar with bolometer theory. The detector module requires initialisation before it can be used to begin an observation. This is due to the fact that in order to perform an observation an operating point must first be defined and set in to the common blocks used to store detector module parameters. Subsequent time steps compare new inputs with those from a previous time step in order to determine the level of change within the system, and hence the bolometer response, before computing a new output.

In cases where key parameters change, such as the detector array base plate temperature or background power, a recalculation of each bolometer operating point is required. The operating point is found using a Newton Raphson method to compute the correct bias parameter. A bias parameter is set and the associated bias voltage for that parameter found. This is then compared to the actual bias voltage set within the system. Once the bias voltage associated with the bias parameter is within some tolerance, the operating point is obtained. Each time a new operating point is calculated, new values for responsivity and detector time constant are derived, and used in the computation of the detector response.

In cases of high astronomical signal the detector response will become non-linear. A threshold is set for this condition, the value being set from tests or as a compromise for computational power. Up until this threshold is reached the previous operating point and associated parameters are assumed to be constant, and a linear response computed. In cases where the astronomical signal becomes greater than a small fraction of the nominal background power (~5%), the detector's operating point and parameters are recalculated, and the new operating point is compared to the previous voltage and taken as the new voltage change (dV). The time constant is taken to be the mean of the time constant at each operating point.

1.20.1.2 Noise

Noise spectral density estimates are made for each independent detector via a series of equations (Sudiwala et al. 2002). The noise estimate is made based on the initial bolometer parameters. Only one value of noise spectral density is computed for any individual detector. The noise estimates include contributions from photon noise arising from the primary and secondary mirrors (background power dominated), phonon noise, load resistor noise, Johnson, and amplifier noise. These replicate the noise sources specified in the official SPIRE sensitivity document.

These noise estimates are input to a noise time line generator. The noise generator uses this noise estimate along with 1/f noise knee frequency data to output a unique 1/f noise time line for each detector. The 1/f power spectrum is imposed in Fourier space via multiplication with a white noise time line. The white noise has a Gaussian probability distribution with the RMS value set to $e_n \times \sqrt{\Delta f}$, where e_n is the noise spectral density, and Δf is the frequency bandwidth corresponding to the specified simulator time step.

1.20.1.3 Bolometer Parameters

There are two options when selecting the bolometer parameters to be used within the detector model. The first assumes that each detector is identical, giving every bolometer the same nominal bolometer parameters for a given array. The second option is to use the JPL measured bolometer parameters. These are read in from a parameters file. The choice is made by selecting either to have the 'real bolometer parameters' on or off (1/0) in the detectors parameters file (`params_detectors.txt`).

Operating with the real bolometer parameters also provides the measured values of *1/f* noise knee frequency for each detector. These values are used as a series of offset values from the SPIRE nominal detector knee frequency (0.1 Hz). For example, when the nominal knee frequency is set to 0.1 Hz, the realistic values are set. In the case where the knee frequency is set to 1 Hz, the same scatter will be seen but with 1 Hz added to each value.

1.20.2 Module Parameters

Input Parameters

Input category	Parent Module	Parameter	Name	Type	Units	Values	Description/comments
System	Astro-power	Astronomical power timeline	QsigPSW QsigPMW QsigPLW	2D float array	W		
System	Back-ground	Background power timeline	QbackPSW QbackPMW QbackPLW	2D float array	W		
System	Thermal	BDA temperature	T0_PSW T0_PMW T0_PLW	1D float array	K		
User	Optics	Feedhorn efficiencies	eta_feed	float		0.8	
User	Optics	Spillover efficiency	eta_spill			0.8	
System	Optics	Instrument spectral response function	t_PSW t_PMW t_PLW	2D float array			Overall spectral response of the complete system
User	Optics	Telescope obscuration factor	eta_obsc	Float		0.872	
User		Aperture efficiency	eta_A				
User	Optics	Telescope effective diameter	Dtel	Float	m	3.285	
System	Optics	Emissivity profile for each component	e	1D float array			Derived from input data file
System			temp				
User	Optics	lambda	lambda	1D float	m	250,360,52	

				array		0 um	
User	CORE	Simulator time step length	Step_size	Float	s	12ms	
User		Use of real bolometer parameters switch	real_bolo_parameters	Integer		0/1	If set to 0 then nominal values used, else data read from file
User		Nominal 1/f detector noise knee frequency	fknee_nom	Integer	Hz	0.1	
User	Detectors	Implemented 1/f noise knee frequency	fknee	1D float array	Hz		1 value per detector
System		Noise calculation switch	noise_init=en_det				KEYWORD
System		Module initialisation switch	IN				KEYWORD
User	Thermal	Nominal base plate temperature	T0_nom	float	K	0.3	
User	Detectors	Detector noise switch	noise_10	Integer		0/1	
User	Detectors	Detector 1/f noise switch	fnoise_10	Integer		0/1	

Output parameters

Output category	Parent Module	Parameter	Name	Type	Units	Values	Description/comments
Time line	Detectors	Detector voltage output (noiseless)	VoutPSW VoutPMW VoutPLW	2D float array	V		Noiseless voltage time line. Save to disk to save active memory
Time line	Detectors	Signal + noise voltage detector output	nsigPSW nsigPMW nsigPLW	2D float array	V		Noiseless voltage time line. Save to disk to save active memory

1.21 Sampling system (sampling)

This module low-pass filters and samples the output detector data time line. The data is sampled at the rate specified by the user. This system replicates the SPIRE onboard 5 Hz analogue within the physical system.

1.21.1 Module operation

Each detector voltage time line is filtered by multiplication in Fourier space with a 5 Hz filter profile. This filter profile used is restored from a file containing the measured filter data.

The data is then sampled at a given frequency, where the sampling frequency is lower than the simulator step frequency. A linear interpolation is performed when a sampling point does not match an integer number of simulator time steps.

1.21.2 Module Parameters

Input Parameters

Input category	Defining Module	Parameter	Name	Type	Units	Value	Description/comments
User	Core	Simulator time step	Step_size	2D float array	s	Nom = 12 ms (83.3 Hz)	Simulator operating time step
System	Detectors	Noisy voltage detector time line	nsigPSW nsigPMW nsigPLW	2D float array	V		Bolometer output timelines including noise
User	Sampling	Sampled data time step	Samp_step	Float	s	Nom = 36 ms (27.8 Hz)	Sampled output time step (i.e. 1/samping frequency)

Output Parameters

Output category	Defining Module	Parameter	Name	Type	Units	Values	Description/ comments
Sampling	Sampling	Sampled detector timelines	SignalPSW SignalPMW SignalPLW	2D float array	V		Filtered and sampled data timelines.

Appendix I: Bolometer indexing

PSW Simulator	JPL Index	PSW Simulator	JPL Index	PSW Simulator	JPL Index
51	D6	NaN	R1	58	D11
20	B6	61	D16	9	A10
35	C5	141	T1	86	E10
4	A5	30	B16	40	C10
66	E5	45	C15	24	B10
19	B5	14	A15	55	D10
50	D5	60	D15	8	A9
34	C4	29	B15	70	E9
3	A4	44	C14	39	C9
49	D4	59	D14	23	B9
18	B4	13	A14	54	D9
33	C3	12	A13	7	A8
17	B3	28	B14	38	C8
2	A3	43	C13	69	E8
1	A2	27	B13	53	D8
48	D3	58	D13	22	B8
32	C2	11	A12	37	C7
16	B2	42	C12	68	E7
47	D2	57	D12	6	A7
0	A1	26	B12	52	D7
31	C1	72	E11	21	B7
15	B1	10	A11	36	C6
139	DK1	41	C11	67	E6
46	D1	25	B11	5	A6
88	F12	62	E1	97	G5
134	J11	77	F1	113	H6
73	E12	142	T2	129	J6
119	H12	108	H1	82	F6
104	G12	93	G1	98	G6
89	F13	124	J1	114	H7
74	E13	109	H2	83	F7
135	J12	78	F2	130	J7
120	H13	125	J2	99	G7
105	G13	94	G2	115	H8
90	F14	110	H3	84	F8
75	E14	126	J3	110	G8
136	J13	63	E2	131	J8
121	H14	79	F3	85	F9
106	G14	95	G3	116	H9
137	J14	111	H4	101	G9
91	F15	127	J4	132	J9
122	H15	64	E3	86	F10
138	J15	80	F4	117	H10
107	G15	96	G4	102	G10
123	H16	112	H5	87	F11
140	DK2	64	E4	133	J10
92	F16	128	J5	118	H11
91	E15	81	F5	103	G11

PMW Simulator	JPL Index
6	A7
5	A6
18	B6
31	C7
4	A5
17	B5
30	C6
43	D6
16	B4
29	C5
41	D4
3	A4
28	C4
15	B3
27	C3
14	B2
39	D2
2	A3
1	A2
26	C2
13	B1
0	A1
88	DK1
25	C1
56	E7
44	D7
69	F7
57	E8
82	G8
70	F8
58	E9
83	G9
46	D9
71	F9
59	E10
84	G10
72	F10
60	E11
85	G11
73	F11
61	E12
86	G12
74	F12
87	G13
89	DK2
NaN	SH
NaN	SH
NaN	R2
12	A13
90	T1

PMW Simulator	JPL Index
24	B12
37	C13
11	A12
49	D12
36	C12
23	B11
10	A11
62	E13
48	D11
35	C11
22	B10
9	A10
47	D10
21	B9
34	C10
33	C9
8	A9
20	B8
7	A8
45	D8
32	C8
19	B7
NaN	R1
75	G1
91	T2
50	E1
38	D1
63	F1
51	E2
76	G2
64	F2
77	G3
52	E3
40	D3
65	F3
78	G4
53	E4
66	F4
54	E5
42	D5
67	F5
79	G5
55	E6
80	G6
68	F6
81	G7

PLW Simulator	JPL Index
NaN	R1
7	A8
6	A7
5	A6
8	A9
25	C9
16	B8
15	B7
23	C7
13	B5
14	B6
4	A5
43	T1
12	B4
20	C4
11	B3
18	C2
10	B2
9	B1
2	A3
3	A4
0	A1
44	DK1
1	A2
34	E1
35	E2
36	E3
37	E4
26	D1
27	D2
28	D3
29	D4
17	C1
19	C3
21	C5
45	T2
38	E5
22	C6
24	C8
30	D5
31	D6
32	D7
33	D8
40	E7
39	E6
41	E8
46	DK2
42	E9